Mechanistic Insights & Therapeutic Approaches in Endolysosomal Disorders Affecting the Kidney Proximal Tubule

---

Dissertation

zur

Erlangung der naturwissenschaftlichen Doktorwürde
(Dr. sc. nat.)

vorgelegt der

Mathematisch-naturwissenschaftlichen Fakultät

der

Universität Zürich

von

Beatrice Paola Festa

aus

Italien

Promotionskommission

Prof. Dr. Olivier Devuyst (Vorsitz)

Prof. Dr. Andrew Hall
Prof. Dr. Prisca Liberali
Prof. Dr. Francesco Emma
Prof. Dr. Carmine Settembre

Zürich, 2019

Summary

The proximal tubule (PT) cells of the kidney reabsorbs a large amount of ions and solutes including low-molecular weight proteins, glucose, phosphate, water and vitamins, which would be otherwise lost in the urine. This function is based on a very efficient transport system constituted by apical endocytic receptors, which enable the binding and internalization of the urinary solutes inside the PT cells, and a well-developed endolysosomal system, which carry out the recycling of receptors at the apical plasma membrane and the processing of the incoming substrates. The endolysosomal compartment is also pivotal for the removal of damaged organelles and intracellular materials through autophagy, a highly conserved quality control system that sustains cellular homeostasis. Inherited endolysosomal disorders affecting the endocytic receptors (e.g. Donnai–Barrow and Imerslund-Gräsbeck syndrome) or the endolysosomal pathway (e.g. Dent disease 1 and 2, Lowe syndrome and cystinosis) cause PT dysfunctions leading to a massive urinary loss of solutes (renal Fanconi syndrome) and severe metabolic complications that may be associated with chronic kidney disease (CKD). Studies of rare, congenital endolysosomal disorders of the PT have contributed to identify fundamental biological processes that operate in kidney epithelial cells. Furthermore, common genetic variants in the components of the endolysosomal machinery have been associated with the risk of CKD in the general population. Despite progresses in understanding the biological rules governing the cross-talk between endolysosomes and function of PT cells, the mechanisms linking defective endolysosomal proteins with disease of the kidney PT remain unclear. In this thesis, I investigated cystinosis and Dent disease, two paradigmatic endolysosomal disorders causing PT dysfunction. By using pharmacologic and genetic approaches in cellular and animal models, I identified novel pathogenic cascades linking endocytosis, vesicular trafficking, lysosomal function, autophagy, and differentiation/function of PT cells. Based on these findings, I tested drug-repurposing therapeutic interventions, which successfully rescued the tubular functions *in vitro* and *in vivo*. These studies improve our understanding of the regulatory mechanisms maintaining PT cell homeostasis and open new avenues for the treatment of endolysosomal disorders.

List of abbreviations

ARP2/3	Actin-Related Protein 2/3
AJs	Adherent Junctions
AREs	Apical Recycling Endosomes
ASEs	Apical Sorting Endosomes
CLC	Chloride Channels
CKD	Chronic Kidney Disease
CCV	Clathrin-Coated Vesicles
CDK4	Cyclin D/Cyclin-Dependent Kinases 4
CREs	Common Recycling Endosomes
DEPTOR	DEP Domain-Containing mTOR-Interacting Protein
EEs	Early Endosomes
ER	Endoplasmic Reticulum
ESCRT	Endosomal Sorting Complexes Required for Transport
EGF	Epidermal Growth Factor
GSH	Glutathione
HSC70	Heat Shock Cognate 70
LEs	Late Endosomes
LDLR	Low-Density Lipoprotein Receptor
LMW	Low-Molecular-Weight
MLST8	Mammalian Lethal With SEC13 Protein
mTOR	mammalian Target Of Rapamycin
M6PR	Mannose 6-Phosphate Receptors
MVBs	Multivesicular Bodies
OCRL	Oculocerebrorenal
$PI(4,5)P_2$	Phosphatidylinositol-4,5-bisphosphate
PI3K	Phosphatidylinositol 3-Kinase
PT	Proximal Tubule

RHEB	RAS Homolog Enriched in Brain
RAP	Receptor-Associated Protein
RME	Receptor-Mediated Endocytosis
REs	Recycling Endosomes
RAPTOR	Regulatory-Associated Protein of mTOR
RFS	Renal Fanconi Syndrome
SNX9	Sorting Nexin 9
TJs	Tight Junctions
TfR	Transferrin Receptor
TGN	Trans Golgi Network
TSC	Tuberous Sclerosis Complex
V-ATPase	Vacuolar H^+-ATPase
WASP	Wiskott–Aldrich Syndrome protein
ZO-1	Zonula Occludens -1
ZONAB	ZO-1 Associated Nucleic Acid Binding

Table of Contents

I. INTRODUCTION

I.1 PROXIMAL TUBULE OF THE KIDNEY

One of the main functions of the kidney is to maintain fluids and electrolyte homeostasis in the body by controlling the reabsorption of solutes and water. The functional unit of the kidney is called nephron and consists of epithelial cells originating from different embryological lineages (1). The nephrons are constituted by a filtrating element, the glomerulus, and a segmented tubular compartment (**Fig.1**). The glomerular filtration barrier selectively filters blood components, generating a dilute primary urinary filtrate containing water, small solutes and low-molecular-weight (LMW) proteins. Subsequently, the urinary filtrate passes through a connected series of epithelial tubules, starting from the proximal tubules, the loop of Henle, the distal tubules, and a final collecting duct, which modify its compositions. The renal tubules of the nephrons express ion and water channels, as well as receptors and transporters that help to concentrate and adjust the composition of the urinary filtrate by reabsorption and secretion (2). This step is very important for fluid homeostasis and maintenance of electrolyte balance. The cells lining the proximal tubule (PT) segment of the kidney play an essential role in this process, as they are able to reabsorb 65% -70% of the entire glomerular filtered load (3).

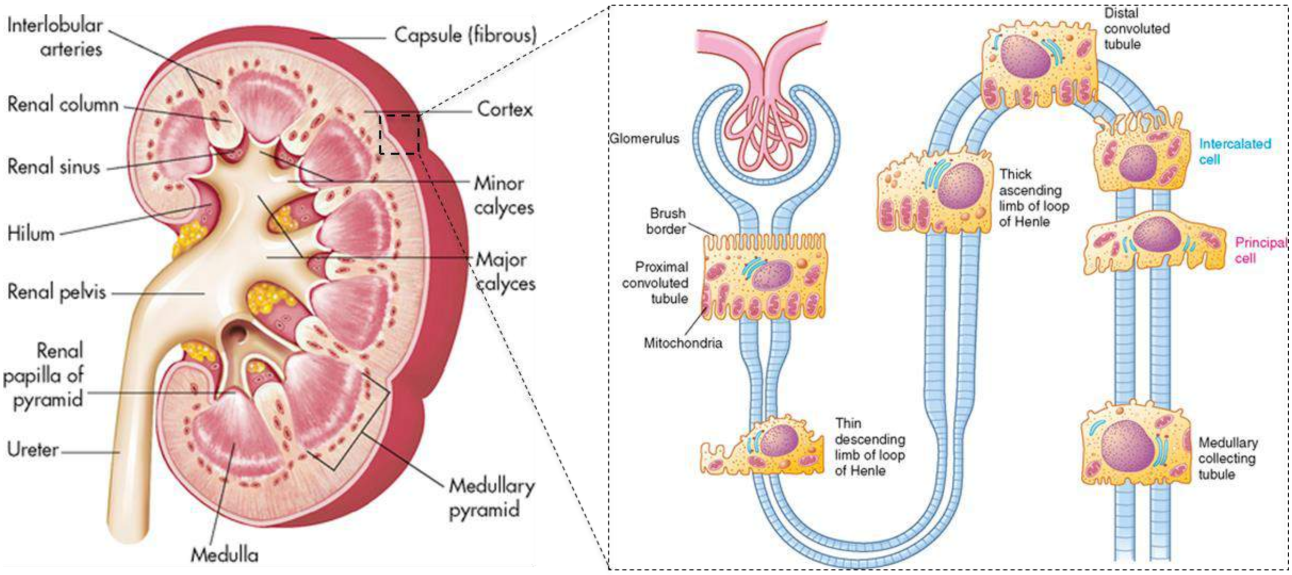

Figure 1: Structure of the nephron, functional unit of the kidney.

Adapted from *McCance K, Huether. Pathophysiology: the basis for disease in adults and children. Ed 6. 2010.*

I.1.1 Structure

The proximal tubule cells are highly differentiated and present numerous morphological adaptations, which aid to carry out their massive transport activity. The presence of tight junctions (TJs) provides a barrier to the paracellular movement and serves as a fence to intramembrane diffusion of components between the apical and basolateral poles (4). The establishment of apico-basal polarity allows an efficient directional transport of molecules from the urine to the blood circulation. Based on differences in cell ultrastructure and function, the PT is classically divided into three segments (S1-S2-S3). Compared to the cells lining the straight segment S3, the cells located in the proximal convoluted segments S1 and S2 are characterized by a more developed apical brush border, which increases the luminal surface and facilitates the reabsorption (3, 5). Compared to S2, S1 presents a higher apical expression of specific cotransporters/receptors, which, along with a prominent endolysosomal system, sustain the uptake and recovery of essential molecules from the urine (**Fig.2a**) (6). The cytosolic region close to the basolateral plasma membrane of PT cells is densely packed with mitochondria (**Fig.2b**). The high quantity of mitochondria is needed to supply energy for the activity of Na+-K+-ATPase, which is necessary to generate the electrochemical gradient triggering both the transcellular and paracellular transport (**Fig.2c**) (7). In summary, the structural characteristics of the PT predispose this kidney segment to perform a highly efficient activity of transport, which is central for maintaining nutrient homeostasis, extracellular electrolyte and fluid balance in the body.

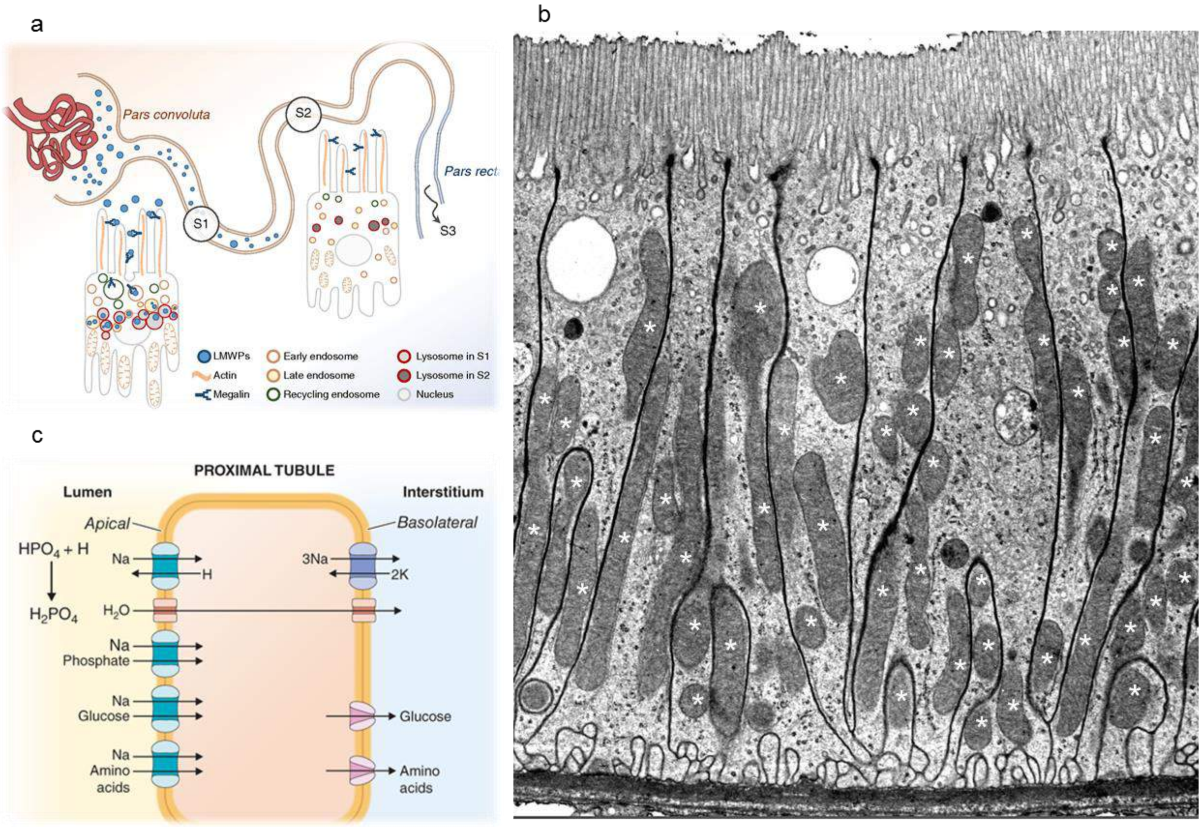

Figure 2: Structure and function of PT.

Adapted from (**a**) *Claus D. Schuh et al. J. Am. Soc. Nephrol. 2018.* (***b-c***) *J. Larry Jameson et al., Harrison's principles of internal medicine. 19th Edition. 2017.*

I.1.2 Function

The proximal tubule controls the body fluid composition and regulates the blood pressure, the intracellular pH and the electrolyte equilibrium by reabsorbing approximately two third of the filtered water and NaCl, a greater proportion of the filtered HCO_3^- and nearly all the nutrients contained in the ultrafiltrate. The primary energy driving the process of PT reabsorption is generated by the basolateral Na^+/K^+-ATPase, which creates an inward negative plasma membrane potential and sets the electrochemical gradient required for Na^+ and $Cl^−$ transport (8). In PT water is passively following the osmolality gradient through transcellular and paracellular pathways. Various cotransporters use the energy of this gradient to promote the transport of solutes (ions, amino acids, and glucose) and the reclamation of $HCO_3^−$, key player of the renal acidification (9). The PT is also the site for the massive reabsorption of LMW (Low-Molecular-Weight) proteins. This function is carried out by multiligand endocytic receptors, which bind and allow the intracellular internalization of a variety of filtered ligands such as albumin, hormones, carrier proteins, enzymes, antigen components and immunoglobulin κ light chains. Once internalized, these substances are metabolized and recovered into the blood circulation; indeed the human urine is virtually devoid of plasma proteins under physiological conditions (6). In addition to the reabsorption of proteins and solutes, the PT is also a metabolic organ. For example, PT cells are the major site of synthesis of the active vitamin D (1,25-dihydroxy-vitamin D), an hormone that increases blood Ca^{2+} levels, contributing to bone mineralization and skeletal health (10). In summary, PT cells have an important role in metabolic clearance, hormones homoeostasis and activation of essential vitamins and provides a protein-free luminal environment for the downstream tubular segments of the nephron (11).

I.2 ENDOCYTOSIS, RECYCLING AND DEGRADATION IN PROXIMAL TUBULE

The uptake of albumin and LMW proteins by PT cells is carried out by a process known as receptor-mediated endocytosis (RME). This process is mediated by the apical expression of multiligand endocytic receptors, which bind the urinary ligands at the apical surface of the cells and allow their intracellular internalization in clathrin-coated vesicles (CCV) (12). Of note, a programmed series of phosphoinositide conversions is required to enable the maturation of these vesicles and their detachment from the plasma membrane (13). Many different cargoes can be packaged through the RME, which is therefore considered a versatile pathway. Once cargoes have been internalized in clathrin vesicles, they are sorted in the early endosomes (EEs) and either recycled to the apical surface or targeted to the late endosomes (LEs) and finally to the lysosomes for degradation (14). Several genetic and acquired (acute and chronic) kidney diseases are characterized by the impairment of the endocytosis and/or defective processing of the urinary ligands within the PT, suggesting that these processes are fundamental for the global renal health. A better understanding of the molecular mechanisms governing these events is needed to identify new therapeutic targets and prevent or limit kidney diseases.

I.2.1 Clathrin-dependent receptor-mediated endocytosis

I.2.1.a Multiligand endocytic receptors

The multiligand endocytic receptors megalin and cubilin mediate the uptake of the majority of proteins and many other molecules, which are filtered daily through the glomerulus. In the kidney, megalin (also known as LRP2 or gp330) is expressed predominantly at the apical surface and in the endocytic compartment of PT epithelial cells. Megalin is a member of the family of low-density lipoprotein receptor (LDLR) and shares many features with the other members of this group of archetypal endocytic receptors (15). The structural elements composing the megalin ectodomain are: (i) four clusters of cysteine rich complement-type repeat motifs, which constitute the ligand-binding regions; (ii) seventeen epidermal growth factor (EGF)-like repeats and (iii) eight beta propeller spacers, characterized by YWTD motifs involved in the release of ligands in the acidified endocytic compartments (15). The cytoplasmic tail of megalin contains two NPXY motifs that mediate the clustering of the cargo/receptor complex in the endocytic vesicles, and an additional NPXY-like motif, known as VENQNY, that may be involved in the targeting of the receptor to the apical surface (**Fig.3a**) (16). It has been shown that the transmembrane domain of megalin undergoes to regulated proteolytic cleavage; however, the physiological significance of this event is unclear (17). Folding and trafficking of megalin from the endoplasmic reticulum (ER) to the plasma membrane is facilitated by the interaction with the chaperone receptor-associated protein (RAP), which prevents the premature binding of the newly synthesized receptor with ligands, thus avoiding megalin aggregation and its retention in the ER (18). The essential role of megalin in the reabsorption of filtered ligands has been substantiated by the striking LMW proteinuria observed in mice lacking this receptor (19, 20). An additional role of megalin in sustaining the proteolytic function of PT cells is mediated via the uptake of lysosomal enzymes from the tubular lumen (21). Megalin can bind ligands independently or in cooperation with cubilin, also known as the intrinsic factor cobalamin receptor. The structure of this receptor is characterized by (i) an initial amino-terminal stretch of 110 amino acids, followed by (ii) eight EGF-like repeats and (iii) 27 tandem

CUB domains, which occupy the majority of the protein sequence and act as binding-sites for a variety of ligands (**Fig.3a**) (22). Cubilin does not exhibit transmembrane domains, therefore it interacts with megalin to stabilize itself at the plasma membrane and participate in the RME (23). The apical sorting of cubilin relies critically on its interaction with Amnionless (AMN). This is a 38–50 kDa transmembrane protein, which plays a key role in ensuring the membrane anchorage of cubilin, its trafficking along the biosynthetic pathway and its recycling to the plasma membrane (24). Cubilin shares many ligands with megalin, however, protein such as transferrin, intrinsic factor-vitamin B12 complex, and apoA1 are bound exclusively by cubilin. Up to now, no animal models harboring targeted deletion of cubilin gene have been published. Previous studies showed that cubilin expression plays a key role during embryogenesis, thus its absence could affect the survival (25). Human mutations in megalin and cubilin result in rare genetic conditions clinically described as Donnai–Barrow (# MIM 222448) and Imerslund-Gräsbeck (# MIM 261100) syndromes, respectively. Previous studies of these genetic disorders demonstrated that loss of function of one or the other protein leads to a reduction of the apical endocytic activity, which results in a dramatic tubular proteinuria. These observations substantiate the essential role of these receptors in the human kidney physiology (6).

I.2.1.b Clathrin-dependent endocytosis

The binding of urinary ligands with megalin and cubilin induces a formation of a ligand-receptor complex, which is internalized in CCV). This process allows to select and gather many different proteins in one vesicle and to coordinate cellular responses to the external environment. In the initial phase of the endocytosis, the heterotrimeric adaptor protein complex AP2 is recruited at the plasma membrane through its binding with phosphatidylinositol-4,5-bisphosphate (PI(4,5)P_2) and with other adaptor proteins, which interact with megalin and cubilin/amnionless complex to ensure their internalization (26, 27). This event creates a platform for the assembly of hexagonal lattices of clathrin triskelia, which are necessary for enhancing membrane tension at the plasma membrane and facilitate vesicles budding (12). The scission of the vesicles rely on the capacity of the BAR domain-containing protein sorting nexin 9 (SNX9) to coordinate membrane dynamics at the neck of the nascent vesicles. Indeed, SNX9 interacts with N-WASP to trigger actin nucleation and increase membrane bedding and with the GTPase dynamin to mediate fission (**Fig.3b**) (28, 29). Once the vesicles detach from the plasma membrane, the clathrin coat is disassembled by the combined action of the ATPase heat shock cognate 70 (HSC70) protein and its cofactor Auxilin (30,31). Of note, changes in the phosphoinositides composition mediated by the inositol polyphosphate 5-phosphatase OCRL (Oculocerebrorenal protein) and other enzymes are also required for the process of uncoating. This event is fundamental as it allows the vesicles to progress their travel and fuse with the target endosomes.

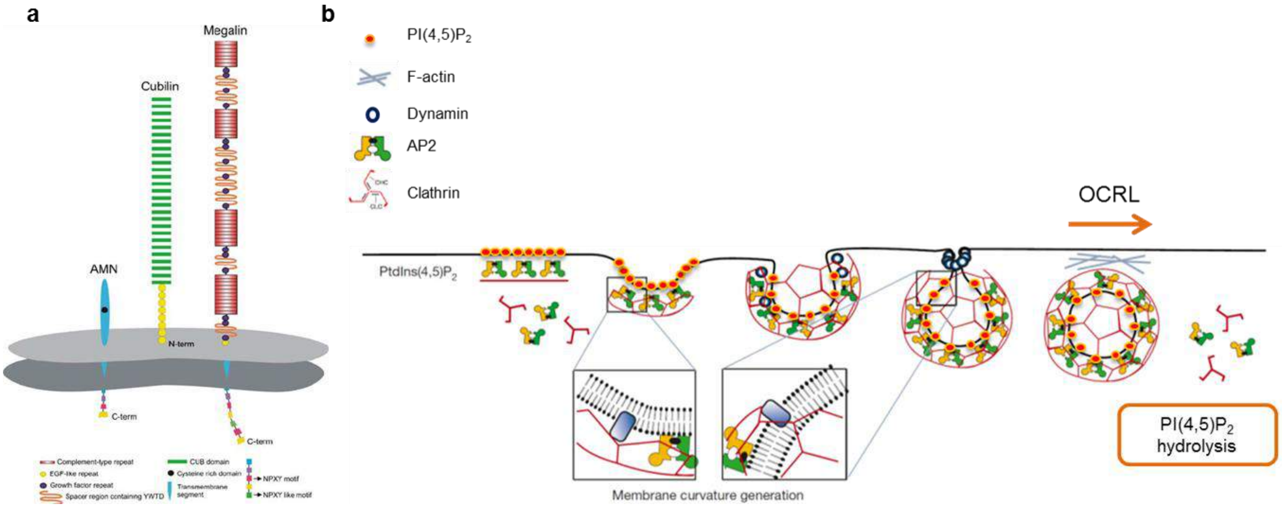

Figure 3: Multiligand endocytic receptors and clathrin-dependent endocytosis.

Adapted from ***(a)*** *Nielsen R, Christensen EI. Pediatr.Nephrol. 2010.* ***(b)*** *Sean D. Conner & Sandra L.Schmid. Nature. 2003.*

I.2.1.c Endocytic players: adaptor proteins, phosphoinositides & cytoskeleton dynamics

Many steps of the endocytic process require directed interactions among membrane lipids, structural elements and regulatory proteins. CCV formation, for instance, is mostly coordinated by AP2, which is attracted at the plasma membrane by high concentrations of PI(4,5)P_2 and, in turn, promotes clathrin assembly and budding of the vesicles. Also other components necessary for the maturation of CCV (including dynamin) are recruited at the plasma membrane via the binding with these lipids (32). Because of their ability to modulate the cytoskeleton dynamics, phosphoinositides are also involved in the excision step of the CCV. Indeed, it has been recently shown that the coincidence of PI(4,5)P_2 and PI(3)P at the membrane of the budding vesicles catalyzes the activation of the SNX-9 dependent signaling pathway (involving N-WASP, and ARP2/3 complex) driving actin polymerization (33). Actin filaments create a tension around the neck of the vesicles, which help them to detach from the plasma membrane. In the subsequent trafficking steps a phosphoinositide conversion from high (plasma membrane) to low (early endosomes) levels of PI(4,5)P_2 is required for uncoating of CCV and actin disassembly. Of note, the 4,5-bisphosphate 5-phosphatase OCRL plays a critical role in this process. Indeed, the loss of OCRL function leads to inefficient clathrin uncoating and impaired release of the actin nucleating machinery resulting in endocytic trafficking defects (34). Although the role of this phosphatase has been described to be particularly relevant in maintaining endocytosis in PT cells, mutations in OCRL result not only in kidney dysfunctions but also in brain, muscle and ocular defects (34). Further investigations are needed to explore the function of this enzyme in the extra-renal tissues.

I.2.2 Trafficking of ligands and receptors along the endocytic pathway

I.2.2.a Recycling of receptors

The trafficking of ligands and receptors along the endocytic route is coordinated by a complex molecular machinery functioning at different stations of the endolysosomal pathway. Key players of this machinery are the members of the Rab proteins family that, by recruiting specific effectors, orchestrate the sorting of the receptor/cargo complex as well as the motility and tethering of the endocytic vesicles. A specific set of Rab GTPases establishes an identity code for each compartment of the endocytic route (35). Rab5, is associated with EEs (pH ~6.9), which are the first membrane-bound organelles to fuse and receive material from the endocytic vesicles. In these slightly acidified organelles, occurs the pH-dependent dissociation of the ligands from the receptors. Receptors are recycled back to the surface in tubular structures originating from the EEs while the ligands are released into the LEs. Receptors can undergo slow or fast recycling. In non-epithelial cells “Fast” recycling is regulated by Rab4 and occurs through the apical sorting endosomes (ASEs) (36) while “slow” recycling is driven by Rab11 or Rab8 and is mediated by the recycling endosomes (REs) localized close to the nucleus (**Fig.4, left**) (14). Studies in polarized epithelial cells demonstrate the involvement of Rab11- and Rab8-positive compartments also in the “*fast apical recycling*” of megalin. In this case, megalin traffics through the Rab4-ASEs and subsequently crosses the Transferrin receptor (TfR) pathways at Rab8-common-recycling endosomes (CREs). Whereas TfR recycles to the basolateral membrane from CREs, megalin reaches the apical membrane via the Rab11-apical recycling endosomes (AREs) (**Fig.4, right**). These recycling cycles last about 15 minutes. The fast recycling of megalin receptor is consistent with its very efficient role in protein reabsorption. In conclusion, it is essential to study endocytic recycling in epithelial polarized cells as non-epithelial cells fail to distinguish the different recycling routes and recycle TfR and megalin through the same compartments, thus providing an artificial trafficking scenario (37).

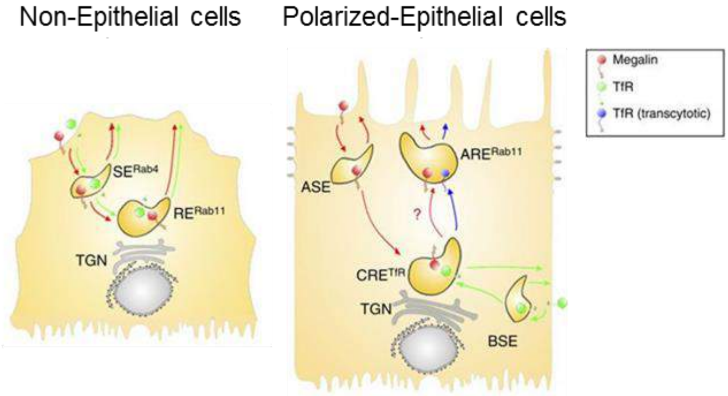

Figure 4: Recycling of endocytic receptors in epithelial and non-epithelial cells.
Adapted from *Andres E. Perez Bay et al. Nat. Commun. 2016.*

I.2.2.b Endosome maturation and cargo sorting

As cargos enter the endosomal network, they are sorted in the EEs towards their final destination. Dissociation of the cargos from the receptors in the EEs and their delivery and degradation into the LEs and lysosomes is dependent on the correct acidification of each of these organelles by the vacuolar H^+-ATPase (V-ATPase). V-ATPase actively transports protons from the cytosol into the endosomal and lysosomal lumen with the energy obtained from the hydrolysis of ATP to ADP. Previous studies show that chloride channels (ClCs) conduct passive Cl− ion current, which counteracts the proton accumulation produced by the V-ATPase. These ClCs stimulate V-ATPase activity at the endolysosomal compartment, thereby facilitating the acidification (38). The crucial role of these channels in maintaining the activity of the endolysosomal network is evidenced by the fact that loss of function of ClCs and pharmacological inhibition of V-ATPase are associated with pathologic conditions characterized by major defects of the endocytic uptake and/or lysosomal impairment (39). The EEs act as major sorting stations, allowing the receptors to recycle back to the cell surface and the ligands to be transported to LEs and finally to lysosomes for degradation (**Fig.5**). The maturation of EEs into LEs is characterized by the formation of multivesicular bodies (MVBs). During this process the endosomal sorting complexes required for transport (ESCRT), drives the sorting of ubiquitinated cargos from the endosomal limiting membrane into luminal vesicles. Subsequent fusion of the mature LEs/MVBs with the lysosomes, results in the degradation of the cargos in the lysosomal lumen (40). This maturation step is accompanied by the exchange of Rab5 to Rab7, which regulates the late endocytic trafficking downstream the biogenesis of MVBs and cargo sequestration (41). Finally, LEs are also involved in the activation of quiescent lysosomes. LEs replenish the lysosomes with acid hydrolases that, upon activation in the lysosomal lumen, enable the digestion of the molecules reabsorbed by endocytosis (42). The tight regulation of the various stages of endosomal maturation, including the sorting of receptors, cargos and hydrolytic enzymes, is essential in PT cells, where a functional processing of endocytic substrates is needed to ensure the high reabsorptive activity.

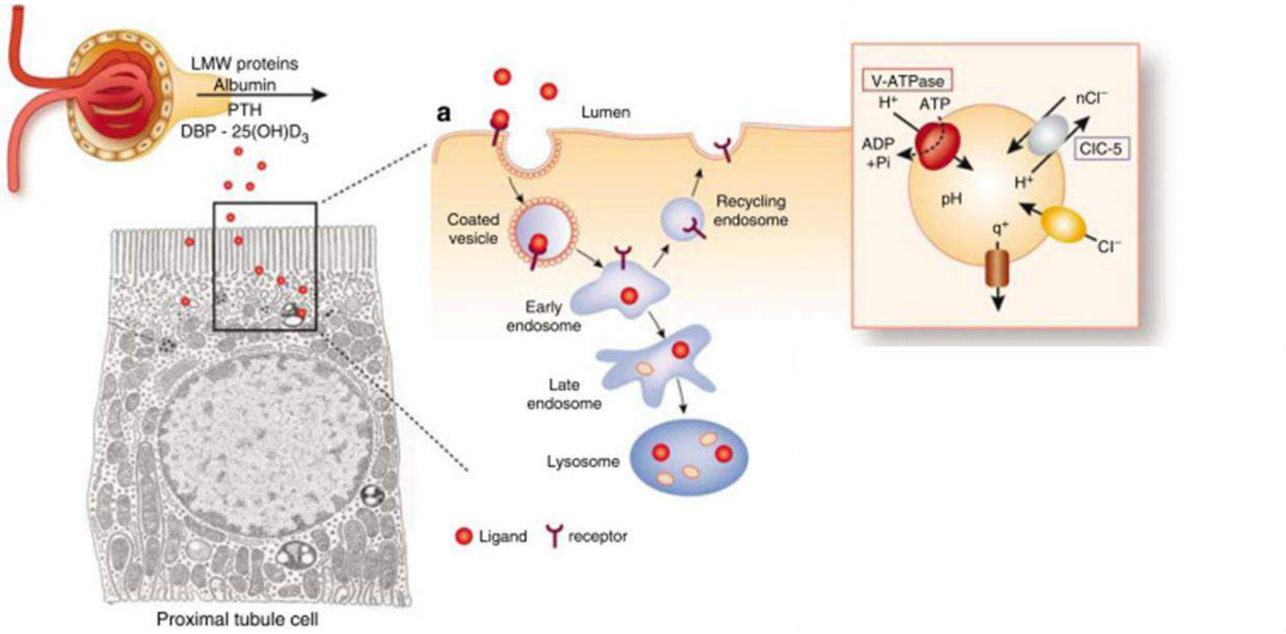

Figure 5: Endocytosis and ligands processing in PT cells.
Adapted from *Devuyst O.and Pirson Y., Kidney Int. 2007.*

I.2.3 Lysosomal degradation of endocytic/autophagy cargo

I.2.3.a Lysosomal dynamics and function

The lysosome, described for the first time by Christian de Duve, is a single-membrane organelle, which is able to degrade a large array of both extracellular and intracellular substrates (43). The majority of extracellular substrates are transported to the lysosomes via the endocytic route (endosomes-lysosomes fusion) while intracellular substrates reach the lysosomes via the autophagic pathway (autophagosomes-lysosomes fusion). By mediating the catabolism of endocytic and autophagy cargos, lysosomes maintain the metabolic balance and cellular homeostasis (44). Lysosomal degradation is critical also for other physiological events, including downregulation of signaling receptors, killing pathogenic organisms and presenting antigens. In addition to LEs and autophagosomes, lysosomes are also able to fuse with the plasma membrane (**Fig.6**) (45). This event allows to repair plasma membrane ruptures and to secrete the lysosomal content in the extracellular space. The latter process mediates important biological functions, such as bone resorption by osteoclasts and cytotoxicity of killer T lymphocytes (44). Lysosomal fusion with other cellular membranes is carried out by a molecular machinery involving Rab7, HOPS complex, and SNARES while the degradative function is executed by luminal hydrolases. Normally, these enzymes are recognized by mannose 6-phosphate receptors (M6PR) at the trans Golgi network (TGN), packed into vesicles and delivered to endosomes and later on to lysosomes for completing lysosomal maturation (46). Most hydrolases are functioning only in acidic pH; therefore a proper lysosomal ionic flux is necessary to ensure their proteolytic activity (47). By driving the proton transport across the lysosomal membrane, the V-ATPase is responsible to generate the acidic pH of the lysosomal lumen (~4.5–5.0). Of note, inhibition of V-ATPase blocks lysosomal acidification and results in impaired lysosomal degradative function (48). Lysosomal degradation of complex molecules is important for energy production and recycling of fundamental units that will be used as building blocks during the biosynthetic process (49). Lysosomal degradation is also necessary for the removal of damaged organelles (e.g., mitochondria), whose intracellular accumulation could be harmful for the cells (50).

Lysosomes are dynamic structures, which undergo to fission and fusion events. Fusion of lysosomes with endocytic or autophagic vesicles generates hybrid organelles from which new primary lysosomes are reformed. Phosphoinositides associated to the lysosomal membrane are involved in this reformation process (51). Indeed, deficiency of either PI(3)P or PI(3,5)P_2 leads to lysosomal swelling and inhibition (52) while defective conversion of PI(4)P to PI(4,5)P_2 is responsible for constitutive lysosomal tubulation (53). Interestingly, the mammalian target of rapamycin (mTOR) covers an important role in controlling the phosphoinositides balance during lysosomal reformation (52). Despite the notable advances during the last decades, much remains to be discovered about the molecular regulation of these complex fusion, fission, and reformation reactions in the late autophagic and endocytic pathway. The investigation of the molecular events underlying the lysosomal homeostatic cycle will be essential for understanding whether these processes are perturbed in the diseases and how to target them.

The transport of substances from the lysosomes back into the cytosol is enabled by specific channels and transporters through mechanisms, which are still not completely understood. Mutations affecting proteins involved in the transport, in lysosomal acidification or linked to the lysosomal function are often associated to a group of about 50 diseases named lysosomal storage disorders. These pathologic conditions are characterized by an accumulation of waste products in the lysosomes, resulting in the formation of large intracellular vacuoles. Most of the patients with a lysosomal storage disorder are born apparently healthy and the symptoms develop progressively. The lysosomal storage diseases have a broad spectrum of clinical phenotypes and may affect a variety of organs including the kidneys (54). Two inherited lysosomal diseases manifesting with kidney dysfunctions are Fabry disease and cystinosis. Previous studies elucidated the key role of the lysosomes for the kidney function; however, further work is needed to characterize the specific implications of lysosomal proteins in kidney disease and setting up new treatments (55).

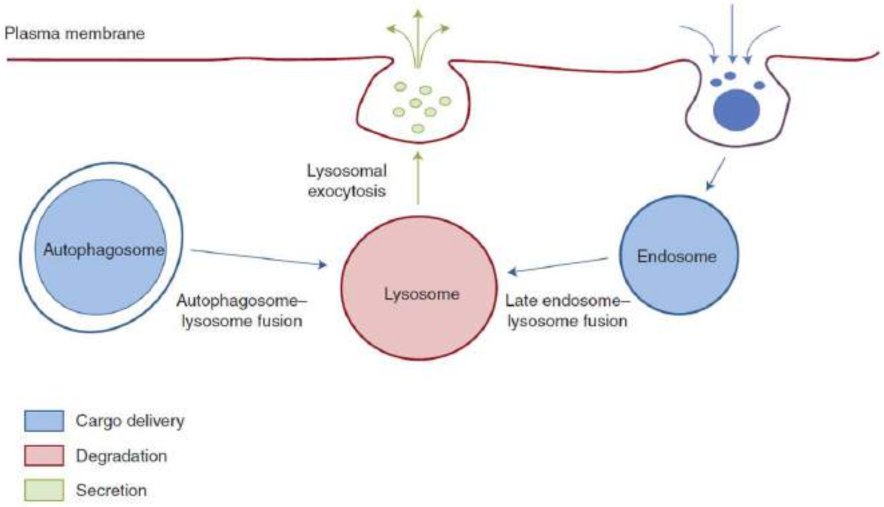

Figure 6: Lysosomes at the crossroad between endocytosis & autophagy pathway.
Adapted from *Carmine Settembre and Andrea Ballabio. Cold Spring Harb. Perspect. Biol. 2014***.**

I.2.3.b Autophagy & organelles homeostasis

Autophagy is an evolutionarily conserved degradative pathway, which occurs at a basal rate in most cell types. This process is needed to eliminate protein aggregates and damaged organelles in order to maintain cytoplasmic homeostasis. This event includes the degradation of dysfunctional mitochondria via mitophagy, a cytoprotective process that limits both the production of reactive oxygen species (ROS) and the release of toxic mitochondrial proteins (56). As functional and numerous mitochondria are essential to carry out the high transport activity of kidney PTs, the homeostatic role of autophagy to regulate the mitochondria life cycle is key to safeguard the function of this kidney segment (57). Autophagy is activated by cellular stresses such as starvation, hypoxia or chemotherapeutic drugs. In these conditions of energy depletion, autophagy degradation of proteins, lipids and carbohydrates is essential to produce energy and to fuel the metabolic needs of the cells (58). Upon induction of autophagy, a protein complex consisting of ULK1/2, ATG13, FIP200 and ATG101 assembles on the pre-autophagosomal structure, called phagophore, and triggers the *initiation* of autophagosomes formation. In mammals, the origin of the autophagosomes membranes is debated. Many studies have identified the site of formation of the isolation membrane at ER in regions called omegasomes. Other potential platforms for the autophagosomes formation include mitochondria, ER-Golgi and ER-mitochondria contact sites, REs and plasma membrane (59). The second step of autophagy is called *nucleation*. At this stage the class III phosphatidylinositol 3-kinase (PI3K) complex consisting of Beclin-1, VPS34, VPS15 and ATG14 is gathered on the phagophore and promotes the local production of PI(3)P, which, in turn, recruit other effector proteins like WIPI1/2 (60). The final *expansion and closure* steps are carried out by two ubiquitin-like conjugation systems. The first system, comprising E1-like Atg7 and E2-like Atg10 proteins, catalyzes the formation of the Atg12-Atg5-Atg16L1 complex, which is needed for the efficient closure of autophagosomes (61). The second ubiquitin-like conjugation system, coordinated by Atg7 and the E2-like Atg3 enzymes, enables the lipidation of LC3/Atg8 on the autophagosomal membrane (**Fig.7**). LC3/Atg8 proteins have multiple functions in autophagy. In addition to promote the expansion and closure of phagophore membranes, they bind adaptor proteins (such as ubiquitin-binding protein sequestosome1 SQSTM1/p62), which mediate the recruitment of different cellular structures and protein aggregates within the autophagosomes (62). To date, LC3-II is the only well-characterized protein that is specifically localized on the autophagic structures, thus its detection directly correlates with the amount of autophagosomes in the cells. When initiation, elongation, and expansion have been completed, the autophagosomes close and fuse with lysosomes to form the autophagolysosomes. In these organelles, the final degradation of intracellular substances takes place (63).

Autophagy is not only acting as a quality control machinery for maintaining cellular homeostasis but it is also involved in many other biological processes including cytoprotective mechanisms, development and differentiation. Furthermore, the induction of autophagy has been shown to promote longevity in many species, suggesting that autophagy may be a player in the ageing process (64). Given its key role in many physiological functions, it is not surprising that defects in autophagy are associated to various human disorders including cancer, neurodegeneration, inflammatory diseases and chronic kidney diseases (65). Considering these observations, pharmacological approaches to modulate this pathway are currently receiving significant attention.

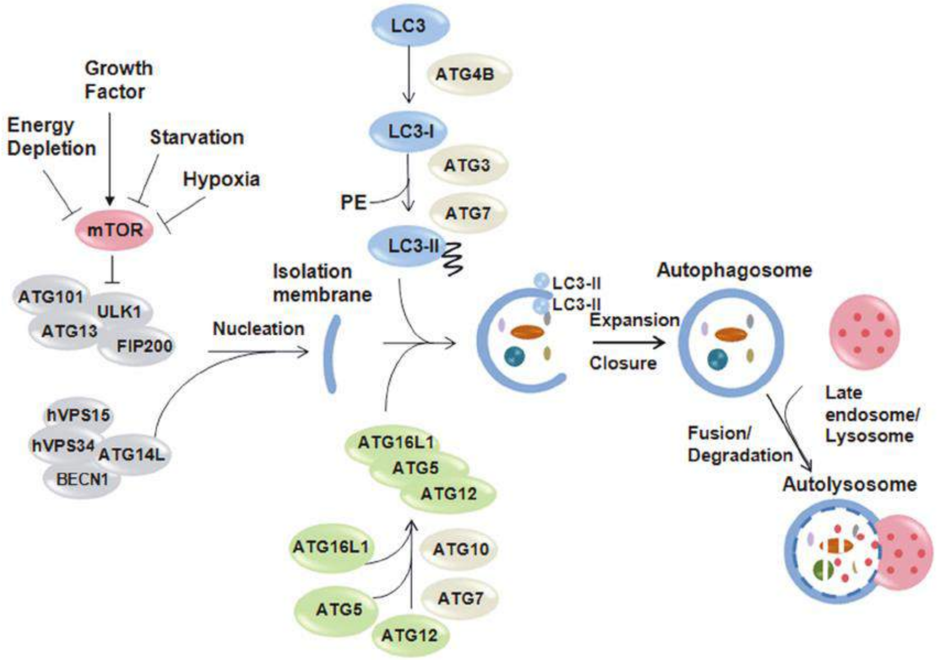

Figure 7: Schematic steps of autophagy in mammals.

Adapted from *Hacer Ezgi Karakaş, Devrim Gözüaçik. Turkish J. Biol. 2014.*

I.2.3.c mTORC1: lysosomal sensing & regulation of autophagy

Autophagy is regulated by upstream signaling including growth factors, amino acids, glucose and energy status. Many of these signals are integrated by the kinase activity of mTOR, which is the target of a molecule named rapamycin -a macrolide produced by Streptomyces Hygroscopius bacteria (66, 67). mTOR is an atypical serine/threonine protein kinase that cooperates with several proteins to form two different complexes called mTOR complex 1 (mTORC1) and 2 (mTORC2). mTORC1, the better characterized of the two complexes, is composed by the scaffolding proteins RAPTOR (regulatory-associated protein of mTOR), mLST8 (mammalian lethal with SEC13 protein), and DEPTOR (DEP domain-containing mTOR-interacting protein). mTORC1 is recruited on the lysosomal surface through physical interactions with the Rag GTPases (RagA or RagB and RagC or RagD). These interactions are enabled by the guanine-exchanging factor (GEF) activity of Ragulator complex, which induces the activation and docking of the Rag GTPases to the lysosomal membrane (68). Once at the lysosome, mTORC1 is activated by the small GTPase Rheb (RAS homolog enriched in brain), which powerfully stimulates its kinase function (69). mTORC1 activity is dependent on the luminal lysosomal content of amino acids. In presence of amino acids, mTORC1 is recruited on the lysosomal membrane and activated through a mysterious mechanism involving conformational changes of the V-ATPase and the Ragulator complex. In contrast, amino acids withdrawal causes the release of mTORC1 from the lysosome and its inactivation (**Fig.8**) (69). By inhibiting Rheb activity, the trimeric tuberous sclerosis complex (TSC) is a powerful negative regulator of mTORC1 function. The activity of TSC complex is under the control of numerous extracellular and intracellular inputs including mitogen and growth factor signaling, energy levels, oxygen availability and genotoxic stress (70).

mTORC1 controls the cellular homeostasis through the downstream regulation of various metabolic pathways: on one side, its activation increases cell growth and biosynthetic processes; on the other side, active mTORC1 represses catabolism through the inhibition of autophagy. Conversely, inhibition of mTORC1 induces down-regulation of biosynthetic pathways and activation of the catabolic-autophagy process through the induction of the transcriptional factor EB (TFEB) (71). This double-way regulation of catabolic and anabolic processes is needed to avoid wasting of energy in uncoordinated cycles of synthesis and degradation (70). Given its central role as signaling hub, mTORC1 emerged as a key metabolic rheostat regulating the physiologic function of many organs and tissues in the body, including kidney epithelial cells. Indeed, mTORC1 deregulation has been observed in many kidney diseases. Aberrant activation of the mTOR pathway was detected in patients and animal models of renal transplant rejection, autosomal dominant polycystic kidney disease, renal cell carcinoma, diabetic nephropathy, lupus nephritis and angiomyolipoma. The frequent hyper-activation of mTOR signaling makes it an attractive target for therapeutic interventions and has driven the development of numerous mTOR inhibitors, which could be potentially used for the treatment of many human disorders (72).

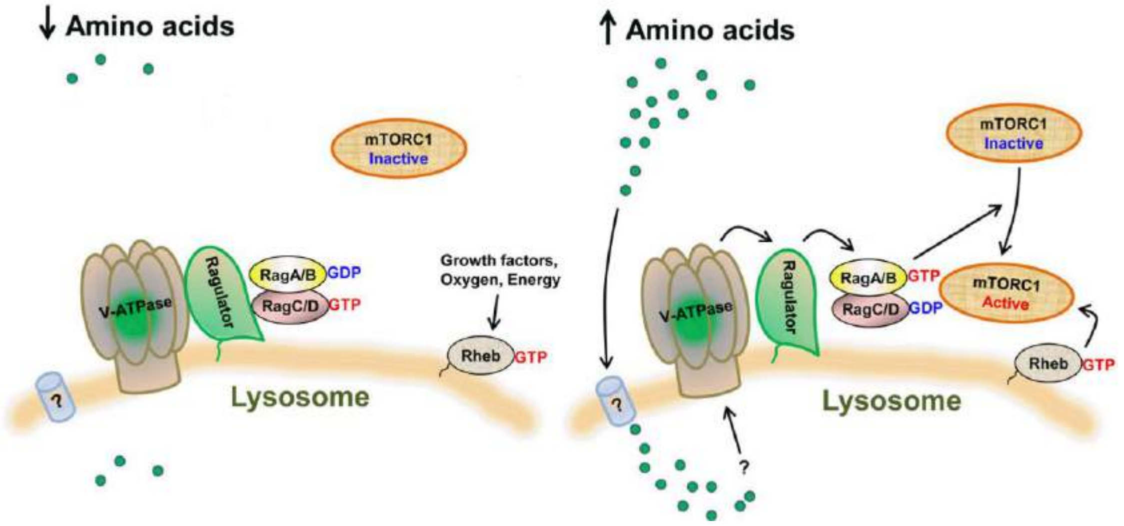

Figure 8: Amino acid signaling to mTORC1.
Adapted from *Kim, S.G., Buel, G. R. & Blenis. J. Mol. Cells. 2013*.

I.3 TIGHT JUNCTIONS AND REGULATION OF CELL DIFFERENTIATION

Epithelia are composed by continuous cellular sheet consisting of polarized cells adhering to each other. The intercellular adhesions of epithelial cells are constituted by the apical junctional complex, which comprises tight and adherent junctions (AJs) as well as desmosomes. The epithelial TJs have three major functions: (i) as constituents of semipermeable barriers controlling paracellular diffusion of solutes and fluids, (ii) as fences maintaining the apical-basal polarity of cells of a confluent epithelium and (iii) as signaling platforms regulating epithelial biogenesis and function (73). The renal tubular epithelium is characterized by the expression of TJs, which play a pivotal role in sustaining the kidney function. Indeed, numerous kidney pathologic conditions, such as ischemia/reperfusion injuries and autosomal dominant polycystic kidney disease present alterations of the TJ complex. The epithelial TJs are composed by proteins belonging to three main families: (i) integral membrane proteins such as claudins, occludins and junctional adhesion molecules, (ii) scaffolding proteins such as zona occludens-1 (ZO-1) and 2 (ZO-2) and (iii) signaling proteins comprising G proteins, kinases and phosphatases (**Fig.9**). Here we focused on the scaffolding protein ZO-1, which not only exerts functions related to preserve the structural barrier of TJ but also participates in signal transduction pathways regulating the transition of renal epithelial cells from proliferative to a differentiated state (74).

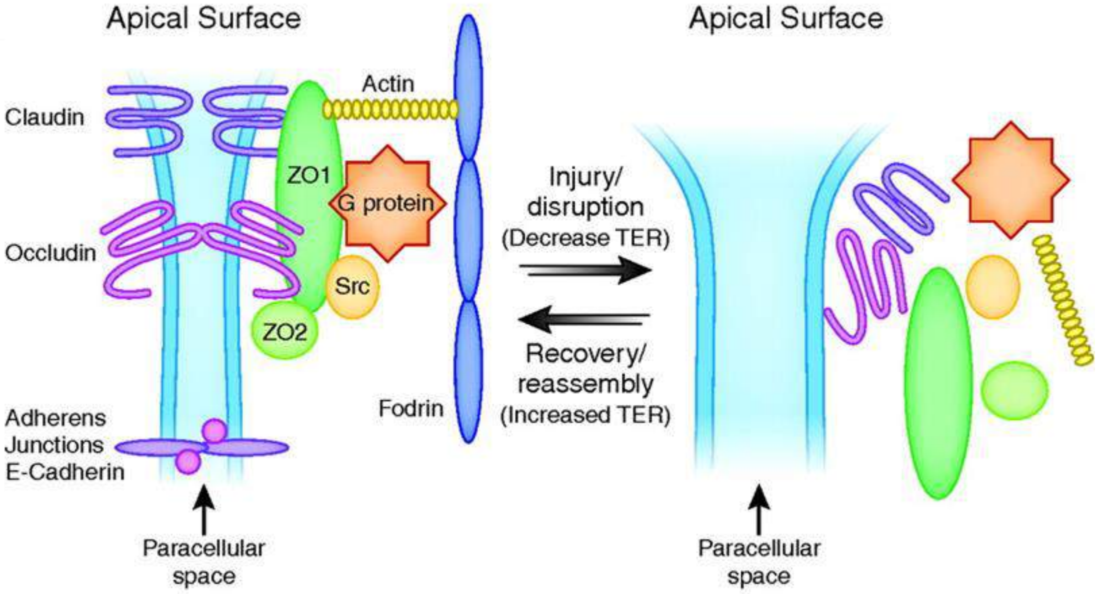

Figure 9: Simplified scheme of major tight junction proteins.
Adapted from *Bradley M. Denker and Ernesto Sabath. J. Am. Soc. Nephrol. 2011.*

I.3.1 Tight junction protein ZO-1

I.3.1.a ZO-1 and plasma membrane barriers

ZO-1 is belonging to the family of membrane-associated guanylate kinase (MAGUK) homologue proteins, which are scaffolding molecules able to stabilize multi-molecular complexes at the cytoplasmic surface of the plasma membrane (75). This function is carried out by the expression of multiple protein-protein interaction domains. ZO-1 interacts with cell adhesion molecules, ion channels and signaling molecules through its PSD-95/discs large/zonula occludens-1 (PDZ) domains. The Src-homology3 (SH3) domains of ZO-1 mediate the interaction with proteins involved in signaling pathways or modulating the cytoskeleton dynamics – such as Ras protein and Src kinase. Finally, the region homologous to mammalian and yeast cytosolic guanylate kinase (GK) is necessary for the assembly of apical surface components, including those guiding the organization of cortical F-actin (**Fig.10**) (76). ZO-1 is a key component of the TJ and plays a central role in the formation of plasma membrane barrier. TJs form two types of barriers: (i) the paracellular ones, which regulate the passive transport of solutes across the tissues and (ii) the intramembrane barriers, which limit the exchange of membrane components between the apical and basolateral pole of the cells. The two barriers overlap for physical location and are structurally related (77). Multiple signaling pathways regulate the integrity of the TJs barriers. One example is represented by Gα12, whose activation leads to tyrosine phosphorylation of ZO-1 proteins resulting in TJ disruption and increased paracellular permeability. Oxidative stress and calcium levels have also been described to govern TJs assembly, however, many other signaling coordinating this process remain to be further explored (78, 79).

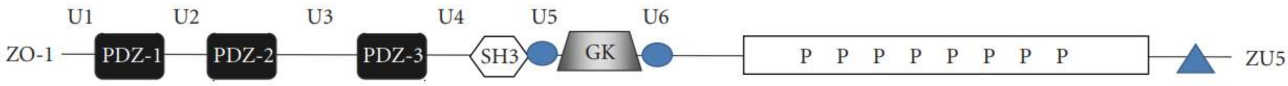

Figure 10: Structural and functional properties of ZO-1.

Adapted from *H. Bauer et al. J. Biomed. Biotechnol.2010*.

I.3.1.b ZO-1 crosstalk with ZONAB signaling pathway

Beyond their role of permeability barriers, TJs are also important signaling platforms. TJs transduce signals to the intracellular environment to regulate various physiologic processes. Recent studies indicate the crucial involvement of the TJ protein ZO-1 in epithelial cell proliferation and differentiation (77). In kidney epithelial cells ZO-1 interacts with the Y-box transcription factor ZONAB (ZO-1 associated nucleic acid binding protein). ZONAB transcriptional activity is inversely correlated with the TJs levels of ZO-1. In confluent polarized kidney cells, the high expression of ZO-1 blocks ZONAB to the TJs. In contrast, the low level of ZO-1 in non-confluent kidney cells results in enhanced translocation of ZONAB in the nucleus (**Fig.11**). Nuclear ZONAB promotes the expression of genes involved in proliferation while repressing the genes driving apical differentiation (80). Thus, the ZO-1 trapping of ZONAB at the TJs is essential for maintaining the differentiated non-proliferative state of polarized epithelial kidney cells (81).

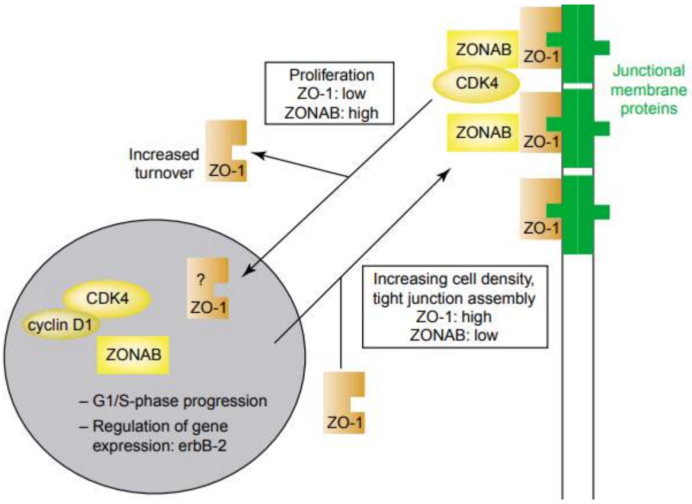

Figure 11: ZO-1/ZONAB axis regulates epithelial proliferation and differentiation.

Adapted from *Maria S. Balda and Karl Matter. Trends Cell Biol. 2003*.

I.3.2 Transcription factor ZONAB

I.3.2.a Proliferation

Y-box transcription factors are multifunctional regulators of gene expression and have been described as major players in cell proliferation. The Y-box transcription factor ZONAB also known as DbpA/Msy3 (DNA binding protein A/Mouse Y box protein3), is particularly relevant for the kidneys, where it contributes to modulate epithelial growth during development. Previous works demonstrated that active nuclear ZONAB is abundant in the peripheral regions of growing kidney cells, which are characterized by low cell density, low TJ expression of ZO-1 and increased proliferation. Conversely, the ZONAB nuclear activation decrease in central regions, where the cell density is high, ZO-1 expression is high and the proliferative rate is low (**Fig.12**) (81). These studies highlighted a direct correlation between nuclear ZONAB and proliferation during kidney ontogeny. Further studies demonstrated that ZONAB regulates the G_1/S-phase transition of the epithelial cell cycle by two mechanisms: (i) the transcriptional regulation of cell cycle factors, such as proliferating cell nuclear antigen A (PCNA) and cyclin D1 and (ii) the modulation of the nuclear shuttling of cyclin D/cyclin-dependent kinases 4 (CDK4) (82). Extensive transcriptional and biochemical analyses demonstrated that PCNA and cyclin D1 are direct target genes of ZONAB. However, ZONAB can regulate epithelial cell cycle also through physical interaction with CDK4. When ZONAB is trapped at the TJs, the entering of CDK4 in the nucleus is prevented. Conversely, the nuclear translocation of ZONAB results in increased nuclear shuttling of CDK4 and progression of cell cycle (**Fig.11**) (81). Taken together, these data suggest that ZONAB is an important player of the mechanisms that sense epithelial density (in this case through ZO-1) and drive the transcriptional program regulating cell proliferation.

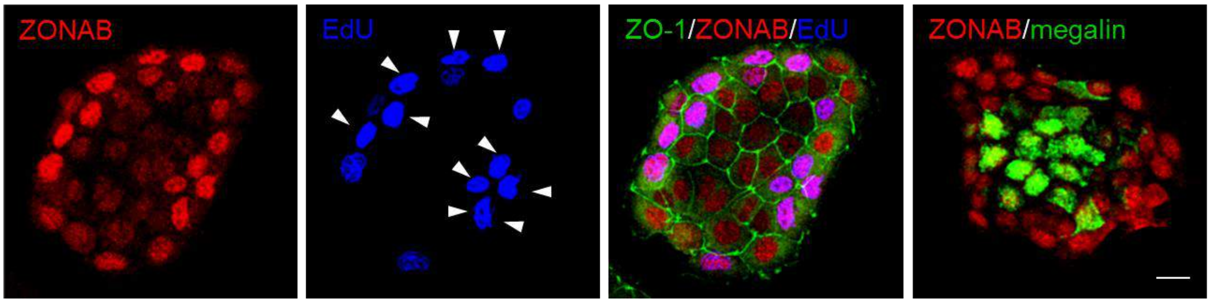

Figure 12: ZONAB overexpression promotes proliferation and represses differentiation.
Adapted from *Wânia R. Lima et al. J. Am. Soc. Nephrol.2010.*

I.3.2.b Differentiation

Previous investigations *in vivo* and *in vitro* showed that ZONAB expression and localization determine the state of proliferation and differentiation of proximal renal tubular cells. At the early stage of kidney development, nuclear ZONAB-expressing cells are highly proliferative (high

PCNA) and scarcely differentiated (low megalin). In the subsequent stage, the decrease of nuclear ZONAB expression is mirrored by a parallel increase of non-proliferating, megalin-expressing cellular population. Further studies confirmed the inverse relation between nuclear ZONAB and apical differentiation (**Fig.12**) (80). *In silico* and chromatin immunoprecipitation analyses demonstrated the presence of ZONAB binding sites in the promoter regions of megalin and cubilin. Functional data indicate that ZONAB is a direct repressor of genes required for apical endocytosis including megalin and cubilin (83). This is important as it suggests that dysregulation of ZONAB activity might be involved in numerous genetic kidney diseases characterized by defective tubular reabsorption.

I.4 DISEASES OF THE PROXIMAL TUBULE OF THE KIDNEY

The epithelial cells that line the kidney PT play a pivotal role in the reabsorption of water, electrolytes and processing of filtered proteins. This function relies on a well-differentiated apical compartment and a particularly well-developed and efficient endolysosomal network. Dysfunction of endosomal and/or lysosomal compartment caused by congenital or acquired disorders often leads to generalized dysfunction of the PT, causing massive urinary loss of solutes (renal Fanconi syndrome) and severe metabolic complications, which can result in the development of CKD (34). The section below provides an overview of our current understanding of the molecular mechanisms underlying Fanconi syndrome in congenital endolysosomal disorders affecting the kidney PT.

I.4.1 Renal Fanconi Syndrome

Renal Fanconi syndrome (RFS) is described as a generalized dysfunction of the PT resulting in polyuria, phosphaturia, glycosuria, calciuria, proteinuria, aminoaciduria and proximal tubular renal acidosis. These urinary metabolic changes are reflected by multiple clinical complications, which include dehydration and electrolyte imbalances, rickets, osteomalacia, growth retardation, failure to thrive, kidney stones and CKD culminating in ESRD (84). RFS is associated with congenital disorders disrupting the function of endolysosomal pathway of PT cells such as Dent disease, Lowe syndrome and cystinosis -the first cause of RFS in pediatric patients. RFS can also be observed in inherited disorders primarily affecting other cellular compartments, whose function is directly related to the activity of the endolysosomal network, such as mitochondriopathies and metabolic diseases. Although an increasing number of genetic causes have been identified, RFS can also occur as an acquired disorder during adulthood, for instance upon exposure to toxins, drugs and immunoglobulin free κ light chains, which accumulate and damage the endolysosomes (84). The primary therapy for RFS is to replace the substances lost in the urine. For instance, in order to prevent dehydration resulting from polyuria, patients are administered with fluids and electrolytes while metabolic acidosis is treated by small boluses of intravenous sodium bicarbonate. Bone defects, also reported in patients with Fanconi syndrome, can be improved by supplementation with active Vitamin D (85). The multimodality of RFS makes difficult the diagnosis and prevents the setup of causal therapies. Genetic forms represent a major concern as they are difficult to manage being associated with disruption in growth and affecting other organs beyond the kidney. Symptomatic management is still the therapy of choice, thus, further investigations regarding etiologies and therapies are required.

I.4.2 Endosomal disorders: Dent disease and Lowe Syndrome

Dent disease is a heterotypic X-linked proximal tubulopathy. The majority of the cases (~60%) are associated with mutations in *CLCN5*, which encodes the electrogenic Cl^{-}/H^{+} exchanger ClC-5 (Dent disease 1, MIM #300009) (86). However, a subgroup of Dent disease patients (~15–20%) harbors mutations in *OCRL*, the gene encoding the type II phosphatidylinositol (PI) bisphosphate 5-phosphatase OCRL (Dent disease 2, MIM #300555). The clinical profile of Dent disease 1 and 2 is similar: they both present with LMW proteinuria and frequently develop hypercalciuria and progressive renal failure. Mutations in *OCRL* are also associated with the oculocerebrorenal syndrome of Lowe (MIM #309000), which includes systemic manifestations such as congenital cataract, cognitive disability and hypotonia (87). The current therapeutic options for these disorders are only supportive. There is no treatment that targets the causes of these diseases, thus, avoiding the burden associated to the disorders and preventing early death. In this respect, the understanding of how loss-of-function mutations in *OCRL* or *CLCN5* give rise to common clinical entities represents an opportunity to identify molecular pathways that could be targeted for treating both conditions.

Studies in *Clcn5*-KO mouse models reveal that the functional loss of ClC-5 generates a trafficking defects involving megalin and cubilin, which underlies the defective endocytosis and PT dysfunction observed in patients with Dent disease 1 (**Fig.13**) (88). These defects could be explained by the role of ClC-5 at the apical-endosomal compartment of the PT epithelial cells. ClC-5 is mainly expressed at the subapical endosomes of the S1 segment of the PT, where it contributes to the endosomal acidification, and partially at the plasma membrane, where it interacts with megalin and other scaffolding proteins. Initially, the disruption of the endosomal acidification was supposed to be the cause of the endocytic defects resulting from the loss of ClC-5 function. However, not all the disease-causing mutations in ClC-5 result in perturbation of the endosomal pH, suggesting that the defective acidification is, at best, only partially responsible for the endocytic dysfunction (89). Alternatively, the endocytic defect could be explained by the disruption of ClC-5 function at the plasma membrane. Indeed, at the apical surface, ClC-5 interacts with megalin and Cofilin and enables the invagination of endocytic vesicles by coordinating the process of actin depolymerization (90). More insights into the function of ClC-5 in apical endocytosis may be extrapolated by investigating its cross-talk with OCRL. The loss of function of this enzyme leads to a renal phenotype very similar to those observed in absence of ClC-5, thus OCRL could cooperate with ClC-5 to coordinate the endocytic process (5).

OCRL is a 97 kDa cytosolic protein ubiquitously expressed, with highest levels in the brain, liver and kidney. OCRL is predominantly located at the *trans*-Golgi network but it is also expressed at the clathrin-coated pits, early and recycling endosomes, cilia, TJs and during cytokinesis. OCRL is able to hydrolyze the phosphate group in position 5 of the inositol rings of $PI(4,5)P_2$ and $PI(3,4,5)P_3$ to generate PI4P and $PI(3,4)P_2$, respectively, with a slight preference for the former. $PI(4,5)P_2$ are abundantly expressed at the plasma membrane, where they regulate fundamental steps of clathrin-mediated endocytosis (34). Studies on immortalized cells revealed that during endocytosis OCRL regulates the transition from a stage with high $PI(4,5)P_2$ levels, which drive the recruitment of actin and clathrin machinery at the plasma membrane, to a stage with low $PI(4,5)P_2$ levels, which allows clathrin uncoating and actin disassembly at the endocytic vesicles enabling their maturation in early endosomes. Recent studies in human cells showed that the loss of OCRL function results in the accumulation of $PI(4,5)P_2$ at the EEs triggering a local hyper-polymerization of actin, which impairs the endocytic trafficking of multiple cellular receptors, including megalin (**Fig.13**).

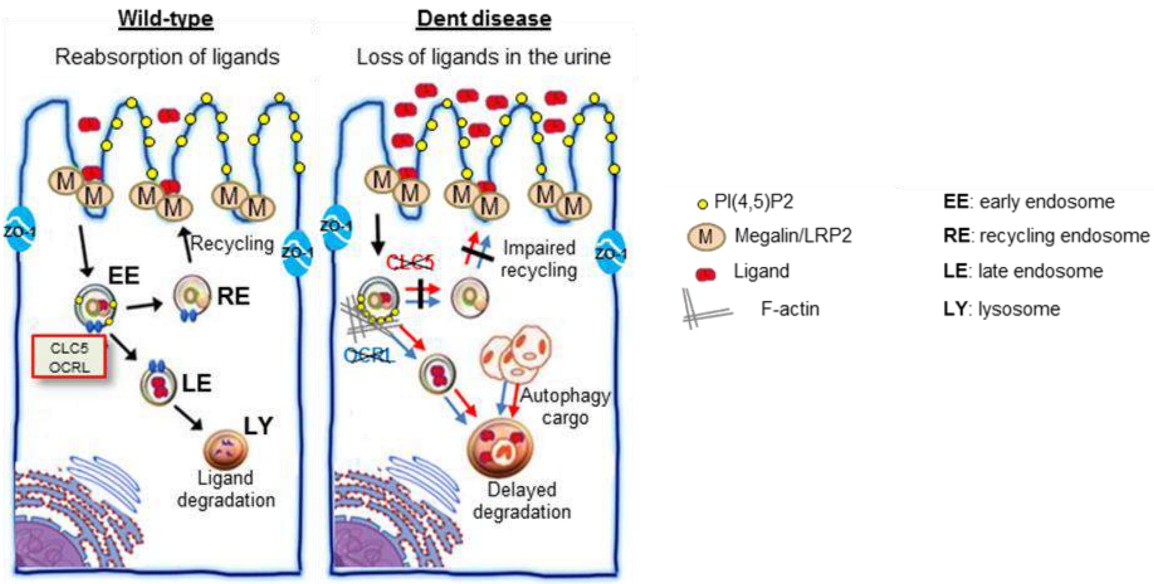

Figure 13: The role of ClC-5 and OCRL in the pathogenesis of Dent disease.
Adapted from *O.Devuyst, A.Luciani. J. Physiol. 2015*.

This event could contribute to the endocytic defect and PT dysfunction observed in Lowe syndrome/Dent disease 2 patients (91). The lack of a reliable *in vivo* model is a significant limitation in demonstrating the involvement of this mechanism in the LMW proteinuria characterizing the kidney disease. The recent availability of a mouse model and primary PT cell systems that mimics the Lowe syndrome/Dent Disease 2 kidney phenotype is predicted to be of significant benefit in this regard (92).

I.4.3 Lysosomal storage disorders: nephropathic cystinosis

Cystinosis is a rare autosomal recessive disorder -general incidence of 1:100,000–1:200,000 live birth -which belongs to the family of lysosomal storage diseases. Cystinosis is caused by mutations or deletions in *CTNS* gene encoding cystinosin- a lysosome proton-symporter, which enables the excretion of cystine from the lysosome to the cytosol (93). Loss of cystinosin function results in accumulation of cystine inside the lysosomes and formation of lysosome cystine crystals within multiple organs including the kidney PT (94, 95). Patients presenting with infantile cystinosis (#MIM 219800), the most frequent and severe form of cystinosis, appear normal at birth but exhibit failure to thrive, rickets and PT dysfunction (RFS) by 6–18 months of age. Continual loss of kidney function in absence of treatment eventually leads towards ESRD. Other systemic complications, appearing later on in the life of cystinosis patients, involve photophobia, painful cornea erosions, hypothyroidism, hypogonadism, diabetes, myopathy and deterioration of the central nervous system. Juvenile (#MIM 219900) and ocular (#MIM 219750) cystinosis are milder and rarer than infantile cystinosis (96). The only available strategy to counteract cystine storage is oral administration of cysteamine, which allows cystine to exit lysosomes. However, cysteamine treatment is hampered by side effects and poor tolerance, and it does not treat nor prevent PT dysfunction. Thus, there is an urgent need to identify novel therapeutic strategies for this devastating disorder (97).

Previous studies show that *Ctns* ko mice are able to recapitulate multiple features of cystinosis, including the renal pathology. Although RFS in mice is delayed compared to patients, *Ctns* ko mice reproduce ESRD, thus mimicking the progression of the human disease. Another human feature recapitulated in *Ctns* ko mice is the accumulation of cystine crystals within PT cells (98). However, these crystals appear at a later stage compared to the PT dysfunction, thus these crystals cannot be the primary trigger for the renal defect. Previous studies in cellular models of cystinosis lead to the identification of several organelles aberrations and trafficking defects, which could contribute to the pathogenic cascade underlying the disease. Studies on immortalized cells derived from *Ctns* ko mice or cystinosis patients have demonstrated that loss of cystinosin is associated to mitochondrial impairment. This event could be explained by the decreased levels of cytosolic cysteine, which is normally used for the synthesis of glutathione (GSH) -a cellular anti-oxidant with a major role in preventing mitochondrial damage. Decrease in cellular ATP and increased levels of oxidative stress could be also explained by the aberrant mitochondrial function (99, 100). Further studies showed that cystinotic lysosomes are dysfunctional and appear enlarged and clustered to the perinuclear region of the cells (101). Impairment of the lysosomal proteolysis results in the accumulation of luminal undigested material, which could potentially affect lysosomal amino acid sensors, such as mTORC1. Of note, co-immunoprecipitation and mass spectrometry studies demonstrate that cystinosin itself interacts with almost all the regulatory subunits of mTORC1 and that cystinosin depletion leads to defective activation and recruitment of mTORC1 on the lysosomal membranes (102, 103). In line with those data, immortalized patient-derived cells show a persistent nuclear translocation of the master regulator of lysosomal biogenesis and autophagy TFEB, whose activity is negatively controlled by mTORC1 phosphorylation (104). Moreover, defects in chaperone-mediated autophagy have been detected in cystinosis models (**Fig.14**). Despite the huge progresses in understanding the molecular mechanisms underlying cystinosis, many questions regarding the cross-talk between mitochondria, lysosomal function, autophagy, mTORC1 signaling and epithelial differentiation remain unsolved.

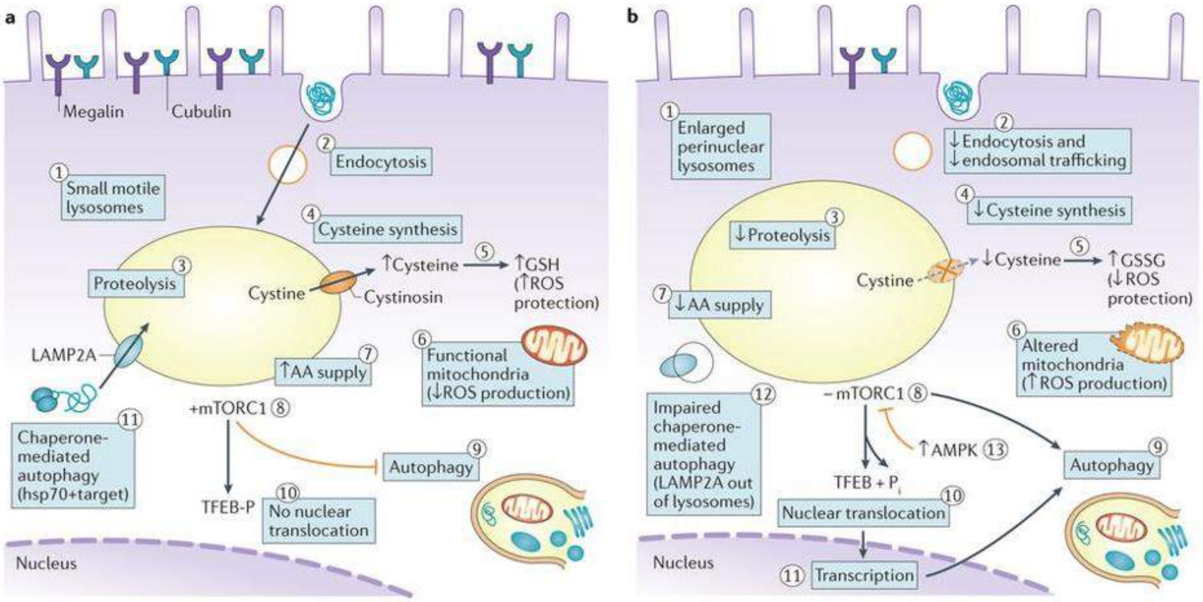

Figure 14: Cell biological alterations in cystinotic cells.
Adapted from *Stephanie Cherqui & Pierre J. Courtoy. Nat. Rev. Nephrol. 2017.*

Of note, the use of immortalized cellular systems as the major tool of investigation could lead to artificial results. Indeed, many methods used for immortalizing the cells affect the activation of autophagy and mTORC1 (105, 106), which are relevant pathways for cystinosis. Thus, studies on *in vivo* models closer to human such as *Ctns* ko rat model and *in vitro* systems mimicking the kidney transport activity like mouse primary culture of PT cells, are required to elucidate the molecular mechanisms associated with the disease and identify reliable druggable targets for therapeutic interventions.

II. AIMS OF THE THESIS

The reabsorptive function of the PT cells of the kidney relies on the responsiveness of the endolysosomal compartment to the stimuli provided by the external environment (107). By internalizing and degrading urinary substrates and recycling receptors and transporters at the apical surface, the endolysosomal system of PT cells governs the recovery of fundamental nutrients that would otherwise be lost in the urine. Impairment of the endolysosomal compartment in PT cells leads to a massive loss of solutes in the urine (renal Fanconi Syndrome) often followed by a deterioration of the global kidney function culminating in renal failure (1). The mechanisms of PT dysfunction associated with these endolysosomal disorders remain largely obscure due to limited availability of faithful animal models and cellular systems with conserved PT transport activity.

The first aim of this thesis was to substantiate the molecular mechanisms underlying kidney PT disorders caused by primary dysfunctions of the early endosomal compartment such as Dent disease and Lowe syndrome. These two clinical entities are caused by loss-of-function mutations in very distinct proteins (a chloride-proton exchanger and a phosphatase, respectively) but they present by overlapping renal phenotypes. We performed a comprehensive phenotyping of kidney function in mouse models lacking the expression of the endosomal exchanger ClC-5 (Dent disease 1) or the 5-phospahatase OCRL (Dent disease 2/ Lowe syndrome) in order **to validate these models of human diseases and to identify potentially common dysfunctional pathways underlying these disorders**. We next derived differentiated primary proximal tubular cells from the kidneys of these mouse models **to explore the role of ClC-5 and OCRL in the reabsorptive function of the PT and their involvement in endocytic trafficking.**

The second aim of the thesis was to analyze the mechanisms linking lysosomal disease and kidney epithelial dysfunction in nephropathic cystinosis - a paradigmatic lysosomal storage disorder caused by mutations in the lysosomal amino acid transporter cystinosin. We used cutting-edge cell biology approaches on *Ctns ko* zebrafish, mouse and cellular models **to investigate the consequences of disrupted lysosomal transport on the autophagy pathway and to explore how these changes affect differentiation and function of PT cells**. Based on these insights we set up a drug-repurposing approach aiming **to improve the kidney function of cystinotic mice**.

In the last section, we used *Ctns* knockout mouse and rat models **to decipher the evolutionary conserved disease-mechanisms linking loss of cystinosin function with disrupted lysosomal identity in PT cells. We specifically focused on mTORC1 pathway, given its central role in bridging amino acids sensing with lysosomal signalling and function.**

These studies have the final aim to expand our understanding of the regulatory mechanisms maintaining the homeostasis of highly specialized epithelial cells which provide essential transport functions in the PT of the kidney. Obtaining insights into the molecular machinery leading to dysfunction of these cells in rare genetic disorders is a prerequisite for the identification of new druggable targets.

III. RESULTS

III.1 DENT DISEASE/ LOWE SYNDROME

III.1.1 Defective endosomal trafficking drives PT dysfunction

III.2 NEPHROPATHIC CYSTINOSIS

III.2.1 Disruption of lysosomal identity triggers PT dysfunction

III.2.2 mTORC1: a novel druggable target for nephropathic cystinosis

III.1 DENT DISEASE/ LOWE SYNDROME

III.1.1 Defective endosomal trafficking drives PT dysfunction

OCRL Deficiency Impairs Endolysosomal Function in a Humanized Mouse Model for Lowe Syndrome and Dent Disease

Beatrice Paola Festa[1#], Marine Berquez[1#], Alkaly Gassama[1], Irmgard Amrein[2,3,4], Hesham M. Ismail[5], Marijana Samardzija[6], Leopoldo Staiano[7], Alessandro Luciani[1], Christian Grimm[4,6,8,], Robert L. Nussbaum[9,10], Maria Antonietta De Matteis[7], Olivier M. Dorchies[5], Leonardo Scapozza[5], David Paul Wolfer[2,3,4], Olivier Devuyst[1*].

[1]Institute of Physiology, University of Zurich, CH-8057 Zurich, Switzerland; [2]Division of Functional Neuroanatomy, Institute of Anatomy, University of Zurich, CH-8057 Zurich, Switzerland; [3]Institute of Human Movement Sciences and Sport, Department of Health Sciences and Technology, ETH Zurich, CH-8057 Zurich, Switzerland; [4]Neuroscience Center Zurich (ZNZ), University of Zurich, CH-8057 Zurich, Switzerland; [5]School of Pharmaceutical Sciences, University of Geneva, CMU 5-6, Rue Michel-Servet 1, Geneva, 1211, Switzerland; [6]Lab for Retinal Cell Biology, Department of Ophthalmology, University Hospital Zurich, University of Zurich, CH-8057 Zurich, Switzerland; [7]Telethon Institute of Genetics and Medicine (TIGEM), 80078 Pozzuoli, Naples, Italy; [8]Center for Integrative Human Physiology (ZIHP), University of Zurich, CH-8057 Zurich, Switzerland; [9]Department of Medicine and Institute of Human Genetics, University of California, CA 94143-0794 San Francisco, California; [10]Invitae Corporation, CA 94103 San Francisco.

# These authors contributed equally to this work.

*Correspondence: Prof. Dr. med. Olivier Devuyst (✉ Olivier.Devuyst@uzh.ch) University of Zurich, Institute of Physiology, Winterthurerstrasse 190, 8057 Zurich, Switzerland; Phone: +41 (0)44 635 50 82; Fax: +41 (0)44 635 68 14

Human Molecular Genetics, Volume 28, Issue 12, 15 June 2019, Pages 1931–1946,
DOI.org/10.1093/hmg/ddy449

ABSTRACT

Mutations in *OCRL* encoding the inositol polyphosphate 5-phosphatase OCRL (Lowe oculocerebrorenal syndrome protein) disrupt phosphoinositide homeostasis along the endolysosomal pathway causing dysfunction of the cells lining the kidney proximal tubule. The dysfunction can be isolated (Dent disease 2) or associated with congenital cataracts, central hypotonia and intellectual disability (Lowe syndrome). The mechanistic understanding of Dent disease 2/Lowe syndrome remains scarce, due to limitations of animal models of OCRL deficiency.

Here, we investigate the role of OCRL in Dent disease 2/Lowe syndrome by using *Ocrl*$^{Y/-}$ mice, where the lethal deletion of the paralogue *Inpp5b* was rescued by human *INPP5B* insertion, and primary culture of proximal tubule cells (mPTCs) derived from *Ocrl*$^{Y/-}$ kidneys.

The *Ocrl*$^{Y/-}$ mice show muscular defects with dysfunctional locomotricity and present massive urinary losses of low-molecular-weight proteins and albumin, caused by selective impairment of receptor-mediated endocytosis in proximal tubule cells. The latter was due to accumulation of phosphatidylinositol 4,5–bisphosphate PI(4,5)P_2 in endolysosomes, driving local hyper-polymerization of F-actin and impairing trafficking of the endocytic LRP2 receptor, as evidenced in *Ocrl*$^{Y/-}$ mPTCs. The OCRL deficiency was also associated with a disruption of the lysosomal dynamic and proteolytic activity. Partial convergence of disease-mechanism and renal phenotypes observed in *Ocrl*$^{Y/-}$ and *Clcn5* $^{Y/-}$ mice suggest shared mechanisms in Dent disease 1 and 2.

These studies substantiate the first mouse model of Lowe syndrome and give insights into the role of OCRL in cellular trafficking of multiligand receptors. These insights open new avenues for therapeutic interventions in Lowe syndrome and Dent disease.

INTRODUCTION

The maintenance of body fluid and electrolyte homeostasis critically depends on the appropriate handling of solutes and water by the epithelial cells lining the proximal tubule (PT) of the kidney(1, 2). These cells are characterized by an efficient endolysosomal pathway involving the apical multiligand receptors megalin (LRP2) and cubilin (3). By processing internalized cargoes and recycling of receptors and transporters at the apical surface, the endolysosomal system of the PT cells recover essential substances that are filtered through the glomerulus, including a large variety of low-molecular-weight (LMW) proteins that would otherwise be lost in the urine (2). Congenital and acquired disorders of the endolysosomal pathway cause PT dysfunction (renal Fanconi syndrome) with massive urinary loss of solutes, dehydration, electrolyte imbalance, rickets, growth retardation, and the development of chronic kidney disease (CKD). Such PT dysfunctions are typically encountered in Dent disease, a rare, X-linked disorder characterized by LMW proteinuria, renal Fanconi syndrome, kidney stones, nephrocalcinosis and progressive renal failure (4, 5).

Dent disease is genetically heterogeneous. The majority of cases (approx. 60%) is due to mutations in the *CLCN5* gene that encodes the electrogenic Cl^-/H^+ exchanger ClC-5 (Dent disease 1, MIM # 300009) (6). In a subset of patients (~15-20%), the disease is caused by mutations in *OCRL*, the gene encoding the type II phosphatidylinositol (PI) bisphosphate 5-phosphatase OCRL (Dent disease 2, MIM #300555). Mutations in OCRL are also associated with the oculocerebrorenal syndrome of Lowe (MIM # 309000), which includes systemic manifestations such as congenital cataracts, cognitive disability and hypotonia (4, 7). OCRL is a protein of 110 kDa which, in addition to the 5-phosphatase catalytic domain, comprises: (i) a pleckstrin homology (PH) domain containing a clathrin-binding site (8); (ii) an ASPM, SPD-2, Hydin (ASH) domain, characteristic of protein that localizes to centrosome and primary cilia (9); and (iii) a RhoGAP-like domain, which mediates interactions involved in cytoskeleton dynamics and progression of cell cycle (10). Almost all the mutations associated with Lowe syndrome occur in exons 8-23 which include the 5-phosphatase catalytic domain, the ASH domain and the RhoGAP-like domain. Conversely, the majority of mutations that cause Dent disease 2 are positioned in exons 1-7 which comprise the PH domain (11). Although mutations in the catalytic domain of *OCRL* have been described in both clinical profiles, the mutations in Dent disease 2 are always missense - compatible with a residual biological activity that could explain a less severe cellular phenotype (7).

The convergence of clinical phenotypes among patients with mutations in *OCRL* and *CLCN5* raises the questions whether these genes products are part of the same pathways and how they cause dysfunction of endolysosomes in PT cells. ClC-5 is predominantly expressed in the EEs of PT cells of the kidney, potentially involved in their maturation towards the degradative compartments or the recycling route (6). Studies in mouse models showed that the functional loss of ClC-5 generates a trafficking defect involving megalin and cubilin, reflected by defective endocytosis and manifestations of PT dysfunction (6, 12). OCRL is located at different stations of the endo-lysosomal pathway where it maintains the cellular metabolism of phosphatidylinositol 4, 5-bisphosphate $PI(4,5)P_2$, an essential regulator of membrane trafficking. Increased $PI(4,5)P_2$ levels and marked vesicular trafficking defects affecting the endocytic network have been observed in cells lacking OCRL, resulting in defective receptor-mediated endocytosis (13).

The direct impact of OCRL on transport events leading to renal Fanconi syndrome cannot be reliably assessed on dedifferentiated cell systems including non-kidney or non-epithelial cell types, or clonal cells isolated from urine (14). Renal biopsy material, usually obtained at an advanced disease stage, is of limited value. Furthermore, limitations of animal models of OCRL deficiency impede the development of translational studies. The first *Ocrl* KO mouse showed no kidney, eye or brain defects (15), due to a compensation by INPP5B, the closest paralogue of OCRL in mice and humans (16). Accordingly, a generalized endocytic defect (affecting both receptor-mediated and fluid-phase endocytosis) was detected in a conditional tubular deletion of *Ocrl* and *Inpp5b* mouse model (17). However, studies performed in this strain do not allow to discriminate the individual role of OCRL and INPP5B in the pathophysiology of Dent disease.

Recently a mouse model expressing human INPP5B in $Ocrl^{Y/-}$; $Inpp5b^{-/-}$ background was generated (18). The replacement of mouse *Inpp5b* with human *INPP5B* in the whole body of $Ocrl^{Y/-}$ mouse provides a humanized background, which therefore allows to investigate the consequences related to the specific loss of OCRL activity. Preliminary studies revealed PT dysfunction in this line (18), with no investigation of the time-course, multi-systemic aspect, and cellular basis of this defect. Here, we analyzed in detail the multi-systemic phenotype of these $Ocrl^{Y/-}$; $Inpp5b^{-/-}$; *BAC-INPP5B* mouse model; compared the kidney dysfunction to that of *Clcn5* KO mice; and investigated the mechanisms underpinning epithelial transport defects in Lowe syndrome.

RESULTS

Ocrl$^{Y/-}$ *mice show early manifestations of proximal tubule dysfunction*

A humanized mouse model for Lowe syndrome/Dent disease 2 was generated by targeted disruption of both *Ocrl* and *Inpp5b* and oocyte injection of a bacterial artificial chromosome (BAC) containing the human gene *INPP5B* to avoid embryonic lethality (18). The mouse littermates lacking *Inpp5b* while harbouring *BAC-INPP5B* expression with *Ocrl* are referred to as *Ocrl*$^{Y/+}$ (*Ocrl*$^{Y/+}$; *Inpp5b*$^{-/-}$; *BAC-INPP5B*) whereas those lacking *Ocrl* are *Ocrl*$^{Y/ -}$ (*Ocrl*$^{Y/-}$; *Inpp5b*$^{-/-}$; *BAC-INPP5B*) mice, respectively. All mice were born at mendelian ratio and were viable and fertile. The genotype of *Ocrl* mice was demonstrated by genomic DNA analyses of *Ocrl*, *Inpp5b* and *BAC-INPP5B* (Suppl. Fig. 1A) and immunoblotting for OCRL (Suppl. Fig. 1B) in kidney samples derived from *Ocrl*$^{Y/-}$ and *Ocrl*$^{Y/+}$ mice. We first used the *Ocrl* mice to characterize the kidney phenotype over time. Growth retardation was observed in *Ocrl*$^{Y/-}$ mice starting from 16 weeks of age onwards (Fig. 1A), whereas manifestations of PT dysfunction appeared in *Ocrl*$^{Y/-}$ mice from 8 weeks of age, with albuminuria (Figs. 1B and 1C) and LMW proteinuria (Figs. 1D and 1E). The inappropriate loss of the LMW clara cell secretory protein 16 (CC16) in the urine of *Ocrl*$^{Y/-}$ mice was observed at all time points analyzed (Fig. 1D). Western blotting of the urine confirmed the major loss of transferrin (TFR) and vitamin D binding protein (VDBP) along CC16 in the urine of *Ocrl*$^{Y/-}$ mice (Fig. 1E). The *Ocrl*$^{Y/-}$ mice did not show manifestations of renal failure, and no polyuria, calciuria, glycosuria and phosphaturia during the timeframe of investigation, suggesting a partial renal Fanconi syndrome (Table 1). The expression levels of *BAC-INPP5B* were not associated with variable levels of PT dysfunction in *Ocrl*$^{Y/-}$ mice (Suppl. Figs. 1C-F). Since mutations in *CLCN5* and *OCRL* produce similar kidney defects in human patients, we compared the severity of PT dysfunction in the *Clcn5*$^{Y/-}$ and *Ocrl*$^{Y/-}$ mouse models. The *Ocrl*$^{Y/-}$ mice display a milder LMW proteinuria (CC16) than that observed in *Clcn5*$^{Y/-}$ mice (Fig. 1F). This difference is most likely reflecting specific roles of ClC-5 and OCRL along the endo-lysosomal pathway.

Ocrl$^{Y/-}$ *mice show a specific defect in receptor-mediated endocytosis*

To determine the mechanism of LMW proteinuria, we followed the *in vivo* uptake of the LMW protein Cy5-labelled β-lactoglobulin in the kidneys of *Ocrl*$^{Y-}$ mice compared to their control littermates. Fifteen minutes after injection, a substantial accumulation of fluorescent vesicles was observed in the brush border of PT cells of the *Ocrl*$^{Y/+}$ mice, contrasting with a considerable reduction of the signal in PT cells from *Ocrl*$^{Y/-}$ mice (Fig. 2A). A similar defective uptake in Cy5-labelled β-lactoglobulin was observed in *Clcn5*$^{Y/-}$ tubules (Fig. 2B). By contrast, the internalization of Alexa 647-dextran, a marker of fluid phase endocytosis, was unaltered in *Ocrl*$^{Y/-}$ mice (Fig.

2C), suggesting that loss of OCRL function impacts specifically on receptor-mediated endocytosis. To substantiate this observation, we investigated the LRP2 receptor and found its expression dramatically decreased in PT cells of the *Ocrl*$^{Y/-}$ kidneys whereas its mRNA level was unchanged (Figs. 2D-F). In line with absent phosphaturia and glycosuria, no modifications in the sodium- phosphate cotransporter IIa (NaPi-IIa), the sodium-glucose cotransporter 2 (SGLT2) or other PT components were observed in *Ocrl*$^{Y/-}$ kidneys (Figs. 2E and 2F). These data reveal that a defective receptor-mediated endocytosis, caused by a decreased protein level of LRP2, characterizes *Ocrl*$^{Y/-}$ mice, similar to *Clcn5*$^{Y/-}$ mice. The renal Fanconi syndrome is restricted to LMW proteinuria in *Ocrl*$^{Y/-}$ mice, contrasting with a more severe PT dysfunction in *Clcn5*$^{Y/-}$ mice. At age 8 weeks, the latter showed a decreased expression of SGLT2 and NaPi-IIa (Suppl. Fig. 2A), explaining glycosuria and phosphaturia along polyuria and calciuria (Table 1; Suppl. Figs. 2C-D), and a defective uptake of fluid-phase endocytosis (dextran) markers (Suppl. Fig. 2B).

Loss of OCRL increases PI(4,5)P_2 and disrupts receptor-mediated endocytosis in vitro

In order to further analyse the endocytic defect observed *in vivo*, we developed primary cultures of PT cells (mPTC) from micro-dissected PT segments of *Ocrl*$^{Y/-}$ mice aged 8 weeks. This cell culture system preserves the differentiation and polarized transport processes and therefore represents a relevant in *vitro* model to investigate mechanisms underlying PT disorders (19). To validate the *Ocrl* cellular system, we evaluated whether the loss of OCRL in mPTC reproduced the typical endosomal accumulation of PI(4,5)P_2 observed in Lowe syndrome/Dent disease 2 (20). Compared to control, *Ocrl*$^{Y/-}$ mPTCs exhibited a remarkable increase of PI(4,5)P_2 in early endosomal structures, as shown by colocalization with the early endosome marker EEA1 (Figs. 3A-B). The unchanged PI3P levels, the PI hallmark of the endosomal system, demonstrated that OCRL disruption in mPTCs exclusively targets the homeostasis of PI(4,5)P_2 (Suppl. Fig. 3A). These results, which are consistent with PI(4,5)P_2 accumulation observed in a transgenic zebrafish model of Lowe syndrome or in OCRL-depleted immortalized cells, substantiate the reliability of *Ocrl* mPTCs system (13, 21). Given that the tight regulation of PI(4,5)P_2 homeostasis is fundamental for a proper endocytic trafficking, we asked whether its increase at the EEs might impair the endocytic function of mPTCs. Functional studies demonstrated that albumin uptake was markedly reduced in *Ocrl*$^{Y/-}$ (-84%) when compared to control mPTCs (Fig. 3C). A similar disruption of the endocytic capacity was observed in *Clc5*$^{Y/-}$ mPTCs (Fig. 3D). Confirming the observations made *in vivo*, fluid phase endocytosis was unaltered in *Ocrl*$^{Y/-}$ mPTCs (Fig. 3E), highlighting the specificity of the defect in receptor-mediated endocytosis.

OCRL deficiency perturbs expression of LRP2 through aberrant F-actin polymerization

We next examined whether the defective uptake capacity of *Ocrl*$^{Y/-}$ mPTCs was reflected by alterations of the endogenous LRP2 expression. LRP2 protein level was reduced in the total lysates of mPTCs lacking OCRL (Fig. 4A), similarly to *Clcn5*$^{Y/-}$ mPTCs (Suppl. Fig. 4A). This reduction was confirmed by the analysis of the confocal Z-stack images, evidencing a decreased LRP2 fluorescent signal in each focal plane throughout the entire volume of *Ocrl*$^{Y/-}$ mPTCs (Fig. 4B and Suppl. Fig. 4B). The latter analysis showed a shift of LRP2 signal from the apical plasma membrane towards a more intracellular compartment in *Ocrl*$^{Y/-}$ mPTCs, whose polarization is defined by the typical apical (wheat germ agglutinin, WGA) and basolateral (Na^+, K^+-ATPase) markers (Fig. 4C and Suppl. Fig. 4C). This result was corroborated by a striking decrease of LRP2 level in the plasma membrane fraction of *Ocrl*$^{Y/-}$ mPTCs (Fig. 4D). These changes were not associated with LRP2 transcriptional modifications or alterations of other PT receptors or transporters (Suppl. Fig. 3B). The intracellular localization of LRP2 in *Ocrl*$^{Y/-}$ mPTCs prompted us to examine its organelles compartmentalization. OCRL is known to modulate the trafficking of endocytic receptors by orchestrating the recycling of endosomal vesicles to the surface (13). Thus, lack of OCRL function might disrupt the return of the endocytic receptors to the apical membrane, leading to their accumulation in endosomal structures. Imaging studies confirmed LRP2 increase within EEA1$^+$ early endosomes in *Ocrl*$^{Y/-}$ mPTCs, suggesting that loss of OCRL function impacts on both expression and distribution of this endocytic scavenger (Fig. 4E). As PI(4,5)P_2 promote the recruitment of the actin nucleating machinery, we asked whether their endosomal accumulation, observed in *Ocrl*$^{Y/-}$ mPTCs, might locally induce an aberrant actin polymerization and, in turn, affect the trafficking of endocytic receptors (22).We observed that, in *Ocrl*$^{Y/-}$ mPTCs, the levels of actin stress fibres decreased and foci of filamentous actin (F-actin) accumulated on internal membranes ruffles (Suppl. Fig. 4D). Compared to controls, an increase of F-actin structures, colocalizing with EEA1, was observed in *Ocrl*$^{Y/-}$ mPTCs (Suppl. Fig. 4E). This uncontrolled actin dynamics might impede the entrance of the endosomes in the recycling route and coerce LRP2 to stick inside them. Supporting this hypothesis, a considerable amount of LRP2 vesicles were coalescent with F-actin membranes (Fig. 4F). Furthermore, by high magnification confocal microscopy, it was possible to visualize the formation of F-actin basket-like structure surrounding LRP2 (Suppl. Fig. 4F). These data indicate that the increased association of F-actin with early endosomes may affect the endocytic trafficking and prevent the recycling of LRP2 to the apical surface. In order to substantiate the role of OCRL in maintaining the recycling activity, we investigated the localization of the canonical recycling marker transferrin receptor (TfR), which crosses the same endocytic stations traveled by LRP2 (plasma membrane - early endosomes/recycling endosomes) (23). Our data showing the redistribution of TfR from the plasma membrane to enlarged cytoplasmic structures, which also trap LRP2, provide another evidence of defective endocytic recycling in *Ocrl*$^{Y/-}$ mPTCs (Suppl. Fig. 5A and Fig. 4G). We also tested whether the lack of OCRL might affect the trafficking of the cation-independent mannose 6-phosphate receptor (CI-MPR), which is required for the transport of lysosomal enzymes and travels through intracellular itineraries diverging from those exploited by LRP2 (TGN-LEs- plasma membrane) (24). An increase in the CI-MPR associated with peripheral structures and a decrease in the perinuclear pool was observed in the kidneys and mPTCs from *Ocrl*$^{Y/–}$ mice compared to controls (Suppl. Figs. 5B-C), indicating a defective retrograde transport of CI-MPR from the endosomes to the Golgi. All together, these data suggest that the actin-trapping mechanism impairing the recycling of LRP2 extends to other receptors traveling through the endosomal structures of *Ocrl*$^{Y/-}$ mice, highly relevant for the molecular basis of Lowe syndrome.

OCRL depletion alters lysosomal dynamics and function

It has been recently shown that, under lysosomal overload conditions, OCRL translocates on the lysosomal membrane, where it ensures adequate levels of PI(4,5)P_2 necessary for fusion and subsequent degradation of cargo vesicles (25). We thus explored whether loss of OCRL function might generate a rearrangement of PI(4,5)P_2 at the lysosomal membrane and, consequently, affect lysosomal morphology. Confocal microscopy analysis showed that *Ocrl* deletion increased the number of PI(4,5)P_2 positive structures colocalized with LAMP1-labeled lysosomes (Fig. 5A). These changes were associated with dramatic modifications in the dynamics of lysosomes as evidenced by their abnormal increase in number and size (Fig. 5B). As changes in lysosomal dynamics could affect their proteolytic activity, we examined whether OCRL disruption impairs the lysosomal cargo degradation in *Ocrl*$^{Y/-}$ mPTCs. To this end we used dequenched BSA (BSA-DQ) reagent, which is readily incorporated by cells via fluid-phase endocytosis. Upon fusion with endo-lysosomes, BSA-DQ is digested into smaller fragments, thereby relieving its self-quenching properties and causing a fluorescent signal that reflects lysosomal degradative capacity (26). *Ocrl*$^{Y/-}$ mPTCs showed a remarkable decrease in BSA-DQ fluorescent puncta colocalized with LAMP1 (Fig. 5C), indicating a specific impairment of lysosomal proteolysis as fluid phase endocytosis was not affected by the loss of OCRL. To substantiate the defective lysosomal activity, we tested the processing of the EGFR, an endogenous protein which, upon EGF induced internalisation, is normally sorted to endo-lysosomal proteolytic pathway for degradation (27). Control mPTCs, 90 min after EGF stimulation, showed an efficient degradation of EGFR. On the contrary, at the same time frame, the levels of EGFR remained high in *Ocrl*$^{Y/-}$ mPTCs, suggesting a delayed lysosomal processing of the receptor (Fig. 5D). One mechanism by which cargo clearance might be impeded is a defective maturation of lysosomal cathepsins. Western blot analyses of cathepsin D (Cts-D) showed a decreased generation of the 32kDa mature Cts-D in *Ocrl*$^{Y/-}$ mPTCs compared to control (Fig. 5E). We next tested the lysosomal Cts-D activity by incubating the cell with Bodipy-FL-PepstatinA (PepA), a fluorescence-tagged PepA that binds to the active site of Cts-D in acidic lysosomes. Although the majority of lysosomes were co-stained with PepA in control mPTCs, the number of PepA-labeled vesicles colocalizing with LAMP1 were substantially lower in *Ocrl*$^{Y/-}$ mPTCs (Fig. 5F). Similarly, the lysosome-based processing of the LMW β-lactoglobulin, which is normally internalized and degraded by endolysosomes, was dramatically reduced in *Ocrl*$^{Y/-}$ proximal tubules compared to wild-type (Fig. 5G). To investigate whether mis-sorting of lysosomal hydrolases in the extracellular space might contribute to the aberrant lysosomal proteolysis observed in *Ocrl*$^{Y/-}$ mice, we tested for and detected significantly increased levels of the lysosomal protease Cts-D (immature form) in the plasma of these mice (Suppl. Fig. 6A). This result was in line with the mis-trafficking of CI-MPR at the cell periphery and with previous studies performed in patients with Lowe syndrome (13). Collectively these data indicate that OCRL is important to maintain lysosome homeostasis, itself crucial for PT function. Of note, impaired lysosomal proteolysis and insufficient degradation of β-lactoglobulin was also observed in *Clcn5*$^{Y/-}$ proximal tubules (Suppl. Figs. 6B-D) indicating that OCRL and ClC-5 are part of the same cellular pathways.

The Ocrl$^{Y/-}$ *mice show dysfunctional locomotricity associated with muscular defects*

In order to test whether the deletion of OCRL in this model was reflected by extra-renal manifestations, we performed comprehensive behavioral tests of *Ocrl* mice to examine basic motor activity, learning and memory skills, social behaviour and vision. To identify disturbances in locomotor activity, we evaluated the general mobility of the mice by challenging them with the open field large arena test, which has been extensively used for analyzing the locomotor defects exhibited by Parkinson and Huntington mouse models (28, 29). While velocity was comparable between genotypes (data not shown), *Ocrl*$^{Y/-}$ mice exhibited an overall decreased locomotor activity, as scored by the measurement of their trajectories (Figs. 6A and 6B). The *Ocrl*$^{Y/-}$ mice presented more resting episodes than controls, as well as fewer lingering and walking events during the test (Fig. 6C). Of note, center-field avoidance was robust and equal in both genotypes (data not shown), suggesting that the impaired motor activity in *Ocrl*$^{Y/-}$ mice was more likely driven by a muscular defect rather than an abnormal anxiety-related response. To test the latter hypothesis, we pursued mice analyses in IntelliCage, an automated system, which allowed the evaluation of the spontaneous behaviour of the animals (30). During free adaptation phase, *Ocrl*$^{Y/-}$ mice made fewer corner visits compared to controls, confirming the reduced locomotor and exploratory activity shown in the test above (data not shown). However, *Ocrl*$^{Y/-}$ mice showed an incompetent licking pattern, which became more evident during the drinking restriction protocol and was associated with slower progress of water intake during drinking sessions (Fig. 6D).We excluded an influence of the kidney defect on the licking pattern as similar water intake was detected between genotypes (Suppl. Fig. 7A). Thus, the impaired licking of *Ocrl*$^{Y/-}$ mice was most likely caused by a global muscular dysfunction, which affected also the oro-lingual motor apparatus. To explore whether the defective locomotricity evidenced in *Ocrl*$^{Y/-}$ mice was driven by muscular defects, we performed whole body composition analysis (EchoMRI), which evidenced a striking decrease in lean mass/body weight ratio in *Ocrl*$^{Y/-}$ mice compared to controls (Fig. 6E), with a global reduction of the mass of several hind limb (gastrocnemius, triceps surae, plantaris, tibialis posterior/anterior and quadriceps) muscles relative to body weight (Fig. 6F) demonstrating skeletal muscle atrophy. These changes were paralleled by a strong increase in plasma creatine kinase (CK) activity, suggesting membrane fragility of striated muscles. (Fig. 6G). These events, which are in line with the muscle hypotonia observed in Lowe Syndrome patients (7), support the motor defect detected in *Ocrl*$^{Y/-}$ mice. To assess the cognitive function of *Ocrl* mice we applied IntelliCage standard protocol which investigated the hippocampus-dependent spatial learning ability of the animals. No sign of dysfunctional learning was observed in OCRL deficient mice, even during the most challenging chaining task (data not shown). Aggressive behavior reported in patients with Lowe syndrome was also not reflected in *Ocrl*$^{Y/-}$ mice, which showed intact sociability (Suppl. Fig. 7B). Given that congenital cataract and glaucoma are hallmarks of Lowe syndrome, we also examined the visuospatial and visuoperceptual ability of *Ocrl* mice. During water maze cue navigation, *Ocrl*$^{Y/-}$ mice exhibited a robust learning without evidences for an inadequate vision (Suppl. Fig. 7C). In addition no noticeable differences were observed in lens epithelium and in retinal morphology between control and *Ocrl*$^{Y/-}$ mice. Irrespective of the *Ocrl* genotype, an impairment of retinal photoreceptor layer was observed in mice harboring *rd8* (retinal degeneration 8) mutation in *Crb1* gene, a spontaneous mutation associated with C57BL/6N genetic background, leading to photoreceptor rosette-like structures when expressed homozygously (*rd8/rd8*). (Suppl. Figs.7D and 7E) (31).

DISCUSSION

In these studies, we present the first OCRL-deficient mouse model that associates renal and extra-renal manifestations encountered in patients with Lowe syndrome. The absence of OCRL in kidney proximal tubule triggers endolysosomal defects and epithelial dysfunction, with a consistent LMW proteinuria reflecting defective receptor-mediated endocytosis due to decreased expression of LRP2 endocytic receptor, in absence of renal failure. We also evidence a partial convergence of disease-mechanism and kidney tubular phenotype between mouse models deficient in ClC-5 (Dent disease 1) and OCRL (Lowe syndrome/Dent disease 2). These results provide insights into the mechanisms of endocytosis and the pathophysiology of Dent disease/Lowe syndrome.

In contrast with a previous kidney tubular conditional *Ocrl* and *Inpp5b* KO mouse model, where the phenotype reflects the combined loss of OCRL and INPP5B (17), the genetic architecture of the mouse line investigated here allows to directly address dysfunctions related to the single loss of OCRL activity (18). The reinsertion of human INPP5B in the $Ocrl^{-/-}$; $Inpp5b^{-/-}$ background, irrespective of its level of expression, was fundamental for survival but it was not compensating for the renal defect. This observation is in line with studies on cells derived from patients with Lowe syndrome, which exhibit INPP5B-independent phenotypic variability (32). Although the renal defect was observed in all the $Ocrl^{Y/-}$ mice analysed, a noticeable spread was observed comparing individual animals. This individual variability was not due to different levels of INPP5B expression. The possibility that compensatory changes in kinases or phosphatases crossing the same metabolic pathway than OCRL may contribute to such variability should be further investigated.

The differences between the conditional double *Ocrl* and *Inpp5b* KO and the humanized transgenic $Ocrl^{Y/-}$ mice studied here are evident when comparing the defective tubular endocytic phenotypes. The conditional deletion of OCRL and INPP5B resulted in an unspecific impairment of the clathrin-dependent and clathrin-independent endocytosis. By contrast, the single lack of OCRL in $Ocrl^{Y/-}$ transgenic mice resulted in a selective dysfunction of the clathrin receptor-mediated endocytosis, as evidenced by the defective uptake of β-lactoglobulin and the unaffected internalization of the fluid-phase marker dextran. These differences are in line with the function of OCRL in regulating the membrane trafficking of clathrin-coated vesicles (33).

Defective receptor-mediated endocytosis was reflected in $Ocrl^{Y/-}$ mice by a consistent LMW proteinuria, occurring early, in absence of renal failure. In contrast, the $Ocrl^{Y/-}$ mice did not show glycosuria, phosphaturia and calciuria, even at old age, mimicking the partial renal Fanconi syndrome typically present in the majority of patients carrying mutations in OCRL (7, 34) . The $Clcn5^{Y/-}$ mice showed a similar defect in receptor-mediated endocytosis, causing a severe LMW proteinuria. The $Clcn5^{Y/-}$ mice also showed a defective uptake of fluid phase endocytosis markers, in line with previous data from mouse models and patient-derived cells (35-37) but not with others (12). The presence of a more complete form of renal Fanconi syndrome in the *Clcn5*$^{Y/-}$ mouse model was evidenced by the hypercalciuria, phosphaturia and glucosuria detected at 8 weeks, paralleled by a decreased expression of SGLT2 and NaPi-IIa in addition to LRP2.

Filtered LMW proteins are reabsorbed through megalin /LRP2 and cubilin endocytic receptors expressed at the apical membrane of PT cells. This reabsorptive function is maintained by the degradative and recycling activity of the endolysosomal system, as evidenced by severe defects in tubular homeostasis associated with endolysosomal disorders (1, 2). Our investigations characterize the involvement of LRP2 in the pathogenesis of Lowe syndrome, and demonstrate analogies with the endocytic defect associated with the loss of ClC-5 in Dent disease1/*Clcn5*$^{Y/-}$ mouse model (12). Previous studies, relying on OCRL-deficient immortalized cells expressing LRP2 mini-receptor, showed a redistribution of LRP2 from the apical membrane to the intracellular compartments rather than a defective expression (13). Here, analyses on kidney tissues reveal a remarkable decrease of LRP2 protein in the proximal tubule from *Ocrl*$^{Y/-}$ mice, similar to that observed in *Clcn5*$^{Y/-}$ mice. These findings are in line with observations made in zebrafish pronephros, demonstrating the evolutionary conservation of the role of OCRL in endocytosis (21). The identification of converging kidney phenotypes in mouse models for Lowe syndrome and Dent disease supports the view that the endosomal exchanger ClC-5 and the 5-phosphatase OCRL impact on common pathways operating in kidney tubular cells. In absence of transcriptional changes, the mechanism by which the loss of ClC-5 or OCRL might affect LRP2 protein levels remains to be clarified. First, the decrease of apical LRP2 may reflect an increased shedding of the receptor in the urine in response to the endolysosomal engorgement observed in *Ocrl*$^{Y/-}$ mice. Previous studies showed that LRP2 is a substrate for metalloproteases and is constitutively subjected to ectodomain shedding (38). This event produces LRP2 membrane-associated fragments, which in turn form the substrate for γ- secretase, the main player of regulated intramembrane proteolysis. Preliminary data showing a higher abundance of LRP2 fragments in *Ocrl*$^{Y/-}$ urine, together with a transcriptional increase of all subunits composing the γ-secretase (39) are in line with this hypothesis (data not shown). Alternatively, the loss of LRP2 could be explained by an increased urinary excretion of (full length) LRP2-containing exosomes. A third mechanism might be an aberrant degradation of LRP2, mediated by the proteasome in response to altered lysosomal proteolysis (see below). Further studies of post-translational modifications potentially triggering LRP2 to the proteasome are necessary to test this hypothesis (40).

By establishing differentiated and polarized proximal tubular cell cultures (mPTCs) directly derived from *Ocrl*$^{Y/-}$ mouse kidneys (19), we were able to reconstitute critical aspects of the disease *in vitro*. The *Ocrl*$^{Y/-}$ mPTCs recapitulate the selective impairment of receptor-mediated endocytosis and the ectopic accumulation of $PI(4,5)P_2$ in early endosomes (20). The latter is due to the loss of 5-phospatase activity of OCRL that regulates the transition from high (plasma membrane) to low (early endosomes) levels of $PI(4,5)P_2$ in clathrin coated vesicles, enabling progression of the cargo/receptor along the endocytic pathway (33, 41). The $PI(4,5)P_2$ dynamic is critical for actin assembly at the plasma membrane ruffles and early endosomes, hence, for the regulation of membrane trafficking (42, 43). Accordingly, the endosomal accumulation of $PI(4,5)P_2$ in *Ocrl*$^{Y/-}$ mPTCs triggers an aberrant F-actin polymerization, which impairs the recycling of residual LRP2, thus impeding the endocytic uptake. The actin-trapping mechanism impairing LRP2 recycling might be extended to other receptors, as evidenced by the redistribution of the canonical recycling marker TfR in *Ocrl*$^{Y/-}$ mPTCs. These defects in receptor recycling represent an appealing druggable target for rescuing the epithelial dysfunction associated with the disease.

It has been shown recently that OCRL can translocate to the lysosome under cargo overload conditions, where its fine regulation of $PI(4,5)P_2$ balance is instrumental for maintaining lysosomal function (25). Here, we demonstrate that lack of OCRL induces an abnormal lysosomal accumulation of $PI(4,5)P_2$ leading to altered lysosomal dynamics and defective lysosomal function, as scored by decreased expression and activity of lysosomal cathepsin D and impaired processing of lysosomal substrates in *Ocrl*$^{Y/-}$ kidney and mPTCs. These results, which are consistent with previous observations on biopsies derived from Lowe patients (25), raise the issue of the mechanisms responsible for lysosomal dysfunction associated with loss of OCRL. The peripheral mislocalization of the CI-MPR, a protein regulating the transport of lysosomal hydrolases from the Golgi to lysosomes, along with increased levels of lysosomal protease cathepsin D (immature form) in the plasma, indicates that misrouting of lysosomal enzymes could be involved. This finding is in line with previous studies performed in Lowe syndrome patients (13). Alternatively, the lysosomal engulfment of $PI(4,5)P_2$ driven by the loss of OCRL may somehow alter the V-ATPase complex, thereby impairing lysosome acidification and activation of cathepsins. It should be noted that similar defects in receptor-mediated endocytosis and lysosomal dynamic and activity are observed in mouse and cellular models deficient for the endosomal ClC-5 or lysosomal cystinosin (CTNS) transporters, highlighting the role of the endolysosome network as crucial signaling hub to ensure epithelial homeostasis (44).

Studies on the locomotor, neurological and vision abnormalities detected in patients with Lowe syndrome have been hindered by the limitations of available mouse models. Deep phenotyping analyses unveiled a defective locomotricity in *Ocrl*$^{Y/-}$mice, which reflects a global impairment of the muscular apparatus, as indicated by the increased plasma activity of protein creatine kinase and atrophy of several hind limb muscles. This phenotype was reminiscent of the muscle hypotonia associated with Lowe syndrome and therefore highly relevant (45). Whether this defective muscular/motor pattern originates from a primary myopathy or is rather a consequence of neurological alterations and how OCRL contributes in maintaining muscular tone remains to be further investigated. Behavior, learning-memory function and vision were not altered in *Ocrl*$^{Y/-}$mice. The discrepant clinical manifestations in mice and humans could be partly explained by differences in tissue-specific expression of enzymes with overlapping functions or by specific roles of OCRL in the tissues affected by the disease (46, 47).

Collectively, these studies validate the first mouse model of Lowe syndrome and give insights into the role of OCRL in cellular trafficking of multiligand receptors. Partial convergence of disease-mechanism and renal phenotypes observed in *Ocrl*$^{Y/-}$ and *Clcn5* $^{Y/-}$ mice suggest shared mechanisms in Dent disease 1 and 2. These insights open new avenues for therapeutic interventions in Lowe syndrome and Dent disease.

.

MATERIALS AND METHODS

Antibodies and reagents. The following antibodies were used: rabbit anti-human transferrin (A0061, Dako); rabbit anti-human Gc-globulin (also known as VDBP, A0021, Dako); rabbit anti-uteroglobin (also known as CC16, ab40873, Abcam); rabbit anti-SLC1A5 (also known as SGLT2, ab84903, Abcam); rabbit NaPi-IIa (gift from C.A.Wagner, University of Zurich, Zurich, Switzerland); rabbit anti-human AQP1 (ab2219, Millipore); mouse anti-β-actin (A2228, Sigma-Aldrich); mouse conjugated to Fluorescein (FITC) anti-PI(4,5)P$_2$ (Z-G045, Echelon Biosciences Inc.); mouse anti-EEA1 (610456, BD Bioscience); rabbit anti-RFP (600-401-379, ROCKLAND); sheep anti-LRP2 (gift from P. Verroust and R. Kozyraki, INSERM, Paris, France); mouse anti Flotillin-1(610821, BD Bioscience); mouse anti-α-tubulin (T5168, Sigma-Aldrich); rabbit anti-GAPDH (2118, Cell Signaling Technology); rat anti-LAMP1 (sc-19992, Santa Cruz Biotechnology); goat anti-cathepsin-D (Cts-D; sc-6486, Santa Cruz Biotechnology); rabbit anti-EGFR (1005 sc-03, Santa Cruz Biotechnology); Alexa-488 Phalloidin (F-actin , A12379, Thermofisher Scientific); mouse anti-Transferrin Receptor Antibody (H68,4, ThermoFisher Scientific), wheat germ agglutinin (WGA) FITC Conjugate (L 4895, Sigma-Aldrich), mouse anti-Na$^+$/K$^+$-ATPase subunit α1 (C464.6 EMD Millipore), rabbit anti-MPR and rabbit anti-OCRL (gift from A. De Matteis, Telethon Institute of Genetics and Medicine (TIGEM), Pozzuoli, Italy).

Mouse models. Experiments were conducted on age- and gender-matched *Ocrl*$^{Y/+}$; *Inpp5b*$^{-/-}$; and *Ocrl*$^{Y/-}$; *Inpp5b*$^{-/-}$ mouse littermates harboring BAC-*INPP5B* expression in equal copies (BAC1) (129S/SvEv * 129S6/SvEvTac * FVB/N* C57BL/6 background), (18) and *Clcn5*$^{Y/+}$and *Clcn5*$^{Y/-}$ mice littermates (C57BL/6 background) (48). All the mice used in this study were expressing similar levels of *INPP5B* as analyzed by RT-qPCR (see below). Mice were maintained under temperature-and humidity-controlled conditions with 12 h light/12 h dark cycles with free access to appropriate standard diet in accordance with the institutional guidelines of National Institutes of Health Guide for the Care and Use of Laboratory Animals.

Renal function parameters. Mice were placed overnight in metabolic cages with ad libitum access to food and drinking water. Urines were collected over ice and body weight, water intake and diuresis were measured at the indicated time point (49). Blood (from sublingual vein) was obtained after anesthesia with ketamine/xylazine or isoflurane. Urine and blood parameters were measured using a UniCel DxC 800 pro Synchron (Beckman Coulter, Fullerton, CA, USA), whereas urinary Clara cell protein (CC16) concentration was measured in duplicate by enzyme-linked immunosorbent assay (ELISA; BIOMATIK EKU03200) (44). Albuminuria was measured by Coomassie Blue staining by using ProtoBlue Safe (EC-722, national diagnostics) according to manufacturer instructions.

Kidney isolation and primary cultures of proximal tubule cells. The kidneys were harvested from *Ocrl*$^{Y/+}$ and *Ocrl*$^{Y/-}$ mice and *Clcn5*$^{Y/+}$and *Clcn5*$^{Y/-}$ mice as previously described (44). Briefly, one half of the kidney was fixed in 4% PFA and processed for immunostaining while the other half was used for protein isolation or RT-qPCR analysis. The contralateral kidney was taken to generate primary cultures of mouse proximal tubule cells (mPTCs) according to a previously established protocol (14). Confluent monolayers of mPTCs, characterized by a high endocytic uptake capacity, were expanded from tubular segments after 6–7 days.

Genotyping. Genomic DNA was isolated from ear biopsies from *Ocrl*$^{Y/+}$*; Inpp5b* $^{-/-}$*; BAC-INPP5B* and *Ocrl*$^{Y/-}$*; Inpp5b* $^{-/-}$ *; BAC-INPP5B* mice by using E.Z.N.A Forensic DNA Kit (OMEGA bio-tek) according to the manufacturer instruction. PCR was performed by using the following primers: *Ocrl wild-type:* the forward primer 5'-CCC TTT TCATCTGTTAGGAGAAATC-3'is located at the junction of intron 18 and the 5'end of exon 19. The reverse primer 5'- GCATGG TTAAACGCACTATGTGG-3' is located in intron 19, which is deleted in the *Ocrl*$^{Y/-}$ line. *Ocrl knock-out*: the forward primer 5'GCCCTTTGATTCTAATCCCTTTTC ATC-3' is located in the intron positioned just before the exon 19. The reverse primer 5'-TCT GAGCCCAGAAAGCGAAG-3' is located in the PGK promoter, which is part of the *neo*-cassette gene targeting vector. *Inpp5b knock-out*: the forward primer 5'-TAAAGTCTGAAA ATCCAAGGC-3' is located in exon 25. The reverse primer 5'-CTCATTTCTCCTTGATTC CAAT-3' is located in exon 34. *BAC-INPP5B*: the forward primer 5'-CCACCCCACGATTGACTC-3' is localized in exon 1. The reverse primer 5'-GGTGTCCCAGCCCTCAG-3' is localized also in exon 1. PCR conditions were: 32 cycles of 94°C for 30 sec, 55°C for 30 sec and 72°C for 1min.

Quantitative real-time PCR. Total RNA was extracted from mouse kidney tissues using Aurum Total RNA Fatty and Fibrous Tissue Kit according to manufacturer's protocol (Bio-Rad, Hercules, CA). DNAse I treatment was performed to eliminate genomic DNA contamination. Total RNA was extracted from primary cell cultures with RNAqueous kit (Applied Biosystems, Life Technologies). 1 µg of RNA was used to perform the reverse transcriptase reaction with iScript™ cDNA Synthesis Kit (Bio-Rad). Changes in target gene mRNA levels were determined by relative RT-qPCR with a CFX96™ Real-Time PCR Detection System (BioRad) by using iQ™ SYBR Green Supermix (Bio-Rad). RT-qPCR analyses were performed in duplicate. Specific primers were designed by using Primer3 (Supplementary Table 1). PCR conditions were 95°C for 3 min followed by 40 cycles of 15 sec at 95°C, 30 sec at 60°C. The PCR products were sequenced with the BigDye terminator kit (Perkin Elmer Applied Biosystems, Thermo Fischer Scientific). The efficiency of each set of primers was determined by dilution curves (Supplementary Table 1). The relative changes in targeted genes over *Gapdh, Actb, Hprt1, Ppiase, 18S, 36B4* mRNAs were calculated using the $2^{-\Delta\Delta}$Ct formula (50).

Immunofluorescence and confocal microscopy. Mouse kidneys were fixed by perfusion with 50‑60 ml of 4% PFA in PBS before being snap-frozen in cryogenic Tissue-Tek OCT compound (Electron Microscopy Sciences, Hatfield, USA). The embedded tissues were sectioned at 5 µm and processed for immunofluorescent staining as previously described (44). The slides were acquired on Leica SP5 confocal laser scanning microscope (Center for Microscopy and Image Analysis, University of Zurich) equipped with a Leica APO 63x NA 1.4 oil immersion objective at a definition of 1024 x 1024 pixels, adjusting the pinhole diameter to 1 Airy unit for each emission channel. Quantitative image analysis was performed by selecting random visual fields containing at least 3-5 proximal tubules (LTL-positive) each one and acquired with the same setting parameters. For quantification of β-lactoglobulin and dextran internalization, the integrated density signal detected within each LTL-positive tubule was calculated. Internalization was then expressed as a ratio between the internal fluorescence and tubule area. Tubules at the border of the picture were excluded. ImageJ software was used for the analysis (17).

The mPTCs were fixed in 4% PFA and processed for immunofluorescent staining as previously described (44). Briefly, after incubation with blocking/permeabilization solution (0.1% Saponin ,0.5% BSA and 50mM NH_4Cl in PBS), mPTCs were stained overnight with the appropriate primary antibodies and 45 minutes with the suitable fluorophore-conjugated Alexa secondary antibodies (Invitrogen) or with Alexa-488 Phalloidin (F-actin) or 10 minutes with wheat germ agglutinin (WGA) FITC Conjugate. Immunostained mPTCs were analyzed by a Leica SP5 confocal laser scanning microscope using the settings described above. The quantitative cell image analyses were performed by using ImageJ software and the open-source cell image analysis software CellProfiler™ (51). More details regarding the quantifications are described in Supplementary Materials.

Endocytosis assays. Proximal tubules endocytic capacity of *Ocrl* and *Clcn5* mice was examined by measuring β-lactoglobulin and dextran uptake. β-lactoglobulin was tagged with Cy5 using TM2 Ab labeling kit (Amersham) in accordance with the manufacturer's instructions. 15 minutes after tail-vein injection of Cy5 β-lactoglobulin (1mg/kg B.W., L3908, Sigma) or 30 minutes after injection of 10 kDa Alexa 647-dextran (6 mg/kg B.W.; D22914, Thermo Fisher Scientific), mice were anesthetized and their kidneys were harvested and processed for confocal microscopy. The endocytic capacity of *Ocrl* and *Clcn5* mPTCs was examined by measuring albumin and dextran uptake as described previously (44). Briefly mPTCs were incubated at 37°C with 100µg/mL Alexa488-BSA (A13100, Thermo Fisher Scientific) or 250µg/mL Alexa 647-dextran diluted in medium without FBS supplementation, for 15 and 30 min respectively. After washing, the cells were fixed in 4% PFA and processed for confocal microscopy

PI(4,5)P_2 and PI3P staining. mPTCs were grown on 35mm dishes and PI(4,5)P_2 or PI3P staining were performed according to previously established protocols (25). Briefly, mPTCs were fixed for 15 min in 2% PFA and permeabilized for 5 min with 20µM digitonin in buffer A (20mM PIPES pH 6.8, 137mM NaCl, 2.7mM KCl) for PI(4,5)P_2 or buffer A^1 (150 mM NaCl, 20 mM Hepes, pH 7.4, and 2 mM EDTA) for PI3P. Next, mPTCs were incubated for 45 minutes with buffer A containing 10% fetal bovine serum and anti-PI(4,5)P2 antibody or in buffer A^1 supplemented with 5% goat serum and mCherry-2×FYVE PI3P-binding domain (gift from J.Gallop, Gurdon Institute, University of Cambridge). Anti –RFP was used for amplifying m-cherry staining. Studies of colocalization with early endosomes or lysosomes were performed by 1h incubation at room temperature with anti-EEA1 or anti-LAMP1 antibodies respectively. After washing and subsequent incubation with appropriate secondary antibodies, mPTCs were post-fixed for 5 min in 2% PFA and analyzed by confocal microscopy.

Lysosomal activity and degradation assays. The detection of lysosomal activity and degradative capacity in mPTCs was performed by using Bodipy-FL-PepstatinA (P12271, Thermo Fischer Scientific) and DQ-RED BSA (D12051, Thermo Fischer Scientific), respectively. Briefly, mPTCs were pulsed with 1µM Bodipy-FL-Pepstatin A or with 10µg/mL DQ-RED BSA in pre-warmed media at 37°C for 1h. After washing, cells were fixed, immunostained with anti-LAMP1 and suitable secondary antibody and subsequently analyzed by confocal microscopy (14, 26). Lysosomal processing in *Ocrl* and *Clcn5* mice was measured by confocal analysis of kidney proximal tubules after 120 minutes from tail-vein injection of Cy5 β-lactoglobulin.

Western blotting. Proteins were extracted from mouse kidney tissues or primary cultured cells and lysed as previously described (44). Samples were normalized for protein or urinary creatinine levels before loading (20 µg/lane or 4µg/lane, respectively), diluted in Laemmli buffer and separated by SDS–PAGE in reducing conditions. Briefly, gels were blotted onto PVDF membranes, blocked in 5% non-fat milk and probed with appropriate primary and peroxidase-labeled secondary antibody. Protein bands were visualized by chemiluminescence (WBKLS0050, Millipore, Life technologies). Image intensity was measured by ImageJ.

Plasma membrane isolation. mPTCs were lysed in a fractionation buffer (250mM sucrose, 20mM HEPES, 10mM KCL, 1.5mM $MgCl_2$, 1mM EDTA, 1mM EGTA) containing protease and phosphatase inhibitors and passed through a 25G needle. Cell lysates were kept on ice for 20 minutes and centrifuged at 720 g (5 minutes at 4°C). The resultant postnuclear supernatants were centrifuged at 10,000 g (5 minutes at 4°C) to eliminate mitochondria. The postmitochondria supernatant were centrifuged at 100,000 g (1h at 4°C) to separate cytosolic (supernatant) and membrane fractions (pellet). The membrane pellets were washed in fractionation buffer by centrifugation (100,000 g for 45min at 4°C) and suspended in lysis buffer (10% glycerol and 0.1% SDS supplemented with protease and phosphatase inhibitors). The cytosolic and membrane fractions were analyzed by SDS-PAGE and western blotting.

Behavioral tests. Open field large arena test, water maze cue navigation and three chambers sociability test were performed on a cohort of 32 male mice aged 32 weeks (16 *Ocrl*$^{Y/+}$;*Inpp5b* $^{-/-}$;*BAC-INPP5B* and 16 *Ocrl*$^{Y/-}$; *Inpp5b* $^{-/-}$;*BAC-INPP5B*) in order to investigate motor coordination, vision and spatial learning and the social attitude of the mice respectively. Behavior testing procedures will be described briefly here and in more detail in the Supplementary Materials**.** ***Open field large arena test.*** Each subject was released near the wall of the arena and observed for 10 min on two subsequent days. Movements were tracked using Noldus EthoVision. ***Water-maze cue navigation.*** Animals were trained for 2 days to reach the goal platform hidden under milky-water and marked by a salient cue. The localization of the platform in the pool changed for every trial. All subjects were trained on the same sequence of goal positions and released from the same start points (52). ***Three-chambers sociability test.*** The test consisted of a 10-minutes trial where a test mouse was given the choice to spend time in the chamber with the novel object (the cylinder) plus the unfamiliar mouse (social stimulus) and the chamber containing only the empty cylinder. The time spent by the test mouse in the lateral chambers was noted (53).

IntelliCages experiments. Intellicages experiments were performed on a cohort of 28 male mice aged 24 weeks (13 *Ocrl*$^{Y/+}$; *Inpp5b* $^{-/-}$, *BAC-INPP5B* and 15 *Ocrl*$^{Y/-}$; *Inpp5b* $^{-/-}$; *BAC-INPP5B*). More details regarding the description of IntelliCage apparatus and mice preparation for IntelliCage experiments are provided in the Supplementary Materials.
Exploration and free adaptation. During the first 4-7 days in IntelliCage all doors were open providing free access to all 8 drinking bottles (free adaptation). Data of the first 24h of free adaptation were analyzed separately to monitor exploration and habituation of the mice in the new environment (IntelliCage exploration). **Nosepoke adaptation**. During 3-7 days, all doors were closed but can be opened at any time with a nosepoke for 5s once per visit. **Drinking session adaptation**. During 3-7 days the mice were adapted to a fixed drinking schedule with doors opening in response to nose pokes only in the following time spots: 04:00-05:00, 11:00-12:00, 16:00-17:00 and 23:00-00:00. (30).

Epon embedding and retinal morphology. 36 weeks old mice were euthanized and perfused with PFA 4%. Eyes were enucleated and post-fixed in 4% PFA or 2.5% glutaraldehyde before being embedded in paraffin or epon plastic, respectively. For light microscopy, paraffin sections (including the lens, 5 µm) were stained with hematoxylin-eosin (HE), while plastic-embedded semi-thin cross-sections (0.5 µm) were counterstained with toluidine blue as described previously (54, 55) . Retinal morphology was analyzed by light microscopy (Zeiss, Axioplan, Jena, Germany).

Muscle analyses. Muscles analyses were performed on *Ocrl*$^{Y/+}$ *vs. Ocrl*$^{Y/-}$ male mice aged 24 weeks. Lean mass/body weight ratio was determined in 6 pairs of live mice by using the whole body composition analyzer EchoMRI™ (Zinsser Analytic, Frankfurt, Germany) (56) . Five pairs of mice were used for muscle and blood sampling. The mice were slightly sedated using isoflurane before being anesthetized with an i.p. injection of a mixture containing urethane (1.5 g/kg) and diazepam (5 mg/kg) and killed by exsanguination. Blood and muscle tissues were collected as previously described (57). Selected leg muscles (triceps surae, soleus, plantaris, gastrocnemius, tibialis anterior, tibialis posterior, quadriceps) were carefully dissected bilaterally and weighed. Muscle mass was expressed relative to body weight. Creatine kinase (CK) activity in plasma was determined by spectrophotometry using a kit (C184-0B ; Catachem, Nuuchem, Oxford, CT, USA) according to the manufacturer's instructions (57).

Data analysis and Statistics. The quantitative data were expressed as means ± standard error of the mean (s.e.m.). Differences between experimental groups were evaluated using analysis of variance followed by post hoc test, when appropriate. When only two groups were compared, unpaired or paired two tailed Student's *t*-tests were used as appropriate. No statistical methods were used to predetermine the sample size. The sample size (n of biological replicates derived from distinct mice) of each experimental group is described in figure legends. GraphPad Prism software was used for all statistical analyses. Statistical significance was set at a $P<0.05$.

REFERENCES

1. Eckardt, K.U., Coresh, J., Devuyst, O., Johnson, R.J., Kottgen, A., Levey, A.S. and Levin, A. (2013) Evolving importance of kidney disease: from subspecialty to global health burden. Lancet, 382, 158-169.

2. Devuyst, O. and Luciani, A. (2015) Chloride transporters and receptor-mediated endocytosis in the renal proximal tubule. J. Physiol., 593, 4151-4164.

3. Christensen, E.I., Verroust, P.J. and Nielsen, R. (2009) Receptor-mediated endocytosis in renal proximal tubule. Pflugers. Arch., 458, 1039-1048.

4. Devuyst, O. and Thakker, R.V. (2010) Dent's disease. Orphanet J. Rare Dis., 5, 28.

5. Devuyst, O., Knoers, N.V., Remuzzi, G. and Schaefer, F. (2014) Rare inherited kidney diseases: challenges, opportunities, and perspectives. Lancet, 383, 1844-1859.

6. Devuyst, O., Christie, P.T., Courtoy, P.J., Beauwens, R. and Thakker, R.V. (1999) Intra-renal and subcellular distribution of the human chloride channel, CLC-5, reveals a pathophysiological basis for Dent's disease. Hum. Mol. Genet., 8, 247-257.

7. De Matteis, M.A., Staiano, L., Emma, F. and Devuyst, O. (2017) The 5-phosphatase OCRL in Lowe syndrome and Dent disease 2. Nat. Rev. Nephrol., 13, 455-470.

8. Mao, Y., Balkin, D.M., Zoncu, R., Erdmann, K.S., Tomasini, L., Hu, F., Jin, M.M., Hodsdon, M.E. and De Camilli, P. (2009) A PH domain within OCRL bridges clathrin-mediated membrane trafficking to phosphoinositide metabolism. Embo j., 28, 1831-1842.

9. Ponting, C.P. (2006) A novel domain suggests a ciliary function for ASPM, a brain size determining gene. Bioinformatics, 22, 1031-1035.

10. Faucherre, A., Desbois, P., Satre, V., Lunardi, J., Dorseuil, O. and Gacon, G. (2003) Lowe syndrome protein OCRL1 interacts with Rac GTPase in the trans-Golgi network. Hum. Mol. Genet., 12, 2449-2456.

11. Hichri, H., Rendu, J., Monnier, N., Coutton, C., Dorseuil, O., Poussou, R.V., Baujat, G., Blanchard, A., Nobili, F., Ranchin, B. et al. (2011) From Lowe syndrome to Dent disease: correlations between mutations of the OCRL1 gene and clinical and biochemical phenotypes. Hum. mutat., 32, 379-388.

12. Christensen, E.I., Devuyst, O., Dom, G., Nielsen, R., Van der Smissen, P., Verroust, P., Leruth, M., Guggino, W.B. and Courtoy, P.J. (2003) Loss of chloride channel ClC-5 impairs endocytosis by defective trafficking of megalin and cubilin in kidney proximal tubules. Proc. Natl. Acad. Sci. U. S. A., 100, 8472-8477.

13. Vicinanza, M., Di Campli, A., Polishchuk, E., Santoro, M., Di Tullio, G., Godi, A., Levtchenko, E., De Leo, M.G., Polishchuk, R., Sandoval, L. et al. (2011) OCRL controls trafficking through early endosomes via PtdIns4,5P(2)-dependent regulation of endosomal actin. Embo j., 30, 4970-4985.

14. Luciani, A., Sirac, C., Terryn, S., Javaugue, V., Prange, J.A., Bender, S., Bonaud, A., Cogne, M., Aucouturier, P., Ronco, P. et al. (2016) Impaired Lysosomal Function Underlies Monoclonal Light Chain-Associated Renal Fanconi Syndrome. J. Am. Soc. Nephrol., 27, 2049-2061.

15. Janne, P.A., Suchy, S.F., Bernard, D., MacDonald, M., Crawley, J., Grinberg, A., Wynshaw-Boris, A., Westphal, H. and Nussbaum, R.L. (1998) Functional overlap between murine Inpp5b and Ocrl1 may explain why deficiency of the murine ortholog for OCRL1 does not cause Lowe syndrome in mice. J. Clin. Invest., 101, 2042-2053.

16. Norris, F.A., Atkins, R.C. and Majerus, P.W. (1997) The cDNA cloning and characterization of inositol polyphosphate 4-phosphatase type II. Evidence for conserved alternative splicing in the 4-phosphatase family. J. Biol. Chem., 272, 23859-23864.

17. Inoue, K., Balkin, D.M., Liu, L., Nandez, R., Wu, Y., Tian, X., Wang, T., Nussbaum, R., De Camilli, P. and Ishibe, S. (2017) Kidney Tubular Ablation of Ocrl/Inpp5b Phenocopies Lowe Syndrome Tubulopathy. J. Am. Soc. Nephrol., 28, 1399-1407.

18. Bothwell, S.P., Chan, E., Bernardini, I.M., Kuo, Y.M., Gahl, W.A. and Nussbaum, R.L. (2011) Mouse model for Lowe syndrome/Dent Disease 2 renal tubulopathy. J. Am. Soc. Nephrol., 22, 443-448.

19. Terryn, S., Jouret, F., Vandenabeele, F., Smolders, I., Moreels, M., Devuyst, O., Steels, P. and Van Kerkhove, E. (2007) A primary culture of mouse proximal tubular cells, established on collagen-coated membranes. Am. J. Physiol. Renal. Physiol., 293, F476-485.

20. Zhang, X., Hartz, P.A., Philip, E., Racusen, L.C. and Majerus, P.W. (1998) Cell lines from kidney proximal tubules of a patient with Lowe syndrome lack OCRL inositol polyphosphate 5-phosphatase and accumulate phosphatidylinositol 4,5-bisphosphate. J. Biol. Chem., 273, 1574-1582.

21. Oltrabella, F., Pietka, G., Ramirez, I.B., Mironov, A., Starborg, T., Drummond, I.A., Hinchliffe, K.A. and Lowe, M. (2015) The Lowe syndrome protein OCRL1 is required for endocytosis in the zebrafish pronephric tubule. PLoS. Genet., 11, e1005058.

22. Senju, Y., Kalimeri, M., Koskela, E.V., Somerharju, P., Zhao, H., Vattulainen, I. and Lappalainen, P. (2017) Mechanistic principles underlying regulation of the actin cytoskeleton by phosphoinositides. Proc. Natl. Acad. Sci. U. S. A., 114, E8977-e8986.

23. Perez Bay, A.E., Schreiner, R., Benedicto, I., Paz Marzolo, M., Banfelder, J., Weinstein, A.M. and Rodriguez-Boulan, E.J. (2016) The fast-recycling receptor Megalin defines the apical recycling pathway of epithelial cells. Nat. Commun., 7, 11550.

24. Pfeffer, S.R. (2009) Multiple routes of protein transport from endosomes to the trans Golgi network. FEBS Lett., 583, 3811-3816.

25. De Leo, M.G., Staiano, L., Vicinanza, M., Luciani, A., Carissimo, A., Mutarelli, M., Di Campli, A., Polishchuk, E., Di Tullio, G., Morra, V. et al. (2016) Autophagosome-lysosome fusion triggers a lysosomal response mediated by TLR9 and controlled by OCRL. Nat. Cell. Biol., 18, 839-850.

26. Perera, R.M., Stoykova, S., Nicolay, B.N., Ross, K.N., Fitamant, J., Boukhali, M., Lengrand, J., Deshpande, V., Selig, M.K., Ferrone, C.R. et al. (2015) Transcriptional control of autophagy-lysosome function drives pancreatic cancer metabolism. Nature, 524, 361-365.

27. Miaczynska, M. (2013) Effects of membrane trafficking on signaling by receptor tyrosine kinases. Cold Spring Harb. Perspect. Biol., 5, a009035.

28. Taylor, T.N., Greene, J.G. and Miller, G.W. (2010) Behavioral phenotyping of mouse models of Parkinson's disease. Behav. Brain. Res., 211, 1-10.

29. Fowler, S.C. and Muma, N.A. (2015) Use of a force-sensing automated open field apparatus in a longitudinal study of multiple behavioral deficits in CAG140 Huntington's disease model mice. Behav. Brain. Res., 294, 7-16.

30. Vannoni, E., Voikar, V., Colacicco, G., Sanchez, M.A., Lipp, H.P. and Wolfer, D.P. (2014) Spontaneous behavior in the social homecage discriminates strains, lesions and mutations in mice. J. Neurosci. Methods., 234, 26-37.

31. Luhmann, U.F., Carvalho, L.S., Holthaus, S.M., Cowing, J.A., Greenaway, S., Chu, C.J., Herrmann, P., Smith, A.J., Munro, P.M., Potter, P. et al. (2015) The severity of retinal pathology in homozygous Crb1rd8/rd8 mice is dependent on additional genetic factors. Hum. Mol. Genet., 24, 128-141.

32. Montjean, R., Aoidi, R., Desbois, P., Rucci, J., Trichet, M., Salomon, R., Rendu, J., Faure, J., Lunardi, J., Gacon, G. et al. (2015) OCRL-mutated fibroblasts from patients with Dent-2 disease exhibit INPP5B-independent phenotypic variability relatively to Lowe syndrome cells. Hum. Mol. Genet., 24, 994-1006.

33. Nandez, R., Balkin, D.M., Messa, M., Liang, L., Paradise, S., Czapla, H., Hein, M.Y., Duncan, J.S., Mann, M. and De Camilli, P. (2014) A role of OCRL in clathrin-coated pit dynamics and uncoating revealed by studies of Lowe syndrome cells. eLife, 3, e02975.

34. Bockenhauer, D., Bokenkamp, A., van't Hoff, W., Levtchenko, E., Kist-van Holthe, J.E., Tasic, V. and Ludwig, M. (2008) Renal phenotype in Lowe Syndrome: a selective proximal tubular dysfunction. Clin. J. Am. Soc. Nephrol., 3, 1430-1436.

35. Piwon, N., Gunther, W., Schwake, M., Bosl, M.R. and Jentsch, T.J. (2000) ClC-5 Cl- -channel disruption impairs endocytosis in a mouse model for Dent's disease. Nature, 408, 369-373.

36. Gorvin, C.M., Wilmer, M.J., Piret, S.E., Harding, B., van den Heuvel, L.P., Wrong, O., Jat, P.S., Lippiat, J.D., Levtchenko, E.N. and Thakker, R.V. (2013) Receptor-mediated endocytosis and endosomal acidification is impaired in proximal tubule epithelial cells of Dent disease patients. Proc. Natl. Acad. Sci. U. S. A., 110, 7014-7019.

37. Novarino, G., Weinert, S., Rickheit, G. and Jentsch, T.J. (2010) Endosomal chloride-proton exchange rather than chloride conductance is crucial for renal endocytosis. Science (New York, N.Y.), 328, 1398-1401.

38. Biemesderfer, D. (2006) Regulated intramembrane proteolysis of megalin: linking urinary protein and gene regulation in proximal tubule? Kidney. Int., 69, 1717-1721.

39. Zou, Z., Chung, B., Nguyen, T., Mentone, S., Thomson, B. and Biemesderfer, D. (2004) Linking receptor-mediated endocytosis and cell signaling: evidence for regulated intramembrane proteolysis of megalin in proximal tubule. J. Biol. Chem., 279, 34302-34310.

40. Norden, A.G., Lapsley, M., Igarashi, T., Kelleher, C.L., Lee, P.J., Matsuyama, T., Scheinman, S.J., Shiraga, H., Sundin, D.P., Thakker, R.V. et al. (2002) Urinary megalin deficiency implicates abnormal tubular endocytic function in Fanconi syndrome. J. Am. Soc. Nephrol., 13, 125-133.

41. Zoncu, R., Perera, R.M., Balkin, D.M., Pirruccello, M., Toomre, D. and De Camilli, P. (2009) A phosphoinositide switch controls the maturation and signaling properties of APPL endosomes. Cell, 136, 1110-1121.

42. Di Paolo, G. and De Camilli, P. (2006) Phosphoinositides in cell regulation and membrane dynamics. Nature, 443, 651-657.

43. Symons, M.H. and Mitchison, T.J. (1991) Control of actin polymerization in live and permeabilized fibroblasts. J. Cell. Biol., 114, 503-513.

44. Festa, B.P., Chen, Z., Berquez, M., Debaix, H., Tokonami, N., Prange, J.A., Hoek, G.V., Alessio, C., Raimondi, A., Nevo, N. et al. (2018) Impaired autophagy bridges lysosomal storage disease and epithelial dysfunction in the kidney. Nat. Commun., 9, 161.

45. Park, E., Choi, H.J., Lee, J.M., Ahn, Y.H., Kang, H.G., Choi, Y.M., Park, S.J., Cho, H.Y., Park, Y.H., Lee, S.J. et al. (2014) Muscle involvement in Dent disease 2. Pediatr. Nephrol., 29, 2127-2132.

46. Erdmann, K.S., Mao, Y., McCrea, H.J., Zoncu, R., Lee, S., Paradise, S., Modregger, J., Biemesderfer, D., Toomre, D. and De Camilli, P. (2007) A role of the Lowe syndrome protein OCRL in early steps of the endocytic pathway. Dev. Cell., 13, 377-390.

47. Bothwell, S.P., Farber, L.W., Hoagland, A. and Nussbaum, R.L. (2010) Species-specific difference in expression and splice-site choice in Inpp5b, an inositol polyphosphate 5-phosphatase paralogous to the enzyme deficient in Lowe Syndrome. Mamm. Genome., 21, 458-466.

48. Wang, S.S., Devuyst, O., Courtoy, P.J., Wang, X.T., Wang, H., Wang, Y., Thakker, R.V., Guggino, S. and Guggino, W.B. (2000) Mice lacking renal chloride channel, CLC-5, are a model for Dent's disease, a nephrolithiasis disorder associated with defective receptor-mediated endocytosis. Hum. Mol. Genet., 9, 2937-2945.

49. Raggi, C., Luciani, A., Nevo, N., Antignac, C., Terryn, S. and Devuyst, O. (2014) Dedifferentiation and aberrations of the endolysosomal compartment characterize the early stage of nephropathic cystinosis. Hum. Mol. Genet., 23, 2266-2278.

50. Vandesompele, J., De Preter, K., Pattyn, F., Poppe, B., Van Roy, N., De Paepe, A. and Speleman, F. (2002) Accurate normalization of real-time quantitative RT-PCR data by geometric averaging of multiple internal control genes. Genome Biol., 3, Research0034.

51. Carpenter, A.E., Jones, T.R., Lamprecht, M.R., Clarke, C., Kang, I.H., Friman, O., Guertin, D.A., Chang, J.H., Lindquist, R.A., Moffat, J. et al. (2006) CellProfiler: image analysis software for identifying and quantifying cell phenotypes. Genome Biol., 7, R100.

52. Mohajeri, M.H., Madani, R., Saini, K., Lipp, H.P., Nitsch, R.M. and Wolfer, D.P. (2004) The impact of genetic background on neurodegeneration and behavior in seizured mice. Genes Brain Behav., 3, 228-239.

53. Nadler, J.J., Moy, S.S., Dold, G., Trang, D., Simmons, N., Perez, A., Young, N.B., Barbaro, R.P., Piven, J., Magnuson, T.R. et al. (2004) Automated apparatus for quantitation of social approach behaviors in mice. Genes Brain Behav., 3, 303-314.

54. Grimm, C., Wenzel, A., Williams, T., Rol, P., Hafezi, F. and Reme, C. (2001) Rhodopsin-mediated blue-light damage to the rat retina: effect of photoreversal of bleaching. Invest. Ophthalmol. Vis. Sci., 42, 497-505.

55. Heynen, S.R., Tanimoto, N., Joly, S., Seeliger, M.W., Samardzija, M. and Grimm, C. (2011) Retinal degeneration modulates intracellular localization of CDC42 in photoreceptors. Mol. Vis., 17, 2934-2946.

56. Krizo, J.A., Moreland, L.E., Rastogi, A., Mou, X., Prosser, R.A. and Mintz, E.M. (2018) Regulation of Locomotor activity in fed, fasted, and food-restricted mice lacking tissue-type plasminogen activator. BMC Physiol., 18, 2.

57. Dorchies, O.M., Reutenauer-Patte, J., Dahmane, E., Ismail, H.M., Petermann, O., Patthey- Vuadens, O., Comyn, S.A., Gayi, E., Piacenza, T., Handa, R.J. et al. (2013) The anticancer drug tamoxifen counteracts the pathology in a mouse model of duchenne muscular dystrophy. Am. J. Pathol., 182, 485-504.

ACKNOWLEDGEMENTS & FUNDING

We are grateful to the Cystinosis Research Foundation (Irvine, CA, USA), the Swiss National Science Foundation (project grant 31003A-169850), the clinical research priority program (KFSP) RADIZ (Rare Disease Initiative Zurich) of the UZH, the Swiss National Centre of Competence in Research (*NCCR) Kidney* Control of Homeostasis (*Kidney.CH) for support and* Junior Grant (to A.L.), and the Fondation Suisse de Recherche sur les Maladies Musculaires (FSRMM).

We acknowledge Jennifer Gallop, Jonathan Gadsby, Andrew Hall and Eric Olinger for fruitful discussions, Marcello Polesel, Claus-Dieter Schuh, Huguette Debaix and Nadine Nagele for providing technical assistance, Jonathan R. Gadsby, Renata Kozyraki, Pierre Verroust and Carsten A. Wagner for providing reagents. We thank the Center for Microscopy and Image Analysis of the University of Zurich (Zurich, Switzerland) for providing the equipment for imaging acquisition and the support for imaging analysis.

Competing financial interests: The authors declare no competing financial interests

Figure 1

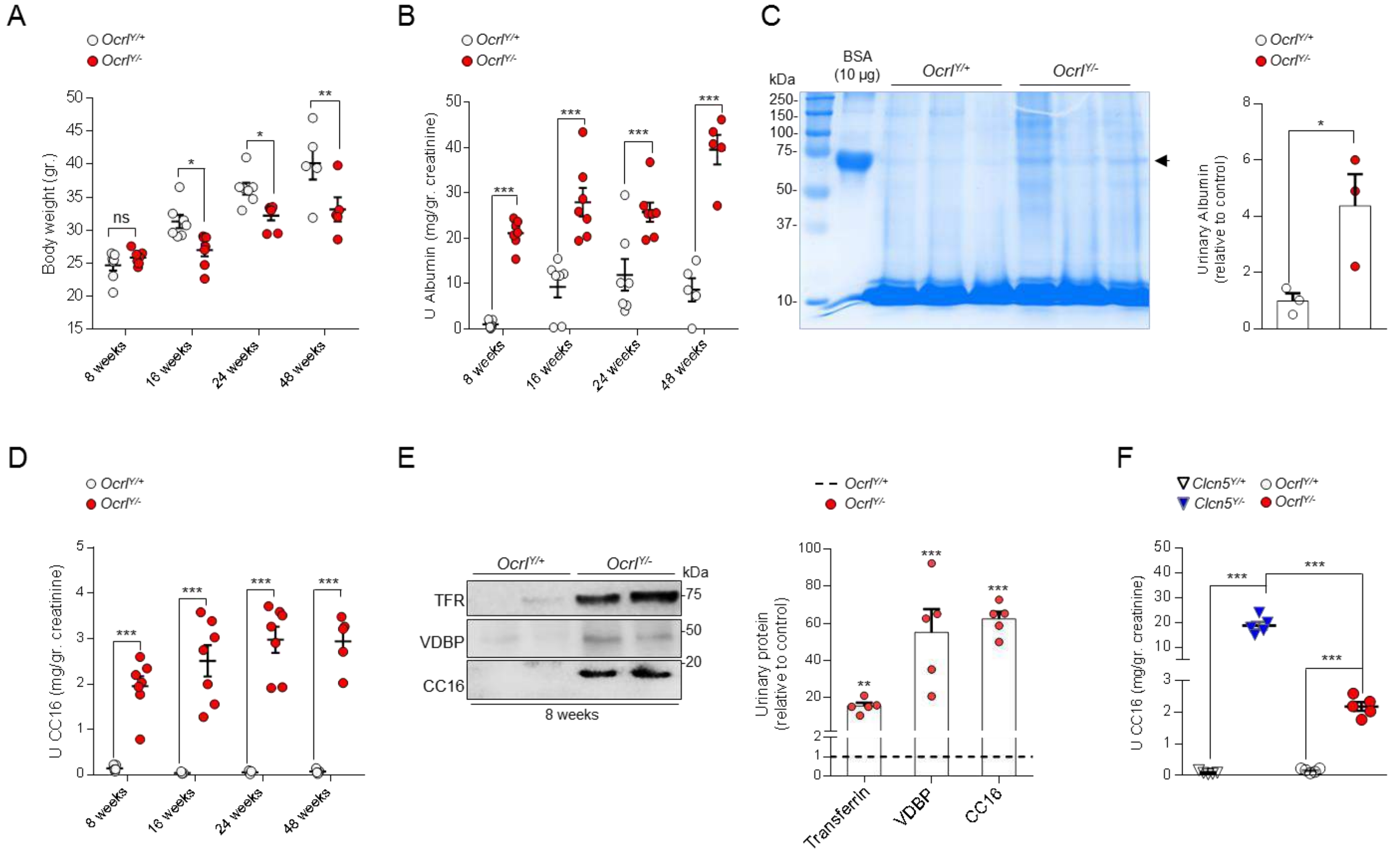

Figure 1. **Growth retardation and renal phenotype in a whole body *Ocrl*$^{Y/-}$ mouse model.** (**A**) Dot plot representing the measurement of body weight, (**B**) albumin and (**D**) clara cell protein 16 (CC16) urinary excretion in *Ocrl* male mice at 8, 16, 24 and 48 weeks after birth (8 weeks n= 7 mice per group, 16 weeks n= 7 mice per group, 24 weeks n=7 mice per group, 48 weeks n=5 mice per group). (**C**) Coomassie blue-stained SDS-PAGE analysis of urine derived from 8 weeks old *Ocrl* mice and densitometry quantification of Albumin (n=3 mice per group).10 µg of bovine serum albumin (BSA) were loaded as positive control (first lane; molecular weight (MW) ≈66.5 kDa). (**E**) Representative western blotting and densitometry quantification of transferrin (TFR), vitamin D binding protein (VDBP) and CC16 in urine derived from 8 weeks old *Ocrl* mice. (TFR, VDBP and CC16 n= 5 mice per group). (**F**) Quantification of CC16 urinary excretion in 8 weeks old *Clcn5* and *Ocrl* mice (n=5 mice per group). All the urine parameters were normalized to urinary creatinine concentration. Plotted data represent mean ± SEM. Each dot of the graphs represents one mouse. Two-tailed unpaired Student's t-test, $^*P < 0.05$, $^{**}P < 0.01$ and $^{***}P < 0.001$ relative to *Ocrl*$^{Y/+}$ or *Clcn5*$^{Y/+}$ mice. ns: not significant.

Figure 2

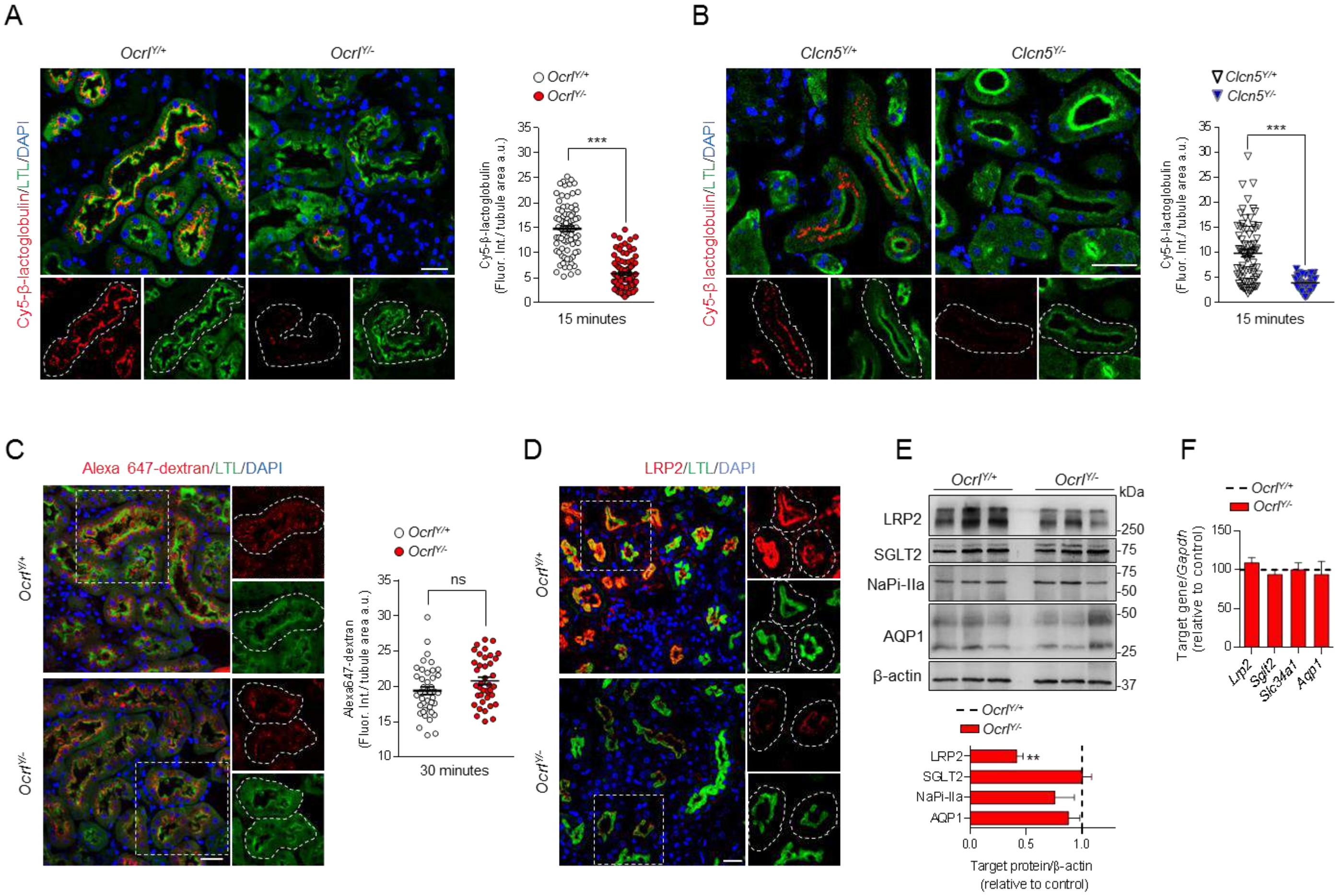

Figure 2. **Defective receptor-mediated endocytosis in *Ocrl*$^{Y/-}$ mice**. (**A-B**) Representative confocal micrographs showing Cy5 labeled β-lactoglobulin (red, 1mg/kg B.W.) or (**C**) Alexa 647–labeled dextran uptake (red, 6 mg/kg B.W.) after 15 and 30 minutes from tail vein injections respectively and quantifications of the corresponding fluorescent signal in LTL^{+} (*Lotus Tetragonolobus Lectin*, green) proximal tubules from *Ocrl* and *Clcn5* mouse kidneys (n=90 *Ocrl* and n=70 *Clcn5* proximal tubules for Cy5 labeled β-lactoglobulin uptake; n = 40 *Ocrl* proximal tubules for Alexa 647 dextran uptake); n=2 per group, each dot representing fluorescence intensity in one proximal tubule*;* fluorescence intensity was normalized on tubule area; two-tailed unpaired Student's t-test, ***P < 0.001 relative to *Ocrl*$^{Y/+}$ *or Clcn5*$^{Y/+}$ kidneys. ns: not significant). Insets: high magnification of Cy5 labeled β-lactoglobulin^{+} or Alexa 647 dextran^{+} structures in LTL^{+} proximal tubules. (**D**) Representative confocal micrographs showing LRP2 (red) expression in LTL^{+} (green) proximal tubules of *Ocrl* mouse kidneys. Insets: high magnification of LRP2^{+} structures in LTL^{+} proximal tubules. (**E**) Western blotting and densitometry analyses of LRP2, SGLT2, NaPi-IIa and AQP1 protein levels in whole kidney lysates from *Ocrl* mice. β-actin was used as loading control. Protein levels normalized on β-actin and relative to *Ocrl*$^{Y/+}$ mice (black dotted line), (LRP2 n = 6 mice per group; SGLT2, NaPiIIa and AQP1 n=3 mice per group. Mann-Whitney U test, **P < 0.01 relative to *Ocrl*$^{Y/+}$ kidneys). (**F**) The mRNA kidney levels of *Lrp2*, *Sglt2*, *Slc34a1* and *Aqp1* were analyzed by real-time qPCR. Gene target expression normalized to *Gapdh* and relative to *Ocrl*$^{Y/+}$ mice (black dotted line), (n = 3 mice per group). Nuclei counterstained with DAPI (blue) in **A**, **B**, **C** and **D**. Scale bars 25µm. Plotted data represent mean ± SEM.

Figure 3

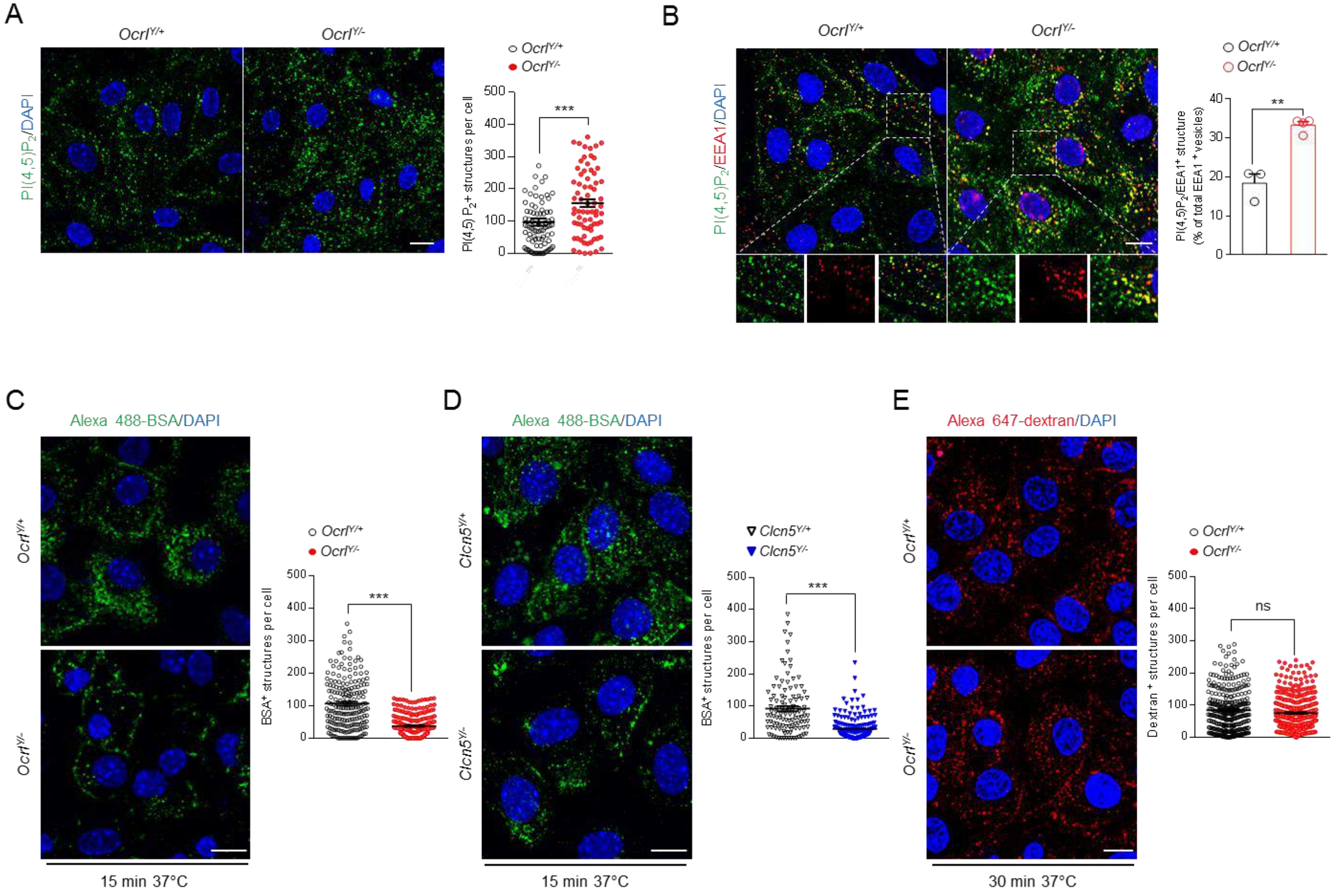

Figure 3. Altered PI(4, 5) P_2 subcellular distribution and receptor-mediated endocytosis in *Ocrl*$^{Y/-}$ mPTCs. (**A**) Representative confocal micrographs and quantification of PI(4,5)P_2^+ structures (green) in *Ocrl* mPTCs (n ≈ 80 cells pooled from three mouse kidneys per condition; each dot representing the number of PI(4,5) P_2^+ structures in a cell). (**B**) Representative confocal micrographs of *Ocrl* mPTCs immunostained with anti- PI(4,5)P_2 (green) and anti-EEA1 (red, early endosomes) and quantification (adjacent panel) of the number of PI(4,5)P_2/EEA1$^+$ structures by confocal microscopy (percentage of total EEA1$^+$ vesicles; n= 3 *Ocrl*$^{Y/+}$; n=4 *Ocrl*$^{Y/-}$ randomly selected fields per condition, each containing ≈ 15-20 cells). Insets: high magnification of PI(4,5)P_2/EEA1$^+$ structures. (**C-D**) *Ocrl* and *Clcn5* mPTCs were loaded with Alexa 488-BSA (green, 100 µg ml^{-1} for 15 min at 37 °C), fixed, and analyzed by confocal microscopy. Quantification of the number of Alexa 488-BSA$^+$ structures (n ≈150-250 cells pooled from three mouse kidneys per condition; each point representing the number of BSA$^+$ structures in a cell). (**E**) *Ocrl* mPTCs were loaded with Alexa 647-dextran 10kDa (red, 250 µg ml^{-1} for 30 min at 37 °C), fixed, and analyzed by confocal microscopy. Quantification of the number of Al647-dextran$^+$ structures (n≈ 200-250 cells pooled from three mouse kidneys per condition; each dot representing the number of dextran$^+$ structures in a cell). Nuclei counterstained with DAPI (blue). Scale bars in **A** and **B** 15µm, in **C**, **D** and **E** 10 µm. Plotted data represent mean ± SEM. Two-tailed unpaired Student's t-test, **P < 0.01, ***P < 0.001 relative to *Ocrl*$^{Y/+}$ *or Clcn5*$^{Y/+}$ mPTCs. ns: not significant.

Figure 4

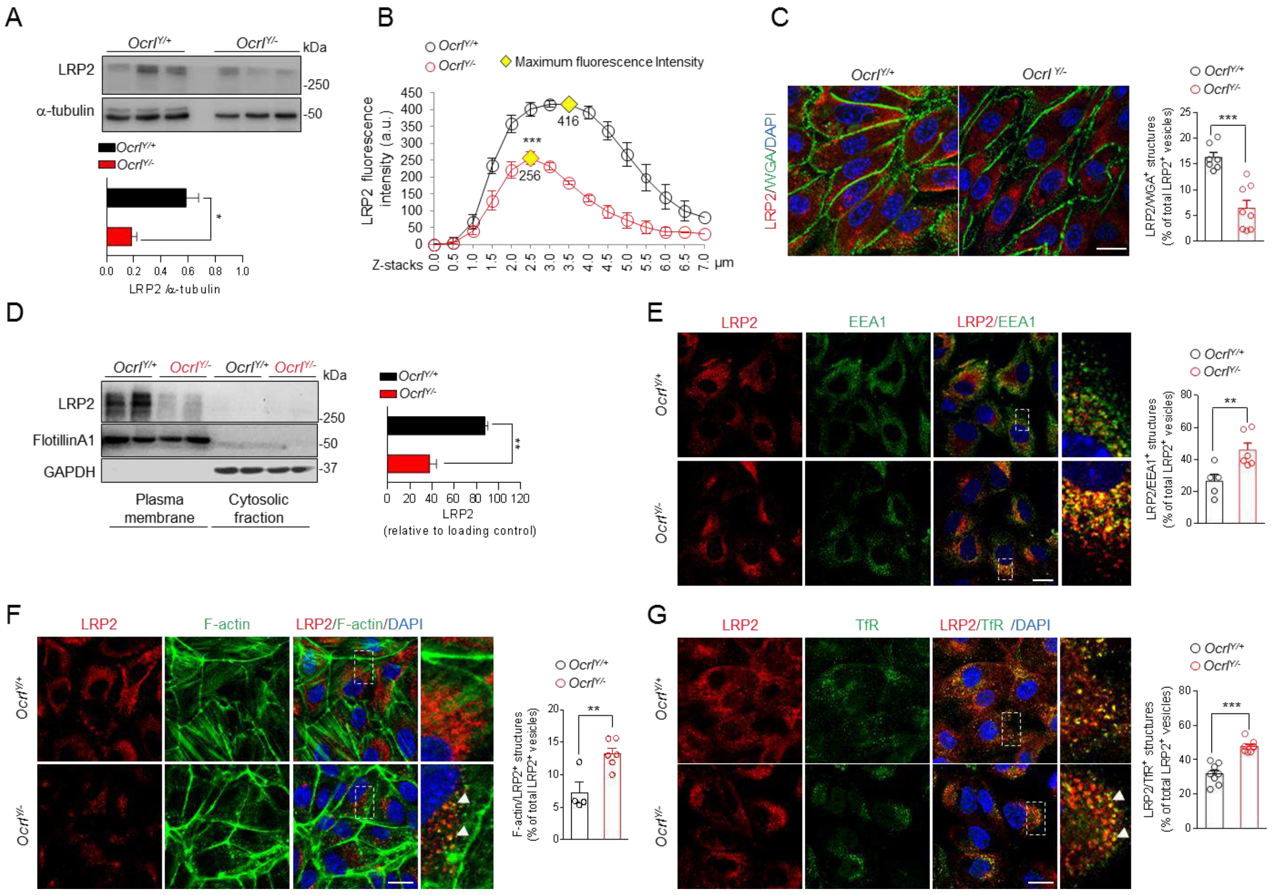

Figure 4. *Ocrl*$^{Y/-}$ mPTCs exhibit decreased expression of LRP2 and defective endocytic recycling. (**A**) Representative western blotting and quantification of LRP2 in whole *Ocrl* mPTCs lysates. α- tubulin was used as loading control (n=4 mice per group). (**B**) Dot plot representing distribution and average fluorescence intensity of LRP2 along Z-stacks projections in *Ocrl* mPTCs. Yellow rhombus represents the maximum peak of fluorescence intensity. Quantifications of Z-stacks were obtained from 3 randomly selected fields per condition, with each containing ≈ 15-20 cells. (**C**) Representative confocal micrographs and quantification of LRP2/WGA^{+} structures by confocal microscopy (in percentage of total LRP2^{+} vesicles, n=7 *Ocrl*$^{Y/+}$; n=8 *Ocrl*$^{Y/-}$ randomly selected fields per condition, each containing ≈10-15 cells). (**D**) Representative western blotting and quantification of LRP2 protein levels in plasma membrane fraction derived from *Ocrl* mPTCs. Flotillin A1 and GAPDH were used as purity marker and loading control of the plasma membrane and cytosolic fractions respectively (n=3 independent experiment). (**E**) Representative confocal micrographs of *Ocrl* mPTCs immunostained with anti-LRP2 (red) and anti-EEA1 (green, early endosomes) and quantification (adjacent panel) of the number of LRP2/EEA1^{+} structures by confocal microscopy (percentage of total LRP2^{+} vesicles; n=5 *Ocrl*$^{Y/+}$; n=6 *Ocrl*$^{Y/-}$ randomly selected fields per condition, each containing ≈ 15-20 cells). Insets: high magnification of LRP2/EEA1^{+} structures. (**F**) Representative confocal micrographs of *Ocrl* mPTCs immunostained with anti-LRP2 (red) and Alexa-Fluor-488-phalloidin (green, F-actin). Quantification (adjacent panel) of the number of F-Actin/LRP2^{+} structures (in percentage of total LRP2^{+} vesicles, n= 4 *Ocrl*$^{Y/+}$; n=6 *Ocrl*$^{Y/-}$ randomly selected fields per condition, each containing ≈10-15 cells). Insets: high magnification of F-actin/LRP2^{+} structures. (**G**) Representative confocal micrographs of *Ocrl* mPTCs stained with anti-TfR (green) and anti-LRP2 (red) and quantification of the number of TfR/LRP2^{+} structures by confocal microscopy (in percentage of total LRP2^{+} vesicles, n=8 randomly selected fields per condition, each containing ≈20-25 cells). Insets: high magnification of TfR/LRP2^{+} structures. Nuclei counterstained with DAPI (blue) in **C**, **E, F** and **G.** Scale bars in **E**, **F** and **G** 15μm and in **C** 20μm. Plotted data represent mean ± SEM. Two-tailed unpaired Student's t-test, *P < 0.05, **P < 0.01 and ***P < 0.001 relative to *Ocrl*$^{Y/+}$ mPTCs.

Figure 5

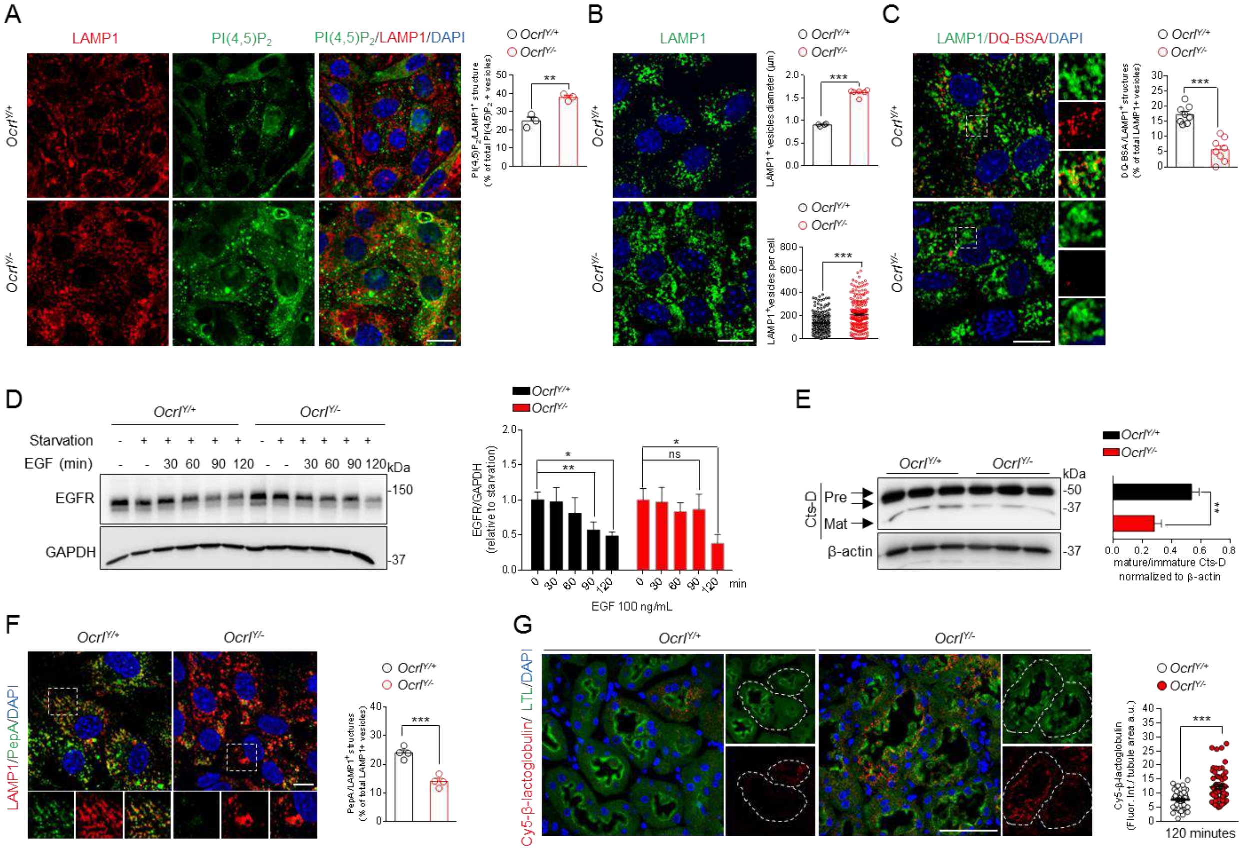

Figure 5. Altered lysosomal dynamics and degradative capacity in *Ocrl*$^{Y/-}$ mPTCs. (**A**) *Ocrl* mPTCs were immunostained with anti-PI(4,5)P$_2$ (green) and anti-LAMP1 (red, lysosomes) and the number of PI(4,5)P$_2$ /LAMP1$^+$ structures were quantified by confocal microscopy (in percentage of total PI(4,5)P$_2$$^+$ vesicles; n=3 randomly selected fields per condition, each containing ≈ 40-50 cells). (**B**) Representative confocal micrographs of *Ocrl* mPTCs immunostained with anti-LAMP1 (green). Quantification of the average LAMP1$^+$ vesicles diameter (top, n= 4 *Ocrl*$^{Y/+}$; and n=6 *Ocrl*$^{Y/-}$ randomly selected fields per condition, each containing ≈ 50-60 cells) and number of structures (bottom, n≈200-220 cells pooled from 3 *Ocrl* kidneys per group, each point representing the number of LAMP1$^+$ structure in a cell). (**C**) *Ocrl* mPTCs were loaded with DQ (dequenched) Red BSA (red, 10 µg ml^{-1} for 1h at 37 °C), immunostained with anti- LAMP1 (green, lysosomes) fixed and analyzed by confocal microscopy. Quantification of number of DQ Red BSA /LAMP1+ structures (in percentage of total LAMP1$^+$ structures, n = 8 randomly selected fields per condition, with each containing ≈ 10–15 cells). Insets: high magnification of DQ Red BSA / LAMP1$^+$ vesicles. (**D**) *Ocrl* mPTCs were serum starved for 24 h and then stimulated with EGF (100 ng/ml) for the indicated times. EGFR protein levels were evaluated by western blotting and quantified relative to time 0 (starved cells). (n=3mice per group; two-tailed unpaired Student's t-test, $^*P < 0.05$, $^{**}P < 0.01$ relative to *Ocrl*$^{Y/+}$ or *Ocrl*$^{Y/-}$ starved mPTCs. ns: not significant). (**E**) Western blotting and densitometry analyses of cathepsin D (Cts-D) protein levels in *Ocrl* mPTCs (n= 4mice per group). (**F**) *Ocrl* mPTCs were loaded with Bodipy-FL-PepA (1 µM, for 1 h at 37 °C, green), immunostained with anti- LAMP1 antibody (red) and analysed by confocal microscopy. Quantification of numbers of PepA/LAMP1$^+$ structures (in percentage of total LAMP1$^+$ structures; n = 4 randomly selected fields per condition, with each containing ~ 20–25 cells). (**G**) Representative confocal micrographs showing Cy5 labeled β-lactoglobulin (red) after 120 minutes from tail vein injections and quantifications of the corresponding fluorescent signal in LTL$^+$ proximal tubules from *Ocrl* mouse kidneys (n=50 *Ocrl* proximal tubules; each dot representing fluorescence intensity in one proximal tubule*;* fluorescence intensity was normalized on tubule area). Nuclei counterstained with DAPI (blue) in **A, B, C, F** and **G**. Scale bars in **A**, **B** and **C** 15 µm; in **F** 10 µm and in **G** 50 µm. Plotted data represent mean ± SEM. Two-tailed unpaired Student's t-test. $^{**}P < 0.01$, $^{***}P < 0.001$ relative to *Ocrl*$^{Y/+}$ mPTCs or kidneys.

Figure 6

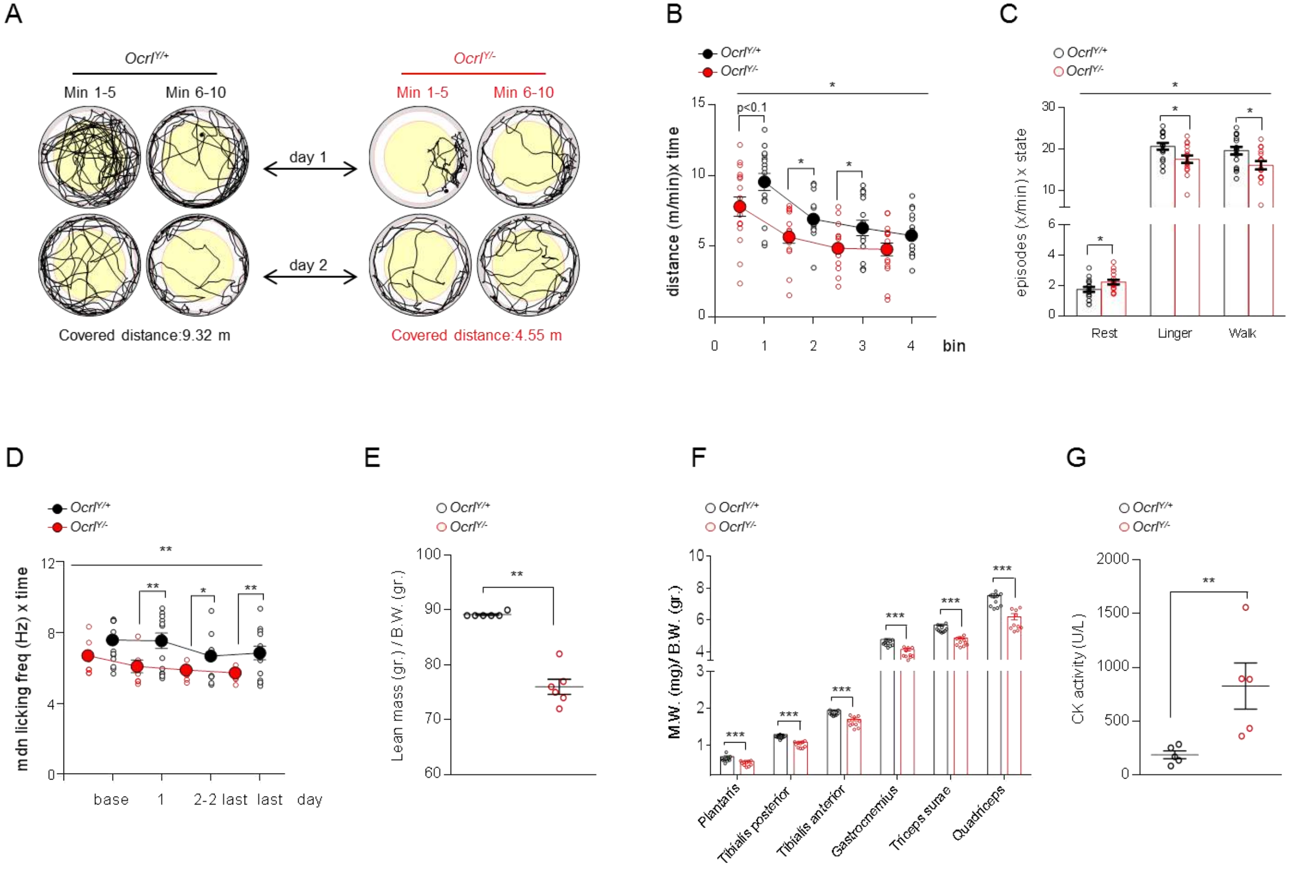

Figure 6. Impaired locomotor activity and muscular defects in $Ocrl^{Y/-}$ mice. (**A-C**) Open field large arena test was performed during 10 minutes of two subsequent days in a circular arena with a diameter of 150 cm on a cohort of 16 $Ocrl^{Y/+}$and 16 $Ocrl^{Y/-}$ age matched male mice. (**A**) Illustrative pictures representing the trajectories traveled by *Ocrl* mice during the open field large arena test. (**B**) Dot plot representing the distance covered by *Ocrl* mice during the large open field arena test. The distance traveled by each mouse is normalized to 1 minute observation time and plotted as function of time for each bin (bin=5 minutes) (split ANOVA effects followed by post-hoc tests between genotype for each bin: Bin1 ’P < 0.1, Bin2 *P < 0.05, Bin3 *P < 0.05). (**C**) Dotted bar graph representing the frequency of resting, lingering and walking episodes exhibited by *Ocrl* mice during the open field large arena test (split ANOVA effects followed by post-hoc tests between genotype for each state: rest *P < 0.05, linger, *P < 0.05, walk *P < 0.05). (**D**) IntelliCage experiments were performed on a cohort of age matched male *Ocrl* mice (13 $Ocrl^{Y/+}$and 13 $Ocrl^{Y/-}$). Dot plot representing the median licking frequency during drinking restriction protocol. Base indicates the licking frequency during the last 24h of nose poke adaptation phase (split ANOVA effects followed by post-hoc tests between genotype for each time point: Day1 **P < 0.01, Day 2-2last *P < 0.05, Last day **P < 0.001). (**E**) Lean mass/body weight ratio determined by whole body composition analysis in *Ocrl* mice (n=6 mice per group). (**F**) Muscle mass, relative to body weight, of selected hind limb muscles obtained by bilateral dissection of 5 pairs of *Ocrl* mice (n=10 values for symmetrical leg muscles). (**G**) Plasma creatine kinase activity (CK) in the corresponding 5 pairs of *Ocrl* mice (as in B). Plotted data represent mean ± SEM. In **B**, **C** and **D** One-way ANOVA between subject factor genotype: *P < 0.05; **P < 0.01 (on the top of each graph); in **E**, **F** and **G** Mann Withney test, **P < 0.01; ***P < 0.001 relative to $Ocrl^{Y/+}$ mice.

Table 1. Body weight, urine and blood parameters in *Ocrl* and *Clcn5* mice.

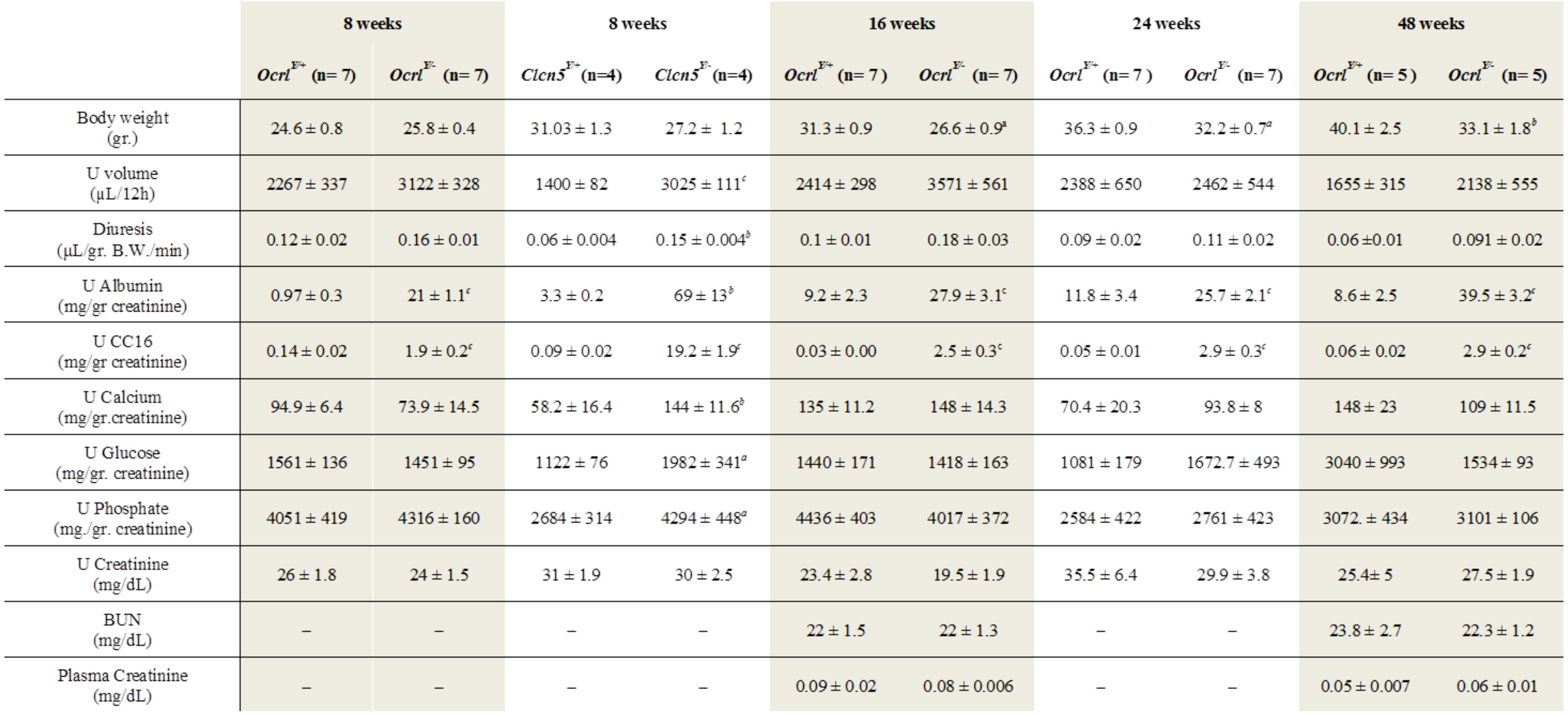

	8 weeks		**8 weeks**		**16 weeks**		**24 weeks**		**48 weeks**	
	Ocrl$^{Y/+}$ **(n= 7)**	***Ocrl***$^{Y/-}$ **(n= 7)**	***Clcn5***$^{Y/+}$ **(n=4)**	***Clcn5***$^{Y/-}$ **(n=4)**	***Ocrl***$^{Y/+}$ **(n= 7)**	***Ocrl***$^{Y/-}$ **(n= 7)**	***Ocrl***$^{Y/+}$ **(n= 7)**	***Ocrl***$^{Y/-}$ **(n= 7)**	***Ocrl***$^{Y/+}$ **(n= 5)**	***Ocrl***$^{Y/-}$ **(n= 5)**
Body weight (gr.)	24.6 ± 0.8	25.8 ± 0.4	31.03 ± 1.3	27.2 ± 1.2	31.3 ± 0.9	26.6 ± 0.9^{a}	36.3 ± 0.9	32.2 ± 0.7^{a}	40.1 ± 2.5	33.1 ± 1.8^{b}
U volume (µL/12h)	2267 ± 337	3122 ± 328	1400 ± 82	3025 ± 111^{c}	2414 ± 298	3571 ± 561	2388 ± 650	2462 ± 544	1655 ± 315	2138 ± 555
Diuresis (µL/gr. B.W./min)	0.12 ± 0.02	0.16 ± 0.01	0.06 ± 0.004	0.15 ± 0.004^{b}	0.1 ± 0.01	0.18 ± 0.03	0.09 ± 0.02	0.11 ± 0.02	0.06 ±0.01	0.091 ± 0.02
U Albumin (mg/gr creatinine)	0.97 ± 0.3	21 ± 1.1^{c}	3.3 ± 0.2	69 ± 13^{b}	9.2 ± 2.3	27.9 ± 3.1^{c}	11.8 ± 3.4	25.7 ± 2.1^{c}	8.6 ± 2.5	39.5 ± 3.2^{c}
U CC16 (mg/gr creatinine)	0.14 ± 0.02	1.9 ± 0.2^{c}	0.09 ± 0.02	19.2 ± 1.9^{c}	0.03 ± 0.00	2.5 ± 0.3^{c}	0.05 ± 0.01	2.9 ± 0.3^{c}	0.06 ± 0.02	2.9 ± 0.2^{c}
U Calcium (mg/gr.creatinine)	94.9 ± 6.4	73.9 ± 14.5	58.2 ± 16.4	144 ± 11.6^{b}	135 ± 11.2	148 ± 14.3	70.4 ± 20.3	93.8 ± 8	148 ± 23	109 ± 11.5
U Glucose (mg/gr. creatinine)	1561 ± 136	1451 ± 95	1122 ± 76	1982 ± 341^{a}	1440 ± 171	1418 ± 163	1081 ± 179	1672.7 ± 493	3040 ± 993	1534 ± 93
U Phosphate (mg./gr. creatinine)	4051 ± 419	4316 ± 160	2684 ± 314	4294 ± 448^{a}	4436 ± 403	4017 ± 372	2584 ± 422	2761 ± 423	3072. ± 434	3101 ± 106
U Creatinine (mg/dL)	26 ± 1.8	24 ± 1.5	31 ± 1.9	30 ± 2.5	23.4 ± 2.8	19.5 ± 1.9	35.5 ± 6.4	29.9 ± 3.8	25.4± 5	27.5 ± 1.9
BUN (mg/dL)	–	–	–	–	22 ± 1.5	22 ± 1.3	–	–	23.8 ± 2.7	22.3 ± 1.2
Plasma Creatinine (mg/dL)	–	–	–	–	0.09 ± 0.02	0.08 ± 0.006	–	–	0.05 ± 0.007	0.06 ± 0.01

U, Urine; CC16, Clara cell protein 16; BUN, Blood urea nitrogen. All the measurements were performed on *Ocrl*$^{Y/+}$ and *Ocrl*$^{Y/-}$ male mice matched per age. Plotted data represent mean ± SEM. Two-tailed unpaired Student's t-test was applied between genotypes for the indicated time point.

$^{a}p < 0.05$ versus *Ocrl*$^{Y/+}$ or *Clcn5*$^{Y/+}$; $^{b}p < 0.01$ versus *Ocrl*$^{Y/+}$ *or Clcn5*$^{Y/+}$; $^{c}p < 0.001$ versus *Ocrl*$^{Y/+}$ *or Clcn5*$^{Y/+}$.

OCRL Deficiency Impairs Endolysosomal Function in a Humanized Mouse Model for Lowe Syndrome and Dent Disease

Beatrice Paola Festa, Marine Berquez, Alkaly Gassama, Irmgard Amrein, Hesham M. Ismail, Marijana Samardzija, Leopoldo Staiano, Alessandro Luciani, Christian Grimm, Robert L. Nussbaum, Maria Antonietta De Matteis, Olivier M. Dorchies, Leonardo Scapozza, David Paul Wolfer, Olivier Devuyst.

Materials and Methods

Cell profiler quantifications
Behavioral tests
IntelliCages apparatus and mice preparation
Additional references

Supplementary Information

Suppl. Figures 1-7
Suppl. Table 1

MATERIALS AND METHODS

Cell profiler quantifications. The pipeline “Speckle counting” derived from the open source Cell Profiler image analysis software was used to identify dots ($PI(4,5)P_2$ or PI3P or BSA or Dextran or LAMP1 or MPR-positive structures) surrounding nuclei and to perform per-nuclei aggregate measurements (eg. the number of dots/nucleus), as described by Carpenter et al. (2006) and De Leo et al. (2016). Briefly, the images were converted to greyscale using the module “ColorToGray”. The “IdentifyPrimaryObjects” module was used to identify nuclei and dots while cells were identified by using the module “IdentifySecondaryObjects”. “MaskObject” and “RelateObject” modules were used to establish a parent-child relationship between the cells and the dots, identified as masked objects, and to calculate the average of dots per cell. The module “MeasureObjectIntensityDistribution” was used to score the fluorescence intensity of MPR and TfR positive structures contained into perinuclear region (area defined by the first 10 bin) and peripheral region (area defined by the last 10 bin) of the cells. Briefly, the software generates 20 concentrically bin around the nucleus of each cell and calculates the intensity distribution for each bin. The module “MeasureObjectSizeShape” was used to score the vesicle size of LAMP1. The pipeline “Cell/particle counting, and scoring the percentage of stained objects” was used to score the percentage of $EEA1^+$ structures colocalizing with $PI(4,5)P_2$ or F-actin, the percentage of $LRP2^+$ structures colocalizing with F-actin, EEA1 or TfR and the percentage of $LAMP1^+$ structures colocalizing with $PI(4,5)P_{2,}$ DQ-BSA or PepA. Briefly, the images were converted to greyscale using the module “ColorToGray”. Then the “ObjectIdentification” module was used to identify the nuclei and the aforementioned stained structures/vesicles. The “RelateObject” module was used to establish a parent-child relationship between the stained objects. In this case, a “parent” object is one that touches, overlaps or encloses a “child” object. Objects1 that touch or overlap with an Object2 are considered to be colocalized and will be assigned as a parent to a corresponding child. The “ClassifyObjects” and “FilterObjects” modules were used to categorize structures that were either colocalizing or not-colocalizing, and to calculate the percentage of colocalizing structures on the total amount per image. Fluorescence intensity of LRP2 was measured from a Z stack of 55 serial images acquired, according to Nyquist theorem, every 0.13 µm to maximize the spatial information. The average fluorescence intensity of LRP2 was calculated every 0.5 µm of the Z-stacks projection by using ImageJ software. Qualitative analysis of F-actin dynamics was performed by maximal projection of Z-stack images acquired throughout the entire volume of the cells.

Behavioral tests. ***Open field large arena test.*** The large open-field arena is circular with a diameter of 150 cm, a slightly roughened white plastic floor, and 35cm high smooth sidewalls made of white polypropylene. Illumination is performed by indirect diffuse room light (4 40W bulbs, 12 lux). Each subject is released near the wall and observed for 10 min on two subsequent days. Movements are tracked using Noldus EthoVision. Between subjects, the arena is thoroughly cleaned with water and dried. ***Water-maze cue navigation.*** The water maze is constituted by a round white poly-propylene pool with a diameter of 150 cm with 68 cm high walls. It is filled with water (24-26° C, depth 15 cm) which is rendered opaque by addition of 1l of milk (UHT whole milk 3.5% fat, Coop, Switzerland). The white quadratic goal platform (14x14 cm) is made of metallic wire mesh and painted white. It is hidden 0.5 cm below the water surface in the center of one of the 4 quadrants, approximately 30 cm from the side wall. Salient extra-maze cues made of black cardboard are placed on the walls of the testing room. Computer and experimenter are hidden behind a curtain. Illumination is performed by indirect diffuse room light (4 40W bulbs, 12 lux at the center of the pool). During the test animals are trained for 2 days with the goal platform marked by a salient cue and placed in a different quadrant for every trial. All subjects are trained on the same sequence of goal positions and released from the same start points. ***Three-chambers sociability test.*** The 3-chamber cage is a polycarbonate type III cage (20.5 cm high, 58 × 40 cm top, 55 × 37.5 cm bottom, Techniplast, 2000P, Buguggiate, Italy). Two dividers provided with gates regulate the access of the test mouse from the middle to the lateral chambers. One unfamiliar stimulus mouse is placed inside a metallic cylinder in one of the two lateral chambers. The cylinder allows visual and olfactory contact between the test mouse and the stimulus mouse, reducing the possibility of physical contact. In the other lateral empty chamber, an empty cylinder is placed giving then the test mouse the choice to spend time in the chamber with the novel object (the cylinder) plus the unfamiliar mouse (social stimulus) and the chamber containing only the empty cylinder. This test runs for 10 minutes after which the stimulus mouse is considered to be familiar to the test mouse. The time spent by the test mouse in the lateral chambers is noted.

IntelliCage apparatus and mice preparation. The IntelliCage apparatus (TSE Systems, Bad Homburg, Germany) is placed in a polycarbonate cage (20.5 cm high, 58 × 40 cm top, 55 × 37.5 cm bottom, Techniplast, 2000P, Buguggiate, Italy) and accommodates up to 16 mice. Its aluminum top contains a freely accessible food rack filled with standard mouse chow (Standard 3430, Kliba Nafag, Kaiseraugst, Switzerland). The floor is covered with woodchip bedding and provides 4 central red shelters (Techniplast, Buguggiate, Italy). Four triangular conditioning chambers (15×15×21 cm) are fitted in the cage corners and provide room for one mouse at a time. Each chamber contains two drinking bottles, accessible via two round openings that can be opened and closed with motorized doors. Mice were tagged with RFID-transponders, subcutaneously implanted under isoflurane anesthesia, which can be read by a circular RIFD antenna located at the entrance of each chamber. The duration of their visit is determined by both the antenna reading and a temperature sensor that detects the presence of the animal inside the corner. During a visit, number and duration of individual nosepokes at each door are recorded using IR-beam sensors. Licking episodes at each bottle are monitored using lickometers (duration of the episode, number of licks, total contact time). IntelliCages have individual controllers and are connected to a central PC running the software that permits to design and control experiments remotely, as well as to analyze the recorded data (IntelliCage Plus, TSE Systems, Bad Homburg, Germany). After RIFD implantation, mice are allowed to recover for one week in groups of 8-16 mice in standard Type III cages with water and food ad libitum. The same grouping is maintained when the mice are later transferred to IntelliCages. During all adaptation phases and tasks in IntelliCage, mice are fed ad libitum. Ambient lights are on 20:00-08:00. Room temperature is kept constant at 23°C.

Additional References:

Carpenter, A.E., Jones, T.R., Lamprecht, M.R., Clarke, C., Kang, I.H., Friman, O., Guertin, D.A., Chang, J.H., Lindquist, R.A., Moffat, J. et al. (2006) CellProfiler: image analysis software for identifying and quantifying cell phenotypes. *Genome Biol*., **7**, R100.

De Leo, M.G., Staiano, L., Vicinanza, M., Luciani, A., Carissimo, A., Mutarelli, M., Di Campli, A., Polishchuk, E., Di Tullio, G., Morra, V. et al. (2016) Autophagosome-lysosome fusion triggers a lysosomal response mediated by TLR9 and controlled by OCRL. *Nat. Cell. Biol*., **18**, 839-850

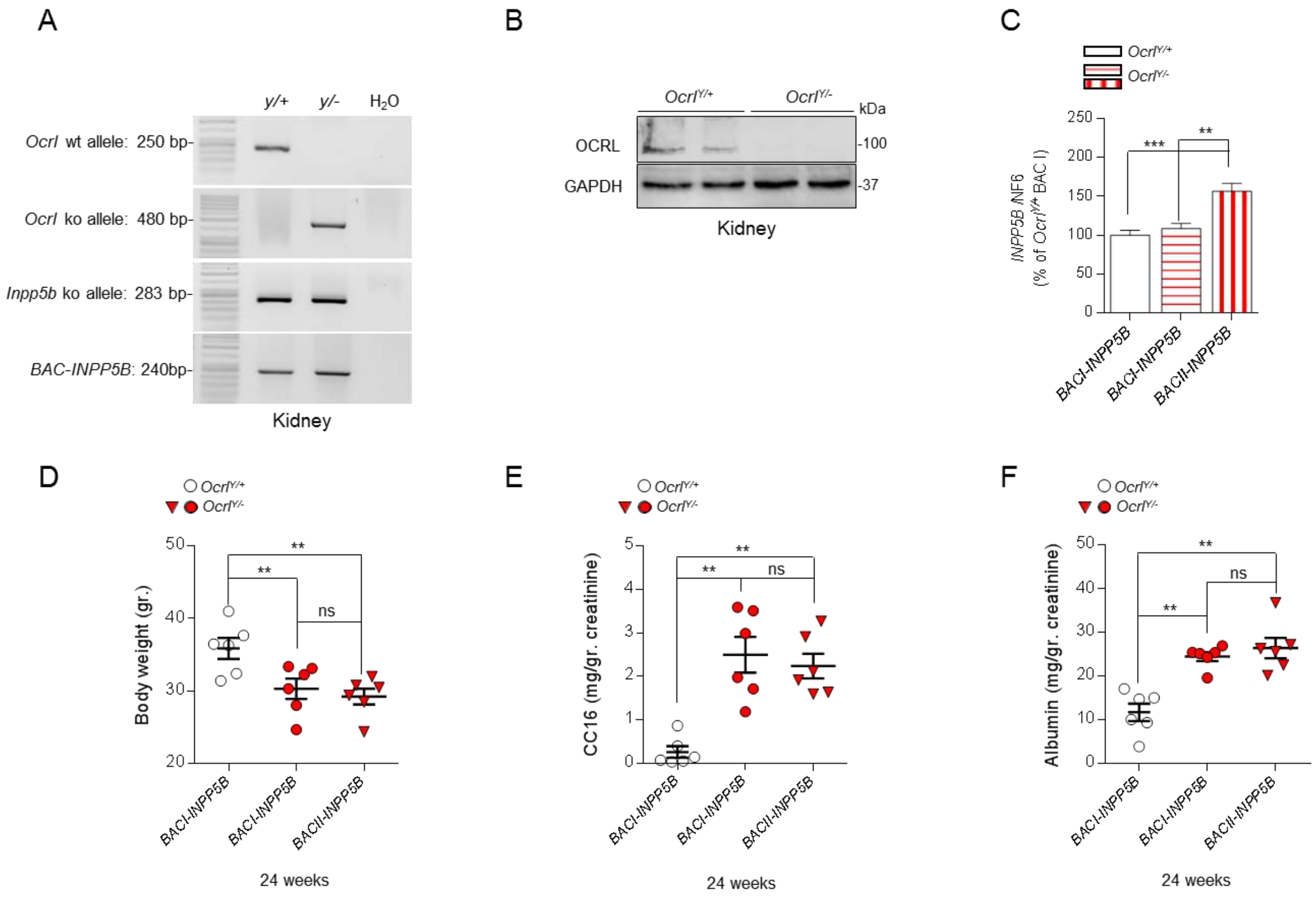

Supplementary Figure 1. **Genotype confirmation and analyses of the kidney phenotype in *Ocrl*$^{Y/-}$ mice harboring different levels of human *BAC-INPP5B* expression**. (**A**) *Ocrl*, *Inpp5b* and *BAC-INPP5B* genomic DNA analyses by PCR and agarose gel electrophoresis isolated from kidney biopsies derived from *Ocrl* mice. (**B**) Western blotting of OCRL protein level in whole kidney lysates from *Ocrl* mice. GAPDH was blotted as loading control. (**C**) *BAC-INPP5B* mRNA expression in kidneys derived from *Ocrl* mice was analyzed by quantitative RT-PCR. Gene target expression was normalized on 6 housekeeping genes and expressed as relative to *Ocrl*$^{Y/+}$ *BACI-INPP5B* (n=5 mice per condition). (**D**) Dot plot representing the measurement of the body weight, (**E**) Clara cell secretory protein (CC16) and (**F**) albumin urinary excretion in *Ocrl* mice harboring different level of *BAC-INPP5B* expression as shown in **C**. Each dot represents one mouse (n=6 mice per group). All the analyses in **D**, **E** and **F** were performed on mice matched for age (24 weeks) and gender (male). All the urine parameters were normalized to urinary creatinine concentration. Plotted data represent mean ± SEM. Two-tailed unpaired Student's t-test, **P < 0.01 relative to *Ocrl*$^{Y/+}$ or *Ocrl*$^{Y/-}$ *BACI-INPP5B* mice. ns: not significant.

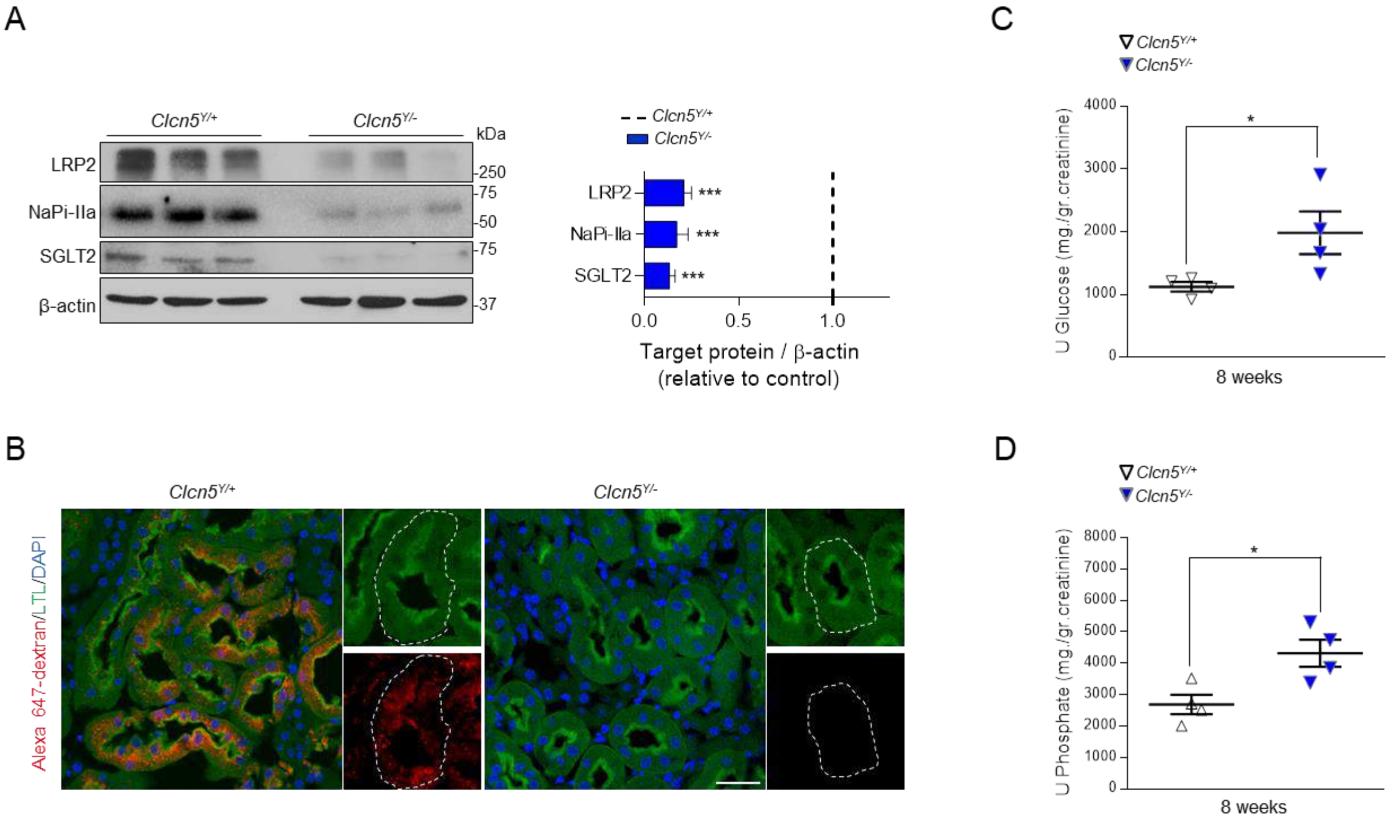

Supplementary Figure 2. **Proximal tubule dysfunction in *Clcn5*$^{Y/-}$ mice**. (**A**) Western blotting and densitometry analysis of LRP2, NaPi-IIa and SGLT2 protein levels in whole kidney lysates from *Clcn5* mice. β-actin was used as loading control. (n= 3 mice per group). (**B**) Representative confocal micrographs showing Alexa 647–labeled dextran uptake (red, 6 mg/kg B.W.) in LTL$^+$ (*Lotus Tetragonolobus Lectin*, green) proximal tubules of *Clcn5* mouse model after 30 minutes from tail vein injections. Nuclei counterstained with DAPI (blue). Scale bar 25µm. (**C**) Dot plot representing the measurement of glucose and (**D**) phosphate urinary excretion in 8 weeks old *Clcn5* mice. Each dot represents one mouse (n=4 mice per group). All the urine parameters were normalized to urinary creatinine concentration. Plotted data represent mean ± SEM. Two-tailed unpaired Student's t-test, *P < 0.05, ***P < 0.001 relative to *Clcn5*$^{Y/+}$ mice.

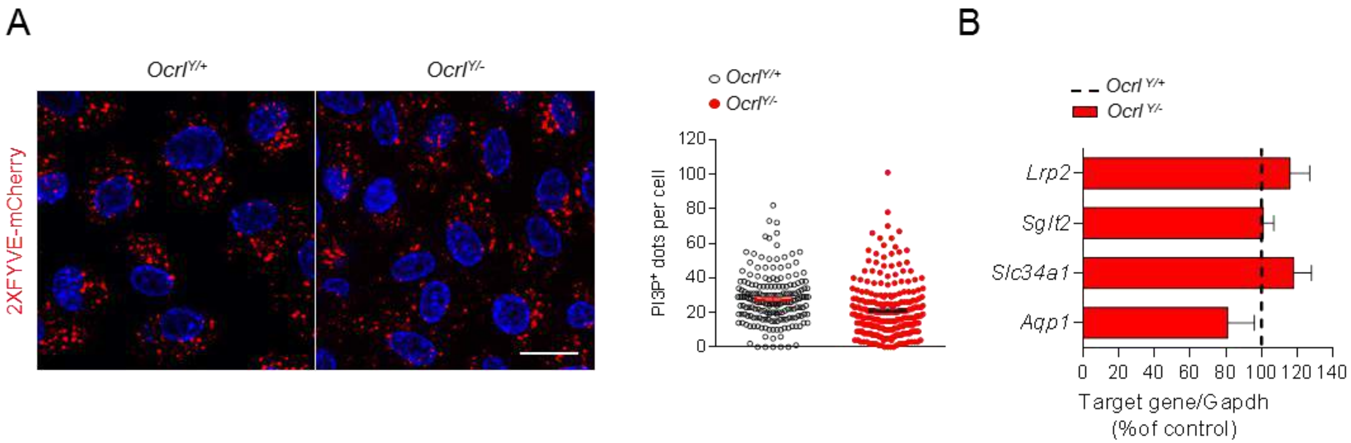

Supplementary Figure 3. ***Ocrl***$^{Y/-}$ **mPTCs exhibit no changes in PI3P (Phosphatidylinositol 3 phosphate) levels and no transcriptional alterations of proximal tubule receptors and channels.** (**A**) Representative confocal micrographs and quantification of the number of PI3P$^+$ structures stained by 2XFYVE-mcherry domain (red) in *Ocrl* mPTCs (n≈ 200-250 cells pooled from three *Ocrl* kidneys per group; each point representing the number of PI3P$^+$ vesicles in a cell). Nuclei counterstained with DAPI (blue). Scale bar 15µm. **(B)** The mRNA mPTCs levels of *Lrp2*, *Sglt2*, *Slc34a1* and *Aqp1* were analyzed by real-time qPCR. Genes target expression normalized to *Gapdh* and relative to *Ocrl*$^{Y/+}$ (n = 3 mice per group). Plotted data represent mean ± SEM.

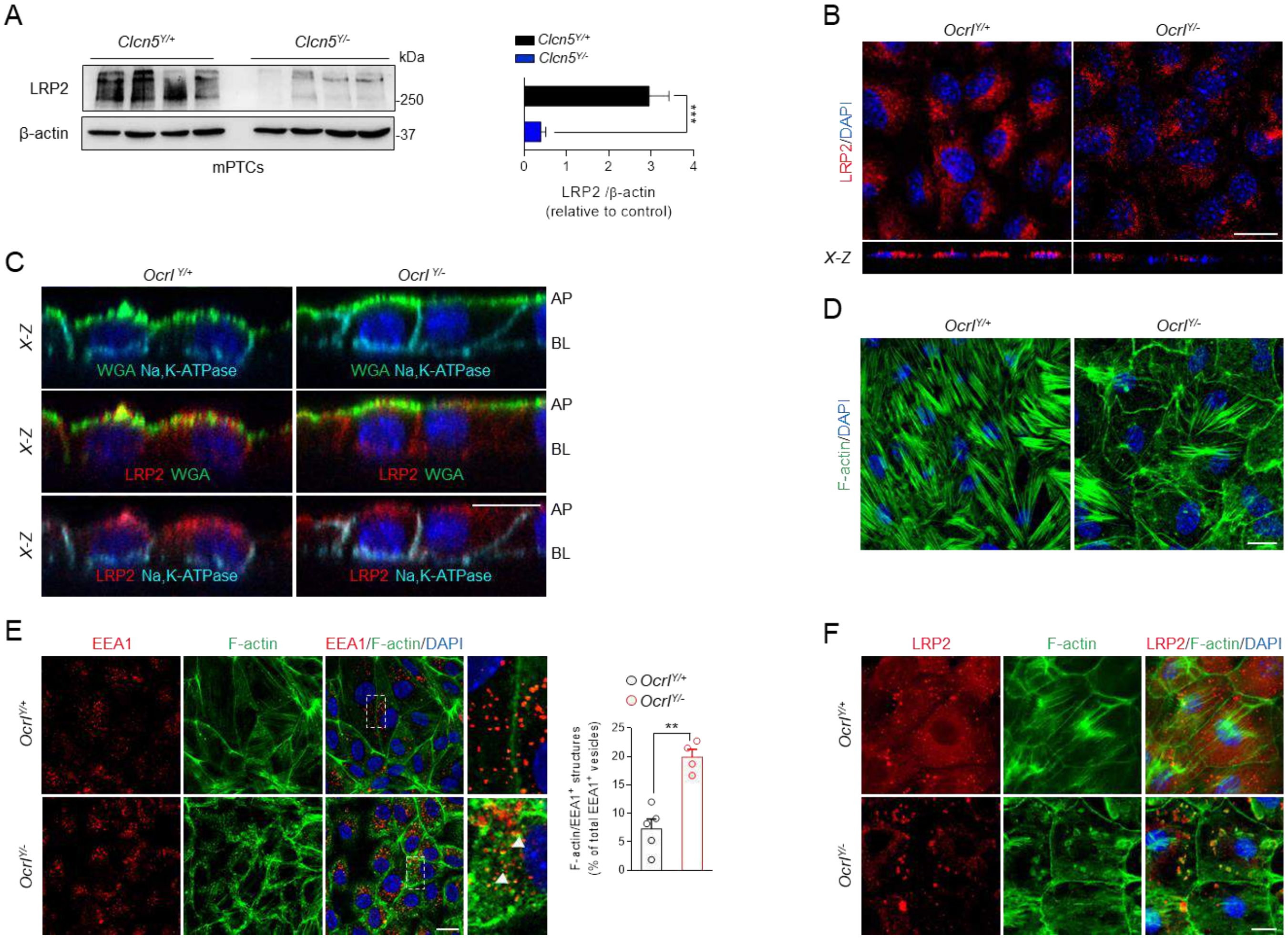

Supplementary Figure 4. LRP2 dynamics in Dent disease. *(***A***)* Western blot and densitometry analysis of LRP2 in whole *Clcn5* mPTCs lysates. β-actin was used as loading control (n= 4 mice per group). (**B**) Representative confocal micrographs and X–Z side view of *Ocrl* mPTCs immunostained with anti-LRP2 (red). (**C**) Representative confocal micrographs of X–Z side view of a z-stack performed on *Ocrl* mPTCs immunostained with WGA (green) and Na,K-ATPase (cyan) in the upper panels, WGA (green) and LRP2 (red) in the middle panels and Na,K-ATPase (cyan) and LRP2 (red) in the lower panels. (**D**) Maximum intensity projection of a confocal Z-stacks series representing *Ocrl* mPTCs immunostained with Alexa-Fluor-488-phalloidin (green, F-actin). (**E**) Representative confocal micrographs of *Ocrl* mPTCs immunostained with anti-EEA1 (red, early endosomes) and Alexa-Fluor-488-phalloidin (green, F-actin). Quantification of F-actin/EEA1^{+} structures (in percentage of total EEA1^{+} vesicles, n=5 *Ocrl*$^{Y/+}$; n=4 *Ocrl*$^{Y/-}$ randomly selected fields per condition, each containing ≈ 10-15 cells). Insets: high magnification of F-actin/EEA1^{+} structures. (**F**) High magnification confocal micrographs of *Ocrl* mPTCs immunostained with anti-LRP2 (red) and Alexa-Fluor-488-phalloidin (green, F-actin). Nuclei counterstained with DAPI (blue) in **B**-**F**. Scale bars in **C** 10μm**,** in **B**, **D**, **E** and **F** 15μm. Plotted data represent mean ± SEM. Two-tailed unpaired Student's t-test, **P < 0.01, ***P < 0.001 relative to *Clcn5* $^{Y/+}$ or *Ocrl* $^{Y/+}$ mPTCs.

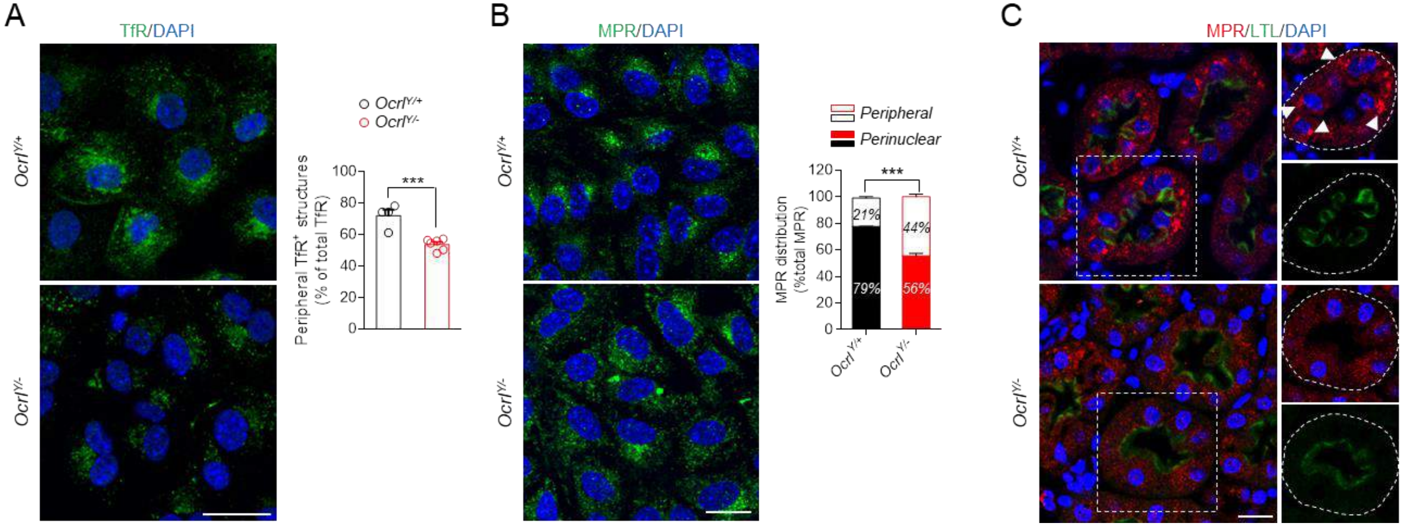

Supplementary Figure 5. Impaired trafficking of MPR and TfR cellular receptors in *Ocrl*$^{Y/-}$ mPTCs. (**A**) Representative confocal micrographs and quantification of TfR$^+$ structures distribution (green) in *Ocrl* mPTCs (in percentage of the total TfR$^+$ vesicles, n=4 *Ocrl*$^{Y/+}$; n=6 *Ocrl*$^{Y/-}$ randomly selected fields per condition, each containing ≈ 20 cells). Two-tailed unpaired Student's t-test, ***P < 0.001 relative to *Ocrl*$^{Y/+}$ mPTCs. (**B**) Representative confocal micrographs and quantification of distribution of MPR$^+$ structures (green) in *Ocrl* mPTCs (perinuclear vs peripheral in percentage of the total MPR$^+$ vesicles, n=3 randomly selected fields per condition, each containing ≈ 40-50 cells). Two-tailed unpaired Student's t-test, Peripheral/perinuclear MPR$^+$ vesicles ***P < 0.001 relative to *Ocrl*$^{Y/+}$ mPTCs. (**C**) Representative confocal micrographs showing MPR$^+$ structures (red) in LTL$^+$ (*Lotus Tetragonolobus Lectin*, green) proximal tubules of *Ocrl* mouse kidneys. Plotted data represent mean ± SEM. Nuclei counterstained with DAPI (blue). Scales bars in **A** 20µm **B** and **C** 15µm.

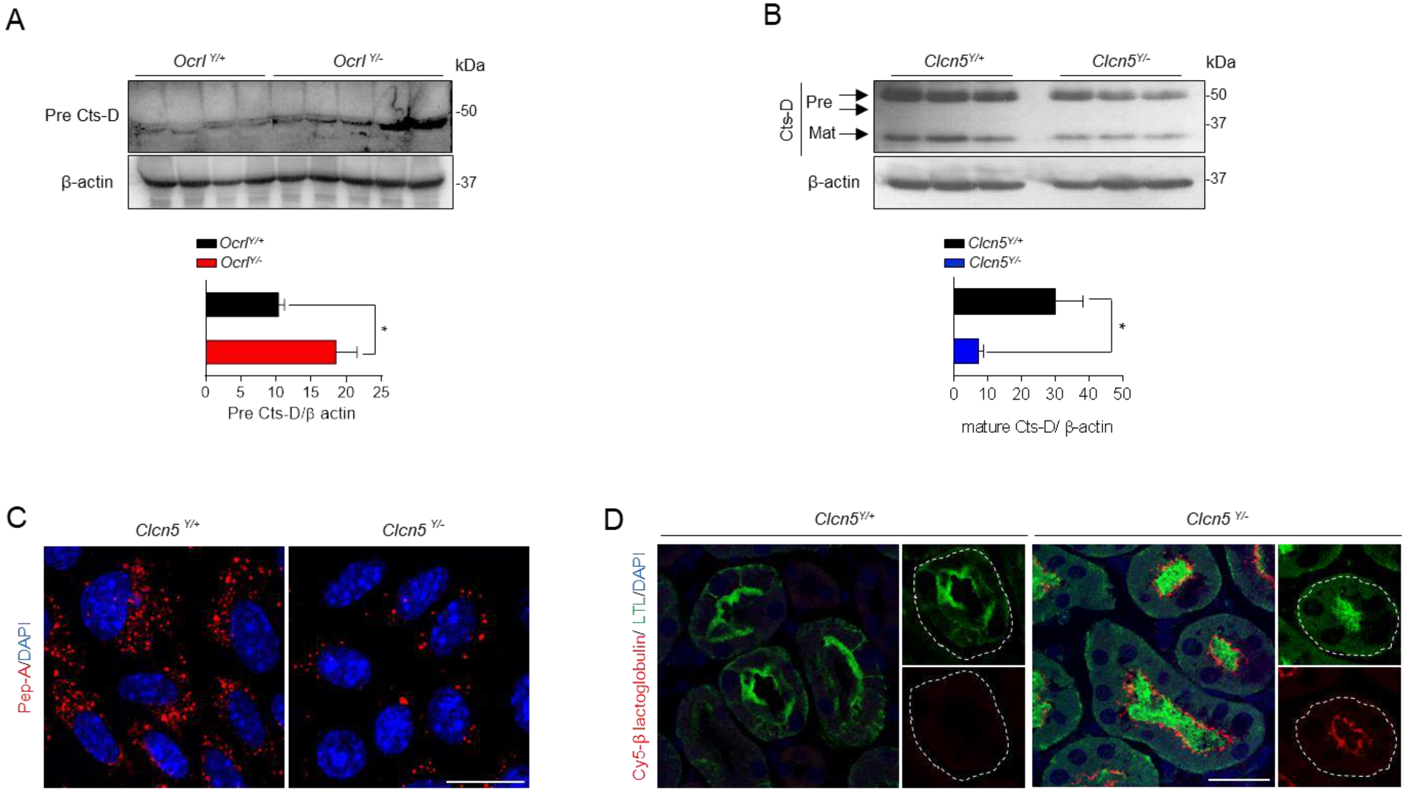

Supplementary Figure 6. Altered lysosomal activity in Dent disease. (**A-B**)Western blotting and densitometry analysis of cathepsin D (Cts-D) protein levels in (**A**) plasma samples from *Ocrl* mice (n= 4 *Ocrl*$^{Y/+}$ and n= 5 *Ocrl*$^{Y/-}$ mice) and in (**B**) *Clcn5* mPTCs (n= 3 mice per group). β-actin was used as loading control. Plotted data represent mean ± SEM. Two-tailed unpaired Student's t-test, *P < 0.05 relative to *Ocrl*$^{Y/+}$ plasma or *Clcn5*$^{Y/+}$ mPTCs. (**C**) Confocal micrographs showing *Clcn5* mPTCs immunostained with Bodipy-FL-PepA (1 µM, for 1 h at 37 °C, green). (**D**) Representative confocal micrographs showing Cy5 labeled β-lactoglobulin (red, 1mg/kg B.W.) after 120 minutes from tail vein injections in LTL^{+} proximal tubules from *Clcn5* mouse kidneys. Nuclei counterstained with DAPI (blue) in **C** and **D**. Scale bars 15µm in **C** and 25µm in **D.**

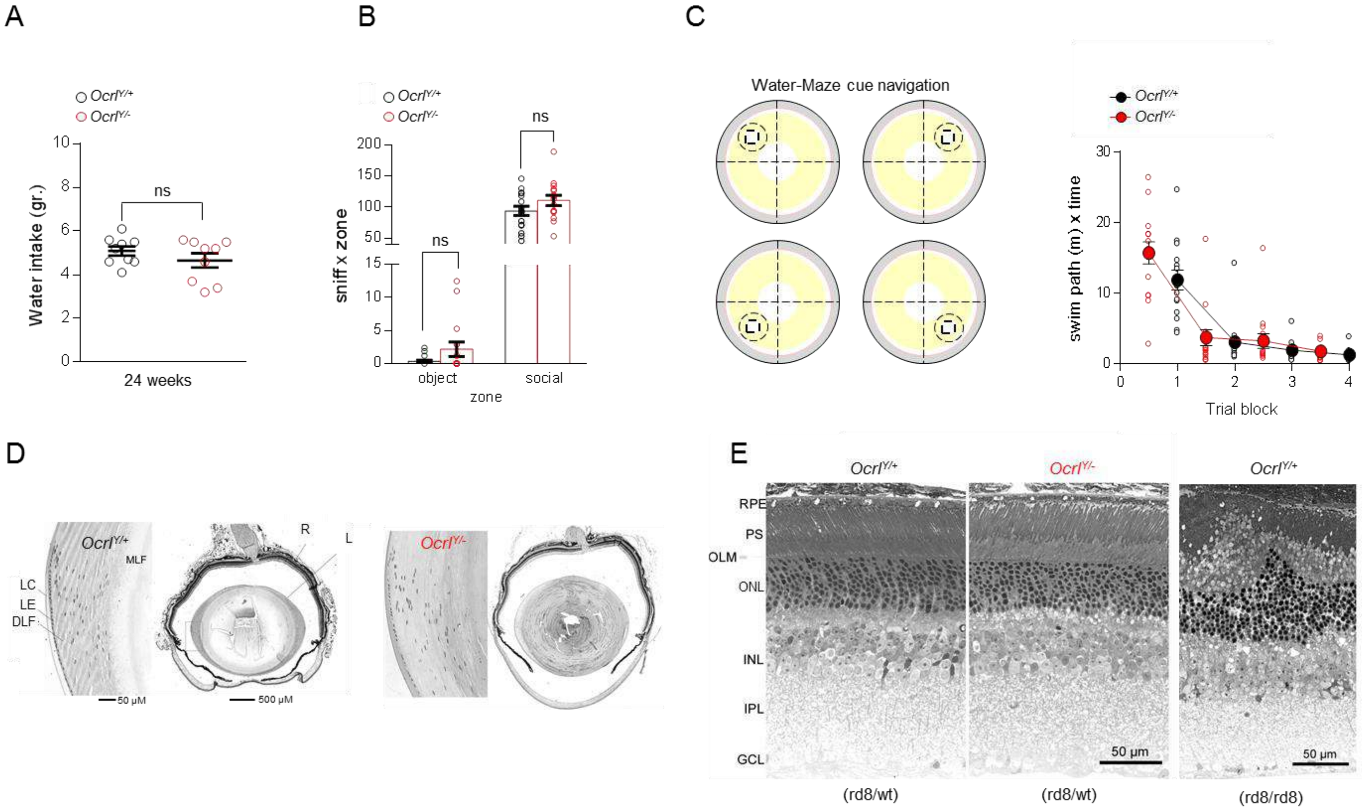

Supplementary Figure 7. **No impairment of social behavior neither defective ocular morphology is observed in *Ocrl*$^{Y/-}$ mice.** (**A**) Dot plot representing the measurement of water intake, over 12 hours, in 24 weeks old *Ocrl* male mice. Each dot represents one mouse. (**B**) Dotted bar graph representing the number of nose contact time with the social (cage with mouse) and object (empty cage) stimulus during the 3 chambers sociability test. Plotted data represent mean ± SEM. Each dot of the graphs represents one mouse. (**C**) Schematic representation of the water maze cue navigation test (left panel): animals are trained in the water maze to reach a platform marked by a salient cue and placed in a different quadrant for every trial. Dot plot (right panel) representing the swim path as function of 3 trial blocks. Each dot of the graphs represents one mouse. (**D**) Light microscopy representative pictures of high magnification hematoxylin-eosin stained lens (left panels, scale bars 50μm) and midsagittal sections of whole eyes (right panels, scale bars 500μm) derived from *Ocrl* mice. LC (lens capsule), LE (lens epithelium), DFL (differentiating lens fiber), MFL (mature lens fiber), L (lens) and R (retina). (**E**) Toluidine blue stained retina derived from *Ocrl* mice in presence or absence of the spontaneous rd8 (retinal degeneration 8) mutation in *Crb1* gene (right panel, rd8/rd8). RPE (retinal pigment epithelium), PS (photoreceptor segments), OLM (outer limiting membrane), ONL (outer nuclear layer), INL (inner nuclear layer), IPL (inner plexiform layer), GCL (ganglion cell layer); Scale bars 50μm. ns: not significant.

Table S1: Primer pairs for gene expression analysis.

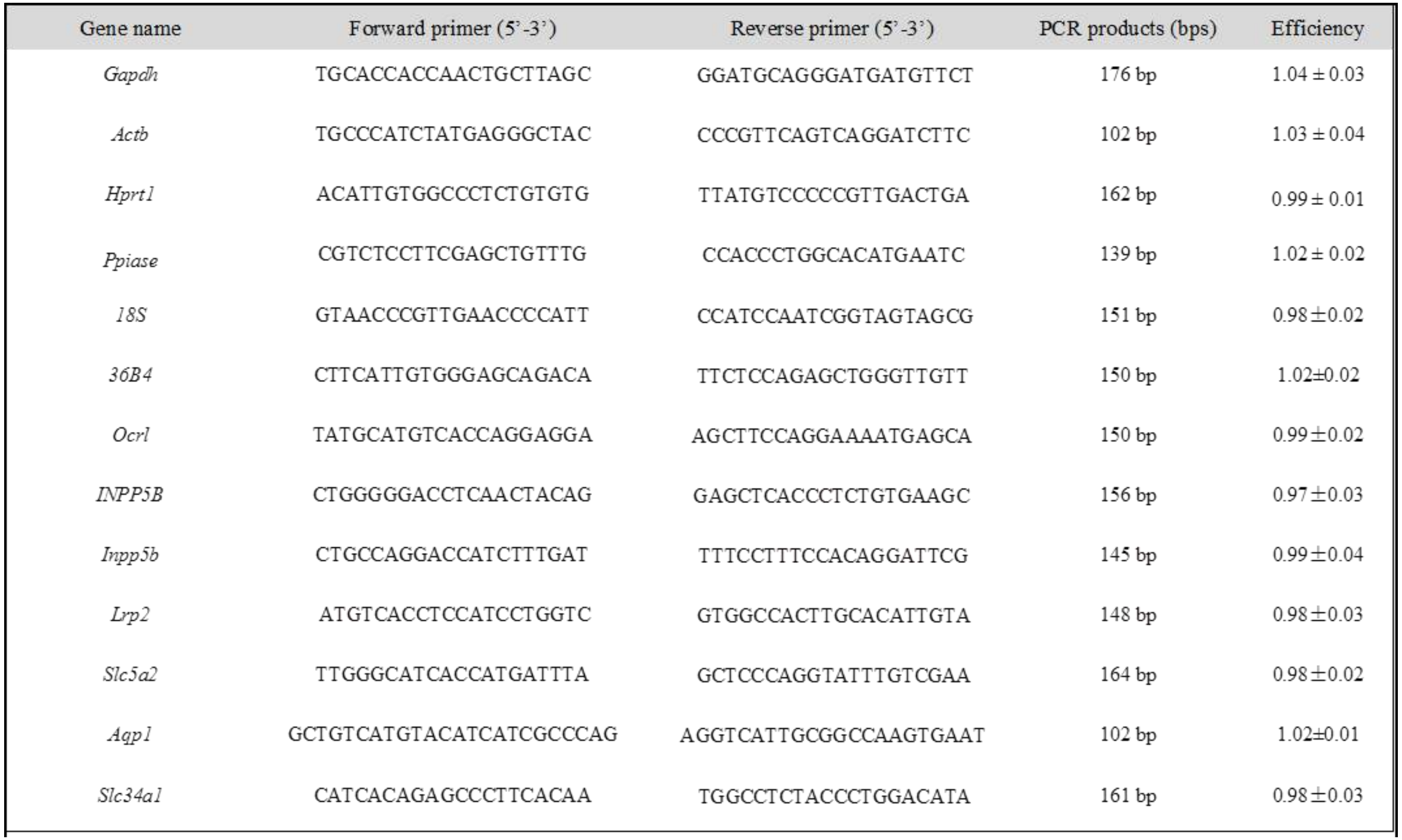

Gene name	Forward primer (5'-3')	Reverse primer (5'-3')	PCR products (bps)	Efficiency
Gapdh	TGCACCACCAACTGCTTAGC	GGATGCAGGGATGATGTTCT	176 bp	1.04 ± 0.03
Actb	TGCCCATCTATGAGGGCTAC	CCCGTTCAGTCAGGATCTTC	102 bp	1.03 ± 0.04
Hprt1	ACATTGTGGCCCTCTGTGTG	TTATGTCCCCCGTTGACTGA	162 bp	0.99 ± 0.01
Ppiase	CGTCTCCTTCGAGCTGTTTG	CCACCCTGGCACATGAATC	139 bp	1.02 ± 0.02
18S	GTAACCCGTTGAACCCCATT	CCATCCAATCGGTAGTAGCG	151 bp	0.98±0.02
36B4	CTTCATTGTGGGAGCAGACA	TTCTCCAGAGCTGGGTTGTT	150 bp	1.02±0.02
Ocrl	TATGCATGTCACCAGGAGGA	AGCTTCCAGGAAAATGAGCA	150 bp	0.99±0.02
INPP5B	CTGGGGGACCTCAACTACAG	GAGCTCACCCTCTGTGAAGC	156 bp	0.97±0.03
Inpp5b	CTGCCAGGACCATCTTTGAT	TTTCCTTTCCACAGGATTCG	145 bp	0.99±0.04
Lrp2	ATGTCACCTCCATCCTGGTC	GTGGCCACTTGCACATTGTA	148 bp	0.98±0.03
Slc5a2	TTGGGCATCACCATGATTTA	GCTCCCAGGTATTTGTCGAA	164 bp	0.98±0.02
Aqp1	GCTGTCATGTACATCATCGCCCAG	AGGTCATTGCGGCCAAGTGAAT	102 bp	1.02±0.01
Slc34a1	CATCACAGAGCCCTTCACAA	TGGCCTCTACCCTGGACATA	161 bp	0.98±0.03

III.2 NEPHROPATHIC CYSTINOSIS

III.2.1 Disruption of lysosomal identity triggers PT dysfunction

Impaired Autophagy Bridges Lysosomal Storage Disease and Epithelial Dysfunction in the Kidney

Beatrice Paola Festa[1], Zhiyong Chen[1], Marine Berquez[1], Huguette Debaix[1], Natsuko Tokonami[1], Jenny Ann Prange[1], Glenn van de Hoek[2], Cremonesi Alessio[3], Andrea Raimondi[4], Nathalie Nevo[5], Rachel H. Giles[2], Olivier Devuyst[1,]* and Alessandro Luciani[1,]*

[1]Institute of Physiology, University of Zurich, Zurich, Switzerland; [2]Department of Nephrology and Hypertension, University Medical Center Utrecht, Hubrecht Institute, Utrecht, The Netherlands; [3]Division of Clinical Chemistry and Biochemistry, University Children's Hospital Zurich, Zurich, Switzerland; [4]San Raffaele Scientific Institute, Experimental Imaging Center, Milan, Italy; [5]INSERM U1163, Université Paris Descartes, Institut Imagine, Hôpital Necker Enfants Malades, Paris, France.

*OD and AL co-directed and contributed equally to this study.

Corresponding authors: Prof. Dr. Olivier Devuyst or Dr. Alessandro Luciani, Institute of Physiology, University of Zurich, Winterthurerstrasse 190, CH-8057 Zürich; E-mails: olivier.devuyst@uzh.ch or alessandro.luciani@uzh.ch; Phone: +41 44 635 50 82.

Nature Communications. 2018 Jan 11; 9(161).DOI: 10.1038/s41467-017-02536-7

ABSTRACT

The endolysosomal system sustains the reabsorptive activity of specialized epithelial cells. Lysosomal storage diseases such as nephropathic cystinosis cause a major dysfunction of epithelial cells lining the kidney tubule, resulting in massive losses of vital solutes in the urine. The mechanisms linking lysosomal defects and epithelial dysfunction remain unknown, preventing the development of disease-modifying therapies. By combining genetic and pharmacologic approaches *in vitro* and *in vivo*, we demonstrate that the lysosomal dysfunction in cystinosis results in defective autophagy-mediated clearance of damaged mitochondria, generating oxidative stress that stimulates Gα12/Src-mediated phosphorylation of tight junction ZO-1 and triggers a signaling cascade involving the ZO-1-associated Y-box factor ZONAB, that leads to epithelial cell proliferation and transport defects. Correction of the primary lysosomal defect, neutralization of mitochondrial oxidative stress, and blockage of tight junction-associated ZONAB signaling rescue the epithelial dysfunction. This work unveils a link between defective lysosome-autophagy degradation pathways and epithelial dysfunction, providing new therapeutic perspectives for lysosomal storage disorders.

INTRODUCTION

The epithelial cells lining the proximal tubules (PT) of the kidney constitute a paradigm of effective communication between the environment and endomembrane compartments, allowing the reabsorption of essential nutrients. By processing incoming substances and recycling receptors and transporters at the apical plasma membrane, the endolysosomal system dictates cell differentiation, hence the maintenance of homeostasis (1,2). The PT uptake accounts for ~80% of the clearance of small proteins and peptides, which are continuously filtered and completely reabsorbed by apical endocytosis involving the multi-ligand receptors, megalin and cubilin (3). Alterations in these transport processes lead to generalized PT dysfunction (an entity named renal Fanconi syndrome, RFS), causing urinary loss of solutes and low molecular weight (LMW) proteins, often complicated by dehydration, electrolyte imbalance, rickets, growth retardation and development of chronic kidney disease (CKD). Such PT dysfunctions are typically encountered in congenital disorders due to defective endolysosomal transporters, particularly in nephropathic Cystinosis (4).

Cystinosis is a lysosomal storage disease (LSD) caused by recessive, inactivating mutations in the *CTNS* gene coding for the proton-driven cystine transporter cystinosin which exports cystine out of lysosomes (5). The loss of cystinosin causes an accumulation of cystine in tissues, leading to renal failure, diabetes, hypothyroidism, myopathy, and central nervous system deterioration. Infantile (MIM #219800) and juvenile (MIM #219900) forms of Cystinosis represent a frequent cause of congenital PT dysfunction and RFS, most often complicated by CKD (6). The only available strategy to counteract cystine storage is oral administration of cysteamine, which allows cystine to exit lysosomes. However, cysteamine treatment is hampered by side effects and poor tolerance, and it does not treat nor prevent PT dysfunction (6,7). Thus, there is an urgent need to identify novel therapeutic strategies for this devastating disorder. Recent studies based on a *Ctns* mouse model that recapitulates multiple features of Cystinosis (8) have demonstrated that the loss of cystinosin is associated with aberrations of the endolysosomal compartment, and abnormal proliferation and dysfunction of PT cells (9). Despite identification of cellular defects associated with Cystinosis in different models and cell systems (10), a unifying mechanism linking loss of cystinosin, lysosomal dysfunction and defective epithelial transport has not been deciphered.

In most mammalian cells, the endolysosomal system captures and degrades intracellular worn-out constituents through autophagy (11). This homeostatic process is particularly active in renal PT cells, whose reabsorptive and transport activities require the maintenance of mitochondria network (12). The autophagy-mediated turnover of damaged mitochondria is required for protecting the PT from acute tubular injury (13), whereas deletion of essential autophagy genes dacells through defective mitochondrial clearance and increased reactive oxygen species (ROS) (14). Of note, accumulation of distorted mitochondria (15) and of autophagy receptor SQSTM1/p62 has been described in kidney biopsies and urinary cells from cystinotic patients (16), suggesting a possible involvement of autophagy. Also, recent evidence shows that cystinosin is a component of the lysosomal mammalian target of rapamycin complex-1 (mTORC1) (17), a hub that regulates autophagy-lysosome functions (18) and nutrient transport in epithelial cells (19). Altogether, these data suggest potential interactions between cystinosin function, the autophagy-lysosome degradation pathway and the transport properties in PT epithelial cells.

In the present study, we decipher a pathway linking loss-of-function of cystinosin, lysosome-autophagy dysfunction, mitochondrial oxidative stress, disruption of tight junction integrity and activation of a signaling cascade causing epithelial cell dysfunction and loss of transport capacity. These insights offer new therapeutic strategies for treating epithelial dysfunction in nephropathic Cystinosis and endolysosomal disorders.

RESULTS

Loss of cystinosin leads to alterations in lysosomal dynamics and autophagy

We first investigated the consequences of *Ctns* deletion on the lysosomal-autophagy pathway in epithelial cells. The loss of cystinosin, reflected by the accumulation of cystine in mouse kidneys and derived PT cells (mPTCs), induced a phenotype switch associating abnormal proliferation and apical dedifferentiation, leading to defective receptor-mediated endocytosis and urinary loss of LMW proteins *in vivo* (Suppl. Fig. 1a-g). These changes, which confirmed the validity of the *Ctns* mouse model and derived mPTCs (8,9), were associated with a dramatic modification in lysosomal dynamics as evidenced by enlarged lysosomes, clustered into the perinuclear region (Fig. 1a; Suppl. Videos 1 and 2). Since the intracellular positioning of lysosomes coordinates autophagy in response to nutrient availability (20), we tested whether the perinuclear clustering of lysosomes reflects changes in autophagy. We used mPTCs because this well-established primary culture system provides a particularly suited model to explore mechanisms of endolysosome disorders in epithelial cells (21,22). Autophagy was assessed by quantifying the conversion of the non-lipidated form of LC3-I to the lipidated, autophagosome-associated form LC3-II and the numbers of LC3 vesicles (23) in mPTCs cultured in nutrient-rich media (hereafter referred to as “fed”) or in nutrient deprived-conditions (hereafter referred to as "starved"). Compared to wild-type cells, *Ctns*$^{-/-}$ cells showed higher numbers of punctate LC3-structures and steady-state levels of LC3-II, which did not further increase in starved conditions (Fig. 1b,c), as well as higher numbers of EM structures compatible with autophagic vacuoles (Fig.1d). Likewise, *Ctns*$^{-/-}$ cells showed larger numbers of aggregates positive for the autophagy receptor SQSTM1(Fig.1e) and higher SQSTM1 protein levels, which did not further increase in starved conditions (Fig.1f). The accumulation of LC3-marking autophagosomes and SQSTM1-positive aggregates was consistently detected in the PTs of *Ctns*$^{-/-}$ kidneys (Fig. 2a,b). To further explore the consequences of cystinosin deletion *in vivo*, we established a novel *ctns* knock-out zebrafish model using the TALENs (transcription activator-like effector nucleases) technique (Suppl. Fig. 2a-c). One mutant zebrafish line showed a 8-bp TALEN-driven deletion (*ctns*$^{del8/del8}$), resulting in a premature stop codon within exon 3 of *ctns*, which would result in a truncated protein deprived of the transmembrane domains of cystinosin. Microinjection of wild-type (but not mutant) human *CTNS* mRNA decreased the cystine storage in *ctns*-deficient embryos to the same extent than cysteamine treatment (Suppl. Fig. 2d). The protein levels of LC3-II and the numbers of autophagic vesicles were remarkably increased in cystine-accumulating pronephric tubules in *ctns*-deficient zebrafish (Fig. 2c-f), demonstrating the evolutionary conservation of this connection. These results demonstrate that the deletion of cystinosin alters lysosomal dynamics and autophagy in PT cells, both *in vitro* and *in vivo*.

Cystinosin deficiency perturbs autophagic clearance in PT cells

An increased number of autophagic vesicles may arise from stimulation of autophagosome biogenesis or from alteration of their degradation by lysosomes. To discriminate between these two possibilities, we treated *Ctns* mPTCs with Bafilomycin A1 (BfnA1), a proton pump inhibitor that prevents lysosome degradation and thus increases autophagic cargoes and substrates exclusively when autophagy is active (23). Treatment with BfnA1 increased the amounts of LC3-II and SQSTM1 in nutrient-deprived *Ctns*$^{+/+}$ cells, whereas it did not change the already elevated levels of these proteins in nutrient-deprived *Ctns*$^{-/-}$ cells (Fig. 3a). We next performed a pulse-chase assay to monitor the degradation of resting autophagosomes in *Ctns* mPTCs. Cells were starved to form autophagosomes and then treated with the class III phosphoinositide 3-kinase (PI3K) vacuolar protein sorting 34 (Vps34) kinase inhibitor SAR-405 (24) to prevent the formation of new autophagosomes. We validated the selectivity of SAR-405 by determining the intracellular phosphatidylinositol-3-phosphate pools (PtdIns-3P, the end-product generated by Vps34 kinase activity) in mPTCs (Suppl. Fig. 3a). The degradation of the formed autophagosomes following SAR-405 treatment was tracked by time-lapse confocal microscopy: in contrast to the autophagic-mediated degradation observed in starved *Ctns*$^{+/+}$ cells, the *Ctns*$^{-/-}$ cells retained almost all the formed autophagosomes (Suppl. Fig. 3b,c). Upstream events regulating autophagosome biogenesis, such as conjugation (ATG7) and phagosome formation (ATG16L+ vesicles), including Beclin-1, remained unchanged in control and *Ctns*$^{-/-}$ PT cells (Suppl. Fig. 4a-c). Taken together, these results indicate that the accumulation of autophagosomes in *Ctns*$^{-/-}$ cells results predominantly from a slower autophagosome clearance rather than augmented biogenesis.

Defective lysosomal function impedes autophagic cargo clearance in Ctns$^{-/-}$ *cells*

A blockade in LC3-II degradation can occur at any step after autophagosome formation and can be induced by delayed trafficking of autophagosomes to lysosomes and/or reduced fusion between both compartments (25). We thus explored whether the delayed autophagosome clearance in *Ctns*$^{-/-}$ cells might be caused by an impaired autophagosome delivery to lysosomes. To test this hypothesis, we examined the subcellular distribution of LC3-labeled autophagic structures and LAMP1-labeled lysosomes in response to short incubations with non-saturating concentrations of BfnA1 (50nM for 1h) (26). Confocal microscopy analysis showed that cystinosin deletion did not decrease the colocalization of LC3 and LAMP1- labeled lysosomes in BfnA1-treated PT cells but rather increased the number of large LAMP1 vesicles filled by LC3 in *Ctns*$^{-/-}$ PT cells (Suppl. Fig. 5a). Electron tomography microscopy and three-dimensional (3-D) reconstructed tomograms confirmed the existence of enlarged, single-membrane structures engulfed with partially digested cellular debris in *Ctns*$^{-/-}$ cells (Suppl. Fig. 5b; Suppl. Video 3). Accumulation of autophagic material in autolysosomes of *Ctns*$^{-/-}$ cells was confirmed by correlative light-electron microscopy (CLEM), where GFP-LC3-positive autophagosome containing intracellular components coalesced within enlarged, single-membrane RFP-LAMP1-positive organelles (Fig. 3b), indicating that the transport and/or autophagosome-lysosome fusion are not compromised. One mechanism by which the autophagic cargo clearance might be impeded is defective lysosomal degradation capacity (11). To substantiate the delayed autophagosome degradation in *Ctns*$^{-/-}$cells, we analyzed trafficking, processing and maturation of lysosomal cathepsins. Western blot analyses of cathepsin-D showed a decreased proteolytic generation of the 32-kDa mature cathepsin-D in *Ctns*$^{-/-}$ compared to *Ctns*$^{+/+}$cells (Fig. 3c). We next tested the lysosomal cathepsin-D activity by incubating mPTCs with Bodipy-FL-PepstatinA (PepA), a fluorescence-tagged PepA that binds to the active site of cathepsin-D in acidic lysosomes (22). Although the majority of lysosomes were co-stained with PepA–labeled cathepsin-D in *Ctns*$^{+/+}$cells, the number of PepA-labeled vesicles and the colocalization of active cathepsin-D with LAMP1 were substantially lower in *Ctns*$^{-/-}$ cells (Fig. 3d). These changes in lysosome dynamics and function were observed despite normal trafficking of cathepsin-D between Golgi and LAMP1 compartments (Suppl. Fig. 5c,d). Similarly, the lysosomal-based processing of the LMW β-lactoglobulin, that is normally internalized and degraded by PT endolysosomes (2,3), was dramatically reduced in pronephric tubules of *ctns*$^{del8/del8}$ compared to *ctns*$^{+/+}$ zebrafish (Fig. 3e). The key role of cystinosin depletion in lysosomal-autophagy dysfunction was assessed by transducing *Ctns*$^{-/-}$ cells with an adenovirus that expresses mouse hemagglutinin (HA)-tagged cystinosin (Ad-*Ctns*-HA; Fig. 4). The functional re-expression of HA-CTNS protein at late endosomal/lysosomal compartments in *Ctns*$^{-/-}$ cells (Fig. 4a; Suppl. Fig. 6) lowered the intracellular cystine content (Fig. 4b), rescued the lysosomal dynamics (Fig. 4c,d), activated cathepsin-B within lysosomes (Fig. 4e), and augmented the lysosome-mediated degradation of autophagy substrates SQSTM1 and LC3-II (Fig. 4f) when compared to *Ctns*$^{-/-}$ cells transduced with an empty vector. These features were abolished by treating the HA-CTNS expressing *Ctns*$^{-/-}$ cells with BfnA1 (Fig.4f), indicating that cystinosin deficiency blocks autophagosome clearance by compromising the lysosome function.

Disruption of autophagy causes mitochondrial oxidative stress and epithelial cell dysfunction

Because autophagy mediates cellular homeostasis, we tested whether and how its disruption may cause epithelial dysfunction. Inactivation of basal autophagy was obtained by transducing mPTCs with an adenovirus-expressing a short hairpin RNA (Ad-shRNA) against *Atg7* or by inhibiting the autophagy Beclin1/Vps-34 complex with SAR-405 or Spautin-1. We confirmed that either *Atg7* shRNA (Fig. 5a) or autophagy inhibitors (Suppl. Fig. 7a-b) prevented the conversion of LC3-I to LC3-II and increased the SQSTM1 protein levels and amounts of aggregate-forming SQSTM1 and ubiquitin-positive inclusions (Fig. 5a-c; Suppl. Fig.7c) in mPTCs. Disruption of autophagy led to the accumulation of dysfunctional mitochondria, as shown by increased levels of prohibitin (an inner mitochondrial membrane protein; Fig. 5d) and decreased resting mitochondrial membrane potential ($\Delta\psi_m$, assessed by quantitative confocal imaging of tetramethylrhodamine methyl ester [TMRM] dye; Fig. 5e; Suppl. Fig 7d), and the induction of a major mitochondrial oxidative stress, as scored by elevated mtROS levels (MitoSOX; Fig. 5f; Suppl. Fig. 7e). Importantly, either the genetic or the pharmacological impairment of autophagy induced the nuclear translocation of tight-junction ZO1-associated Y-box factor ZONAB (Fig. 5g) and its activity (as measured by the regulation of the *Ccdn1*, *Pcna* and *Lrp2* targets (27,28) (Fig. 5h; Suppl. Fig. 7f). These changes were reflected by a phenotype switch that included abnormal cell proliferation, as evidenced by bromodeoxyuridine (BrdU) incorporation (Fig. 5i; Suppl. Fig. 7g), and dedifferentiation, as evidenced by reduced expression of the apical endocytic receptor megalin (Fig. 5h) and by decreased endocytic uptake capacity (Fig. 5j; Suppl. Fig. 7h). Collectively, these data demonstrate that the maintenance of mitochondrial function and homeostasis by autophagy is required for the terminal differentiation, hence regulating the reabsorptive capacity of PT epithelial cells.

Impaired clearance of dysfunctional mitochondria drives oxidative stress in PT cells

Having established that disruption of autophagy recapitulates the phenotype switch of proliferation-dedifferentiation, we next investigated how defective lysosomal degradation of autophagy substrates might lead to epithelial dysfunction in Cystinosis. Because autophagy delivers protein aggregates and organelles to endolysosome for cellular degradation, we analyzed the ability of *Ctns*$^{-/-}$ mPTCs to clear polyubiquitinated aggregates and compromised mitochondria. Correlating with the reduced autophagy flux, we found an accumulation of ubiquitin-forming aggregates and abnormal mitochondria with disorganized cristae in *Ctns*$^{-/-}$ compared to *Ctns*$^{+/+}$ cells (Fig. 6a-c). The defective mitochondria in *Ctns*$^{-/-}$ cells were retained within enlarged, dysfunctional lysosomes (Fig. 6d) and showed a major decrease in $\Delta\psi_m$ (Fig. 6e). Seahorse metabolic flux analyses measuring the overall consumption rates (OCRs) confirmed markedly decreased mitochondrial bioenergetics (baseline respiration, ATP turnover and total respiratory capacity) in *Ctns*$^{-/-}$ compared to *Ctns*$^{+/+}$ mPTCs (Fig. 6f). These changes were paralleled by a major mitochondrial oxidative stress, as scored by the elevated mtROS levels (MitoSOX; Fig. 6g) and increased anti-oxidant response (HO1; data not shown). Overall these findings indicate that impaired lysosome-mediated autophagic degradation of dysfunctional mitochondria causes a major oxidative stress in cystinosin-deficient cells.

Abnormal tight junction signaling leads to epithelial dysfunction

Oxidative stress has been shown to induce the phosphorylation of the zona occludens1 (ZO-1) adaptor protein, disrupting the integrity of the tight junction complex (29). Because ZO-1 traps the Y-box transcription factor ZONAB that is known to regulate the differentiation of PT cells (27,28), an overproduction of ROS by dysfunctional mitochondria might alter tight junction integrity and trigger ZONAB-mediated signaling. To test this hypothesis, we immunoprecipitated ZO-1 from mPTCs and noted that it was more heavily phosphorylated in *Ctns*$^{-/-}$ versus *Ctns*$^{+/+}$ cells (Fig. 7a). This result was supported by the proximity ligation assay (PLA) revealing an increased cytoplasmic phosphorylation of ZO-1 in *Ctns*$^{-/-}$ cells (Fig. 7b). ZO-1, which is normally located at cell membrane boundaries as shown in *Ctns*$^{+/+}$ cells, was found to be trapped in LAMP1-positive compartments in *Ctns*$^{-/-}$ cells (Fig. 7c). Consistent with the loss of integrity of tight junctions, there was a nuclear translocation of ZONAB (Fig. 7d) with subsequent increase in its transcriptional targets *Ccdn1*, *Pcna* and *Lrp2* (Fig. 7e). These changes in *Ctns*$^{-/-}$ cells were coupled to increased proliferation, as evidenced by measuring cell growth curves (Fig. 7f) or by the nuclear enrichment of PCNA (Fig. 7h; Suppl. Fig. 1e), contrasting with decreased receptor-mediated endocytosis of albumin (Fig. 7i; Suppl. Fig. 1f). The link between defective autophagy, compromised mitochondria and oxidative stress was substantiated by the increased phosphorylation rate of ZO-1 induced by knockdown of *Atg*7 in mPTCs (Suppl. Fig. 8a) or treatment of the cells with autophagy inhibitors (SAR-405 and Spautin-1; Suppl. Fig. 8b); with H_2O_2 (Suppl. Fig. 8c); or with the mitochondrial complex I inhibitor Rotenone stimulating mitochondria-derived ROS (Suppl. Fig. 8d,e). Treatment with rotenone induced ZONAB translocation and signaling (Suppl. Fig. 8f,g), reflected by increased proliferation (Suppl. Fig. 8h) and decreased endocytic uptake (Suppl. Fig. 8i). The relevance of the abnormal tight junction signaling in Cystinosis was substantiated by gain- and loss-of-function experiments in mPTCs. Knock-down (shRNA) of *Csda* encoding ZONAB (Fig. 7g-i; Supp. Fig. 9a-c) or overexpression of exogenous *TJP1* encoding ZO-1 (Suppl. Fig. 9d,e), which functionally inhibits ZONAB (27,28), significantly decreased the proliferation markers and rescued the endocytic uptake in *Ctns*$^{-/-}$ cells. Conversely, depletion of ZO-1 (shRNA-mediated knock-down of *Tjp1*; Suppl. Fig. 10a-c) or overexpression of *Csda* (Suppl. Fig. 10d) triggered the activation of ZONAB signaling (Suppl. Fig. 10e) with increased cell proliferation and decreased endocytic uptake of albumin (Suppl. Fig. 10f) in wild-type cells.

Mitochondrial ROS disrupt tight junctions through Gα12 /Src activation.

Finally, we investigated how aberrant mitochondria-producing ROS disrupt tight junctions in Cystinosis epithelial cells. Given the accumulation of abnormal mitochondria-producing ROS (Fig. 6) and higher phosphorylation rate of ZO-1 (Fig. 7) in *Ctns*$^{-/-}$ PT cells, we hypothesized that high levels of mitochondrial ROS may stimulate the Gα12 protein that triggers the disruption of tight junctions through Src-mediated phosphorylation of ZO-1 (29-31). This would in turn activate ZONAB signaling and drives the epithelial dysfunction. Consistent with this hypothesis, mPTCs from *Ctns*$^{-/-}$ kidneys (Fig. 8a,b) displayed an increased protein abundance of Gα12 and activated Src tyrosine kinase (monitored by the increased phosphorylation rate of pTyr^{416}-Src; Fig. 8a,b). Likewise, wild-type mPTCs treated with Rotenone (Fig. 8c) or accumulating aberrant mitochondria-producing ROS (*Atg7* knockdown; Fig. 8d) also exhibited an abnormal activation of Gα12/Src. This activation paralleled the increased phosphorylation of ZO-1, tight junction disruption and epithelial dysfunction described above (Fig. 5; Suppl. Fig. 8). Having verified that the high level of mitochondrial ROS drives epithelial dysfunction by activating Gα12/Src kinase pathway, we tested whether the neutralization of mitochondrial ROS/Gα12/Src signaling loop may avert the loss of tight junction integrity and rescue the epithelial dysfunction in Cystinosis cells. We incubated *Ctns*$^{-/-}$ mPTCs with mitochondria-localized-oxygen scavenger Mito-TEMPO (MT, 10μM for 24h; Suppl. Fig. 11a,b; ref. 32) or with a selective c-Src family kinase inhibitor SU6656 (5μM for 24h; ref. 33) or transduced the cells with Ad-shRNA against *Gna12*. The blockage of the mitochondrial ROS/Gα12/Src signaling loop by these pharmacologic or genetic interventions reversed the abnormal activation of Gα12/Src (Fig. 8a,b), preventing the phosphorylation of ZO-1 (Fig. 8e; Suppl. Fig. 11c) and its lysosomal accumulation - which increased ZO-1 abundance at cell boundaries (Suppl. Fig. 11d). In turn, these changes inhibited the nuclear translocation of ZONAB (Fig. 8f) and restored the differentiation and endocytic capacity of Cystinosis cells (Fig. 8g,h). Of note, the rescue induced by MT treatment was prevented by overexpressing *Csda*-HA in *Ctns*$^{-/-}$ mPTCs (Suppl. Fig. 12a,b), supporting the role of ZONAB. Taken together, these data suggest that the excess of mitochondrial ROS, resulting from impaired lysosome mediated autophagic degradation of damaged mitochondria, triggers Gα12/Src-mediated phosphorylation of ZO-1, which disrupts tight junction integrity and activates ZONAB signaling, in turn causing epithelial dysfunction in Cystinosis cells.

Neutralizing mitochondrial oxidative stress improves epithelial dysfunction in Cystinosis.

To enhance the translational potential of these findings, we administered MT (1mg/kg body weight) to 16-week-old *Ctns* mice by daily i.p. injections (Fig. 9a). After 30 days of treatment, mPTCs were isolated from the *Ctns*$^{-/-}$ kidneys to score the epithelial function by measuring the endocytic uptake of albumin. Treatment with MT effectively reduced ROS production and oxidative stress (Fig. 9b,c), lowered levels of the kidney injury marker lipocalin-2 (34) (Fig. 9c), abrogated abnormal cell proliferation (Fig. 9d) and restored abundance of endocytic receptor megalin (Fig. 9e), reflected by a significant recovery of the ligand uptake (Fig. 9f) in *Ctns*$^{-/-}$ cells. Thus, modulation of mitochondrial oxidative stress ameliorates epithelial dysfunction in nephropathic Cystinosis.

DISCUSSION

The endolysosomal system regulates the transport activity of specialized epithelial cells, sustaining their role in homeostasis. Congenital defects in lysosomal transporters, as exemplified by Cystinosis, cause PT cell dysfunction and RFS. By combining genetic and pharmacologic approaches *in vitro* and *in vivo*, we deciphered the link between lysosomal disease and epithelial dysfunction in Cystinosis. We demonstrate that lysosomal dysfunction results in defective autophagy-mediated clearance of damaged mitochondria, mitochondrial oxidative stress, disruption of tight junction integrity and activation of a signaling pathway causing epithelial cell proliferation and dedifferentiation, with loss of reabsorptive capacity (Fig. 10). These data reveal the fundamental importance of autophagic clearance in maintaining epithelial differentiation and offer novel therapeutic perspectives to restore epithelial transport capacity downstream of the primary lysosomal defect.

Cystinosin deficiency induces a major alteration in lysosomal dynamics (9,35,36),paralleled by increased numbers of autophagosomes in the proximal tubules of *Ctns*$^{-/-}$ mice and in the pronephric tubules of *ctns*-deficient zebrafish. The accumulation of the autophagy substrate SQSTM1, which is normally degraded within autolysosomes, suggests an abnormal autophagy flux in cystinosin-deficient PT cells, in line with recent observations stating an impairment of autophagy flux in many lysosome storage diseases (37,38) and evidence in human cells and kidney biopsies from Cystinosis patients (16). Evidence supporting the failure to degrade autophagy cargoes in primary PT *Ctns*$^{-/-}$ cells include: abnormally elevated numbers of mature autophagosomes under-normal growth conditions; failure to clear autophagic vesicles (AVs) formed after starvation-induced autophagy, mimicking BfnA1 action; inability of BfnA1 to further induce the LC3II protein levels; and impaired degradation of the resting AVs by a selective PI3K3/Vps34 inhibitor. In contrast, upstream events regulating autophagosome biogenesis, including Atg7-Atg12 conjugation and phagophore formation were not affected. Altogether, these data indicate that the functional loss of cystinosin, causing lysosomal cystine storage, delays the autophagy flux, causing an accumulation of autophagosomes *in vitro* and *in vivo*. Of note, the autophagy flux was found to be fully functional in fibroblasts derived from *Ctns* mice (39), in contrast with the predictions based on the defective mTORC1 signaling in Cystinosis cells (17). The reason for these discrepancies would require further studies to understand the cell-specific effects of cystinosin depletion.

The question remained how the lysosomal defect could impair autophagy flux and lead to epithelial dysfunction. A blockage of the degradation of autophagic material may occur at any step after autophagosome formation, due to factors regulating the trafficking of autophagosomes to lysosomes or the fusion between both compartments. For instance, accumulation of LC3-positive organelles unable to fuse with lysosomes has been observed in many LSDs (40). Accordingly, a potential cause for the impaired autophagy flux observed in Cystinosis could be a delayed fusion between lysosomes and autophagosomes. However, when treating *Ctns*$^{-/-}$ cells with short incubations of BfnA1, which accurately measure the autophagy flux (41), we observed a substantial co-localization of LC3-positive vesicles with the lysosome marker LAMP1, suggesting that the delivery and autophagosome-lysosome fusion is not compromised in cystinotic cells. Another indication is the perinuclear lysosomal clustering in *Ctns*$^{-/-}$ cells: such centripetal movement of lysosomes has been shown to mediate the autophagic degradation of biomacromolecules (20,42).

Because the autophagy flux also relies on the degradative capacity of lysosomes (11), an impaired lysosomal function may explain the accumulation of autophagosomes in Cystinosis cells. We postulated that cystinosin deficiency may affect lysosome function either by controlling the delivery of newly synthesized lysosomal cathepsins from Golgi to the lysosome or by inhibiting the processing/maturation of cathepsins within endolysosome compartment. Our results support the latter hypothesis, evidencing an impairment of lysosome proteolysis (observed both *in vitro* and *in vivo*) as a result of defective cathepsin activation despite an efficient delivery of newly synthesized cathepsins from Golgi to lysosomes. Furthermore, the rescue of lysosomal cystine homeostasis through the transient expression of cystinosin in *Ctns*$^{-/-}$ cells resulted in multi-level reactivation of the autophagy-lysosome degradative pathway. Taken together, these findings support a role of cystinosin -beyond its function in cystine transport- in maintaining the lysosomal response to the arrival of the autophagy cargoes, hence in cellular homeostasis.

The conjugation of impaired lysosomal dynamics and altered lysosomal degradative capacity is strikingly similar to the cellular changes resulting from the accumulation of monoclonal light chains (κLCs) within endolysosomes of PT cells, causing a similar epithelial dysfunction (22). Furthermore, the uncontrolled increase in lysosomal PtdIns(4,5)P_2 that results from the loss-of-function of the PtdIns (4,5)P_2 5-phosphatase OCRL, leads to lysosomal dysfunction and autophagosome accumulation in PT cells from patients with Lowe syndrome, another congenital disorder causing PT dysfunction and RFS (43). These data suggest that lysosomal accumulation of cystine or specific κLCs or PtdIns (4,5)P_2 may have similar functional consequences on the epithelial phenotype, emphasizing the role of endolysosomes as crucial signaling hub to ensure cellular homeostasis. Since lysosomal acidification is necessary for the activation of cathepsins, one could speculate that the V-ATPase complex might be altered in absence of cystinosin (44). Potential factors affecting V-ATPase efficiency in LSD may include: storage of cholesterol in the endolysosome membranes (45); luminal oxidation of lysosomal thiols by free cystine (46); and accumulation of cystine sustaining mTORC1activity and negatively regulating lysosome biogenesis by suppressing TFE/MiTF signaling (47). Recent studies showing that cystinosin is a member of the lysosomal machinery that controls mTORC1 activity *in vitro* (17) and that overexpression of TFEB stimulates lysosomal cargo processing (48) support the concept. Regardless of the mechanism, impaired cellular clearance leads to accumulation of autophagy substrates, such as dysfunctional mitochondria and ubiquitinated proteins. Although autophagy deficits have been reported in LSDs (37,38,49), the impact of lysosome-autophagy defects on epithelial cell function remains unknown. Basal autophagy operates to preserve the integrity of subcellular compartments, including damaged mitochondria (50,51). Lack of autophagy completion, due to impaired lysosomal degradation capacity or through inactivation of essential genes, leads to the persistence of ubiquitinated proteins (including p62/SQSTM1) and dysfunctional, ROS-producing mitochondria (38). Our results demonstrate the importance of this cellular quality-control mechanism for the function of epithelial cells. Genetic or pharmacologic blockage of basal autophagy resulted in accumulation of ubiquitinated proteins and damaged/dysfunctional mitochondria, leading to abnormal cell proliferation and apical dedifferentiation reflected by decreased uptake capacities. Similar to the changes observed in autophagy-deficient cells, there was a remarkable accumulation of SQSTM1- and ubiquitin-forming aggregates in *Ctns*$^{-/-}$ cells, with dysfunctional mitochondria accumulating within enlarged, non-degradative lysosomes and generating enhanced levels of mitochondrial ROS. These results indicate the importance of maintaining a healthy mitochondria repertoire to substantiate the solute transport activity in PT cells (52). In fact, primary mitochondrial diseases cause epithelial transport defects and RFS (4,52).

The link between abnormal mitochondrial autophagy and oxidative stress is well-documented (53,54), but how excessive mitochondrial ROS production may cause epithelial cell dysfunction? Highly specific junctions modulate the epithelial phenotype along the renal tubule segments. The levels of the tight junction adaptor protein ZO-1 and the localization of ZONAB, a Y-box transcription factor that interacts with ZO-1, modulate the switch from a proliferative to differentiated state in PT cells (28). For instance, absence of the endosomal channel CFTR (55) leads to reduced ZO-1 stability, promoting nuclear translocation of ZONAB and cell proliferation (56). Similarly, knockdown of *Tjp1* encoding ZO-1 in primary PT cells triggers an aberrant activation of tight junction-associated (ZONAB) signaling, with subsequent induction of a phenotype switch associating abnormal cell proliferation and dedifferentiation, mimicking the epithelial dysfunction associated with Cystinosis. An abnormal activity of ZONAB has also been evidenced when κLCs accumulate within dysfunctional endolysosomes (22). Furthermore, gain-of-function interventions targeting tight junction-associated ZONAB signaling rescue epithelial differentiation and reabsorptive capacity in Cystinosis PT cells. Taken together, these data suggest that the maintenance of tight junction integrity acts an essential regulator of epithelial cell differentiation.

Recent advances have illuminated the understanding of regulatory mechanisms involved in tight junction architecture and remodelling (29-31). In particular, changes in the cellular rate of Gα12/Src-mediated phosphorylation of ZO-1 associated with oxidative stress may disrupt tight junctions and cause cell damage (29-31). In line with these observations , our results substantiate that the aberrant production of mitochondrial-ROS enhances the Gα12/Src-mediated phosphorylation of ZO-1 and its subsequent mistargeting to enlarged, non-degradative endolysosomes. In turn, the loss of tight junction integrity promotes ZONAB signaling and transcription of target genes increasing cell proliferation and decreasing cell differentiation (27,28) resulting in defective endocytosis in *Ctns*$^{-/-}$ cells. The relevance of this abnormal cascade is supported by the gain- and loss-of-function approaches targeting Gα12 or ZO-1/ZONAB or by pharmacological interventions impeding the activation Gα12/Src signaling axis in *Ctns*$^{-/-}$ PT cells and also in *Ctns*$^{+/+}$ PT cells under mitochondria-derived oxidative stress conditions (Rotenone or blockade of autophagy). Consistent with this, treatment of *Ctns*$^{-/-}$ mice and their derived mPTCs with mitochondrial-targeted antioxidants, which are clinically tested in various mitochondrial diseases (57), not only repaired dysfunctional mitochondria and averted mitochondrial oxidative stress, but also rescued the integrity of tight junctions and the differentiation and endocytic uptake capacity of the cells. These data extend the previous findings showing that swan-neck deformities of PT segments (58) could be delayed in *Ctns*-knockout mice by administrating mitoquinone, an anti-oxidant compound that acts on mitochondria.

In conclusion, we identified a novel link between lysosomal storage and dysfunction, impaired autophagic clearance and loss of transport capacity in epithelial cells. These findings substantiate the role of endolysosome system in preserving the autophagy-mediated quality control of mitochondria, which are crucial for the high transport activities performed by specialized epithelial cells. They also demonstrate the cross-talk between mitochondria and tight-junction associated signal transduction pathways regulating the epithelial phenotype. The effect of an antioxidant compound specifically targeting mitochondria on the function of *Ctns*$^{-/-}$ cells provides a promising approach to alleviate the loss of vital metabolites in nephropathic Cystinosis.

METHODS

Antibodies and reagents. The following antibodies were used in this study: rat anti-LAMP1 (sc-19992, Santa Cruz Biotechnology); rabbit anti-LC3(PM036, MBL), rabbit anti-LC3 (NB100-2331, Novus Biologicals), rabbit anti-p62/SQSM1 (PM045, MBL); rabbit anti-GAPDH (2118, Cell Signaling Technology); mouse anti-β-actin (A2228, Sigma-Aldrich); goat anti-cathepsin-D (CtsD; sc-6486, Santa Cruz Biotechnology); rabbit anti-GM130 (ab52649, Abcam); mouse anti-Ubiquitin (sc-8017, Santa Cruz Biotechnology); mouse anti-PCNA (M0879, DAKO); rabbit anti-Histone-3 (H3; ab4729, Abcam); mouse anti-α-tubulin (T5168, Sigma-Aldrich); rabbit anti-Prohibitin (ab28172, Abcam); rabbit anti-ATG16L (D6D5) (#8089, Cell Signaling); rabbit anti-ATG7 (A2856, Sigma-Aldrich); mouse anti-BECN1(sc-48341, Santa Cruz Biotechnology); rat anti-Hemagglutinin (HA; 11867423001, Roche); rabbit anti-Calnexin (C4731, Sigma-Aldrich); mouse anti-Phospho-Tyr-99 (PY99; sc-7020, Santa Cruz Biotechnology); rabbit anti-ZO-1(sc-10804, Santa Cruz Biotechnology); rabbit anti-ZONAB (A303-070A, Bethyl Laboratories); mouse anti-Gα12 (sc-515610, Santa Cruz Biotechnology); rabbit anti-Phospho-Src Family (pTyr^{416}; #6943, Cell Signaling), rabbit anti-Src (#2109, Cell Signaling); mouse anti-PtdIns-3P (Z-P003, Echelon Biosciences Inc.); rabbit anti-Heme Oxygenase-1 (HO1; ab13243, Abcam); rabbit anti-Lipocalin-2 (ab63929, Abcam); goat anti-GFP (AB0020-500, SICGEN). Sheep anti-LRP2 antibody was kindly provided by P. Verroust and R. Kozyraki (INSERM, Paris, France). Compounds included Bafilomycin-A1 (ALX-380-030, Enzo Life Sciences), PIK3C3/Vps34 inhibitor SAR-405 (A8883, APExBIO), autophagy inhibitor Spautin-1 (S7888, Selleckchem.com), hydrogen peroxide (H1009 Sigma-Aldrich), Rotenone (R8875, Sigma-Aldrich), SU6656 (s9692, Sigma-Aldrich) and mito-TEMPO (MT; ALX-430-150-M005, Enzo Life Sciences).

Generation and maintenance of ctns zebrafish. *ctns*-specific left and right TALENs (ctns-TALENs) were constructed in according to Golden Gate TALEN assembly protocol and using the Golden Gate TALEN and TAL Effector Kit 2.0 (Addgene, Kit # 1000000024). CIscript-GoldyTALEN was a gift from Daniel Carlson & Stephen Ekker (Addgene, plasmid # 38142). TALENs were designed with the TAL Effector Nucleotide Targeter 2.0 software on the Website of Cornell University. The TALENs target the exon 3 of zebrafish *ctns* gene, with sequence left TALEN-F: TCTTTTAATCCTTTGTGTTCACA and right TALEN-R: CATCTGTAACGGTTTATTTCAAT. The spacer between two TALEN target sites is ~15 nucleotides and contains an *AciI* restriction site in the middle, which is used for mutant screening. The TALEN expression plasmids were linearized with BamHI and then used for *in vitro* transcription (mMESSAGE mMACHINE T3 kit, Ambion). Approximately 1 nL of TALEN messenger ribonucleic acid (mRNAs, 400 ng/µL) was injected into one-cell stage zebrafish (*Danio rerio*) embryos. After 24 h, genomic DNA was extracted from injected embryos with normal appearance. Targeted genomic loci were amplified by using primers designed to anneal approximately 240 base pair, and mutant allele was detected by *AciI* digestion of PCR product. The TALEN injected embryos were raised to adulthood (F0) and outcrossed with wild-type fish. The embryos were then raised to adulthood (F1) for screening of heterozygous carriers. We identified a heterozygous carrier harboring *ctns* $^{+/del8}$ mutation and (F1) generations were crossed for obtaining homozygous mutant carrying *ctns*$^{del8/del8}$. Zebrafish were kept at day/night cycle of 14/10 h at 28°C (Westerfield M. 2007). Where indicated, the zebrafish embryos were obtained through natural spawning in the facility of the University of Zurich and raised in E3 medium containing 0.01% methylene blue and prepared for analyses. Where indicated, adult zebrafish were produced in the zebrafish facility of Hubrecht Institute (Utrecht, Netherlands). Zebrafish were euthanatized by immersion in system water containing 300µg/ml tricaine methane sulfonate (MS222). The experiments were approved by the Animal Experimentation Committee of the Royal Netherlands Academy of Arts and Sciences.

Rescue experiments in ctns zebrafish. The plasmids containing wild type or mutant (ΔVVF346-349) human *CTNS* cDNA were kindly provided by C. Antignac (INSERM, Paris, France). The T3 promoter sequence was cloned into the XhoI restriction site of the EGFP vector by using forward primer: TCGAGGATCCATTAACCCTCACTAAAGGGAAC and reverse primer: TCGAGTTCCCTTTAGTGAGGGTTAATGGATCC. Either wild type or mutant *CTNS* messenger RNA was synthesized by using the mMESSAGE mMACHINE T3 transcription Kit (Invitrogen). The microinjection of wild type or mutant *CTNS* mRNA was performed in *ctns* $^{del8/del8}$ zebrafish embryos at one-cell stage and subsequently collected at 5 days post fertilization (d.p.f.) for cystine measurements. Where indicated, a working solution of cysteamine at 1mM was prepared by diluting the stock solution within E3 medium. After dechorionation, *ctns* zebrafish larvae at 2 dpf were incubated in the E3 medium in presence or in absence of cysteamine until to the sampled day (5 dpf), and the zebrafish media were renewed daily. Twenty zebrafish embryos per group were pooled and homogenized by sonication, and prepared for cystine measurements.

Mouse models. Experiments were conducted on age- and gender-matched *Ctns*$^{-/-}$ and *Ctns*$^{+/+}$ littermates (C57BL/6 background; 8,9). Mice were maintained under temperature-and humidity-controlled conditions with 12 h light/12 h dark cycles with free access to appropriate standard diet in accordance with the institutional guidelines of National Institutes of Health Guide for the Care and Use of Laboratory Animals. Mice aged 16 weeks were treated by daily intraperitoneal injection of mito-TEMPO (1mg/kg body weight in NaCl 0.9%) or vehicle (NaCl 0.9%) (n=4 for each group), and sacrificed after 30 days. Kidney tissues and/or urines were collected for analyses (see below). The protocols were approved by the Animal Ethics Committees of the UCL Medical School (Brussels) and the University of Zurich.

Renal function. The mice were placed overnight in metabolic cages with ad libitum access to food and drinking water; urine was collected over ice (9,22). The urine parameters were measured using a UniCel DxC 800 pro Synchron (Beckman Coulter, Fullerton, CA, USA), whereas Clara cell protein (CC16) concentration was measured in duplicate by enzyme-linked immunosorbent assay (ELISA; BIOMATIK EKU03200).

Kidney isolation and primary cultures of mouse proximal tubule cells. The kidneys were harvested from *Ctns*$^{+/+}$ and *Ctns*$^{-/-}$ mice as previously described (9,22). One kidney was split transversally and one half was fixed and processed for immunostaining while the other half was flash-frozen, homogenized by Dounce homogenizer in 1 mL of RIPA buffer that contains protease and phosphatase inhibitors and processed for western blot analysis. The contralateral kidney was taken to generate primary cultures of mPTCs as described (22). Freshly micro-dissected PT segments were seeded onto collagen-coated chamber slides (C7182, Sigma-Aldrich) and/or collagen-coated 6- or 24-well plates (145380 or 142475, Thermo Fisher Scientific), and cultured at 37°C and 5% CO_2 in DMEM/F12 (21041-025, Thermo Fisher Scientific) with 0.5% dialyzed FBS, 15mM HEPES (H0887, Sigma-Aldrich), 0.55mM sodium pyruvate (P2256, Sigma-Aldrich), 0.1ml/L non-essential amino acids (M7145, Sigma-Aldrich), hydrocortisone, human EGF, epinephrine, insulin, triiodothyronine, TF, and gentamicin/amphotericin (Single Quots® kit, CC-4127, Lonza), pH 7.40, 325mOsm/kg. The medium was replaced every 48 h. Confluent monolayers of mPTCs were expanded from the tubular fragments after 6–7 days, characterized by a high endocytic uptake capacity. These cells were mycoplasma free. All experiments were performed on confluent monolayers grown on chamber slides or plates.

Starvation of primary PT cells and treatments. Serum and amino acid removal was performed by washing mPTCs with Hank’s balanced salt solution (HBSS; 55021C, Sigma-Aldrich) and placing them in nutrient-deprived medium. Where indicated, macroautophagy was inhibited by addition of either PIK3C3/Vps34 inhibitor SAR-405 (5μM in cell culture medium for 16h, unless otherwise specified; ref. 59) or Spautin-1(25μM in cell culture medium for 16 h; ref. 60). Lysosomal proteolysis was inhibited by addition of Bafilomycin A1 (BfnA1; 250nM for 4h, unless otherwise stated). Where indicated, oxidative stress was triggered by treating mPTCs with either hydrogen peroxide (0.5mM for 1 h) or with Rotenone (250nM for 8 h).Where indicated, mPTCs were treated with either the mitochondria-targeted oxidant scavenger mito-TEMPO (10μM in culture medium for 12h, Enzo Life Sciences) or with a selective Src-family kinase inhibitor SU6656 (5μM in culture medium for 12 h, Sigma Aldrich). Afterwards, the cells were processed and analyzed as described below.

Adenovirus transduction in primary PT cells. For RNA interference studies, adenovirus constructs used include GFP U6-scrambled short hairpin (shRNA) (control vector) or an individually encoding mouse *Atg7* shRNA or encoding mouse *Ybx3/Csda* shRNA or encoding mouse *Gna12* shRNA or encoding mouse *Tjp1* shRNA. For expression studies, adenovirus constructs used include CMV (null vector) or an individually carrying mouse green fluorescent protein (GFP) tagged-*Map1lc3b* or carrying mouse red fluorescent protein (RFP)/2xFLAG tagged-*Lamp1* or carrying green fluorescent protein (GFP) tagged-*Csda* or carrying human hemagglutinin (HA) tagged-*TJP1* or carrying mouse hemagglutinin (HA) tagged-*Ctns*. The aforementioned adenovirus constructs were purchased from Vector Biolabs (University City Science Center, Philadelphia, USA). Briefly, primary mouse PT cells were plated onto collagen-coated chamber slides or 24-well or 6-well tissue culture plates. Adenovirus transduction was performed 24 h after plating when the cells reach approximately 70-80% confluence. The cells were subsequently incubated for 16 h at 37°C with culture medium containing the virus at the concentration (0.2125×10^9 PFU/mL). The cells were afterwards provided with fresh medium every 2 days, cultured for 5 days (unless otherwise specified) and collected for analyses.

Quantitative real-time PCR. Total RNA was extracted from mouse and zebrafish kidney tissues using Aurum ^{TM} Total RNA Fatty and Fibrous Tissue Kit (Bio-Rad, Hercules, CA). DNAse I treatment was performed to eliminate genomic DNA contamination. Total RNA was extracted from primary cell cultures with RNAqueous^{R} kit (Applied Biosystems, Life Technologies). One μg of RNA was used to perform the reverse transcriptase reaction with iScript ^{TM} cDNA Synthesis Kit (Bio-Rad). Changes in target genes mRNA levels were determined by relative RT-qPCR with a CFX96^{TM} Real-Time PCR Detection System (Bio-Rad) using iQ ^{TM} SYBR Green Supermix (Bio-Rad). RT-qPCR analyses were performed in duplicate with 100nM of both sense and anti-sense primers in a final volume of 20µl using iQ^{TM} SYBR Green Supermix (Bio-Rad). Specific primers were designed using Primer3 (Suppl. Table 1,2). PCR conditions were 95°C for 3 min followed by 40 cycles of 15 sec at 95°C, 30 sec at 60°C. The PCR products were sequenced with the BigDye terminator kit (Perkin Elmer Applied Biosystems) on an ABI3100 capillary sequencer (Perkin Elmer Applied Biosystems). The efficiency of each set of primers was determined by dilution curves (Suppl. Table 1,2). The program geNorm version 3.4 was applied to characterize the expression stability of the candidate reference genes in kidney and six reference genes were selected to calculate the normalization factor (61). The relative changes in targeted genes over *Gapdh* mRNAs were calculated using the $2^{-\Delta\Delta}$Ct formula.

Endocytosis assay. The endocytic uptake was monitored in mPTCs cells following incubation for 60 min at 4°C with 50 μg/mL Bovine Serum Albumin (BSA)-Alexa-Fluor-647 (A34785, Thermo Fisher Scientific) or with 50 μg/mL BSA–Alexa-Fluor-488 (A13100, Thermo Fisher Scientific) in complete HEPES-buffered DMEM. The cells were given an acid wash and warmed to 37°C in growth cell medium for 15 min before being fixed and processed for immunofluorescence analyses (22).

Lysosomal activity. *In mPTCs:* The detection of lysosomal activity was performed using Bodipy-FL-PepstatinA (P12271, Thermo Fischer Scientific) or Magic Red-$(RR)_2$ substrate (MR-CtsB; #938, Immunochemistry Technologies) according to the manufacturer's specifications. Briefly, the cells were pulsed with 1μM Bodipy-FL-Pepstatin A or with 1μM Magic Red-$(RR)_2$ in Live Cell Imaging (A14291DJ, Thermo Fischer Scientific) medium for 1h at 37°C followed by fixation and immunostaining with anti-LAMP1 or anti-HA antibody, and subsequently analyzed by confocal microscopy (22). *In zebrafish:* Bovine β−lactoglobulin (Sigma-Aldrich) was labeled with Cy5 using TM2 Ab labelling kit (Amersham) in accordance to the manufacturer's instructions. After anesthesia (0.2mg/mL tricaine (3-amino benzoic acid ethyl ester, Sigma-Aldrich), *cdh17*::GFP-expressing *ctns* zebrafish embryos were injected at 5dpf with Cy5-lactoglobulin (5μg/μl) via the common cardinal vein. Tracer injection into larvae blood was validated by monitoring the fluorescent vessels after injection. Larvae were incubated in fresh E3 medium for 20 or 120 min and subsequently fixed overnight in 2%PFA/PBS containing 0.1% Tween-20, and analyzed by fluorescent microscope (Zeiss, Germany).The fluorescence intensities and the numbers of β-lactoglobulin^{+} structures were quantified by using cell image analysis software Imaris (Bitplane).

Extracellular flux analysis and metabolic measurement. Oxygen consumption rate (OCR) was measured in XFp Extracellular Flux Analyzers (Agilent Seahorse Biosciences) in mPTCs incubated with XF-Base Medium (non-buffered RPMI 1640 containing either 2mM L-glutamine, 1mM sodium pyruvate and 10mM glucose, pH 7.4). Three measurements were measured under basal conditions and upon addition of 2μM Oligomycin, 0.5μM FCCP, and 1μM rotenone/antimycin A. All the reagents were provided by XFp Cell Mito Stress Test Kit (Agilent Seahorse biosciences). OCR measurements were normalized over the numbers of the cells (TC10^{TM} automated cell counter, Bio-Rad).

Mitochondrial membrane potential measurement. The mitochondrial membrane potential ($\Delta\psi$) was measured according to the manufacturer's specifications. Briefly, the cells were pulsed with 50nM Tetramethylrhodamine Methyl Ester Perchlorate (TMRM, T668 Thermo Fisher Scientific) for 30 min in live cell imaging at 37°C. After washing, the cells were subsequently analysed by confocal microscopy (62). The fluorescence intensity was quantified by using the open-source cell image analysis software CellProfiler^{TM} (63) as described below.

ROS detection. The cells were pulsed with 5µM CellROX® Green Reagent (C10444, Thermo Fisher Scientific) or with 2.5μM MitoSOX Red Mitochondrial Superoxide Indicator (M36008, Thermo Fisher Scientific) for 10 min in live cell imaging at 37°C. After washing, the cells were subsequently analysed by confocal microscopy (62). The fluorescence intensity was quantified by using the open-source cell image analysis software CellProfiler^{TM} (63) as described below.

Immunofluorescence and confocal microscopy. *Mouse kidney tissues*. Fresh mouse kidneys were fixed by perfusion with 50-60 ml of 4% paraformaldehyde in PBS (158127, Sigma-Aldrich). The organs were dehydrated and embedded in paraffin at 58C°. Paraffin blocks were sectioned into consecutive 5µm-thick slices with a Leica RM2255 rotary microtome (Thermo-Fisher Scientific) on Superfrost Plus glass slides (Thermo-Fisher Scientific). Before staining, slides were deparaffinized in changes of CitriSolv (22-143-975, Thermo-Fisher Scientific) and 70% isopropanol. Antigen retrieval was accomplished by incubating in sodium citrate buffer (1.8% 0.1M citric acid, 8.2% 0.1M sodium citrate, in distillated water, pH 6.0) in a rice cooker for 30 minutes. The slides were quenched with 50 mM NH_4Cl, blocked with 0.5% BSA in PBS Ca/Mg (D1283, Sigma-Aldrich) for 30 min and stained with primary antibodies specific for PCNA, LRP2, LC3 and p62/SQSTM1 diluted in blocking buffer overnight at 4°C. After two washes in 0.1% Tween 20 (v/v in PBS), the slides were incubated with corresponding fluorophore-conjugated Alexa secondary antibodies (Invitrogen) diluted in blocking buffer at room temperature for 1h and counterstained with 1µg Biotinylated Lotus Tetragonolobus Lectin (LTL) (B-1325 Vector Laboratories; marker of the PT apical membrane) and 1µM DAPI (#D1306, Thermo Fischer Scientific). The slides were mounted in Prolong Gold Anti-fade reagent (P36930, Thermo Fisher Scientific), acquired on Leica SP8 confocal laser scanning microscope (Center for Microscopy and Image Analysis, University of Zurich) equipped with a Leica APO 63x NA 1.4 oil immersion objective at a definition of 1,024 x 1,024 pixels (average of eight or sixteen scans), adjusting the pinhole diameter to 1 Airy unit for each emission channel to have all of the intensity values between 1 and 254 (linear range). The micrographs were processed with Adobe Photoshop (version CS5, Adobe System Inc., San Jose, USA) software. Quantitative image analysis was performed by selecting randomly ~5 visual fields per each slide that included at least 3-5 PTs (LTL-positive), using the same setting parameters (i.e. pinhole, laser power, and offset gain and detector amplification below pixel saturation). The numbers of LC3 or p62/SQSTM1 structures per proximal tubule (LTL-positive) were counted by using the open-source cell image analysis software CellProfiler^{TM} (63).

Primary cultured cells. The mPTCs were fixed for 10 min with 4% paraformaldehyde in PBS, quenched with 50 mM NH_4Cl and permeabilized for 20 min in blocking buffer solution containing 0.1% Triton X-100 and 0.5% BSA dissolved in PBS. Subsequently, mPTCs were incubated overnight with the appropriate primary antibodies at 4°C. After repeated washing with PBS, the slides were incubated for 45 min with the suitable fluorophore-conjugated Alexa secondary antibodies (Invitrogen), counterstained with 1µM DAPI for 5 min, mounted with the Prolong Gold Anti-fade reagent and analyzed by a Leica SP8 confocal laser scanning microscope (Center for Microscopy and Image Analysis, University of Zurich) using the settings described above. Quantitative image analysis was performed by selecting randomly 5 visual fields pooled from biological triplicates, with each field including at least 20-25 cells, using the same setting parameters (i.e. pinhole, laser power, and offset gain and detector amplification below pixel saturation). Three-dimensional (3-D) reconstructions of LAMP1-positive vesicles were generated in Imaris software using full confocal z-stacks (around 20) of each cell. The quantitative cell image analyses were performed using the open-source cell image analysis software CellProfiler^{TM} (63). In particular, the specific module "Measure-Object-Intensity-Distribution" was used to score the number and the vesicle size of LAMP1or CtsD positive structures and the fractions of LAMP1-positive structures contained into perinuclear region (area within 10µm of the nucleus) and peripheral region (area ≥ 15µm from the nucleus), respectively. The pipeline "Speckle counting" was used to identify smaller objects (LC3 or p62/SQSTM1 or Prohibitin or BSA or CtsD or MR-CtsB or ATG16L-positive structures) surrounding larger objects and to perform per-object aggregate measurements. The pipeline "Cell/particle counting, and scoring the percentage of stained objects" was used to score either the numbers of LAMP1$^+$ vesicles containing LC3$^+$ autophagosomes or PepstatinA or CtsD $^+$ vesicles or tight junction-ZO-1$^+$ structures, or Prohibitin$^+$ mitochondria, or the numbers of CtsD$^+$ vesicles containing MR-CtsB peptides or Golgi protein GM130. The "Cytoplasm-Nucleus Translocation Assay" was used to score the numbers of ZONAB or BrdU or PCNA-positive nuclei.

Electron microscopy and tomography. Zebrafish kidney sections and cultured mPTCs were fixed in 4% paraformaldehyde/0.1% glutaraldehyde in 100nM sodium cacodylate, at pH=7.43, dehydrated and embedded in LR-White resin (LADD Research Industries). The grids were viewed on a Philips CM100 transmission electron microscope at 80kV. Autophagic vacuoles were identified and categorized as autophagosomes or autophagolysosomes according to standard criteria (23). The term autophagic vacuole was used when differentiation between autophagosome and autophagolysosomes was not possible. Primary and secondary lysosomes (identified as single-membrane vesicle of higher density and smaller average diameter) were excluded from the quantification. The number of autophagic vacuoles was determined by using i-TEM software (Olympus, Germany). For electron tomography, 200-250nm thick sections were collected on formvar-coated copper slot grids using a Leica EM UC7 ultramicrotome (Leica Microsystem

GmbH Vienna, Austria). Colloidal gold particles (10nm) were applied as fiducials on both surfaces of the grids and the samples were imaged on a 200 kV Tecnai G2 20 electron microscope (FEI, Eindhoven) at a magnification of 11500x, resulting in pixel sizes of 1.95nm. Single tilted image series (±60° according to a Saxton scheme with the initial tilt step of 2°) were acquired using Xplorer3D (FEI, Eindhoven) with an Eagle 2,048 × 2,048 CCD camera (FEI, Eindhoven). Tilted series alignment, tomographic reconstructions, image segmentation and visualization were done with the IMOD software package.

Correlative light-electron microscopy. The cells were grown on finder grids and prepared for confocal microscopy analyses. Z-stacks of cells of interest were taken with the PerkinElmer UltraView ERS confocal microscope. The coordinates of the cells on the finder grid were determined by bright-field microscopy. Cells were fixed in 1% glutaraldehyde in 0.1M cacodylate buffer (Sigma) and post-fixed with 1.5% potassium ferricyanide, 1% OsO4 in 0.1M cacodylate buffer. Cells were stained with 0.5% uranyl acetate overnight, dehydrated in ethanol and embedded in epon. After baking for 48 h at 60 °C, the resin was released from the glass coverslip by temperature shock in liquid nitrogen. Serial sections (70–90 nm) were collected on carbon-coated formvar slot grids and imaged with a Zeiss LEO 512 electron microscope. Images were acquired by a 2k × 2k bottom-mounted slow-scan Proscan camera controlled by EsivisionPro 3.2 software.

Soluble and insoluble fractionation. Cells were lysed in buffer containing 50mM Tris-HCl, pH=7.5, 150mM NaCl, 0.1% SDS, 1% Triton X-100, 1% sodiumdeoxycholate supplemented with protease and phosphatase inhibitors and centrifuged at 16,000 rpm at 4°C for 20 min to collect the soluble fraction (supernatant). The pellet was re-suspended in a buffer containing 4% SDS and 20mM HEPES, pH=7.5, protease and phosphatase inhibitors and further centrifuged at 18,000 rpm at room temperature for 10 min to collect the insoluble fraction (supernatant). The samples were boiled at 95°C for 5 min and analyzed by western blotting.

Immunoprecipitation. The cells were lysed in a buffer containing 25mM Tris/HCl adjusted to pH= 7.4, 150mM NaCl, 1% NP-40 and 1mM EDTA, 5% glycerol, protease and phosphatase inhibitors for 10 min at 4°C. Lysate were centrifuged at 12,000 rpm for 10 min, and the supernatants were incubated with 1.5μg of primary anti-ZO-1 antibody for 16h at 4°C. After addition of 50μL of protein A sepharose beads (P9424, Sigma), lysates were incubated at 4°C for 12 h with gentle shaking. Agarose beads were washed for three times and then collected through centrifugation at 4,000 rpm for 1 min. Beads were reduced by the addition of 35μL of Laemmli sample buffer, heated at 95°C for 5min and resolved on 10% SDS–PAGE gel, and analyzed by western blotting.

Western blotting. Immunoblotting was performed as described previously (22). Proteins were extracted from mouse or zebrafish kidney tissues or primary cultured cells, lysed in lysis buffer containing protease (1836153001, Roche) and phosphatase inhibitors (04906845001, PhosSTOP Sigma), followed by sonication and centrifugation at 12,000rpm for 10 min at 4°C. The samples were thawed on ice, normalized for protein (20μg/lane), dissolved in Laemmli sample buffer and separated by SDS–PAGE in reducing conditions. After blotting onto PVDF and blocking with 5% non-fat milk (1706404, Bio-Rad Laboratories) diluted in PBS, the membranes were incubated overnight at 4°C with primary antibody, washed, incubated with peroxidase-labeled secondary antibody, and visualized with enhanced chemiluminescence (WBKLS0050, Millipore, Life technologies). For re-probing, the membranes were rinsed, incubated for 30 min at 55°C in a stripping buffer (62.5mmol/L Tris-HCl, 2% SDS, 100mM mercaptoethanol, adjusted to pH =7.4), before incubation with primary antibodies. Quantitative analysis was performed by scanning the blots and measuring the relative density of each band normalized to β–actin, GAPDH or α- tubulin by using ImageJ software.

Proximity ligation assay. The PLA assay was performed using the Duolink *in situ* reagents (Olink Biosciences) according to the manufacturer's specifications. Briefly, cells were fixed with 4% paraformaldehyde in PBS for 15 min at room temperature. After blocking with 0.1% Triton X-100 and 0.5% BSA dissolved in PBS, the cells were incubated overnight at 4°C with primary antibodies (1:100 diluted in blocking buffer). Following incubation with Duolink PLA anti-rabbit Plus and anti-mouse Minus probes (1:5 dilution, Olink Bioscience) at 37°C for 1 h, ligation, rolling circle amplification, and detection were performed using the Duolink In Situ Detection Reagents Red (Olink Bioscience). Nuclei were counterstained with DAPI. PLA signals were documented by a Leica SP8 confocal microscope and quantified by using cell image analysis software CellProfiler^{TM} (63).

PtdIns-3P detection. The detection of PtdIns-3-P was performed as described (64). Briefly, the cells were fixed with 2% formaldehyde in PBS 15 min at RT. After washing in PBS containing 50mM NH_4Cl, the cells were permeabilized for 5 min by the addition of 20µM digitonin in buffer-A (20mM Pipes pH 6.8, 137mM NaCl, 2.7mM KCl). Digitonin was removed by three rinses in buffer and cells were blocked for 45 min with buffer supplemented with 5% (v/v) FBS and 50mM NH_4Cl. Monoclonal mouse anti-PtdIns-3-P antibody were diluted in buffer with 5% FBS for 1 h (1:300). After washing with buffer for three times, anti-mouse IgG secondary antibodies were applied in buffer with 5% FBS (1:400) for 30 min. Cells were underwent to post-fixation for 5 min in 2% paraformaldehyde, washed with PBS containing 50mM NH_4Cl, and then mounted with the Prolong Gold Anti-fade reagent. PtdIns-3-P levels were analyzed by using a Leica SP8 confocal laser scanning microscope and quantified by using CellProfiler^{TM} (63).

Proliferation assay. To measure cell proliferation, the cells were seeded in 24-well plates at a density of 2.0×10^4 cells per well. The cells were cultured for three days and cell medium was renewed daily. Every 24 h afterwards, cells were trypsinized and quantified using the Countess automated cell counter TC10^{TM} automated cell counter (BIO-RAD). The time course experiments were repeated three times using cells derived from three individual mice per each group. Where indicated, cells were incubated with Bromodeoxyuridine (BrdU, 1.5µg mL^{-1}; Sigma-Aldrich) according to the manufacturer's protocol. BrdU-labelled cells were detected by immunostaining using rat anti-BrdU antibody (Oxford Biotechnology; 1:500), followed by the specific secondary biotinylated goat anti-rat antibody (1:300; Jackson Immunoresearch) and mounted with the Prolong Gold Anti-fade reagent. The slides were analyzed by using a Leica SP8 confocal laser scanning microscope and quantified by using CellProfilerTM .

Cystine measurement. Kidney tissues from mice kidney tissue or from zebrafish embryos, and/or primary cultured cells were homogenized and lysed with NEM solution containing 5.2mmol/L N-ethylmaleide in 10mmol/L potassium phosphate buffer adjusted to pH=7.4. The lysates were collected and precipitated with sulfosalicylic acid (12% w/v), and centrifuged at 10.000rpm for 10 min at 10°C. The resulting supernatant was dissolved in citrate loading buffer (Biochrom Ltd, Cambridge, UK) and 50 µL of this solution was analyzed by Biochrom 30 Plus Amino Acid Analyzer (Biochrom Ltd). The protein pellet was dissolved in 0.1mol/L NaOH solution and the protein concentration was determined by Biuret method. The concentration of amino acids was measured by using a lithium high performance physiological column (Biochrom) followed by post-column derivatization with ninhydrin. The amino acids were identified according to the retention time and the ratio of the area between the two wavelengths (570nm and 440nm) and quantified by using EZChrom Elite software (Agilent Technologies Inc., Pleasanton, California, USA). Cystine concentration was normalized to the protein concentration and reported in nmol/mg protein.

Data analysis and Statistics. The quantitative data were expressed as means ± standard error of the mean (s.e.m.). Differences between experimental groups were evaluated using analysis of variance followed by Bonferroni or Dunnet *post hoc* test, when appropriate. When only two groups were compared, unpaired or paired two tailed Student's *t*-tests were used as appropriate. No statistical methods were used to predetermine the sample size. We estimated the sample size considering the variation and mean of the samples. Assumptions for statistical analyses were met (that is, normal distribution and equal variance). The sample size (n of biological replicates derived from distinct mice or zebrafish) of each experimental group is described in figure legends. The results are representative of at least three independent experiments, unless specified in the figure legends. None of the samples/animals was excluded from the experiment, and the animals were not randomized. The investigators were not blinded to allocation during the experiments and outcome assessment. GraphPad Prism software was used for all statistical analyses. Statistical significance was set at a $P<0.05$.

REFERENCES

1. Eckardt, K.U., Coresh, J., Devuyst, O., Johnson, R.J., Köttgen, A. *et al.* Evolving importance of kidney disease: from subspecialty to global health burden. *Lancet* **382**, 158-169 (2013).

2. Devuyst, O. & A. Luciani. Chloride transporters and receptor-mediated endocytosis in the renal proximal tubule. *J. Physiol*. **593**, 4151-4164 (2015).

3. Christensen, E.I. P.J. Verroust, & R. Nielsen. Receptor-mediated endocytosis in renal proximal tubule. *Pflugers Arch*. **458**, 1039-1048 (2009).

4. Devuyst, O., Knoers, N.V., Remuzzi, G., Schaefer, F., Antignac, C. *et al.* Rare inherited kidney diseases: challenges, opportunities, and perspectives. *Lancet* **383**,1844-1859 (2014).

5. Town, M., Jean, G., Cherqui, S., Attard, M., Forestier, L. *et al.* A novel gene encoding an integral membrane protein is mutated in nephropathic cystinosis. *Nat. Genet.* **18**, 319-324 (1998).

6. Gahl, W.A., J.G. Thoene, & J.A. Schneider. Cystinosis. *N. Engl. J. Med*. **347,** 111-121 (2002).

7. Brodin-Sartorius, A., Tete, M.J., Niaudet, P., Antignac, C., Guest, G. *et al.* Cysteamine therapy delays the progression of nephropathic cystinosis in late adolescents and adults. *Kidney Int.* **81**,179-189 (2012).

8. Nevo, N., Chol, M., Bailleux, A., Kalatzis, V., Morisset, L. *et al.* Renal phenotype of the cystinosis mouse model is dependent upon genetic background. *Nephrology Dialysis Transplantation* **25**, 1059-1066 (2010).

9. Raggi, C., Luciani, A., Nevo, N., Antignac, C., Terry, S. *et al.* Dedifferentiation and aberrations of the endolysosomal compartment characterize the early stage of nephropathic cystinosis. *Hum. Mol. Genet.* **23**, 2266-2278 (2014).

10. Cherqui, S., Courtoy, P.J. The renal Fanconi syndrome in cystinosis: pathogenic insights and therapeutic perspectives. *Nat. Rev. Nephrol*. **13**, 115-131 (2017).

11. Settembre, C., Fraldi, A., Medina D. L. & Ballabio, A. Signals from the lysosome: a control centre for cellular clearance and energy metabolism. *Nature Reviews Molecular Cell Biology* **14**, 283-296 (2013).

12. Fougeray, S., & Pallet, N. Mechanisms and biological functions of autophagy in diseased and ageing kidneys. *Nature Reviews Nephrology* **11**, 34-45 (2015).

13. Isaka, Y., Kimura, T. &Takabatake, Y. The protective role of autophagy against aging and acute ischemic injury in kidney proximal tubular cells. *Autophagy* **7**, 1085-1087 (2011).

14. Yamamoto, T., Takabatake, Y., Kimura, T., Takahashi, A., Namba, T. *et al.* Time-dependent dysregulation of autophagy: Implications in aging and mitochondrial homeostasis in the kidney proximal tubule. *Autophagy* **12**, 801-813 (2016).

15. Sansanwal, P. & Sarwal, M.M. Abnormal mitochondrial autophagy in nephropathic cystinosis. *Autophagy* **6**, 971-973 (2010).

16. Sansanwal, P. &Sarwal, M.M. p62/SQSTM1 prominently accumulates in renal proximal tubules in nephropathic cystinosis. *Pediatr. Nephrol.* **27**, 2137-2144 (2012).

17. Andrzejewska, Z., Nevo. N., Thomas, L., Chhuon, C., Bailleux, A. *et al.* Cystinosin is a component of the vacuolar H+-ATPase-ragulator-Rag complex controlling mammalian target of rapamycin complex 1 Signaling. *J. Am. Soc. Nephrol*. **27**, 1678-88 (2016).

18. Bar-Peled, L. & Sabatini, D.M. Regulation of mTORC1 by amino acids. *Trends Cell Biol.* **24**, 400-406 (2014).

19. Grahammer, F., Ramakrishnan, S.K., Rinschen, M.M., Larionov, A.A., Syed, M. *et al.* mTOR regulates endocytosis and nutrient transport in proximal tubular cells. *J. Am. Soc. Nephrol.* **28**, 230-241 (2017).

20. Korolchuk, V.I., Saiki, S., Lichtenberg, M., Siddigi, F.H., Roberts, E.A. *et al.* Lysosomal positioning coordinates cellular nutrient responses. *Nat. Cell Biol.* **13,** 453-460 (2011).

21. Prange, J.A., Bieri, M., Segerer, S., Burger, C., Kaech, A. *et al.* Human proximal tubule cells form functional microtissues. *Pflugers Arch.* 468, 739-750 (2016).

22. Luciani, A., Sirac, C., Terryn, S., Javaugue, V., Prange, J.A. *et al*. Impaired Lysosomal Function Underlies Monoclonal Light Chain-Associated Renal Fanconi Syndrome. *J. Am. Soc. Nephrol.* **27**, 2049-61 (2016).

23. Klionsky, D.J., Abdelmohsen, K., Abe, A., Abedin, M.J., Abeliovich, H. *et al.* Guidelines for the use and interpretation of assays for monitoring autophagy (3rd edition). *Autophagy* **12,** 1-222 (2016).

24. Ronan, B., Flamand, O., Vescovi, L., Dureuil, C., Durand, L. *et al.* A highly potent and selective Vps34 inhibitor alters vesicle trafficking and autophagy. *Nat. Chem. Biol.* **10**, 1013-1019 (2014).

25. Ktistakis, N.T. & Tooze, S.A. Digesting the Expanding Mechanisms of Autophagy. *Trends Cell. Biol.* **26**, 624-635(2016).

26. Klionsky, D.J.E., Seglen, P. O. & Rubinsztein, D. C. Does bafilomycin A1 block the fusion of autophagosomes with lysosomes? *Autophagy* **4**, 849-850(2008).

27. Sourisseau, T., Georgiadis, A., Tsapara, A., Ali, R.R., Pestell, R. *et al.* Regulation of PCNA and cyclin D1 expression and epithelial morphogenesis by the ZO-1-regulated transcription factor ZONAB/DbpA. *Mol Cell Biol.* **26**, 2387-2398 (2006).

28. Lima, W.R., Perreira, K.S., Devuyst, O., Caplanusi, A., N'kuli, F. *et al.* ZONAB promotes proliferation and represses differentiation of proximal tubule epithelial cells. *J. Am. Soc. Nephrol.* **21**, 478-488 (2010).

29. Yu, W., Beaudry, S., Negoro, H., Boucher, I., Tran, M. *et al.* H2O2 activates G protein, alpha 12 to disrupt the junctional complex and enhance ischemia reperfusion injury. *Proc. Natl. Acad. Sci. U S A* **109**, 6680-6685(2012).

30. Meyer, T.N., Schwesinger, C. & Denker, B.M. Zonula occludens-1 is a scaffolding protein for signaling molecules. Galpha(12) directly binds to the Src homology 3 domain and regulates paracellular permeability in epithelial cells. *J. Biol. Chem.* **77**, 24855-24858 (2002).

31. Meyer, T.N., Hunt, J., Schwesinger, C. & Denker BM. Galpha12 regulates epithelial cell junctions through Src tyrosine kinases. *Am. J. Physiol. Cell. Physiol.* **285**, C1281-1293 (2003).

32. Murphy, M.P. & Smith, R.A. Targeting anitoxidants to mitochondria by conjugation to lipophilic cations. Annu. Rev. Pharmacol. Toxicol. **47**, 629-656 (2007).

33. Zhang, J., Wang, S., Jiang, B., Huang, L., Ji ,Z. *et al.* c-Src phosphorylation and activation of hexokinase promotes tumorigenesis and metastasis. *Nat Commun.* **8**, 13732 (2017).

34. Viau, A., El Karoui, K., Laouari, D., Burtin, M., Nguyen, C., *et al.* Lipocalin 2 is essential for chronic kidney disease progression in mice and humans. *J. Clin. Invest.* **120,** 4065-4076 (2010).

35. Ivanova, E. A., De Leo, M. G., Van Den Heuvel, L., Pastore, A., Dijkman, H. *et al.* Endo-lysosomal dysfunction in human proximal tubular epithelial cells deficient for lysosomal cystine transporter cystinosin. *PLoS One* **10**, e0120998 (2015).

36. Gaide Chevronnay, H. P., Janssens, V., Van Der Smissen, P., N'Kuli, F., Nevo, N., Y. et al. Time course of pathogenic and adaptation mechanisms in cystinotic mouse kidneys. *J. Am. Soc. Nephrol.* **25**, 1256-1269 (2014).

37. Settembre, C., Fraldi, A., Jahreiss, L., Spampanato, C., Venturi, C. *et al.* A block of autophagy in lysosomal storage disorders. *Hum. Mol. Genet.* **17**, 119-129 (2008).

38. Platt, F.M., Boland, B. & van der Spoel, A.C. The cell biology of disease: lysosomal storage disorders: the cellular impact of lysosomal dysfunction. *J. Cell. Biol.* **199**, 723-734 (2012).

39. Napolitano, G., Johnson, J.L., He, J., Rocca, C.J., Monfregola, J. *et al*. Impairment of chaperone-mediated autophagy leads to selective lysosomal degradation defects in the lysosomal storage disease cystinosis. EMBO Mol. Med. **7**, 158-174 (2015).

40. Ballabio, A. & Gieselmann, V. Lysosomal disorders: from storage to cellular damage. *Biochim. Biophys. Acta* **1793,** 684-96(2009).

41. Bento, C.F.A., Ashkenazi, A., Jimenez-Sanchez, M. & Rubinsztein, D. C. The Parkinson's disease-associated genes ATP13A2 and SYT11 regulate autophagy via a common pathway. *Nat. Commun.* **7**, 11803 (2016).

42. Li, X., Rydzewski, N., Hider, A., Zhang, X., Yang, J. *et al.* A molecular mechanism to regulate lysosome motility for lysosome positioning and tubulation. *Nat. Cell. Biol.* **18**, 404-17 (2016).

43. De Leo, M.G., Staiano, L., Vicinanza,M., Luciani, A., Carissimo, A. *et al. Nat. Cell. Biol.***18**, 839-850 (2016).

44. Zoncu, R., Bar-Peled, L., Efeyan, A., Wang, S., Sancak, Y. *et al.* mTORC1 senses lysosomal amino acids through an inside-out mechanism that requires the vacuolar H(+)-ATPase. *Science* **334**, 678-83(2011).

45. Cox, B.E., Griffin, E.E., Ullery, J.C. & Jerome, W.G. Effects of cellular cholesterol loading on macrophage foam cell lysosome acidification. *J Lipid Res.* **48**, 1012-1021 (2007).

46. Cherqui, S. & Courtoy, P.J. The renal Fanconi syndrome in cystinosis: pathogenic insights and therapeutic perspectives. *Nat. Rev. Nephrol.* **13**, 115-131 (2017).

47. Efeyan, A., Zoncu, R. & Sabatini, D.M. Amino acids and mTORC1: from lysosomes to disease. *Trends Mol. Med.* **18**, 524-533 (2012).

48. Rega, L.R., Polishchuk, E., Montefusco, S., Napolitano, G., Tozzi, G. *et al.* Activation of the transcription factor EB rescues lysosomal abnormalities in cystinotic kidney cells. *Kidney Int.* **89**, 862-73(2016).

49. Liebarman, A.P., Puertollano, R., Raben, N., Slaugenhaupt, S., Walkley, S.U. *et al.* Autophagy in lysosomal storage disorders. *Autophagy* **8**, 719-730 (2012).

50. Galluzzi, L., Pietrocola, F., Bravo-San-Pedro, J.M., Amaravadi, R.K., Baehrecke, E.H. *et al.* Autophagy in malignant transformation and cancer progression. *EMBO J.* **34**, 856-680 (2015).

51. Narendra, D., Kane, L.A., Hauser,D.N, Fearnley, I.M., Youle, R. J. p62/SQSTM1 is required for Parkin-induced mitochondrial clustering but not mitophagy; VDAC1 is dispensable for both. *Autophagy* **6**, 1090-1106 (2010).

52. Emma, F., Montini,G., Parikh,S.M. & Salvati, L. Mitochondrial dysfunction in inherited renal disease and acute kidney injury. *Nat. Rev. Nephrol.* **12**, 267-280(2016).

53. Scherz-Shouval, R. & Elazar, Z. Regulation of autophagy by ROS: physiology and pathology. *Trends Biochem. Sci.* **36**, 30-38 (2011).

54. Li, X.T., Wang, H.Z., Wu, Z.W., Yang, T.Q., Zhao, Z.H. *et al.* miR-494-3p regulates cellular proliferation, invasion, migration, and apoptosis by PTEN/AKT signaling in human glioblastoma cells. *Cell Mol. Neurobiol.* **35**, 679-687 (2015).

55. Jouret, F., Bernard, A., Hermans, C., Dom, G., Terryn, S. *et al.* Cystic fibrosis is associated with a defect in apical receptor-mediated endocytosis in mouse and human kidney. *J. Am. Soc. Nephrol.* **18**, 707-718 (2007).

56. Ruan, Y.C., Wang,Y., Da Silva, N., Kim, B., Diao, R.Y. *et al.* CFTR interacts with ZO-1 to regulate tight junction assembly and epithelial differentiation through the ZONAB pathway. *J. Cell Sci.* **127**, 4396-4408 (2014).

57. Wang, W., Karamanlidis, G. & Tian, R. Novel targets for mitochondrial medicine. *Science Translational Medicine* **8**, 326rv3 (2016)

58. Galarreta, C., Forbes, M.S., Thornhill, B.A., Antignac, C., Gubler, M.C. *et al.* The swan-neck lesion: proximal tubular adaptation to oxidative stress in nephropathic cystinosis. *Am. J Physiol. Renal Physiol.* **308**, F1155-1166 (2015).

59. Pasquier, B. SAR405, a PIK3C3/Vps34 inhibitor that prevents autophagy and synergizes with MTOR inhibition in tumor cells. *Autophagy* **11**, 725-726(2015).

60. Cinque, L., Forrester, A., Bartolomeo, R., Svelto, M., Venditti, R. *et al.* FGF signaling regulates bone growth through autophagy. *Nature **528***, 272-5(2015).

61. Vandesompele, J., De Preter, K., Pattyn, F., Poppe, B., Van Roy, N. *et al.* Accurate normalization of real-time quantitative RT-PCR data by geometric averaging of multipleinternal control genes. *Genome Biol.* 3, RESEARCH0034 (2002).

62. Luciani, A., Vilella, V.R., Esposito, S., Brunetti-Pierri, N., Medina, D., Settembre, C. *et al.* Defective CFTR induces aggresome formation and lung inflammation in cystic fibrosis through ROS-mediated autophagy inhibition. *Nat. Cell Biol.***12**, 863-875(2010).

63. Carpenter, A.E., Jones, T.R., Lamprecht, M.R., Clarke, C. Kang, I.H. et al. CellProfiler: image analysis software for identifying and quantifying cell phenotypes. *Genome Biol.* 2006. **7**, R100 (2006).

64. Hammond, G.R., Schiavo, G. & Irvine, R.F. Immunocytochemical techniques reveal multiple, distinct cellular pools of PtdIns4P and PtdIns(4,5)P(2). *Biochem J.* **422**, 23-35 (2009).

ACKNOWLEDGEMENTS

We are grateful to Fonds National de la Recherche Scientifique and the Fonds de la Recherche Scientifique Médicale (Brussels, Belgium), the European Community's Seventh Framework Programme (FP7/2007-2013) under grant agreement n° 305608 (EURenOmics), the Cystinosis Research Foundation (Irvine, CA, USA), the Swiss National Science Foundation (project grant 31003A-169850), the clinical research priority programs (KFSP) Molecular Imaging Network Zurich (MINZ) and RADIZ (Rare Disease Initiative Zurich) of the UZH, the Dutch Kidney Foundation (project grant 16OI06) and the Swiss National Centre of Competence in Research (NCCR) Kidney Control of Homeostasis (Kidney.CH) for support and Junior Grant (to A.L.). We acknowledge Benjamin Klormann and Ive Logister for providing technical assistance; the Hubrecht Institute Zebrafish Caretaker team; Corinne Antignac (Imagine, Paris) for fruitful discussions and for providing the *Ctns* mice; and Pierre Verroust and Renata Kozyraki for providing reagents. We thank ALEMBIC facility at San Raffaele Scientific Institute (Milan, Italy) for providing electron microscopy assistance. Imaging was performed with equipment maintained by the Center for Microscopy and Image Analysis, University of Zurich.

Author contributions: O.D. and A.L. supervised the entire project; B.P.F., O.D. and A.L. designed the research concept, planned the overall experimental design, performed cellular and mouse studies, analysed and interpreted the data, and wrote the paper with inputs and final approval from all the authors; Z.C., G. V. D. H. and R. H. G. generated and analyzed the *ctns* knock-out zebrafish model and contributed to the interpretation and analysis of the data; M.B. and J.A.P. performed primary cultures of PT cells and immunoblot experiments; N.T. performed the seahorse metabolic flux analyses; H.D. performed RNA and cellular studies and contributed to the interpretation and analysis of the data; A.C. performed the measurements of the cystine levels on primary cells and kidney tissues; A.R. performed transmission and tomography microscopy studies, and contributed to the interpretation and analysis of the data; N.N. provided and analyzed *Ctns* mice and contributed to the interpretation of the data.

Competing financial interests: The authors declare no competing financial interests

Figure 1

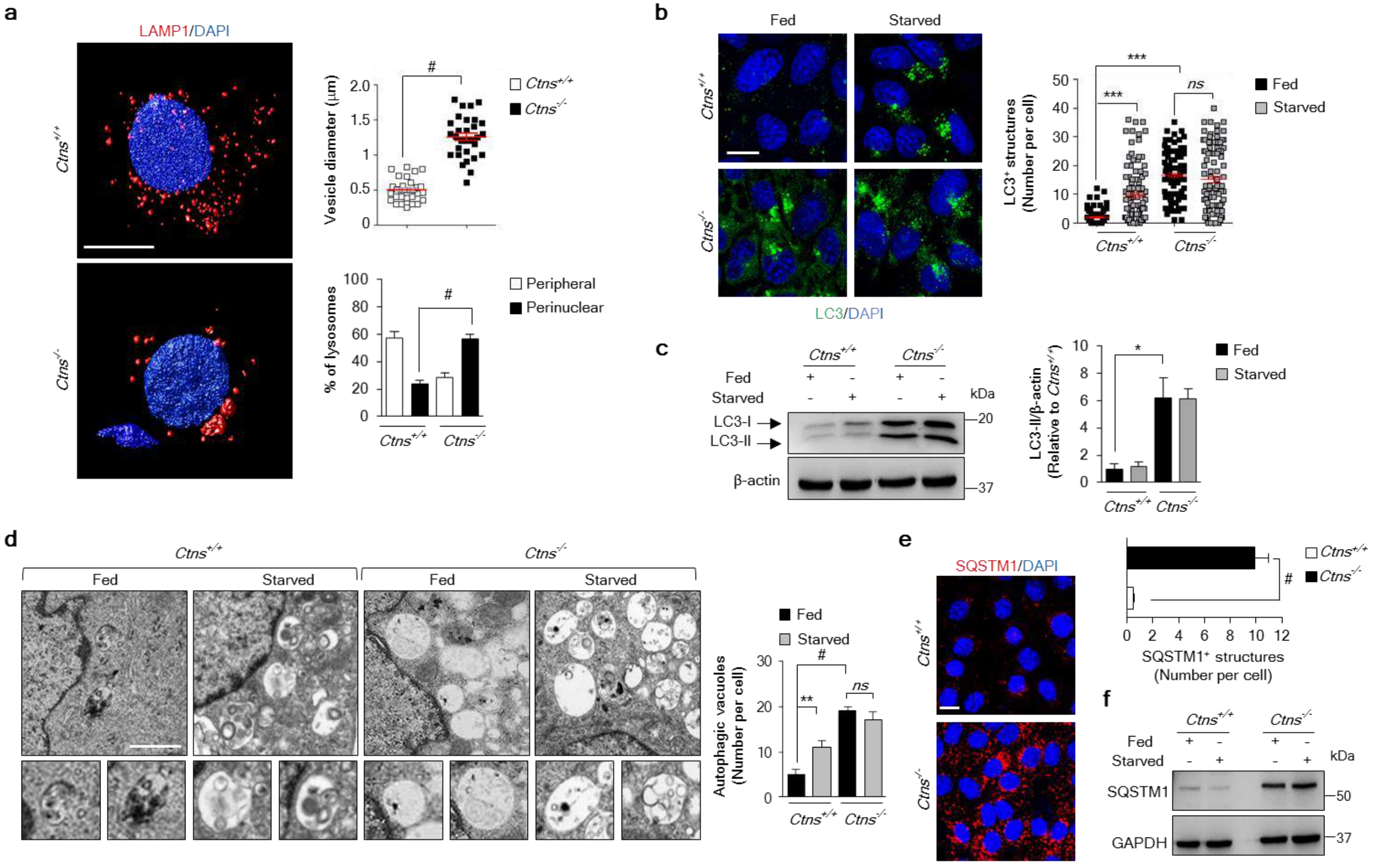

Figure 1. Abnormal lysosome dynamics and autophagy in CTNS-deficient PT cells. (**a**) Left: confocal microscopy and three-dimensional (3D) reconstruction of *Ctns* mPTCs labelled with anti-LAMP1 (red) antibody. Right: Quantification of changes in vesicle size (top, each point representing the average diameter of LAMP1^{+} vesicles in a cell) and lysosome positioning (bottom, percent of perinuclear or peripheral distribution) (n=30 mPTCs pooled from 3 *Ctns* kidneys per group; two tailed unpaired *t* test, $^{\#}$*P*<0.0001 relative to *Ctns*$^{+/+}$ mPTCs). (**b**-**f**) *Ctns* mPTCs were cultured in normal growth (Fed; 8h) or nutrient-deprived cell medium (Starved; 8h). (**b**) Representative confocal micrographs (left) and quantification (right) of numbers of LC3 structures (green) in *Ctns* mPTCs (*n*=100 cells pooled from three *Ctns* kidneys per group; each point representing the number of LC3^{+} vesicles in a cell; one-way analysis of variance (ANOVA) followed by Bonferroni's *post hoc* test, ****P*<0.001 relative to *Ctns*$^{+/+}$ mPTCs under fed conditions; *ns*, not significant.). (**c**) Western blotting and densitometric analyses of LC3 protein levels. β-actin was used as a loading control. Two tailed unpaired Student's *t* test, **P*<0.05 relative to *Ctns*$^{+/+}$ mPTCs under fed conditions. (n=3 independent experiments). (**d**) Representative electron micrographs (left) and quantification (right) of numbers of autophagic vacuoles per cell (n=10 micrographs per each condition; one-way ANOVA followed by Bonferroni's *post hoc* test, ***P*<0.01 and $^{\#}$*P*<0.0001 relative to *Ctns*$^{+/+}$ mPTCs under fed conditions; *ns*, not significant). Insets: autophagic vacuoles at higher magnification. (**e**) Representative confocal micrographs and quantification of SQSTM1 structures (red) in *Ctns* mPTCs (*n*=100 cells pooled from three *Ctns* kidneys per group; two tailed unpaired Student's *t* test, $^{\#}$*P*<0.0001 relative to *Ctns*$^{+/+}$ mPTCs). (**f**) Representative western blotting of SQSTM1 in *Ctns* mPTCs. GAPDH was used as a loading control. (n=3 independent experiments). Plotted data represent mean±s.e.m. Nuclei are stained with DAPI (blue). Scale bars are 10μm in **a**, **b** and **e** and 2μm in **d**.

Figure 2

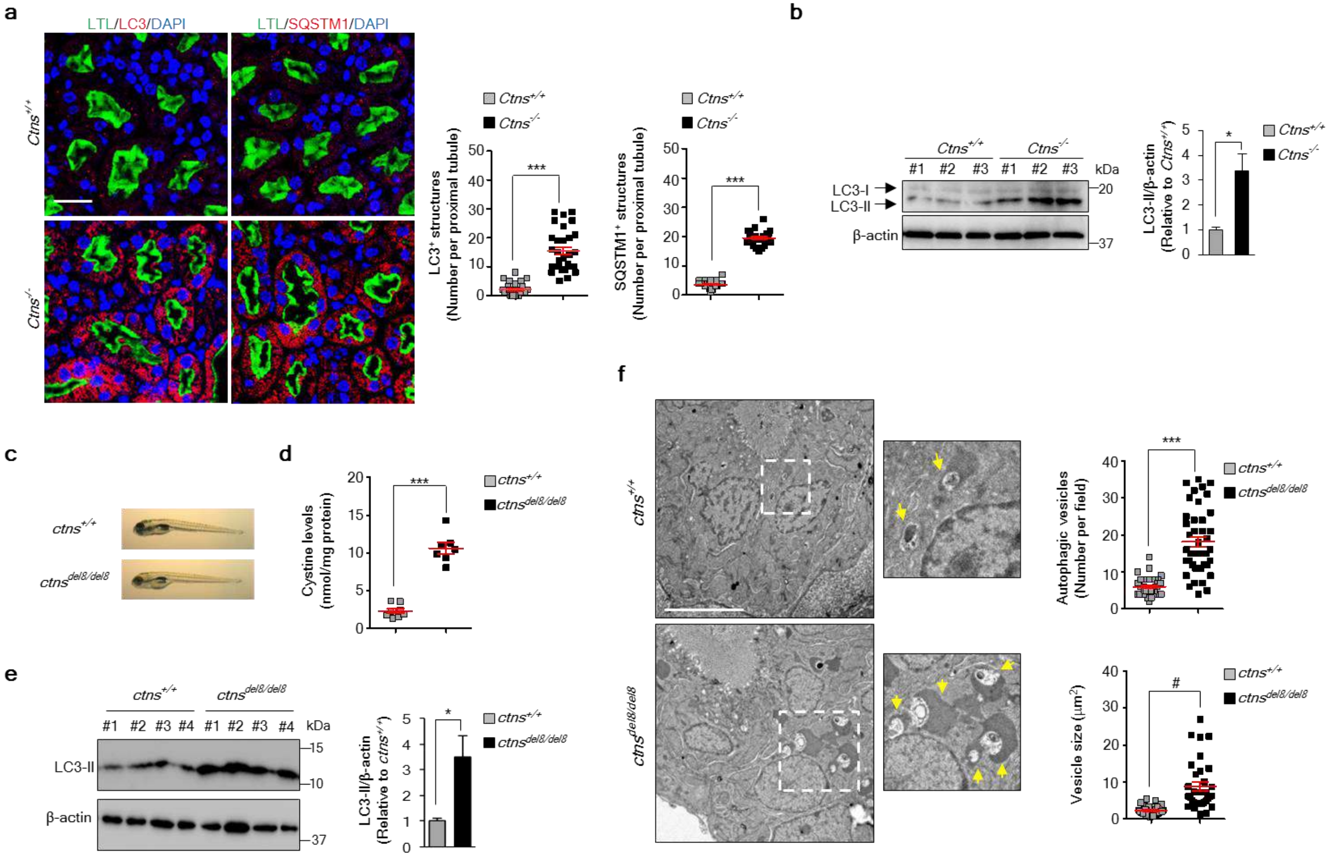

Figure 2. Cystinosin deficiency alters autophagy in proximal tubules of mouse and zebrafish kidneys. (**a**) Representative confocal micrographs and quantification of the numbers of LC3 (left panel; red) or SQSTM1structures (right panel; red) in LTL (green)-positive proximal tubules in *Ctns* mouse kidneys (n=30 proximal tubules pooled from three kidneys per group; each point representing the number of LC3^{+} or SQSTM1^{+} vesicles in a proximal tubule; two tailed unpaired Student's *t* test, ****P*<0.001 relative to *Ctns*$^{+/+}$ kidneys). Nuclei counterstained with DAPI (blue). (**b**) Western blotting and densitometric analyses of LC3 protein levels in whole kidney lysates from *Ctns* mice (two tailed unpaired Student's *t* test, **P*=0.029 relative to *Ctns*$^{+/+}$ kidneys, n=3 mice per group). (**c**) Representative images of *ctns*$^{+/+}$ and *ctns*$^{del8/del8}$ zebrafish embryos at 5 days post fertilization (dpf) and (**d**) quantification of cystine levels by HPLC in pronephric tubules from corresponding *ctns*$^{+/+}$ and *ctns* $^{del8/del8}$ zebrafish embryos (two tailed unpaired Student's *t* test,****P*<0.001 relative to *ctns*$^{+/+}$embryos , n=8 *ctns*$^{+/+}$ zebrafish and n=7 *ctns* $^{del8/del8}$ zebrafish). (**e**) Western blotting and densitometric analyses of LC3 protein levels in pronephric tubules from 3-month-old *ctns*$^{+/+}$ and *ctns* $^{del8/del8}$ zebrafish (n=4 per group; two tailed unpaired Student's *t* test, **P*=0.03 relative to *ctns*$^{+/+}$ kidneys). (**f**) Representative electron micrographs and quantifications of the numbers and size of autophagic vacuoles in pronephric tubules of *ctns*$^{+/+}$ and *ctns*$^{del8/del8}$ zebrafish embryos at 5dpf. Dotted white squares contain images at higher magnification. Yellow arrowhead indicates autophagic vacuoles. Number of autophagic vesicles: n= 43 (*ctns*$^{+/+}$) and n=42 (*ctns*$^{del8/del8}$) randomly selected micrographs were pooled from eleven *ctns*$^{+/+}$ and twelve *ctns*$^{del8/del8}$ zebrafish. Vesicle size: n= 32 (*ctns*$^{+/+}$) and n=33 (*ctns*$^{del8/del8}$) randomly selected micrographs were pooled from eleven *ctns*$^{+/+}$ and twelve *ctns*$^{del8/del8}$ zebrafish. Two tailed unpaired Student's *t* test, ****P*<0.001 and $^{\#}$*P*<0.0001 relative to *ctns*$^{+/+}$ zebrafish kidneys. β-actin was used as a loading control in **b** and **e**. Plotted data represent mean±s.e.m. Scale bars are 50μm in **a** and 5μm in **f**.

Figure 3

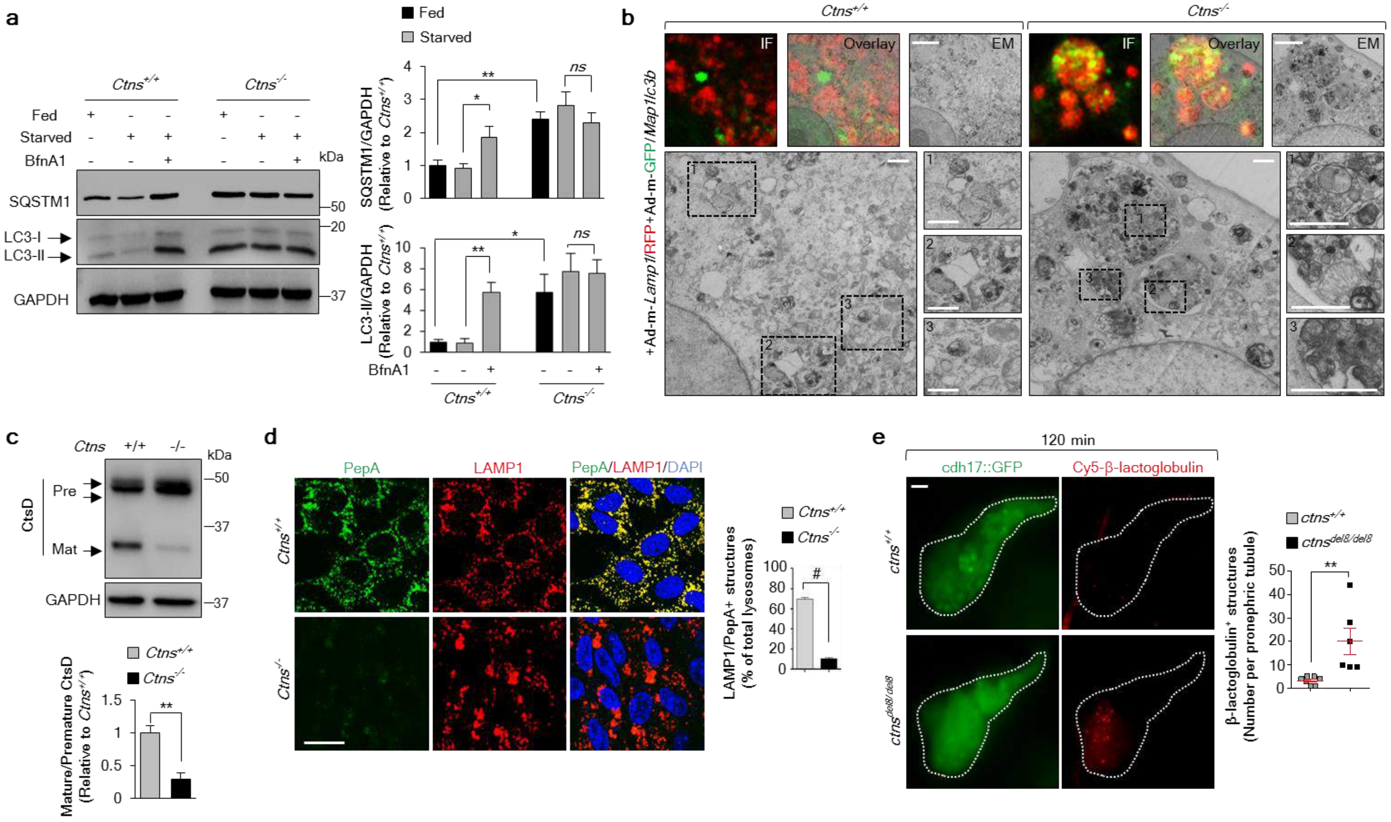

Figure 3. Cystinosin deficiency delays the clearance of autophagosomes by impairing lysosome function. (**a**) Western blotting and densitometric analyses for LC3 and SQSTM1 protein levels in *Ctns* mPTCs cultured in fed or starved medium in presence or in absence of 250 nM BfnA1for 4h (n=3 independent experiments). Two tailed unpaired Student's *t* test, $**P<0.01$ (SQSTM1) and $*P<0.05$ (LC3) relative to fed *Ctns*$^{+/+}$ mPTCs $*P=0.05$ (SQSTM1) and $**P=0.009$ (LC3) relative to starved *Ctns*$^{+/+}$ mPTCs. (**b**) Correlative light-electron microscopy (CLEM) in *Ctns* mPTCs transduced with both RFP-tagged *Lamp1* (*LAMP1*/RFP) and GFP-tagged *Map1lc3b* (*Map1lc3b*/GFP) bearing adenoviral particles for 2 days. The colocalization of GFP-LC3 and RFP-LAMP1 was monitored by confocal IF. Selected cells were further processed and serial sections analysed by electron microscopy. Dotted black squares contain images at higher magnification. Scale bars are 2µm (top panel) and 500 nm (bottom panel). (**c**) Western blotting and densitometric analyses of CtsD protein levels in *Ctns* mPTCs; two tailed unpaired Student's *t* test, $**P<0.01$ relative to *Ctns*$^{+/+}$ mPTCs (n=3 independent experiments). (**d**) *Ctns* mPTCs were loaded with Bodipy-FL-PepA (1µM, for 1h at 37°C, green), immunostained with anti- LAMP1antibody (red) and analysed by confocal microscopy. Quantification of numbers of PepA/LAMP1 co-localizing structures (in percentage of total lysosomes; n=5 randomly selected fields per condition, with each containing ~20-25 cells; two tailed unpaired Student's *t* test, $^{\#}P<0.0001$ relative to *Ctns*$^{+/+}$ mPTCs). (**e**) 5dpf-*ctns* zebrafish embryos expressing *cdh17*::GFP (green, pronephric tubule marker) were injected with Cy5-tagged-β-lactoglobulin. At 120 min after the injection of the tracer, zebrafish embryos were imaged using light sheet fluorescent microscopy. A similar rate of internalization of Cy5-tagged-β-lactoglobulin was observed at 20min in both *ctns*$^{+/+}$ and *ctns*$^{del8/del8}$ zebrafish embryos, validating the uptake of the tracer by pronephric tubules. Representative micrographs (left) and quantification (right) of numbers of β-lactoglobulin^{+} structures (red) in *ctns* zebrafish pronephric tubule (n=6 zebrafish per group; two tailed unpaired Student's *t* test, $**P=0.01$ relative to ctns$^{+/+}$ zebrafish). GAPDH was used as loading control in **a** and **c**. Plotted data represent mean±s.e.m. Nuclei are counterstained with DAPI (blue). Yellow indicates colocalization. Scale bars are 10µm in **d** and 50µm in **e**.

Figure 4

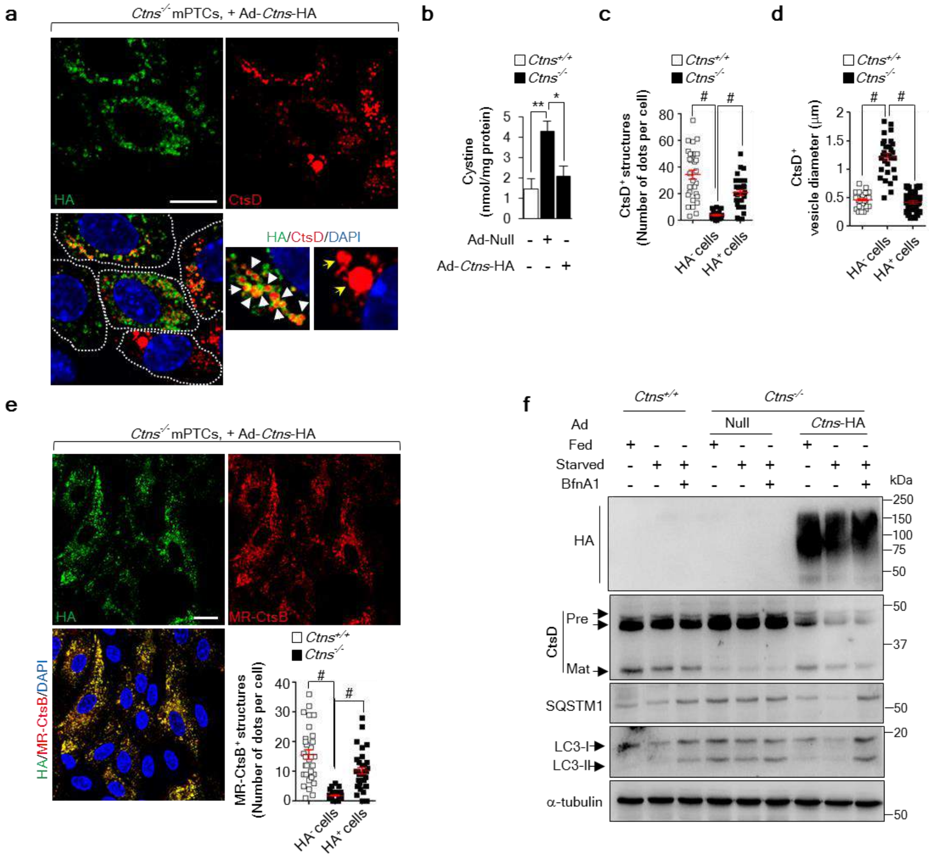

Figure 4. Rescue of lysosome-autophagy pathway by re-expressing CTNS in *Ctns*$^{-/-}$ cells. (**a-f**) *Ctns*$^{-/-}$ mPTCs were transduced with either Null (Ad-Null) or hemagglutinin-tagged *Ctns* (Ad-*Ctns*-HA) bearing adenoviral particles for 2 days. (**a**) Cells were immunostained with anti-HA (green) and anti-CtsD (red) antibodies and analysed by confocal microscopy. Insets: high magnification of *Ctns*-HA^{+} vesicles containing CtsD. (**b**) Intracellular cystine levels were measured by HPLC. Two tailed unpaired *t* test, ***P*<0.01 relative to *Ctns*$^{+/+}$ mPTCs; **P*<0.05 relative to *Ctns*$^{-/-}$ mPTCs transduced with Ad-Null. (**c**) Quantification of changes in the number of CtsD^{+} and (**d**) in the average vesicle size in cells from **a** (*n*=30 randomly selected cells pooled from three *Ctns* kidneys per condition; each point representing the number or the average diameter of CtsD^{+} vesicles in a cell; one-way ANOVA followed by Bonferroni's *post hoc* test, $^{\#}$*P*<0.0001 relative to *Ctns*$^{+/+}$ mPTCs or to HA^{-} *Ctns*$^{-/-}$ mPTCs. (**e**) *Ctns* mPTCs were loaded with MR-CtsB peptide (1μM, for 1h at 37°C) and immunostained with anti-HA antibody. Quantification of the number of MR-CtsB structures (n=33 randomly selected cells pooled from three *Ctns* kidneys per condition, each point representing the number of MR-CtsB^{+} dots in a cell; two tailed unpaired Student's *t* test, $^{\#}$*P*<0.0001 relative to *Ctns*$^{+/+}$ mPTCs or to HA^{-} *Ctns*$^{-/-}$ mPTCs). (**f**) *Ctns* mPTCs were cultured in fed or starved medium in presence or in absence of 250 nM BfnA1 for 4h. The cells were lysed and subjected to western blotting analysis for the protein levels of HA, CtsD, SQSTM1and LC3. α-tubulin was used as a loading control (n=3 independent experiments). Plotted data represent mean±s.e.m. The nuclei are counterstained with DAPI (blue). Yellow indicates colocalization. Scale bars are 10μm.

Figure 5

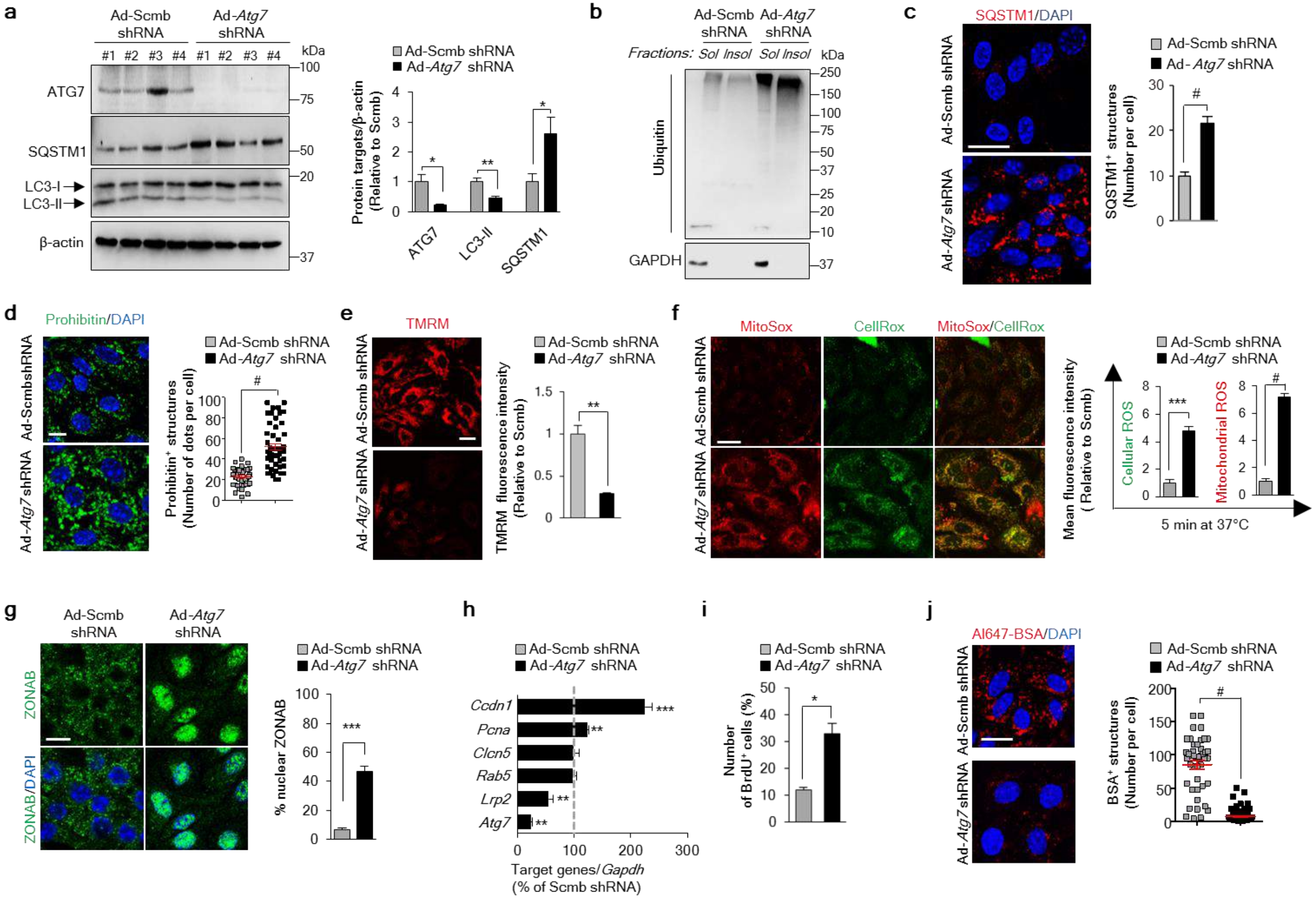

Figure 5. Failure of autophagy causes proliferation and dedifferentiation of PT cells. (a-j) mPTCs were transduced with either scrambled or *Atg7* adenoviral shRNAs for 5 days. (**a**) Western blotting and densitometric analyses of ATG7, SQSTM1and LC3 levels. β-actin was used as a loading control (n=4 independent experiments). (**b**) Representative western blotting of the soluble and insoluble fractions derived from mPTCs and immunoblotted for ubiquitin and GAPDH (n=3 independent experiments). (**c**) Cells were immunostained for SQSTM1 and analysed by confocal microscopy. The adjacent panel shows the quantification of the number of SQSTM1 structures in mPTCs. (**d**) mPTCs were immunostained with an anti-prohibitin antibody and analysed by confocal microscopy. Quantifications of the number of prohibitin structures. (**e**) The cells were loaded with tetramethylrhodamine methyl ester and analysed by live confocal microscopy. Quantification of TMRM fluorescence intensity obtained from 5 randomly selected fields per condition. (**f**) mPTCs were loaded with CellROX and Mito SOX analysed by live confocal microscopy. Quantifications of CellROX or MitoSOX fluorescence intensity obtained from three randomly selected fields per condition. (**g**) mPTCs were immunostained with an anti-ZONAB (green) antibody and analysed by confocal microscopy. The adjacent panel show the quantification of ZONAB positive nuclei (in percentage of the total nuclei) from 5 randomly selected fields per condition (**h**) The mRNA levels of *Atg7, Clcn5, Rab5, Lrp2, Ccdn1 and Pcna* were analysed by real-time PCR (n=4 independent experiments). (**i**) mPTCs were loaded with bromodeoxyuridine, immunostained with anti- BrdU antibody and analysed by confocal microscopy. Quantification of numbers of BrdU positive cells was obtained from 5 randomly selected fields per condition. (**j**) The cells were loaded with Al647-BSA and imaged by confocal microscopy. Quantifications of the number of Al647-BSA. Plotted data represent mean±s.e.m. Two tailed paired Student's *t* test, $^*P<0.05$, $^{**}P<0.01$, $^{***}P<0.001$ and $^{\#}p<0.0001$relative to mPTCs transduced with Scmb shRNAs; *ns*, not-significant. Nuclei are counterstained with DAPI (blue). Scale bars are 10μm.

Figure 6

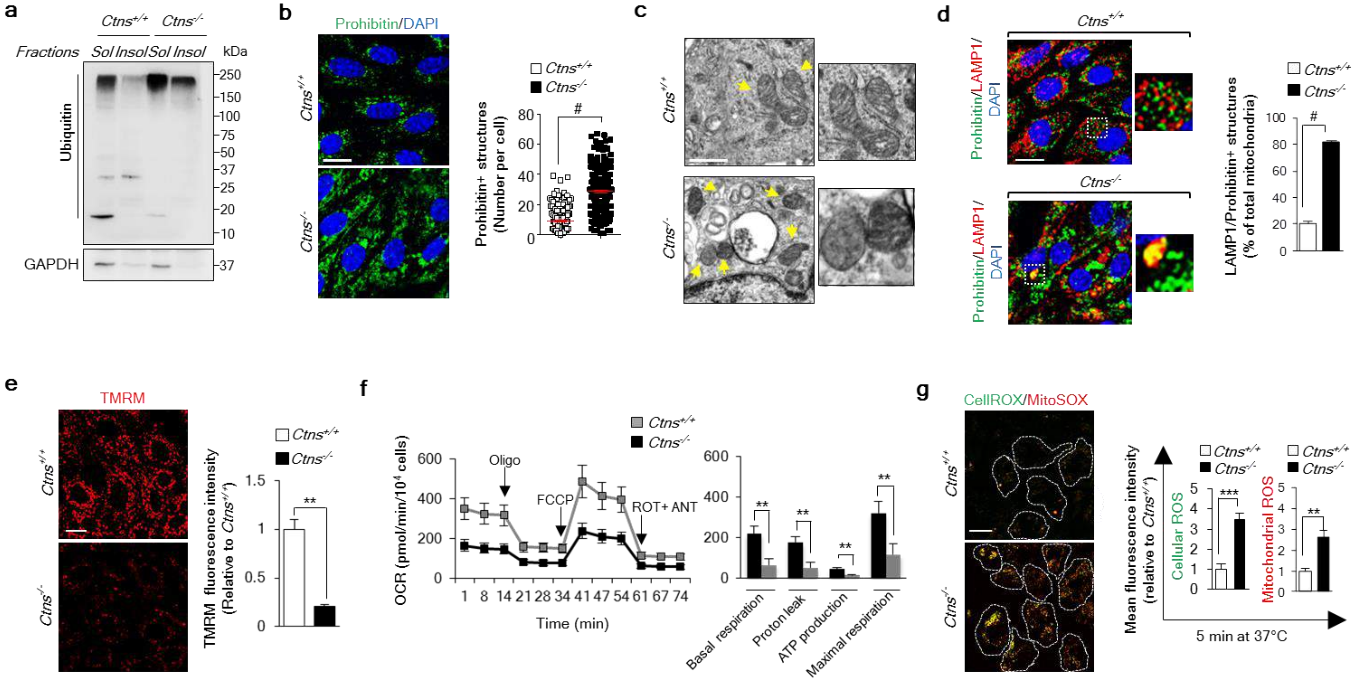

Figure 6. Accumulation of dysfunctional ROS-producing mitochondria in *Ctns*$^{-/-}$ cells. (**a**) Representative western blotting of the soluble and insoluble fractions derived from *Ctns* mPTCs were immunoblotted for ubiquitin and GAPDH. (n=3 independent experiments). (**b**) *Ctns* mPTCs were immunostained with an anti-prohibitin antibody (green) and analysed by confocal microscopy. Quantifications of the number of prohibitin structures (n=240-280 cells randomly selected cells pooled from three mouse kidneys per condition; each point representing the number of prohibitin^{+} structures in a cell). (**c**) Representative electron micrographs of mitochondria in *Ctns* mPTCs. Insets: mitochondria at higher magnification. (**d**) *Ctns* mPTCs were immunostained against prohibitin (green) and LAMP1 (red), and the numbers of LAMP1/prohibitin^{+} co-localizing structures were quantified by confocal microscopy (percentage of total lysosomes; *n*=5 randomly selected fields per condition, each containing ~20-25 cells). (**e**) *Ctns* mPTCs were loaded with tetramethylrhodamine methyl ester (TMRM; mitochondrial membrane potential fluorescent probe, 50nM for 30 min at 37°C) and analysed by live confocal microscopy. Quantifications of TMRM fluorescence intensity obtained from 5 randomly selected fields per condition, with each containing ~20-25 cell. (**f**) Oxygen consumption rate (OCR) and individual parameters for basal respiration, ATP production, proton leak and maximal respiration. Oxygen consumption rates (OCRs) was measured under basal level and after the sequential addition of oligomycin (Oligo, 1μM), FCCP (0.5μM) and Rotenone (ROT; 1.0μM) + antimycin A (ANT; 1.0μM), n=3 independent experiments. (**g**) *Ctns* mPTCs were loaded with CellROX (cellular ROS probe; 5 μM for 10 min at 37°C) and MitoSOX (mitochondrial ROS probe; 2.5 μM for 10 min at 37°C) and analysed by live confocal microscopy. Quantification of CellROX or MitoSOX fluorescence intensity was obtained from 5 randomly selected fields per condition, with each containing ~20-25 cells. Plotted data are mean±s.e.m. Two tailed paired Student's *t* test $^{**}P<0.01$, $^{***}P<0.001$ and $^{\#}p<0.0001$relative to *Ctns*$^{+/+}$ mPTCs. Nuclei are counterstained with DAPI (blue). Scale bars are 10μm in **b**, **d**, **e** and **g;** 1μm in **c**.

Figure 7

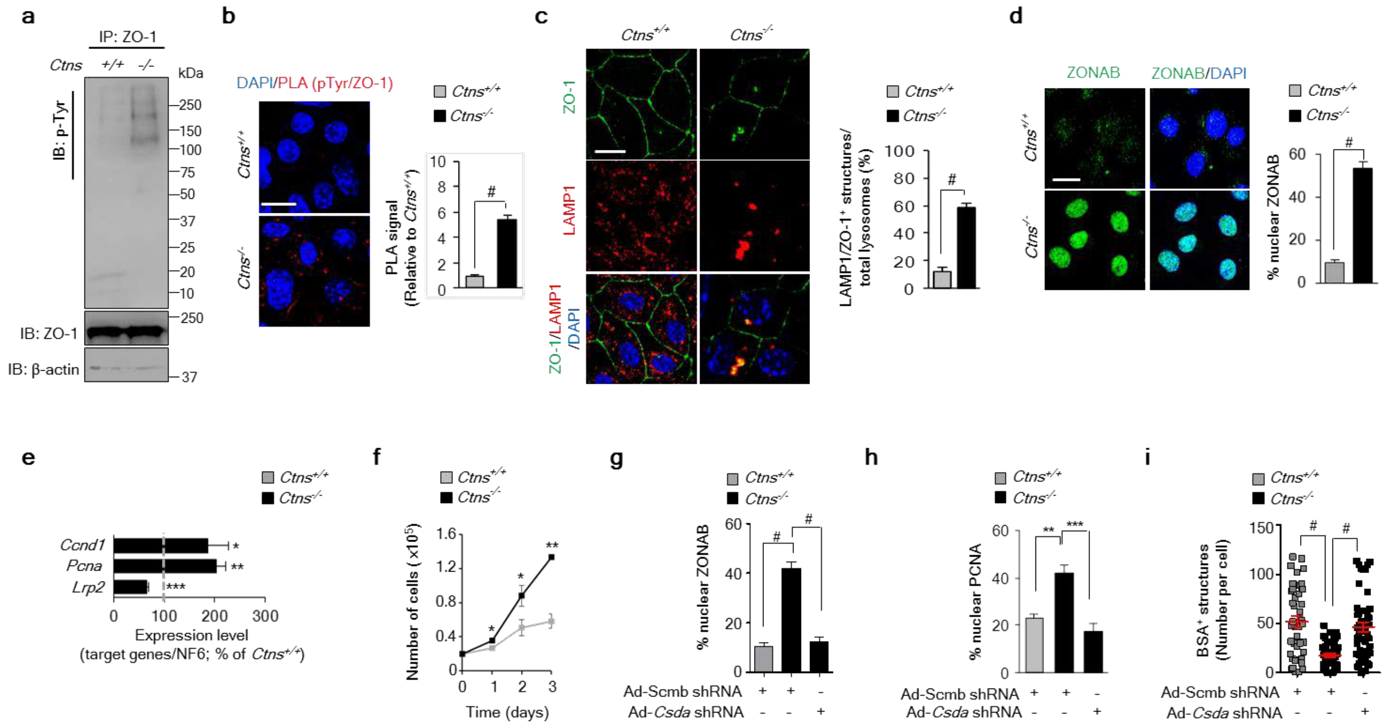

Figure 7. Augmented phosphorylation rate of ZO-1 promotes epithelial dysfunction in *Ctns*$^{-/-}$ cells. (**a**) Tight junction ZO-1 protein was immunoprecipitated (IP) from *Ctns*$^{+/+}$ and *Ctns*$^{-/-}$ mPTCs and its phosphorylation rate was examined by immunoblotting (n=2 independent experiments). (**b**) Representative confocal micrographs and quantifications of endogenous phosphorylation of ZO-1 by proximity ligation assay (PLA) using primary antibodies against ZO-1 and phopsho-Tyr (PY99). The quantifications were obtained from 5 randomly selected fields per condition, with each containing ~20-25 cells. Two tailed unpaired Student's *t* test, $^{\#}$*P*<0.0001 relative to *Ctns*$^{+/+}$ mPTCs. (**c**) Cells were immunostained for LAMP1 and ZO-1, and analysed by confocal microscopy. The adjacent panel shows the quantifications of the ZO-1/LAMP1 co-localizing structures (in percentage of the total lysosomes) assessed by confocal microscopy. The quantifications were obtained from 5 randomly selected fields per condition, with each containing ~20-25 cells. Two tailed unpaired Student's *t* test, $^{\#}$*P*<0.0001 relative to *Ctns*$^{+/+}$ mPTCs (**d**) *Ctns* mPTCs were immunostained with an anti-ZONAB antibody (green) and analysed by confocal microscopy. Quantification of ZONAB^{+} nuclei (in percentage of the total nuclei) obtained from 4 randomly selected fields per condition, with each containing ~20-25 cells. Two tailed unpaired Student's *t* test, $^{\#}$*P*<0.0001 relative to *Ctns*$^{+/+}$ mPTCs. (**e**) The mRNA levels of *Lrp2*, *Ccdn1 and Pcna* in *Ctns* microdissected proximal tubules were analysed by real-time PCR (n=3 mice per group). Two tailed unpaired Student's *t* test, **P*<0.05, ***P*<0.01 and ****P*<0.001 relative to *Ctns*$^{+/+}$microdissected proximal tubules. (**f**) Growth curves of *Ctns* mPTCs. Two tailed unpaired Student's *t* test, **P*<0.05 and ***P*<0.01 relative to *Ctns*$^{+/+}$ mPTCs, n=3 independent experiments. (**g-i**) *Ctns* mPTCs were transduced with Scmb or *Csda* adenoviral shRNAs for 5 days. (**g**) *Ctns* mPTCs were immunostained with an anti-ZONAB antibody (green) and analysed by confocal microscopy. Quantification of ZONAB^{+} nuclei (in percentage of the total nuclei) obtained from 4 randomly selected fields per condition, with each containing ~20-25 cells. One-way ANOVA followed by Bonferroni's *post hoc* test, $^{\#}$*P*<0.0001 relative to *Ctns*$^{+/+}$ mPTCs transduced with Ad-Scmb shRNA or to *Ctns*$^{-/-}$ mPTCs transduced with Ad-Scmb shRNA. (**h**) *Ctns* mPTCs were immunostained with an anti-PCNA antibody (red) and analysed by confocal microscopy. Quantification of PCNA^{+} nuclei (in percentage of the total nuclei) obtained from 4 randomly selected fields per condition, with each containing ~20-25 cells. One-way ANOVA followed by Bonferroni's *post hoc* test, ***P*<0.01 and ****P*<0.001 relative to *Ctns*$^{+/+}$ mPTCs transduced with Ad-Scmb shRNA or to *Ctns*$^{-/-}$ mPTCs transduced with Ad-Scmb shRNA. (**i**) The cells were loaded with Al647-BSA (50µg/mL for 15 min at 37°C) and imaged by confocal microscopy. Quantifications of the number of Al647-BSA (n=45-50 cells randomly selected field pooled from three mouse kidneys per condition; each point representing the number of BSA^{+} structures in a cell). One-way ANOVA followed by Bonferroni's *post hoc* test, $^{\#}$*P*<0.0001 relative to *Ctns*$^{+/+}$ mPTCs transduced with Ad-Scmb shRNA or to *Ctns*$^{-/-}$ mPTCs transduced with Ad-Scmb shRNA. Plotted data are mean±s.e.m. Nuclei counterstained with DAPI (blue). Scale bars, 10µM.

Figure 8

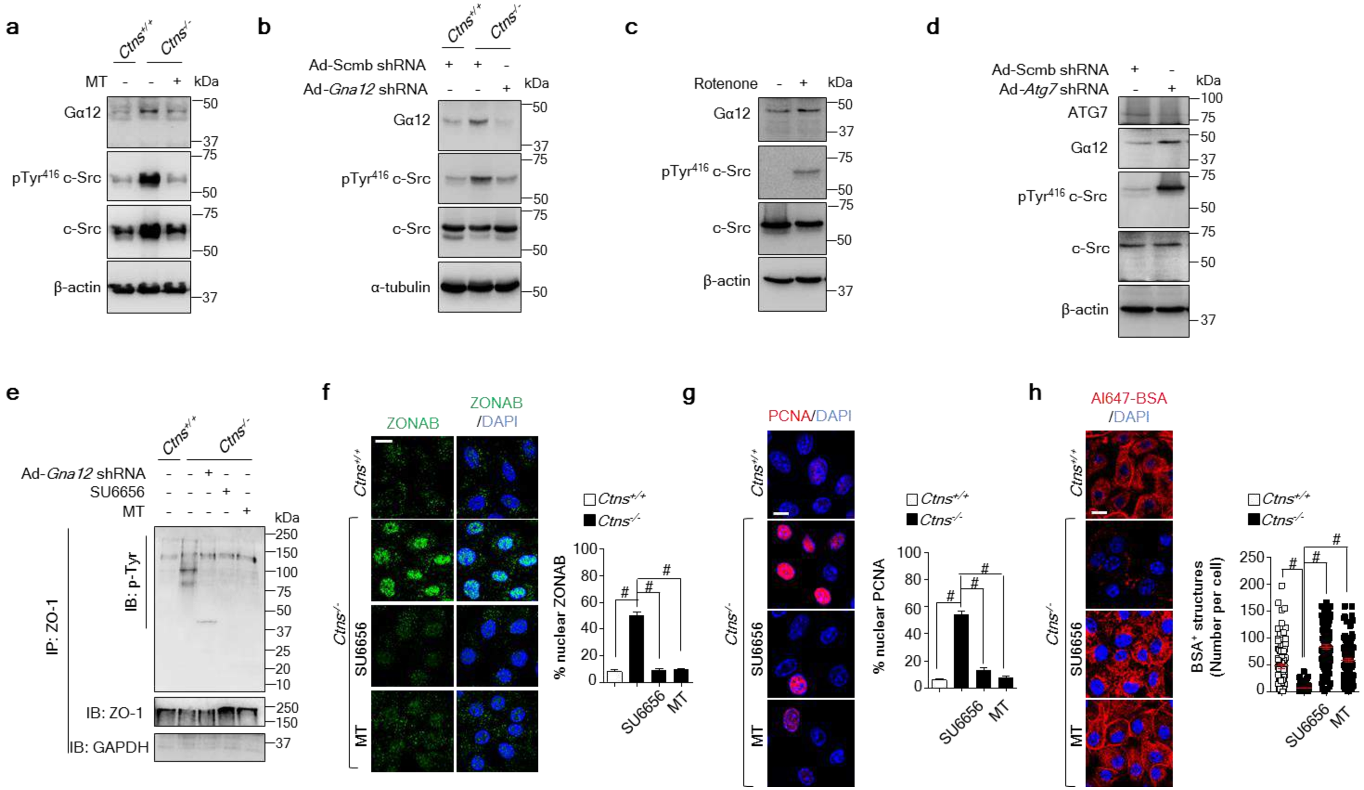

Figure 8. Mitochondrial ROS triggers Ga12/Src-mediated destabilization of ZO-1. (**a**) Representative western blotting of Gα12, pTyr^{416} c-Src and c-Src protein levels in *Ctns* mPTCs treated with or without the mitochondria-targeted antioxidant mito-TEMPO (MT, 10μM for 24h). β-actin was used as a loading control, n=3 independent experiments. (**b**) Representative western blotting of Gα12, pTyr^{416} c-Src and c-Src protein levels in *Ctns* mPTC transduced with either scrambled (Scmb) or *Gna12* adenoviral shRNAs for 5 days. α–tubulin was used as a loading control, n=2 independent experiments. (**c**) Representative western blotting of Gα12, pTyr^{416} c-Src and c-Src protein levels in mPTCs treated with Rotenone (250nM for 8h) or (**d**) transduced with Scmb or *Atg7* adenoviral shRNAs for 5 days. In **c** and **d,** β-actin was used as a loading control, n=3 independent experiments. (**e**) Tight junction ZO-1 protein was immunoprecipitated (IP) from *Ctns*$^{+/+}$ or *Ctns*$^{-/-}$ mPTCs and from *Ctns*$^{-/-}$ mPTCs transduced with Ad-*Gna12* shRNA or treated with either mitochondria-targeted antioxidant MitoTempo (MT, 10μM for 24h) or with a selective Src-kinase inhibitor SU6656 (5μM for 24h) and the phosphorylation rate was examined by immunoblotting. (**f-h**) *Ctns* mPTCs were treated with either mitochondria-targeted antioxidant MitoTempo (MT, 10μM for 24h) or a selective Src-kinase inhibitor SU6656 (5μM for 24h). (**f**) *Ctns* mPTCs were immunostained with an anti-ZONAB (green) antibody and imaged by confocal microscopy. Quantification of ZONAB^{+} nuclei (in percentage of the total nuclei) was obtained from 5 randomly selected fields per condition, with each containing ~20-25 cells. (**g**) *Ctns* mPTCs were immunostained with an anti-PCNA antibody and imaged by confocal microscopy. Quantifications of PCNA^{+} nuclei (in percentage of the total nuclei) obtained from 5 randomly selected fields per condition, with each containing ~20-25 cells. (**h**) The cells were loaded with Al647-BSA (50μg/mL for 15 min at 37°C) and imaged by confocal microscopy. Quantifications of the number of Al647-BSA (n=100 cells randomly selected cells pooled from three mouse kidneys per condition; each point representing the number of BSA^{+} structures in a cell). One-way ANOVA followed by Bonferroni's *post hoc* test, $^{\#}P<0.0001$ relative to *Ctns*$^{+/+}$ mPTCs or to untreated *Ctns*$^{-/-}$ mPTCs. Plotted data are mean±s.e.m. The nuclei are counterstained with DAPI (blue). The scale bars are 10μm.

Figure 9

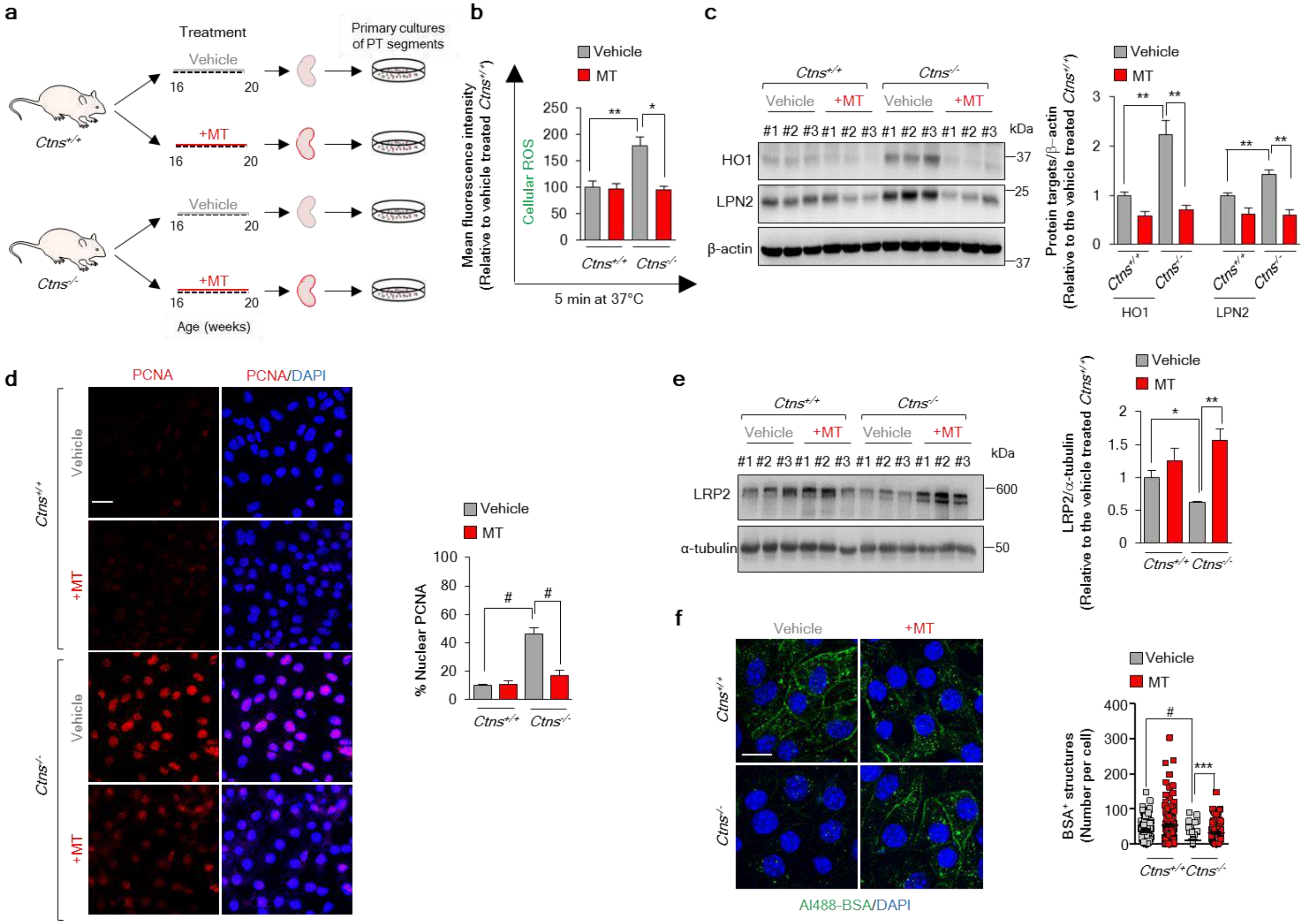

Figure 9. Mitochondrial ROS scavenging ameliorates PT cell dysfunction in *Ctns*$^{-/-}$ mice. (**a**) *Ctns* mice were treated for 30 days with daily intraperitoneal injections of either saline or MT (1mg/kg body weight, n=4 mice for group). Following treatment, mPTCs obtained from microdissected *Ctns* kidneys were analysed. (**b**) The mPTCs were loaded with CellROX (5 µM for 10 min at 37°C) and analysed by live confocal microscopy. Quantifications of fluorescence intensity were obtained from 5 randomly selected fields per condition, with each containing ~20-25 cells. (**c**) Western blotting and densitometric analyses of HO1 and lipocalin-2 (LPN2) protein levels. β−actin was used as a loading control. (**d**) The cells were immunostained for PCNA and imaged by confocal microscopy. Quantifications of PCNA^{+} nuclei (in percentage of the total nuclei) obtained from 5 randomly selected fields per condition, with each containing ~20-25 cells. (**e**) Western blotting and densitometric analyses of LRP2 protein levels. α−tubulin was used as loading control. (**f**) The cells were loaded with Al488- BSA (50µg/mL for 15 min at 37°C), fixed and analyzed by confocal microscopy. Quantification of the number of Al488-BSA (n=100 cells randomly selected cells pooled from three mouse kidneys per condition; each point representing the number of BSA^{+} structures in a cell). Nuclei counterstained with DAPI (blue) in **d** and **f**. All plotted data show mean±s.e.m. One-way ANOVA followed by Bonferroni's *post hoc* test, *P<0.05, **P<0.01, ***P<0.001 and $^{\#}P$<0.0001 relative to mPTCs from vehicle-treated *Ctns*$^{+/+}$ or *Ctns*$^{-/-}$ mice. Scale bars are 10µm.

Figure 10

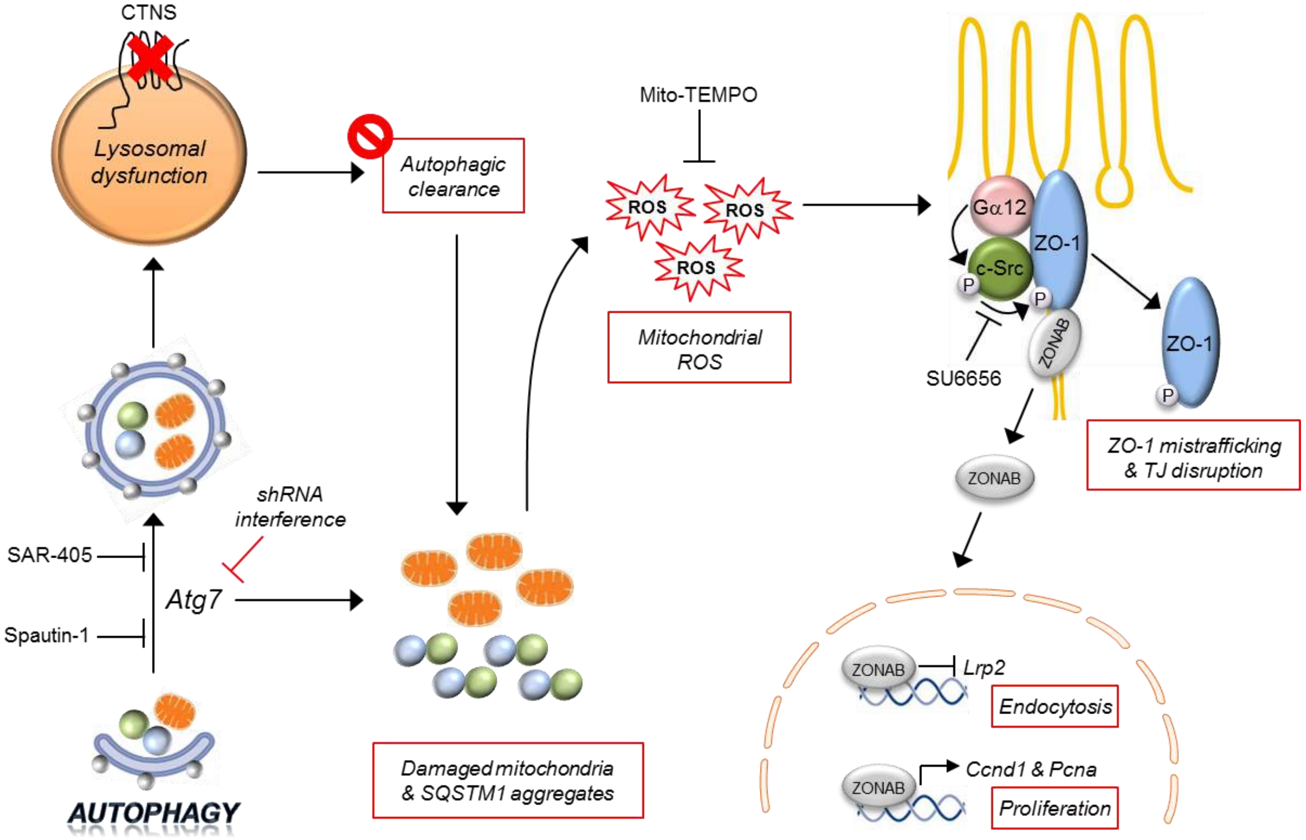

Figure 10. Model bridging lysosomal defect, impaired autophagy and epithelial dysfunction in cystinosis. The black arrows identify the sequence of events that occur in proximal tubule epithelial cells. The endolysosomal system sustains the reabsorptive activity of specialized epithelial cells. Cystinosis is a paradigm of lysosomal storage disease, in which the loss of the cystinosin (CTNS) transport system drives the accumulation of cystine in lysosomes. This accumulation induces lysosome dysfunction which in turn impairs the cellular clearance of autophagosomes containing SQSTM1$^+$ aggregates and/or damaged mitochondria. Similarly, pharmacological (with SAR-405 and Spautin-1 inhibitors) and genetically-induced failure of autophagy (targeting *Atg7*) increases the amount of SQSTM1$^+$ aggregates and/or damaged mitochondria, causing the accumulation of mitochondrial reactive oxygen species (mt-ROS). The increased mitochondrial oxidative stress enables the Gα12/Src-mediated phosphorylation of the tight junction adapter protein ZO-1, resulting in its misrouting to endolysosomal compartment. The disruption of tight junction integrity releases the ZO-1-associated Y-box factor ZONAB, which promotes cell proliferation and represses apical endocytic receptors such as LRP2, causing epithelial dysfunction in PT cells. Conversely, neutralization of excessive mitochondrial oxidative stress (mitochondria-targeted oxygen scavenger mito-TEMPO) or blockade of the Ga12/Src regulatory loop (e.g. treatment with a selective Src-kinase inhibitor Su6656) restores functional properties of epithelial *Ctns*$^{-/-}$ cell

Impaired Autophagy Bridges Lysosomal Storage Disease and Epithelial Dysfunction in the Kidney

Beatrice Paola Festa, Zhiyong Chen, Marine Berquez, Huguette Debaix, Natsuko Tokonami, Jenny Ann Prange, Glenn van de Hoek, Alessio Cremonesi, Andrea Raimondi, Nathalie Nevo, Rachel H. Giles, Olivier Devuyst* and Alessandro Luciani*

Supplementary Information

Suppl. Tables 1-2
Suppl. Figures 1-12

Suppl. Table 1: Mouse primer pairs for gene expression analysis.

Gene name	Forward primer (5'-3')	Reverse primer (5'-3')	PCR products (bps)	Efficiency
Gapdh	TGCACCACCAACTGCTTAGC	GGATGCAGGGATGATGTTCT	176	1.04 ± 0.03
Actb	TGCCCATCTATGAGGGCTAC	CCCGTTCAGTCAGGATCTTC	102	1.03 ± 0.04
Hprt1	ACATTGTGGCCCTCTGTGTG	TTATGTCCCCCGTTGACTGA	162	0.99 ± 0.01
Ppiase	CGTCTCCTTCGAGCTGTTTG	CCACCCTGGCACATGAATC	139	1.02 ± 0.02
18S	GTAACCCGTTGAACCCCATT	CCATCCAATCGGTAGTAGCG	151	0.98±0.02
36B4	CTTCATTGTGGGAGCAGACA	TTCTCCAGAGCTGGGTTGTT	150	1.02±0.02
Tjp1	CCACCTCTGTCCAGCTCTTC	TGGTGGTCTGAAAGTTGCTG	147	0.97±0.03
Lrp2	CAGTGGATTGGGTAGCAGGA	GCTTGGGGTCAACAACGATA	150	0.99±0.04
Pcna	TTGGAATCCCAGAACAGGAG	ATTGCCAAGCTCTCCACTTG	155	0.97±0.04
Ccnd1	AGCAGAAGTGCGAAGAGGAG	CAAGGGAATGGTCTCCTTCA	149	1.03±0.05
Atg7	AGCTTGGCTGCTACTTCTGC	CTGCAGGACAGAGACCATCA	149	0.99±0.03
Map1lc3a	CCTTCTTCCTGCTGGTCAAC	TGACTCAGAAGCCGAAGGTT	138	1.01±0.03
Map1lc3b	CCGAGAAGACCTTCAAGCAG	CCAGGAACTTGGTCTTGTCC	153	0.98±0.04
Becn1	AGGAGCTGGAAGATGTGGAA	ACTCCAGCTGCTGCCTTTTA	141	0.96±0.04
Slc34a1	CATCACAGAGCCCTTCACAA	TGGCCTCTACCCTGGACATA	161	1.02±0.03
Ybx-3/Csda	AGGACGCGGAGAAGAAAGTT	ACTTGCGTGGGTTGTTTTTC	153	0.98±0.04
Erbb2	TTTGTGGTCATCCAGAACGA	CAGGGTCTGGGGAGAAGAAT	151	0.97±0.03
Rab5	TGGGATACAGCTGGTCAAGA	AGGACTTGCTTGCCTTTGAA	153	0.98±0.03
Clcn5	TGGAGGAGCCAATCCCTGGTGT	AGAAAGCATCGCTCACACTG	156	1.01±0.03
Mki67	TGCAAAGGTAGAGGCTCCAT	CAGGTAGGCCAGAGCAAGT	152	1.00±0.02
Spp-1	TCCAATCGTCCCTACAGTCG	CGCTCTTCATGTGAGAGGTG	146	1.02±0.04

Suppl. Table 2: Zebrafish primer pairs for gene expression analysis.

Gene name	Forward primer (5'-3')	Reverse primer (5'-3')	PCR products (bps)	Efficiency
clcn7	GCAGAGTGTTCCTTTCCTCC	GACATCTACAATGGTTCCGAC	126	0.97 ± 0.04
ctns	TACCTTAGCAGCAATGACACTC	GCCACAAAGTAAATCCAGCCA	118	1.02 ± 0.03
actb1	TGAATCCCAAAGCCAACAGAG	TCACACCATCACCAGAGTCC	149	1.03 ± 0.04

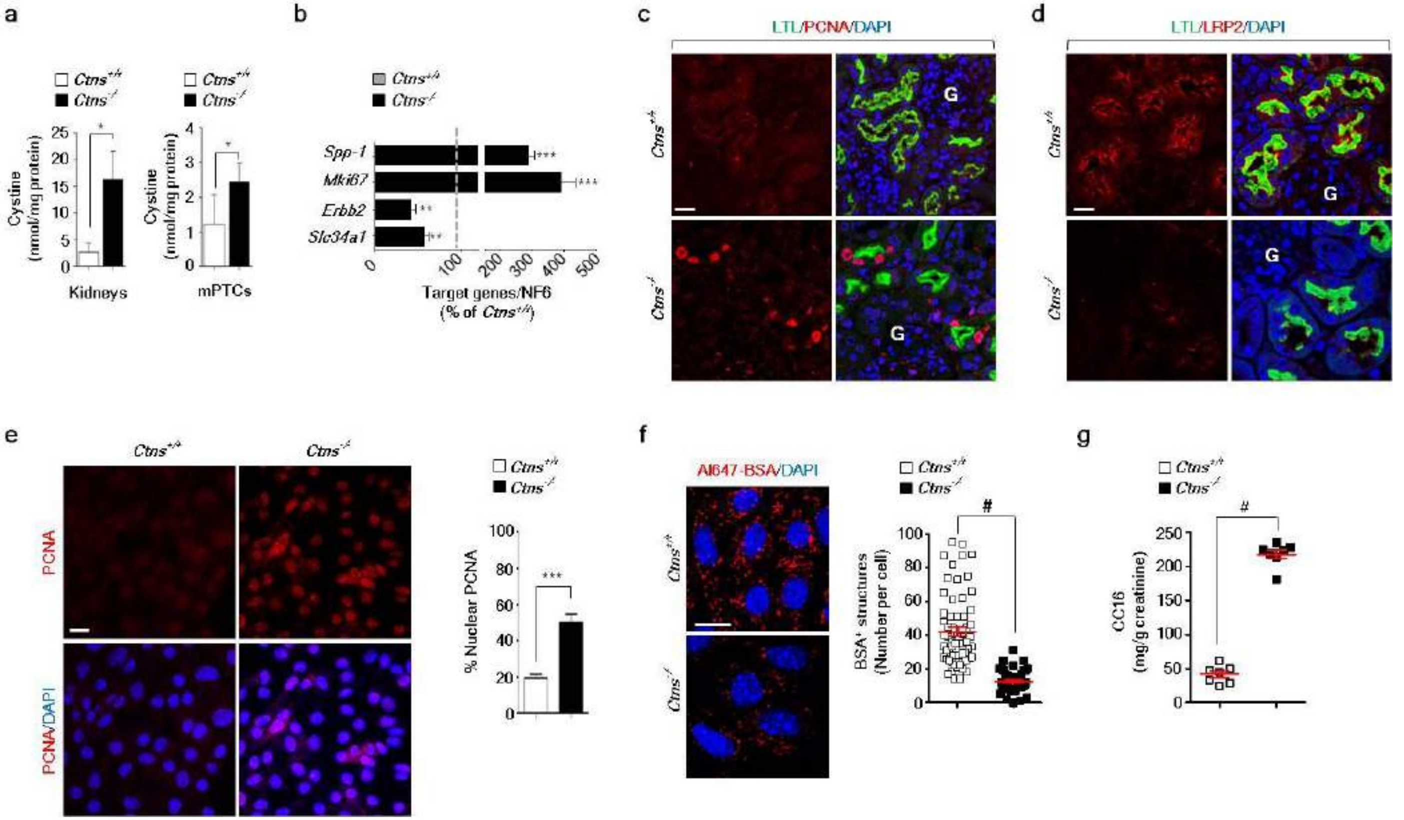

Suppl. Figure 1. Cystine storage, proliferation and dedifferentiation in *Ctns*$^{-/-}$ kidneys and derived PT cells. (a) Cystine levels in kidney cortex from 24-week-old *Ctns* mice (left panel) and in the derived primary mPTCs (right panel) were assessed by HPLC (n=5 per group). (**b**) The mRNA levels of *Slc34a1, Erbb2, Mki67*and *Spp-1* in *Ctns* kidneys were analysed by real-time PCR (n=4 kidneys per group). (**c**) *Ctns* kidneys were immunostained with anti-PCNA (red; left panel) or (**d**) anti-LRP2 (red; right panel) antibodies and stained with Lotus Tetragonolobus Lectin (LTL; proximal tubule marker, green). Scale bar, 50 µm. (**e**) *Ctns* mPTCs were immunostained for PCNA and analysed by confocal microscopy. Quantification of PCNA^{+} nuclei (in percentage of the total nuclei) obtained from 5 randomly selected fields per condition, with each containing ~20-25 cells. (**f**) *Ctns* mPTCs were loaded with Al647-BSA (50µg/mL for 15 min at 37°C) and analysed by confocal microscopy. Quantification of the number of Al647-BSA (n=45-65 cells randomly selected cells pooled from three mouse kidneys per condition; each point representing the number of BSA^{+} structures in a cell). (**g**) CC16 protein levels in urine from 24-week-old *Ctns* mice were measured by ELISA (n=7 mice per group). Plotted data are mean±s.e.m; two tailed unpaired Student's *t* test, $*p<0.05$; $**p<0.01$; $***p<0.001$; $^{\#}p<0.0001$ relative to *Ctns*$^{+/+}$ kidneys or mPTCs. Nuclei counterstained with DAPI (blue) in **c**, **d**, **e** and **f**. Unless otherwise stated, scale bars are 10µm.

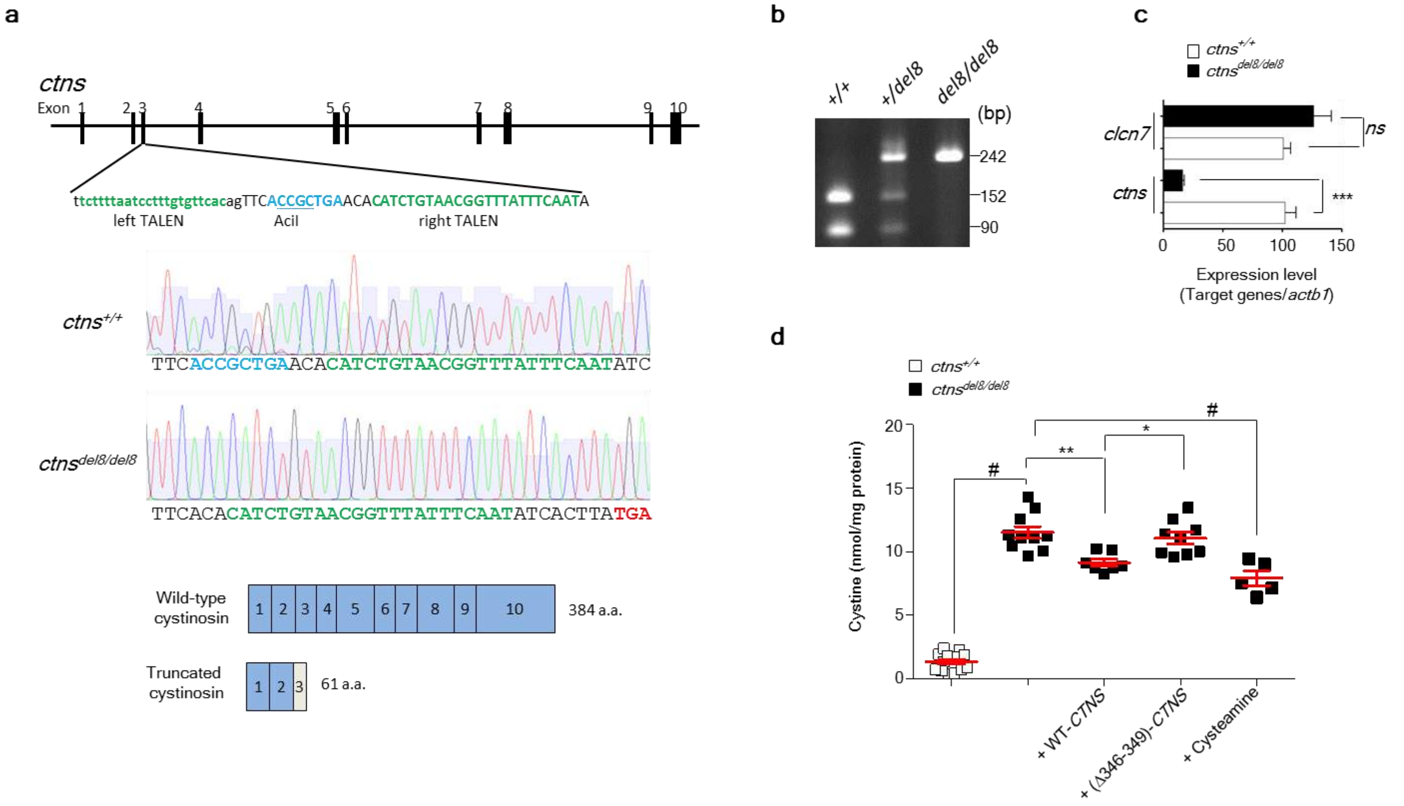

Suppl. Figure 2. Generation and validation of *ctns* knock-out zebrafish model. (**a**) TALEN targeting site (green) and TALEN-induced deletion (blue) generated a frameshift of the open reading frame, resulting in premature stop codon (TGA) within the exon 3 of *ctns* gene (middle panel) producing a truncated protein of 61 amino acids. The underlined sequence represents the AciI site, which is used for the detection of the TALEN-induced deletion. (**b**) AciI digestion of PCR products after the amplification of the TALEN targeting region using genomic DNA extracted from caudal of wild-type (+/+), heterozygous (+/del8) and homozygous (del8/del8) zebrafish. Wild type allele: two lower bands 152bp + 90bp correspond to PCR products cut by AciI, mutant allele: upper band 242bp, resistant to AciI digestion. (**c**) mRNA levels of *ctns* and *clcn7* were analysed by real-time PCR in zebrafish kidneys; n=7 *ctns*$^{+/+}$, n=8 *ctns*$^{del8/del8}$; two tailed unpaired Student's *t* test,****P*<0.001 relative to wild-type zebrafish. (**d**) The mRNA levels of *ctns* and *clcn7* were analysed by real-time PCR in zebrafish kidneys (+/+: n=7, del8/del8: n=8; mean±s.e.m; two tailed unpaired Student's *t* test, ****P*<0.001 relative to wild-type zebrafish). (**e**) Cystine levels were assessed by HPLC in ctns zebrafish injected with wild type or mutant (Δ346-349) human *CTNS* mRNA or incubated in the E3 medium in presence of 1mM cysteamine; n=14 *ctns*$^{+/+}$ zebrafish, n=10 *ctns*$^{del8/del8}$ zebrafish, n=6 *ctns*$^{del8/del8}$ zebrafish injected with wild-type *CTNS*, n=8 *ctns*$^{del8/del8}$ zebrafish injected with mutant *CTNS*, n=5 *ctns*$^{del8/del8}$ zebrafish treated with cysteamine. Each point represents the average cystine levels pooled from 20 zebrafish embryos. Plotted data represent mean±s.e.m. One-way ANOVA followed by Bonferroni post hoc test $^{\#}$P<0.0001 relative to *ctns*$^{+/+}$ or untreated *ctns*$^{del8/del8}$, **P<0.01 relative to *ctns*$^{del8/del8}$, *P<0.05 relative to *ctns*$^{del8/del8}$ zebrafish injected with wild-type *CTNS*.

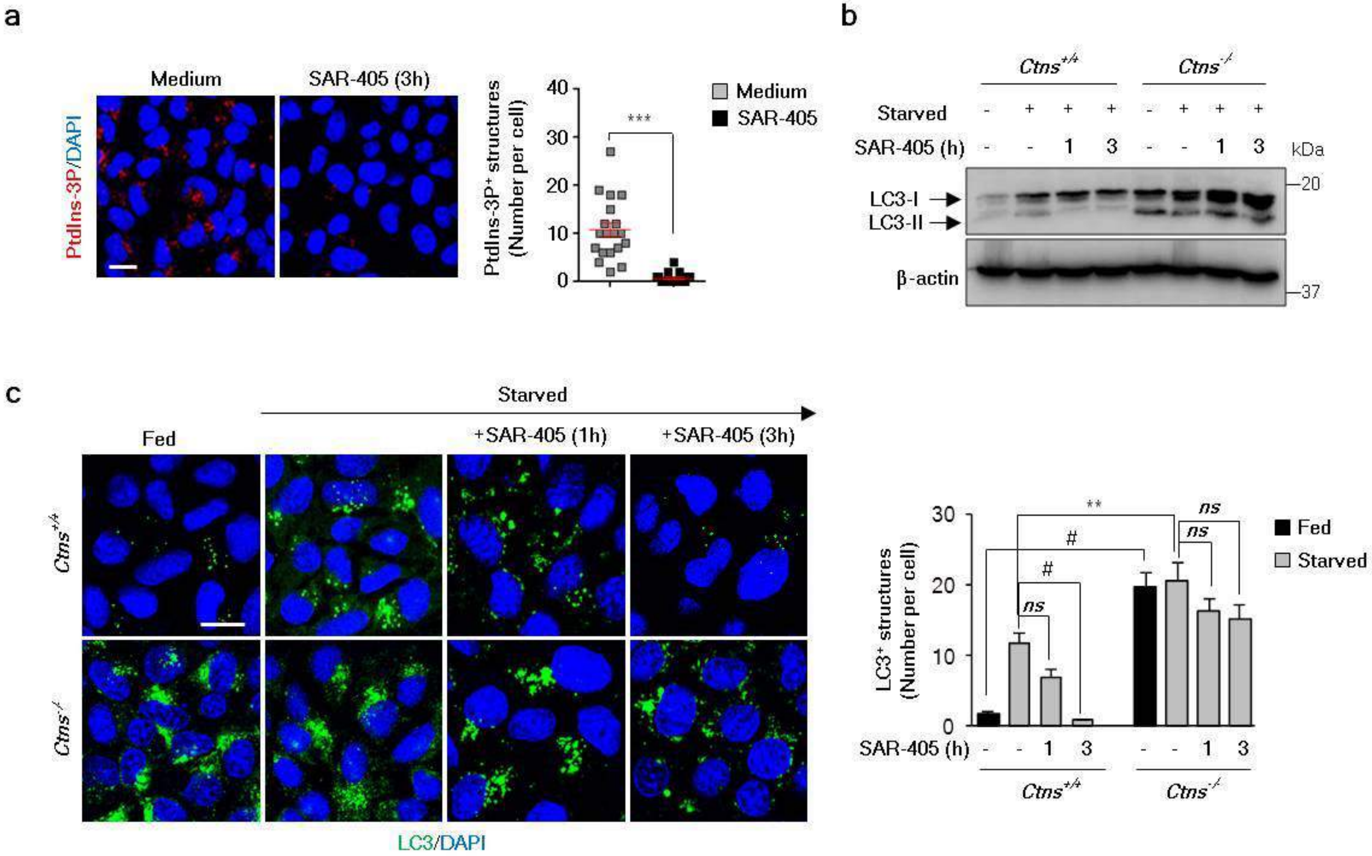

Suppl. Figure 3. Validation of the PIK3C3/Vps34 inhibitor SAR405 and its effect on autophagy in *Ctns* PT cells. (**a**) Primary mPTCs were exposed to SAR405 (5µM, for 3h), immunostained with anti-PtdIns-3P antibody (red) and analysed by confocal microscopy. The adjacent panel shows the quantification of the PtdIns-3P-positive structures per cell (n=20 cells pooled from three mouse kidneys per each condition; each point representing the number of PtdIns-3P$^+$ dots in a cell; mean±s.e.m; two tailed paired t-test, ***p< 0.001 relative to untreated cells). (**b-c**) mPTCs from *Ctns* kidneys were cultured in fed or in starved cell medium in presence of 5µM SAR-405 for the indicated times and subjected to western blotting and confocal microscopy analyses. (**b**) Representative western blotting of LC3 protein levels. β-actin was used as a loading control; n= 2 independent experiments. (**c**) The cells were immunostained for LC3 (green) and analysed by confocal microscopy. The adjacent panel shows the quantification of the LC3-positive structures per cell (*n*=33 cells from three *Ctns* kidneys per condition; mean±s.e.m; one-way ANOVA followed by Bonferroni's *post hoc* test, ***P*<0.01 relative to starved *Ctns*$^{+/+}$ mPTCs; $^{\#}$*P*<0.0001 relative to fed *Ctns*$^{+/+}$ mPTCs; $^{\#}$*P*<0.0001 relative to starved *Ctns*$^{+/+}$ mPTCs; *ns*, not-significant. Nuclei counterstained with DAPI (blue) in **a** and **c**. Scale bars are 20µM.

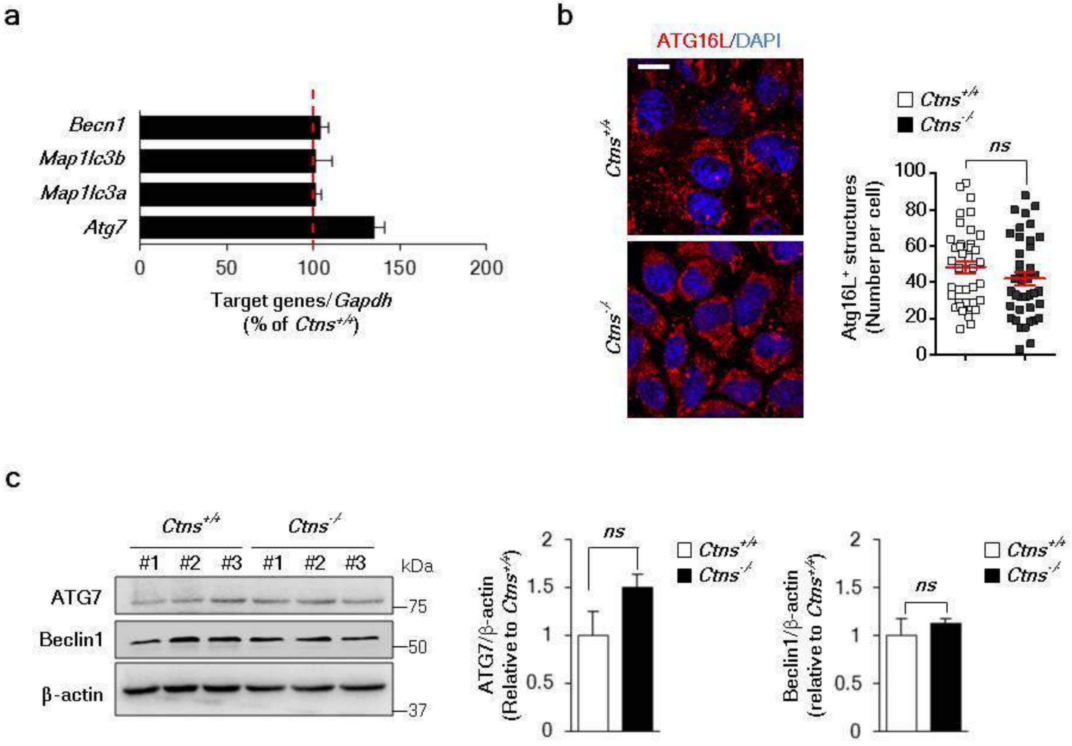

Suppl. Figure 4. Cystinosin deletion does not alter autophagosome biogenesis. (**a**) The mRNA levels of *Becn1*, *Map1lc3b*, *Map1lc3a* and *Atg7* in microdissected proximal tubules from 24-week-old *Ctns* mouse kidneys were analysed by real-time PCR (n=3 *Ctns* kidneys per group). (**b**) Cells were immunostained with anti-ATG16L antibody (red) and analysed by confocal microscopy. Nuclei counterstained with DAPI (blue). Scale bar, 10µm. The adjacent panel shows the quantification of the ATG16L positive structures per cell (n=40 cells pooled from three *Ctns* kidneys per condition); *ns*, not-significant. (**c**)Western blotting and densitometric analyses of the ATG7 and Beclin1 protein levels; n=3 independent experiments. β-actin was used as a loading control. The plotted data represent mean±s.e.m; *ns*, not-significant.

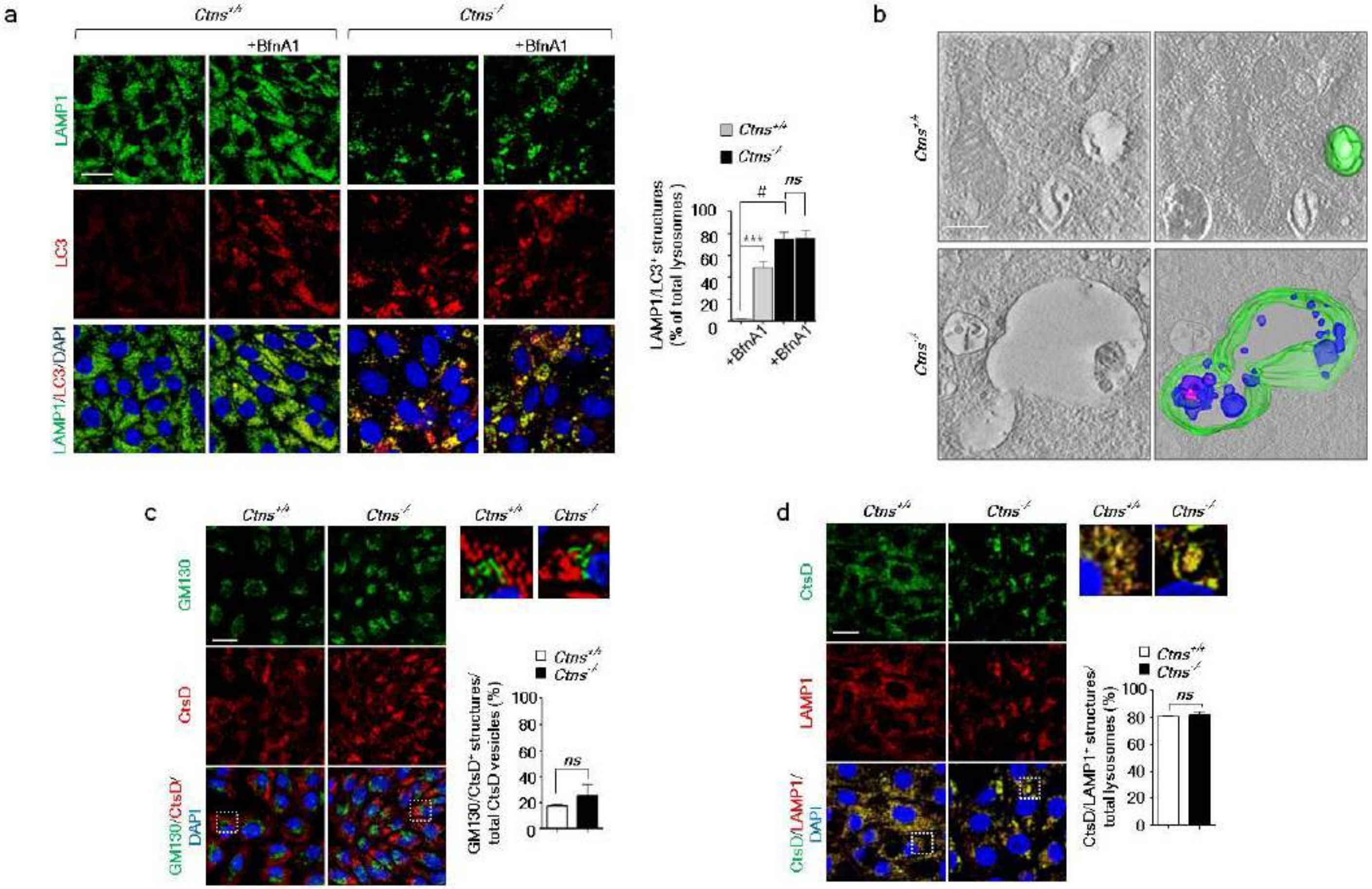

Suppl. Figure 5. Cystinosin deletion affects neither the autophagosome-lysosome fusion nor Golgi-to-lysosome trafficking of lysosomal cathepsins in PT cells. (**a**) Representative confocal micrographs and quantification of LC3/LAMP1 positive structures (in percentage of total lysosomes) in cells cultured with non-saturating concentrations of BfnA1 (50 nM for 1h). Quantification obtained on 5 randomly selected fields per condition, with each containing ~20-25 cells; one way ANOVA followed by Bonferroni *post hoc* test, ***$P<0.001$ or $^{\#}P<0.0001$ relative to untreated *Ctns*$^{+/+}$ mPTCs; *ns*, not-significant). (**b**) Representative electron tomography micrographs and 3-D reconstructed tomograms showing the presence of enlarged, single membranous structures (reminiscent of autolysosome; green) filled with undegraded cellular debris (blue and pink) in *Ctns*$^{-/-}$ mPTCs. (**c**) Cells were immunostained for GM130 (Golgi marker; green) and cathepsin-D (CtsD; red) or (**d**) for CtsD (green) and LAMP1 (late endosome/lysosome marker; red). Yellow indicates colocalization. Nuclei counterstained with DAPI (blue). The dotted white squares show images at higher magnification. Quantifications of the GM130/CtsD co-localizing structures (expressed as percentage of total CtsD$^+$ structures) and of CtsD/LAMP1 co-localizing structures (expressed as percentage of total LAMP1$^+$ structures). n=5 randomly selected fields per condition, with each containing ~20-25 cells. Plotted data are mean±s.e.m; *ns*, not-significant. Scale bars are 10µm in **a**, **c**, **d**, and 0.5 µm in **b**, and 50 µm in **e**.

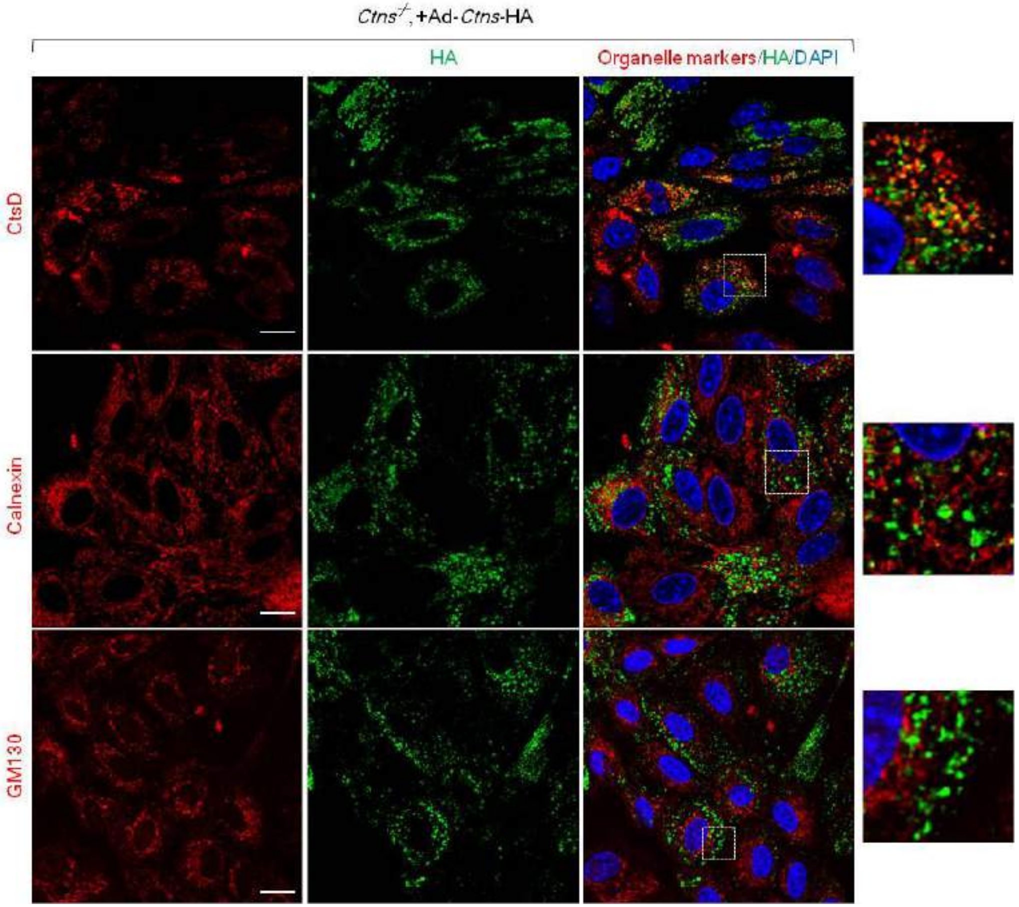

Suppl. Figure 6. Subcellular compartmentalization of rescued CTNS protein in *Ctns*$^{-/-}$ cells. mPTCs from *Ctns*$^{-/-}$ kidneys were transduced with hemagglutinin-tagged *Ctns* (HA-*Ctns*)-bearing adenoviral particles for 2 days. The cells were immunostained for HA (green) and CtsD (red; top panel) or for HA and Calnexin (red; middle panel) or for HA and GM130 (red; bottom panel) and analysed by confocal microscopy. Yellow indicates colocalization. Nuclei counterstained with DAPI (blue). The dotted white squares contain images at higher magnification. Scale bar, 10µm.

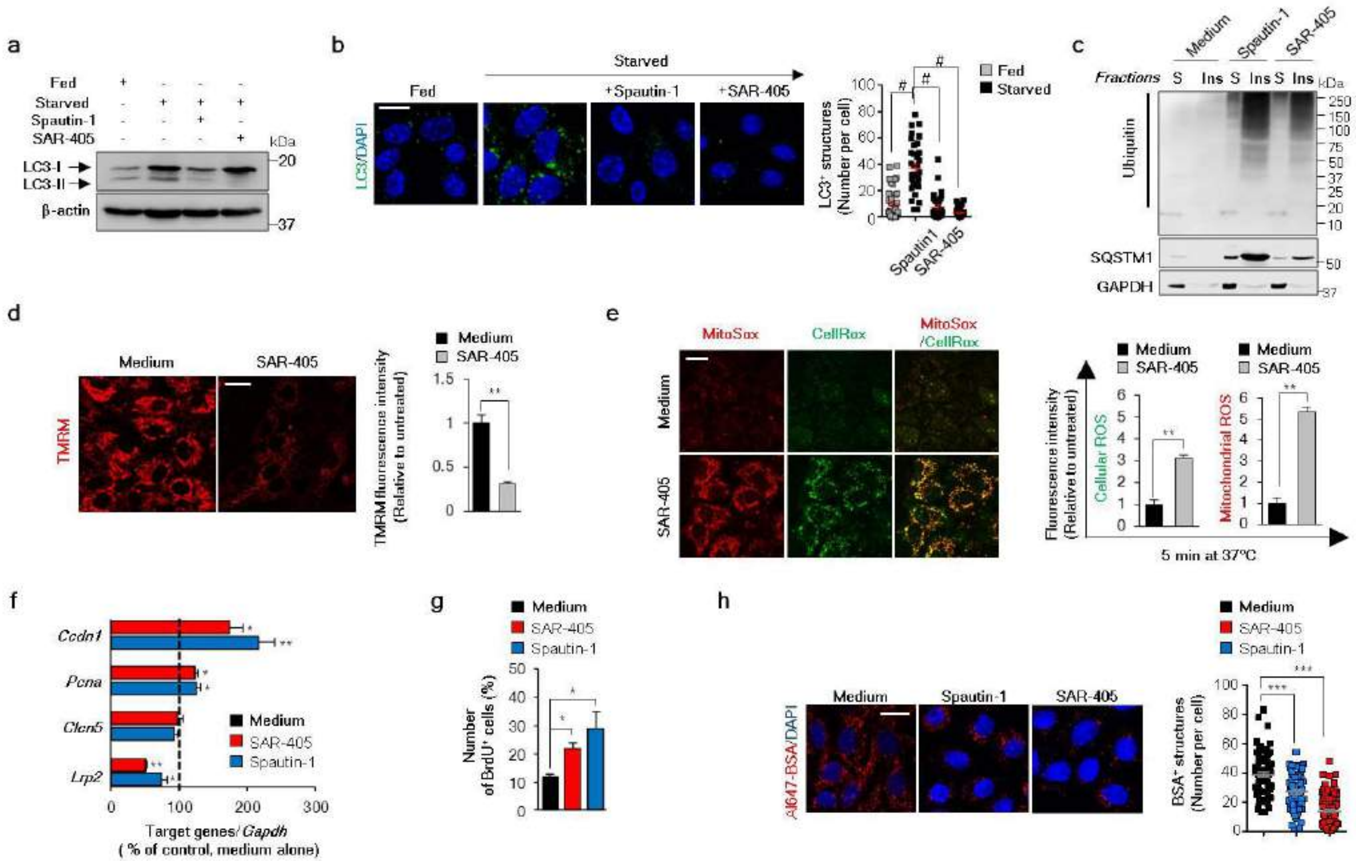

Suppl. Figure 7. Pharmacological blockage of autophagy causes mitochondria-derived oxidative stress, leading to proliferation and dedifferentiation of PT cells. (**a-b**) mPTCs were cultured in fed or starved medium (for 8h), or in starved medium in the presence of PIK3C3/Vps34 inhibitor SAR-405 (5µM, for 8h) or with autophagy inhibitor Spautin-1 (25µM, for 8h). (**a**) Representative western blotting of LC3 protein levels. β-actin was used as a loading control; n= 3 independent experiments. (**b**) Representative micrographs (left) and quantifications (right) of the LC3 structures in mPTCs by confocal microscopy (n=35 cells pooled from three mouse kidneys per condition; each point representing the number of LC3^{+} dots in a cell; one-way ANOVA followed by Bonferroni's *post hoc* test, $^{\#}P<0.0001$ relative to mPTCs under fed conditions or to starved mPTCs). (**c-h**) mPTCs were cultured in presence of either SAR-405 or Spautin-1. (**c**) Representative western blotting of soluble and insoluble fractions obtained from mPTCs and immunoblotted for ubiquitin, SQSTM1 and GAPDH; n= 2 independent experiments. (**d**) The cells were loaded with tetramethylrhodamine methyl ester and analysed by live confocal microscopy. Quantification of TMRM fluorescence intensity obtained from 5 randomly selected fields per condition, with each containing ~20-25 cells. Two tailed paired Student's *t* test, **P<0.01 relative to untreated mPTCs. (**e**) mPTCs were loaded with CellROX and Mito SOX analysed by live confocal microscopy. Quantifications of CellROX or MitoSOX fluorescence intensity obtained from three randomly selected fields per condition, with each containing ~20-25 cells). Two tailed paired Student's t test, **P<0.01 relative to untreated mPTCs. (**f**) The mRNA levels of *Lrp2, Ccdn1 Clcn5 and Pcna* were assessed by real-time PCR (n=4 independent experiments). (**g**) The cells were loaded with bromodeoxyuridine, immunostained with anti- BrdU antibody and analysed by confocal microscopy. Quantification of numbers of BrdU positive cells (in percentage of total nuclei) was obtained from 5 randomly selected fields per condition, with each containing ~20-25 cells. (**h**) The cells were loaded with Al647-BSA and imaged by confocal microscopy. Quantification of the number of Al647-BSA (n=68-105 cells randomly selected cells pooled from three mouse kidneys per condition; each point representing the number of BSA^{+} structures in a cell). All the plotted data represent mean±s.e.m. Plotted data represent mean±s.e.m. Unless otherwise stated, one-way variance (ANOVA) followed by Dunnett's *post hoc* test, *$P<0.05$, **$P<0.01$ and ***$P<0.001$ relative to untreated mPTCs. Nuclei are counterstained with DAPI (blue) in **b** and **h**. Scale bars are 10µm.

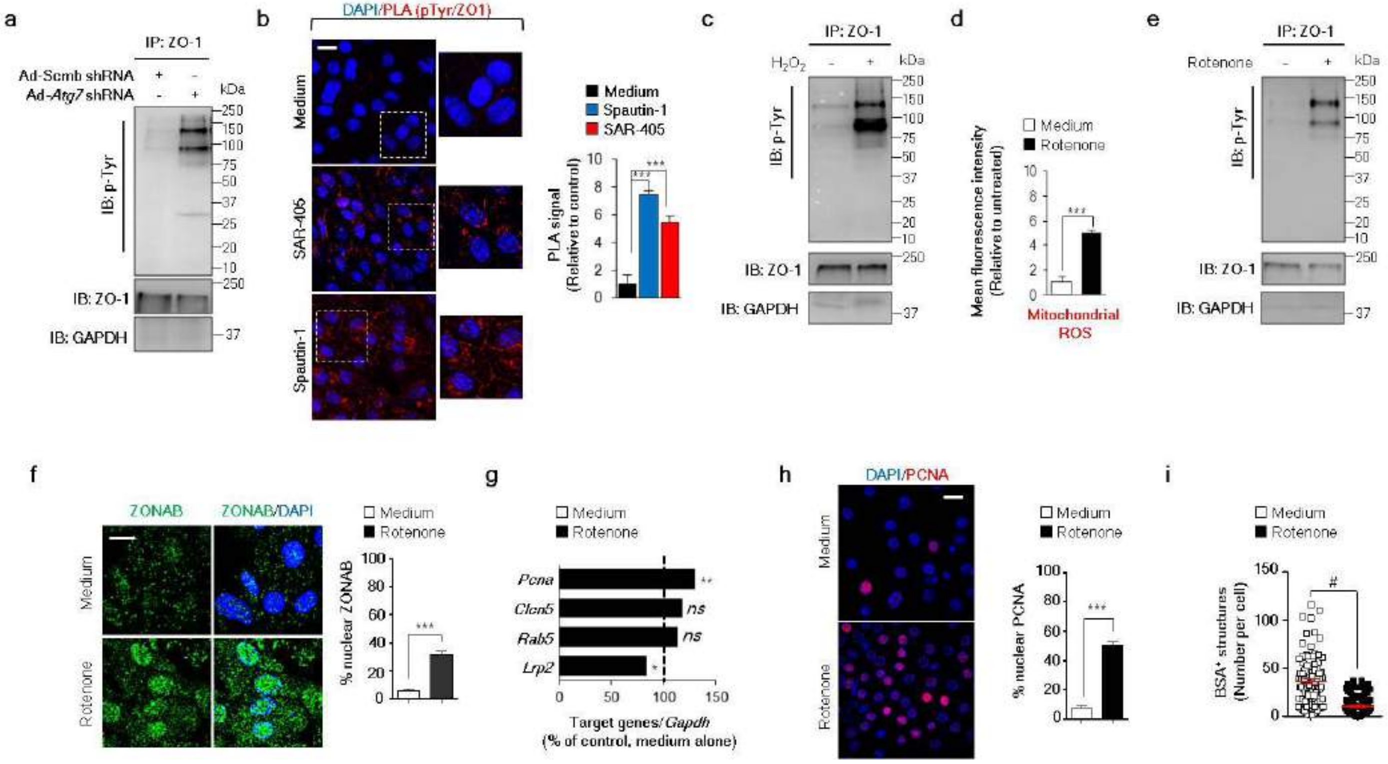

Suppl. Figure 8. Augmented phosphorylation rate of tight junction ZO1 proteins in cystinosis cells or in PT cells experiencing oxidative stress. The cells were transduced with scrambled (Scmb) or *Atg7* adenoviral shRNAs, or (b) cultured in presence of PIK3C3/Vps34 inhibitor SAR-405 (5µM, for 16h) or with the autophagy inhibitor Spautin-1 (25µM for 16h), or in presence (**c**) of hydrogen peroxide (0.5mM for 1h) or (d-e) with mitochondrial complex I inhibitor Rotenone (250 nM for 8h). (**a,c,e**) Tight junction ZO-1 protein was immunoprecipitated (IP) from mPTCs and its phosphorylation rate was examined by immunoblotting; n=2 independent experiments. (**b**) Representative confocal micrographs and quantifications of endogenous phosphorylation of ZO-1 by proximity ligation assay (PLA) using primary antibodies against ZO-1and phopsho-Tyr (PY99). One-way ANOVA followed by Dunnett's *post hoc* test, ***P<0.001 relative to untreated mPTCs. (**d**) The cells were loaded with MitoSOX (mitochondrial ROS probe; 2.5 µM for 5 min at 37°C) analysed by live confocal microscopy. Quantification of MitoSOX fluorescence intensity obtained from three randomly selected fields per condition, with each containing ~20-25 cells. Two tailed unpaired Student's t test, ***P<0.0001 relative to untreated mPTCs. (**f**) The cells were immunostained with an anti-ZONAB (green) antibody and analysed by confocal microscopy. The adjacent panel the quantification of numbers of ZONAB-positive cells (in percentage of total nuclei) was obtained from 5 randomly selected fields per condition, with each containing ~20-25 cells. Two tailed paired Student's *t* test, ***P<0.001 relative to untreated mPTCs. (**g**) The mRNA levels of *Clcn5*, *Rab5*, *Lrp2* and *Pcna* were analysed by real-time PCR (n=4 independent experiments). Two tailed unpaired Student's t test, *P<0.05, **P<0.01 relative to untreated mPTCs; ns, not significant. (**h**)The cells were immunostained with an anti-PCNA (red) antibody and imaged by confocal microscopy. Quantifications of PCNA+ nuclei (in percentage of the total nuclei) obtained from 5 randomly selected fields per condition, with each containing ~20-25 cells. Two tailed unpaired Student's t test, ***P<0.0001 relative to untreated mPTCs. (**i**) The cells were loaded with Al647-BSA (50µg/mL for 15 min at 37°C) and imaged by confocal microscopy. Quantifications of the number of Al647-BSA (n=100 cells randomly selected cells pooled from three mouse kidneys per condition; each point representing the number of BSA+ structures in a cell). Two tailed paired Student's t test, $^{\#}$P<0.0001. Plotted data represent mean±s.e.m. Nuclei are counterstained with DAPI (blue). Scale bars are 10µm.

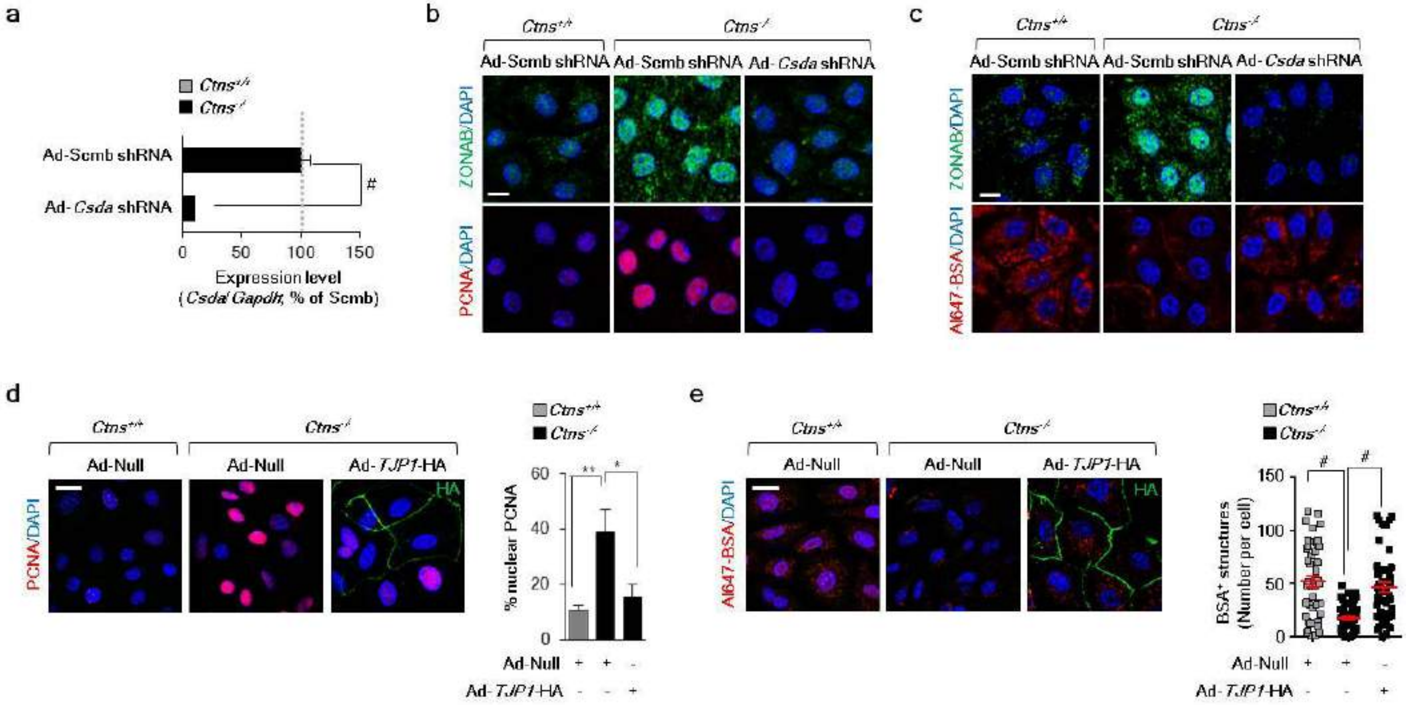

Suppl. Figure 9. Knockdown of *Csda* and the exogenous overexpression of *TJP1* in cystinosis PT cells rescue the epithelial functions. (a,b,c) *Ctns* cells were transduced with Scmb or *Csda* adenoviral shRNAs for 5 days. (**a**) The mRNA levels of *Csda* were analysed by real-time PCR (n=4 independent experiments). (**b**) Representative micrographs of *Ctns* cells stained with an anti-ZONAB (green) and anti-PCNA (red) antibodies or (**c**) loaded with Al647-BSA (red) and stained afterwards with anti-ZONAB (green) antibody. (**d-e**) *Ctns* cells were transduced with a Null or human HA-(*TJP1*)-bearing adenoviral particles for 2 days. (**d**) The cells were immunostained with an anti-PCNA (red) and anti-HA (green) antibodies and imaged by confocal microscopy. Quantifications of PCNA^{+} nuclei (in percentage of the total nuclei) obtained from 5 randomly selected fields per condition, with each containing ~20-25 cells. (**e**) The cells were loaded with Al647-BSA (red; 50µg/mL for 15 min at 37°C), stained with an anti-HA antibody (green) and imaged by confocal microscopy. Quantifications of the number of Al647-BSA (n=50 cells randomly selected cells pooled from three mouse kidneys per condition; each point representing the number of BSA^{+} structures in a cell). Plotted data show mean±s.e.m. One-way ANOVA followed by Bonferroni *post hoc* test, **P*<0.05, ***P*<0.01 and $^{\#}P<0.0001$ relative to *Ctns*$^{-/-}$ transduced with Scmb shRNAs or *Ctns*$^{+/+}$ transduced with Ad-Null or *Ctns*$^{-/-}$ transduced with Ad-Null. Nuclei are counterstained with DAPI (blue). Scale bars are 10µm.

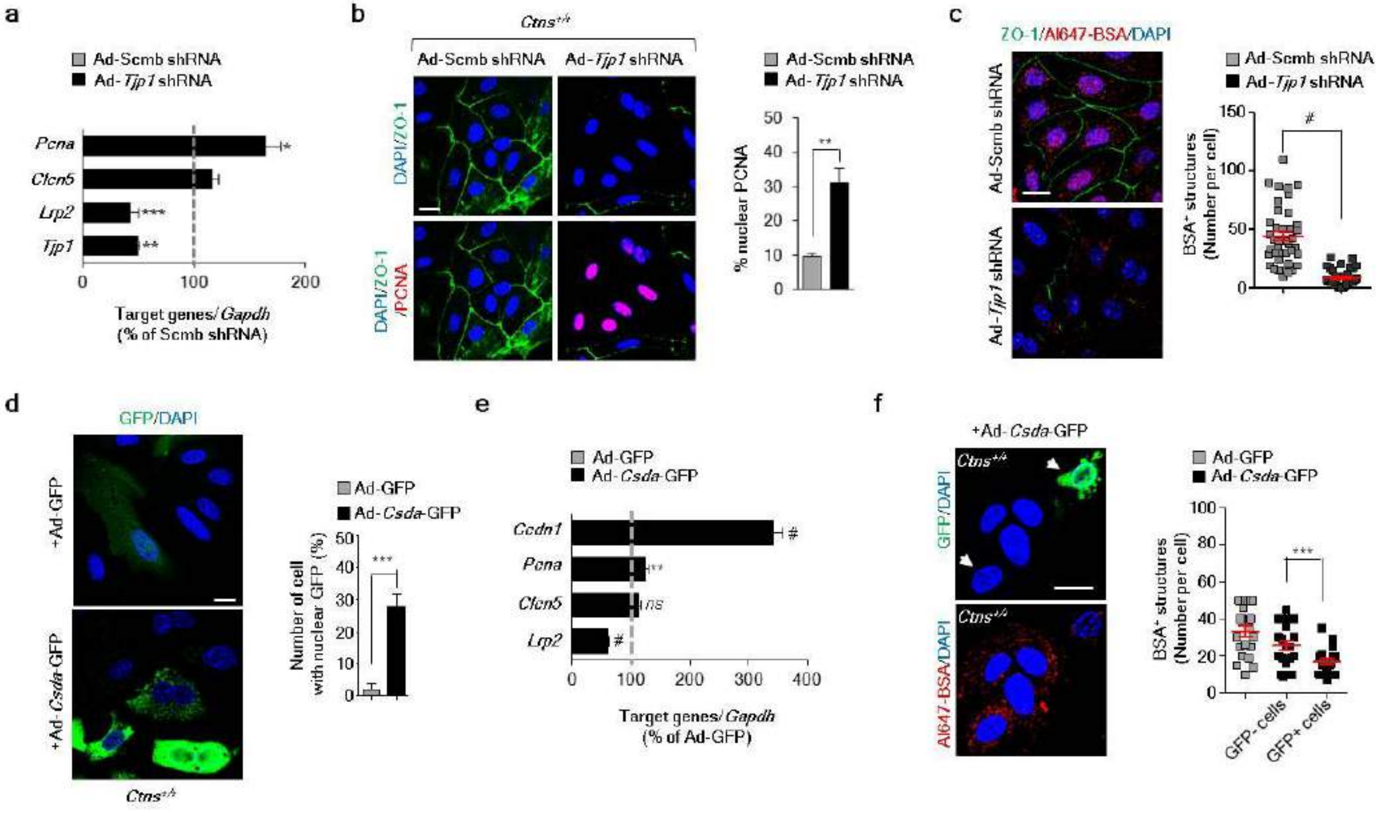

Suppl. Figure 10. Knockdown of *Tjp1* and the exogenous overexpression of *Csda* in PT cells promote epithelial dysfunctions. (**a,b,c**) mPTCs were transduced with Scmb or *Tjp1* adenoviral shRNAs for 5 days. (**a**) The mRNA levels of *Pcna, Clcn5, Lrp2 and Tjp1* were analysed by real-time PCR (n=4 independent experiments). (**b**) The cells were immunostained with an anti-ZO-1(green) and PCNA (red) antibodies and imaged by confocal microscopy. Quantification of PCNA$^+$ nuclei (in percentage of the total nuclei) obtained from 5 randomly selected fields per condition, with each containing ~20-25 cells. (**c**) The cells were loaded with Al647-BSA (red; 50µg/mL for 15 min at 37°C), stained with an anti-ZO-1 (green) antibody and imaged by confocal microscopy. Quantification of the number of Al647-BSA$^+$ structures (n=50 randomly selected cells pooled from three mouse kidneys per condition; each point representing the number of BSA$^+$ structures in a cell). (**d-f**) mPTCs were transduced with Ad-GFP or GFP-tagged-(*Csda*)-bearing adenoviral particles for 2 days. (**d**) The cells were stained with an anti-GFP antibody and imaged by confocal microscopy. Quantification of the number with nuclear GFP (in percentage of the total nuclei; n=20 randomly selected cells per condition). (**e**) The mRNA levels of *Ccdn1, Pcna, Clcn5, Lrp2* were analysed by real-time PCR (n=4 independent experiments). (**f**) The cells were loaded with Al647-BSA (red; 50µg/mL for 15 min at 37°C), stained with an anti-GFP antibody and imaged by confocal microscopy. Quantification of the number of Al647-BSA$^+$ positive structures (n=20 randomly selected cells pooled from three mouse kidneys per condition; each point representing the number of BSA$^+$ structures in cell). Plotted data show mean±s.e.m. Two tailed paired Student's *t* test, *P<0.05, **P<0.01, ***P<0.001, and $^{\#}P$<0.0001 relative to *Ctns*$^{+/+}$ mPTCs transduced with Scmb shRNAs or with Ad-GFP vector; *ns*, not significant. Nuclei are counterstained with DAPI (blue). Scale bars are 10µm.

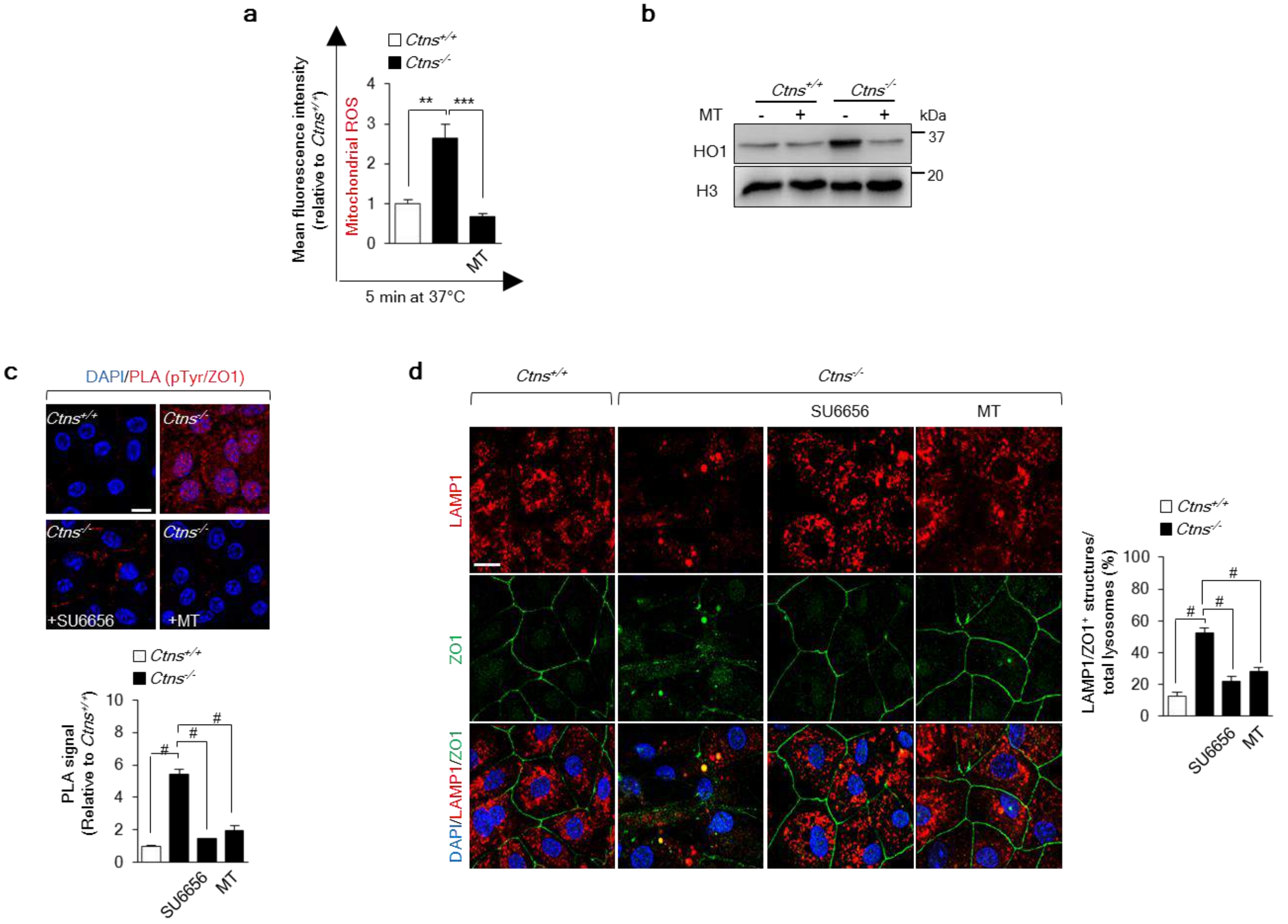

Suppl. Figure 11. Inhibition of mitochondrial ROS restores epithelial functions in cystinosis PT cells. (**a-b**) mPTCs from *Ctns* kidneys were treated with or without the mitochondria-targeted antioxidant Mito-TEMPO (MT, 10µM for 24h). (**a**) The cells were loaded with MitoSOX (2.5µM for 5 min at 37°C) and analysed by live confocal microscopy. Quantification of fluorescence intensity from 5 randomly selected fields per condition, with each containing ~20-25 cells; one-way ANOVA followed by Bonferroni *post hoc* test, ***P*<0.01 relative to *Ctns*$^{+/+}$ mPTCs; ****P*<0.001 relative to untreated-*Ctns*$^{-/-}$ mPTCs. (**b**) Representative western blotting of HO1 protein levels. H3was used as a loading control. (n=2 independent experiments). (**c- d**) *Ctns* cells were treated with MT (10µM for 24h) or with a selective Src kinase inhibitor SU6656 (5µM for 24h). (**c**) Representative confocal micrographs and quantifications of endogenous phosphorylation of ZO-1 by proximity ligation assay (PLA) using primary antibodies against ZO-1 and phopsho-Tyr (PY99). (**d**) Cells were immunostained with an anti-LAMP1 (red) and ZO-1 (green) antibodies, and analysed by confocal microscopy. The adjacent panel shows the quantification of the ZO-1/LAMP1 co-localizing structures (in percentage of the total lysosomes) assessed by confocal microscopy. The quantifications were obtained from three randomly selected fields per condition, with each containing ~20-25 cells. Plotted data represent mean±s.e.m. In **c** and **d,** one way-variance ANOVA, $^{\#}$*P*<0.0001 relative to untreated *Ctns*$^{+/+}$ or *Ctns*$^{-/-}$ mPTCs. Yellow indicates the colocalization in **d**. Nuclei are counterstained with DAPI (blue). Scale bars are 10µm.

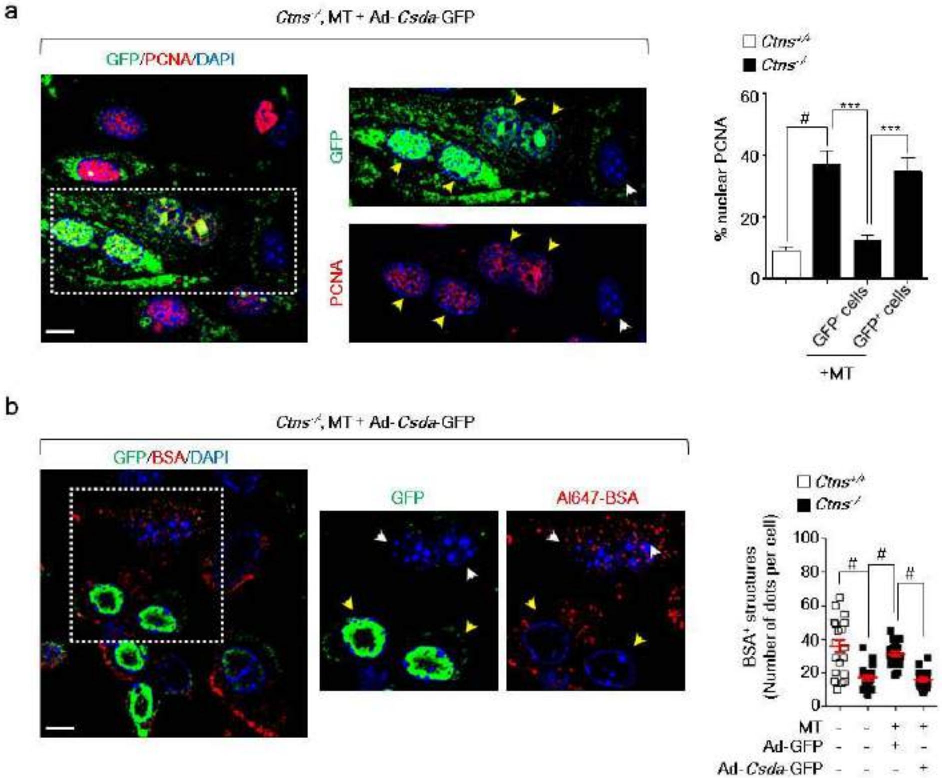

Suppl. Figure 12. *Csda* overexpression abolishes the effects of Mito-TEMPO on the epithelial functions in cystinosis PT cells. (**a-b**) Mito-TEMPO-treated mPTCs were transduced with Ad-GFP or GFP-tagged-(Csda)-bearing adenoviral particles for 2 days. (**a**) The cells were immunostained with an anti- PCNA (red) antibody and imaged by confocal microscopy. Quantification of $PCNA^{+}$ nuclei (in percentage of the total nuclei) obtained from 15 cells negative or positive for nuclear GFP enrichment. One-way ANOVA followed by Bonferroni *post hoc* test, $^{\#}P<0.0001$ relative to $Ctns^{+/+}$ or ***$P<0.0001$ relative to $Ctns^{-/-}$ mPTCs or relative to GFP^{-}/$Ctns^{-/-}$mPTCs treated with MT. (**b**) The cells were loaded with Al647-BSA (red; 50µg/mL for 15 min at 37°C), stained with an anti-GFP (green) antibody and analysed by confocal microscopy. Quantification of the number of Al647-BSA+ positive structures (n=20 cells negative or positive for nuclear GFP enrichment; each point representing the number of BSA+ structures in cell). Plotted data show mean±s.e.m. #$P<0.001$ relative to $Ctns^{+/+}$ or *Ctns*-/- mPTCs or relative to GFP-/$Ctns^{-/-}$ mPTCs treated with MT. Nuclei counterstained with DAPI (blue). Scale bars are 10µm

Aberrant mTORC1 Activation Underlies Proximal Tubule Dysfunction Associated with Lysosomal Storage in Cystinosis

Beatrice Paola Festa[1], Patrick Krohn[1], Marine Berquez[1], Alessio Cremonesi[2], Huguette Debaix[1]
Alessandro Luciani[1] and Olivier Devuyst[1,]

[1]Institute of Physiology, University of Zurich, Zurich, Switzerland; [2]Division of Clinical Chemistry and Biochemistry, University Children's Hospital Zurich, Zurich, Switzerland.

Manuscript in preparation

ABSTRACT

The reabsorptive function of kidney PT cells relies on the endolysosomal system. Mutations in the *CTNS* gene encoding the lysosomal cystine transporter cystinosin (Nephropathic Cystinosis), disrupts cystine homeostasis in the lysosomal lumen and causes a generalized dysfunction of PT cells resulting in Renal Fanconi Syndrome. In our previous work, we deciphered the pathogenic cascade bridging lysosomal defects and the loss of epithelial transport in cystinosis. However, how the primary loss of cystinosin function disrupts the identity of the lysosomal network was not investigated, preventing the development of causal treatments.

Here we demonstrate, by combining genetic and pharmacological approaches *in vivo* and *in vitro*, that cystine accumulation in cystinosis triggers the hyper-activation of mTORC1, which in turn, drives the progression of the lysosomal disease leading to autophagy defects and consequent PT dysfunction. Alterations of mTORC1 were detected in *Ctns*$^{-/-}$ mouse and rat models, demonstrating the evolutionary conservation of this disease-mechanism. Finally, *in vitro* treatment with specific and powerful mTORC1 inhibitors rescued the primary lysosomal defect and consequently restored the downstream pathogenic cascade associated to it, thus improving the PT function.

Altogether, these studies unveiled a novel link between defective mTORC1 activity, lysosome-autophagy degradation pathways and epithelial dysfunction in cystinosis, thus providing new therapeutic perspectives for this and similar lysosomal storage disorders.

INTRODUCTION

The reabsorptive properties of the kidney PT rely on the endolysosomal system, a dynamic network that receives and degrades macromolecules from the endocytic and autophagy pathways with the capacity to promote the recycling of cellular nutrients and to safeguard the cellular homeostasis. By reabsorbing a large amount of filtered ions and solutes from the urine, PT cells play a pivotal role in maintaining body homeostasis. Alterations in the transport activity lead to disrupted PT function (renal Fanconi syndrome, RFS), characterized by the loss of solutes and LMW proteins in the urines and often leading to CKD (1). PT dysfunctions are usually observed in congenital disorders caused by defective endolysosomal proteins, such as nephropathic cystinosis. Cystinosis (OMIM #219800) is caused by autosomal recessive mutations in the *CTNS* gene, which encodes cystinosin (CTNS), a lysosomal cystine-proton symporter exporting cystine into the cytosol. Loss of cystinosin results in the lysosomal accumulation of cystine crystals leading to progressive dysfunction of multiple organs including the kidney. Children with nephropathic cystinosis, the most severe and frequent form of cystinosis, develop PT dysfunction and RFS before 1 year of age, often followed by CKD (2).

We have recently demonstrated that a *Ctns* knock-out mouse model shows an accumulation of cystine within kidney proximal tubule (PT) epithelial cells, which is accompanied by endolysosomal aberrations impairing autophagy flux and disrupting mitochondria homeostasis causing an excessive production of oxidative stress. The latter affect the integrity of the TJs, by phosphorylation of ZO-1, which, in turn, promotes the release of ZO-1-associated nucleic acid binding protein (ZONAB), a Y-box transcription factor known to cause proliferation and apical dedifferentiation in PT cells (3). This work highlights the central role of the lysosomal-autophagy network in maintaining cellular homeostasis in PT cells and deciphers the mechanism bridging lysosome dysfunction with the loss of PT transport activity in cystinosis. However, how the loss of cystinosin impairs the lysosomal identity remains unclear.

Cystinosin has recently been shown to interact with components of the lysosomal V-ATPase controlling mTORC1 signaling (4). mTORC1 is a master regulator of cell growth and metabolism, which regulates the functional activity of lysosomes and related autophagy pathway by controlling the activity and subcellular localization of the helix-loop-helix (HLH) transcription factor TFEB. In various models of lysosomal storage disease, including immortalized cells from cystinotic patients, the overexpression of TFEB activates the lysosomal-autophagy pathway and promotes the clearance of accumulated substrates (5-7).The activity of mTORC1 activity is modulated by lysosomal levels of amino acids. Under amino acid-rich conditions, mTORC1 translocates on the lysosome in its active state and promotes cell growth by stimulating biosynthetic pathways while inhibiting cellular catabolism through the repression of TFEB, hence, downregulation of lysosomal biogenesis and autophagy. Conversely, amino acid- starvation leads to mTORC1 detachment from lysosomes and to its inactivation, which stimulates TFEB nuclear translocation, thus enhancing lysosomal function and autophagy which are essential for cell survival (8). Given that the functional loss of CTNS disrupts the lysosomal exit of cystine, we reasoned that the storage of this amino acid might sustain mTORC1 activity. In turn, hyperactive mTORC1 could exert a negative feedback on the lysosomal function and disrupt the autophagy clearance of damaged organelles and mitochondria leading to the pathologic cascade of events previously described in cystinosis (3).

A current limitation to investigate the contribution of the mTORC1-lysosome-autophagy axis in the pathogenesis of PT dysfunction is due to the use of cystinotic cellular models, which are not suitable for the analysis of this signaling. Indeed the methods used to immortalize CTNS-deficient cells derived from mice or patients could *per se* affect the activity of mTORC1, resulting in misleading interpretations of the data. Moreover, immortalized PT cell systems, which lose transport properties and their capacity of saturable endocytic uptake, yield discordant results - particularly in terms of processes involved in cell differentiation (9). In the last years, we participated in the establishment of faithful rodent models of cystinosis, and validated a well-differentiated primary PT cell culture system (mPTCs) obtained from mouse kidneys (10). The combination of these tools, allowed us to identify the link between loss of cystinosin function, mTORC1 activity, impairment of lyso-autophagy pathway and loss of transport capacity in PT cells. These findings are important as they open realistic therapeutic opportunities for patients with cystinosis. Since mTORC1 inhibitors are clinically used in other pathologic conditions, their repurposing for cystinosis would be appealing (11).

RESULTS

Time course of lysosomal and autophagy dysfunction in the kidneys of Ctns$^{-/-}$ mice

In order to identify the initial biological aberration caused by the absence of cystinosin, we analysed lysosomal and autophagy activity in a time course experiment performed in *Ctns*$^{-/-}$ mice. For this purpose, we analysed *Ctns*$^{-/-}$ mice at a presymptomatic stage (6 week-old), without signs of significant PT dysfunction, and at symptomatic stage (16 week-old), in presence of manifestations of PT dysfunction, as scored by a massive loss of CC16 low molecular weight protein (LMW) in the urines (Suppl. Fig. 1A). Compared to controls, PTs from *Ctns*$^{-/-}$ presymptomatic mice did not exhibit changes in lysosomal dynamics. In contrast, PTs from *Ctns*$^{-/-}$ symptomatic mice showed altered lysosomal size and increased mass, as scored by the size of LAMP1 + vesicles and by LAMP1 immunoblotting performed on the kidney lysates (Figs. 1A-1B). Although changes in lysosomal dynamics were observed only at later stage, the lysosomal function was already perturbed in presymptomatic *Ctns*$^{-/-}$ mice and clearly disrupted in symptomatic *Ctns*$^{-/-}$ mice, as evidenced by the decreased proteolytic generation of the 32 kDa mature form of cathepsin D (CtsD) (Fig. 1B). Given that the autophagy degradative pathway is directly connected to the lysosomal function, we were surprised to see that the homeostasis of autophagy proteins was unchanged in presymptomatic *Ctns*$^{-/-}$ mice (Figs. 1C-1D) but it was disrupted in symptomatic *Ctns*$^{-/-}$ mice, as shown by the increased levels of LC3-II as well as the greater amount of LC3-labelled autophagosomes compared to control mice (Figs. 1C-1D). Later appearance of aberrant autophagy was confirmed by the analysis of the autophagic receptor SQSTM1, whose increase was detected exclusively in the PTs of symptomatic *Ctns*$^{-/-}$ mice (Suppl. Fig. 1B). Altogether, these data show that the lack of cystinosin in PTs leads to an early aberration of the lysosomal function, followed by alterations in lysosomal dynamics and autophagy.

Progressive cystine accumulation and mTORC1 activation in the kidneys of Ctns$^{-/-}$ mice

Our next aim was to investigate the molecular pathway driving the progression of lysosomal dysfunction and dysregulation of autophagy flux in the PTs of symptomatic *Ctns*$^{-/-}$ mice. We focused our analyses on the serine/threonine kinase mTORC1 because: (i) mTORC1 is a master regulator of lysosomal function and autophagy (12), (ii) mTORC1 activity is known to be modulated by the intra-lysosomal levels of amino acids and loss of cystinosin function increases the intra-lysosomal levels of the amino acid cystine (13). Furthermore, cystinosin has been shown to interact with mTORC1 regulatory subunits and could play a role in modulating its activity (4).

We showed that cystine accumulation in our model correlated with disease severity as we detected increased levels in the kidney of symptomatic *Ctns*$^{-/-}$ mice, whereas in the kidney of presymptomatic mice the levels of cystine were unchanged (Fig. 2A). Interestingly, mTORC1 activation, as assessed by the phosphorylation state of its direct substrate S6, was abnormally increased in symptomatic *Ctns*$^{-/-}$ kidneys but unaltered in presymptomatic kidneys (Fig. 2B). The time-dependent upregulation of mTORC1 signaling was confirmed in the LTL-positive proximal tubules (Fig. 2C). These data showing physiologic mTORC1 activity in presymptomatic *Ctns*$^{-/-}$ mice prove that the absence of cystinosin per se is not sufficient for mTORC1 activation. On the other hand, as the alteration of mTORC1 pathway in the PT is temporally associated to cystine levels, we suggest that lysosomal accumulation of this amino acid is required to activate mTORC1 in *Ctns*$^{-/-}$ mice. Of note, abnormal mTORC1 activation could exert a negative feedback on the lysosomal function of *Ctns*$^{-/-}$ kidneys and contribute to the progressive lyso-autophagy defects, thus installing a pathogenic vicious circle.

Novel rat model of cystinosis with aberrant mTORC1 activation and dysfunctional lyso-autophagy path

To further explore the consequences of absent cystinosin in vivo, we established a novel Ctns knock-out rat model by using CRISPR/CAS9 (clustered regularly interspaced short palindromic repeats/ CRISPR associated protein 9) technology. This model was generated by deleting a 12bp sequence, which was replaced by an 8bp insertion resulting in a premature stop codon in exon 3 of Ctns and leading to nonsense-mediated decay of the mRNA and a complete deletion of the protein (Suppl. Figs. 2A-2C). 20 weeks old *Ctns*$^{-/-}$ rats exhibited reduced body weight and impaired PT reabsorption, as scored by the massive loss of Albumin and LMW proteins in the urine (Suppl. Figs. 2D-2G). Phenocopying the cystinotic murine model, the PT dysfunction observed in *Ctns*$^{-/-}$ rats was explained by the decreased expression of PT components, including megalin and cubilin endocytic receptors, and increased expression of proliferative genes (Suppl. Figs. 2H-2J). Similar to mice, depletion of cystinosin in rats provoked an accumulation of renal cystine associated with an increased rate of phosphorylation of S6, specifically observed in the megalin+ PT, decreased production of the mature form of lysosomal cathepsin D and abnormal LC3-II levels (Figs. 3A-3E). These results suggest that (i) cystine storage, (ii) altered mTORC1 pathway and (iii) disrupted lyso-autophagy network are evolutionary conserved pathogenic aberrations characterizing cystinosis.

Disrupted mTORC1 sensing in primary culture of proximal tubule cells (mPTCs) derived from the kidney of Ctns$^{-/-}$ *mice*

mTORC1 signaling is tightly regulated by the availability of amino acids. Under amino acids-rich conditions, mTORC1 translocates on the lysosome in its active state and promotes cell growth by stimulating biosynthetic pathways while inhibiting cellular catabolism through the repression of autophagy and lysosomal biogenesis. Conversely, amino acids starvation leads to mTORC1 detachment from lysosomes and to its inactivation, which stimulates autophagy and lysosomal function-essential to regenerate nutrients and new energy for cell survival (13). In order to investigate whether the mTORC1 dysregulation reported in the kidney of symptomatic *Ctns*$^{-/-}$ mice involved mTORC1 response to amino acids, we derived primary cultures of proximal tubule cells (mPTCs) from mice at this stage and analyse them under starvation and fed conditions (3). Importantly, these cells recapitulated the cystine accumulation observed in the kidneys of symptomatic *Ctns*$^{-/-}$ mice (Suppl. Fig. 3A). As expected, in amino acids deprived *Ctns*$^{+/+}$ mPTCs, mTORC1 was deactivated and localized outside the lysosomes. Refeeding starved *Ctns*$^{+/+}$ mPTCs with amino acids, restored mTORC1 signaling and its recruitment on the lysosomal membranes. Conversely, in *Ctns*$^{-/-}$ mPTCs mTORC1 was active and maintained its lysosomal localization in both starved and amino acids conditions (Figs. 4A-4B). Next, we examined whether sustained activation of mTORC1 in these cells was maintained after prolonged starvation. In control cells, amino acids removal acutely inhibited mTORC1 signaling at each time point analysed over 24 hours, apart from the 12h period, where mTORC1 is probably re-activated by the amino acids derived by the autophagic degradation (Fig. 4C), as shown before (14). Conversely, prolonged starvation of *Ctns*$^{-/-}$ mPTCs did not decrease mTORC1 activity, which remained high at all the time points of the fasting protocol (Fig. 4C). Interestingly, in *Ctns*$^{-/-}$ mPTCs derived from mice at presymptomatic stage, which did not exhibit a significant cystine accumulation, mTORC1 response to amino acids was indistinguishable from the control (Suppl. Fig. 3A-3B). In line with our data in the kidneys, these results indicate that loss of cystinosin affects mTORC1 sensing and signaling only at later stage, when its absence results in a dramatic accumulation of cystine in PT cells.

Cystinosin transport activity is required for maintaining mTORC1 function and lysosomal degradation of autophagy substrates

In order to assess whether the transport function of CTNS was required to maintain mTORC1 function and whether changes in this axis had an impact on the lysosomal degradation of autophagy substrates, we transduced *Ctns*$^{-/-}$ mPTCs with an adenovirus that expresses either mouse hemagglutinin (HA)-tagged wild type cystinosin or mutant cystinosin G339R. This missense mutation, previously identified in patients with infantile cystinosis, abolishes the transport activity of cystinosin and generates cystine accumulation without altering the lysosomal localization of the transporter (15) (Fig. 5A). Compared to *Ctns*$^{-/-}$ mPTCs transduced with the empty vector, the functional re-expression of HA-CTNS protein rescued the mTORC1 response to amino acid availability, as shown by the decreased rate of phosphorylation of S6 ribosomal protein during starvation and its increase upon replenishment with amino acids (Fig. 5B). Furthermore, expression of wild type HA-CTNS restored the degradation of autophagy substrates during starvation, as assessed by the decreased levels of SQSTM1 and LC3-II (Fig. 5C). In contrast, insertion of mutant HA-CTNS G339R in *Ctns*$^{-/-}$ mPTCs did not rescue the altered mTORC1 signaling neither improved the impaired lyso-autophagy flux (Figs. 5B-5C). These data indicate that: (i) abnormal mTORC1 signaling and impaired lysosomal clearance of autophagy cargo are interconnected events, which are strictly related to the lack of cystinosin transport activity; (ii) absent CTNS transporter function, previously shown to result in lysosomal cystine accumulation (15) is sufficient for mTORC1 dysregulation.

Cystine accumulation drives mTORC1 activation

Next, we investigated whether the cystine storage, resulting from the loss of cystinosin transport activity, might be the direct mediator of mTORC1 dysregulation in *Ctns*$^{-/-}$ mice. In order to test this hypothesis, we analysed mTORC1 activity in starved *Ctns*$^{-/-}$ mPTCs treated with the cystine-lowering drug cysteamine. This drug converts the lysosomal cystine into cysteine and cysteamine-cystine mixed disulfide, which is analogous to lysine and thus able to exit lysosomes through the cationic amino acid PQLC2/LAAT-1 transporter. The depletion of the intracellular cystine-storage by cysteamine (Fig. 6A) abolished mTORC1 activity similarly to the treatment with Torin1, which directly inhibits mTORC1 through an ATP-competitive mechanism (Fig. 6B). Of note, Torin1 treatment did not decrease the elevated cystine levels observed in *Ctns*$^{-/-}$ mPTCs (Fig. 6A). These results suggest that cystine accumulation signals upstream of mTORC1 and acts as the trigger for mTORC1 dysregulation in cystinosis. To provide a direct proof that cystine accumulation is sufficient for mTORC1 activation, we artificially raised lysosomal cystine levels in *Ctns*$^{+/+}$ mPTCs and subsequently analysed mTORC1 signaling and localization. To increase the level of lysosomal cystine, mPTCs were treated with an alcohol ester derivate of cystine (CDME), which diffuses across the cellular membranes and quickly accumulates in the lysosomes in its native form (5). As control, we used wild-type mPTCs treated with the same concentration of normal cystine. Starved *Ctns*$^{+/+}$ mPTCs supplemented with normal cystine for 30 minutes exhibited a rapid translocation of active mTORC1 to the lysosomal surface. This event correlated with a significant increase of intracellular cystine compared to starvation condition. mTORC1 activation decreased over time until disappearance at 6h, when intracellular cystine concentration decreased at the level of starved cells (Figs. 6C-6E). The transitory activation of mTORC1 in the first points of the time-course could be explained by the rapid metabolism of cystine. Indeed, the permanence of this amino acid in the lysosome is short as it is rapidly transported in the cytosol where it is converted in cysteine used for GSH synthesis (16, 17). By contrast, when starved *Ctns*$^{+/+}$ mPTCs were exposed to CDME, which causes a time-dependent accumulation of cystine in the cells, mTORC1 kinase activity and its clustering onto the lysosomal surface progressively increased and reach the peak at 6h, when intracellular cystine concentration is remarkably high (Figs. 6C-6E). These data indicate a correlation between cystine accumulation and mTORC1 activity in PT epithelial cells.

mTORC1 activation does not depend on alterations in MAPK/ERK signaling or changes in its regulatory subunits

To rule out the possibility that alteration in MAPK/ERK signalling, involved in the upstream regulation of mTORC1, could contribute to mTORC1 phenotype in *Ctns*$^{-/-}$ mPTCs, we blocked this path by using its inhibitor U0126 (18). Torin1 and Rapamycin inhibitors, which directly affect mTORC1 kinase activity, abolished the sustained phosphorylation of mTORC1 substrates in starved *Ctns*$^{-/-}$ mPTCs, while U0126 treatment did not modify their state of activation (Figs.7A-7B). Of note, the phosphorylation status of Akt, a growth factor/MAPK-dependent upstream regulator of mTORC1, was unchanged in *Ctns*$^{-/-}$ mice (Fig. 7D). These data demonstrate that in *Ctns*$^{-/-}$ mPTCs the mTORC1 hyper-activation is independent on MAPK/ERK pathway. Of note, the protein levels of mTORC1 regulatory subunits Raptor and Rags were also unchanged in both presymptomatic and symptomatic *Ctns*$^{-/-}$ mice (Figs. 7C-7D). These results suggest that abnormal mTORC1 activity in *Ctns*$^{-/-}$ mPTCs occurs through a mechanism, which does not involve homeostatic changes of its regulatory complex neither aberrant activation of growth factors/MAPK cell signaling.

mTORC1 inhibition in Ctns$^{-/-}$ mPTCs rescues lyso-autophagy pathway and PT dysfunction

Given (i) the temporal association between the appearance of abnormal mTORC1 signaling and the onset of impaired lyso-autophagy pathway in the kidney of *Ctns*$^{-/-}$ mice (Figs. 1-2) and (ii) the correlation between rescued mTORC1 function and restored lyso-autophagy clearance upon cystinosin reintroduction in *Ctns*$^{-/-}$ mPTCs (Fig. 5), we postulated a causative link between these two pathways. As active mTORC1 negatively regulates lysosomal biogenesis and autophagy, we reasoned that blocking its sustained activation might improve the functioning of the lyso-autophagy pathway in *Ctns*$^{-/-}$ mPTCs and the downstream cellular aberrations related to it (18). In order to test this hypothesis we treated *Ctns*$^{-/-}$ mPTCs with the mTORC1 inhibitors Torin1 (ATP-competitive mechanism) and Rapamycin (allosteric mechanism), previously shown to be effective in our cell system (Fig. 7B). mTORC1 inhibition reduced the abnormal size of LAMP1-positive vesicles, restored the peripheral lysosomal distribution (Fig. 8A) and restarted the stalled lysosomal function, as scored by the increased proteolytic generation of the 32 kDa mature CtsD and confirmed by the staining with PepA fluorescent probe (Figs. 8B-8C). These events were paralleled by an improvement of the autophagy flux, as shown by the decreased accumulation of LC3 II autophagosomal marker and reduced levels of EM-detected autophagic vacuoles (Fig. 8D and

Suppl. Fig. 4A). These data suggest that mTORC1 inhibition leads to the reactivation of the lyso-autophagy degradative pathway, thus, establishing a clear pathologic connection between these two networks in cystinosis. Our previous studies show that impaired autophagy in cystinotic mice induced a defective clearance of damaged mitochondria-producing ROS, which in turn, disrupts the tight junction integrity. This event caused increased translocation of ZONAB transcription factor into the nucleus and activation of an abnormal transcriptional program leading to cell proliferation and dedifferentiation, with loss of reabsorptive capacity of PT cells (4). Interestingly, restoring the lyso-autophagy pathway by blocking mTORC1 signaling restored basal level of oxidative stress, as scored by decreased level of cellular ROS (Suppl. Fig. 4B). This event was associated with rescued integrity of tight junctions, as evidenced by increased ZO-1 abundance at cell boundaries and subsequent decrease of ZONAB nuclear localization (Fig. 8E and Suppl. Fig. 4C). Accordingly, we observed a decreased cell proliferation and increased apical uptake of albumin in *Ctns*$^{-/-}$ mPTCs (Figs. 8F-8G). Thus, stimulating autophagy-lysosome systems, by shutting off mTORC1 in *Ctns*$^{-/-}$ mPTCs, rescues the functional properties of PT cells. These results identify mTORC1 dysregulation as a central pathological pathway in cystinosis and a powerful druggable target for this disease.

.

DISCUSSION

In this work we unveil the mechanism bridging loss of CTNS function and impairment of lysosomal network in cystinosis. We showed that cystine accumulation induces an aberrant activation of mTORC1, which in turn, disrupts the identity of the lysosomal compartment and the related mechanism of autophagy clearance, leading to PT dysfunction. Hyperactivation of mTORC1 was confirmed in a novel *Ctns*$^{-/-}$ rat model, demonstrating the conservation of these disease-pathways across mammals. Inhibition of mTORC1 pathway in murine *Ctns*$^{-/-}$ PT cells rescues the lyso-autophagy dysfunction, normalizes the level of oxidative stress, restores the TJ integrity and the abnormal ZO-1/ZONAB signalling axis resulting in an improvement of the transport activity of PT cells. Collectively these studies provide insights into the mechanism underlying the primary lysosome defect in cystinosis and offer new therapeutic perspectives for this, and potentially other, lysosome storage disorders. Most importantly, we found that:

- Hyperactivation of mTORC1 was detected in kidneys from both *Ctns*$^{-/-}$ rat and mouse models and derived primary cultures of PT cells. These results are in contrast with the decreased mTORC1 signaling previously shown in immortalized PT cells isolated from the urine of cystinotic patients or from the kidney of CTNS-deficient mice (4, 19). The process of immortalization by infection with the Simian Virus 40 (SV40) used in the latter studies could *per se* decrease the phosphorylation of mTORC1 and its direct substrates, impairing the analysis of the pathway (10).

- Abnormal activation of mTORC1 in *Ctns*$^{-/-}$ mPTCs is driven by cystine accumulation. Data supporting this hypothesis are: (i) the progressive activation of mTORC1 observed upon CDME overload in wild-type PT cells and (ii) the decreased mTORC1 activation observed after the treatment of *Ctns*$^{-/-}$ PT cells with the cystine-depleting agent cysteamine. Future metabolomics studies on lysosomal fractions will help to understand whether cystine accumulation drives the dysregulation of mTORC1 alone or in cooperation with other metabolites and to decipher how metabolic changes within the lysosomal lumen contributes to the disruption of lysosomal identity in cystinosis (20).

- Previous studies in kidney and fibroblast cell lines show that cystinosin interacts with many regulatory subunits of mTORC1. These interactions suggest a regulatory loop between the cystine transporter and the mTORC1 complex (4). However, as mTORC1 dysregulation is not detected in the early life of cystinotic mice, we exclude that the loss of cystinosin alone is sufficient to drive mTORC1 aberration. Further work is needed to deepen the biological meaning of this protein-protein interaction.

- mTORC1 could affect lysosomal function by blocking TFEB nuclear translocation, thus, impairing lysosomal biogenesis. This hypothesis is in line with the abnormal size and reduced number of lysosomes observed in cystinosis and it is supported by the studies of Rega *et al.* showing that activation of TFEB rescues lysosomal abnormalities in cystinotic kidney cells (7). Alternatively, mTORC1 alterations could affect lysosomal homeostasis by interfering with the process of autophagic lysosomal reformation (21). Additional work is needed to investigate these hypotheses.

- mTORC1 is a new druggable target in cystinosis. Indeed, mTORC1 inhibition results in restored lyso-autophagy pathway and related pathogenic cascade in *Ctns*$^{-/-}$ PT cells. These rescue events lead to a significant improvement of the transport activity of PT cells. This finding is significant as a wide range of mTORC1 inhibitors is commercially available and some already used in clinics (22). Further studies using mTORC1 inhibitors *in vivo* in *Ctns*$^{-/-}$ rat model, which presents an early and more prominent kidney phenotype compared to the mouse model and it is closer to human in the evolutionary scale (23), will allow us to establish the beneficial effect of blocking this pathway and rescuing PT dysfunction in cystinosis.

MATERIAL AND METHODS

Antibodies and reagents. The following Antibodies were used: rat anti-LAMP1 (sc-19992, Santa Cruz Biotechnology); rabbit anti-LC3 (PM036, MBL); rabbit anti-p62/SQSTM1 (PM045, MBL); rabbit anti-AQP1(OASA00210; Aviva Systems Biology); rabbit anti-GAPDH (2118, Cell Signaling Technology), mouse anti-β-actin (A5441, Sigma-Aldrich); goat anti-CtsD (sc-6486, Santa Cruz Biotechnology); mouse anti-α-tubulin (T5168, Sigma-Aldrich); rat anti-HA (11867423001, Roche); rabbit anti-ZO-1 (sc-10804, Santa Cruz Biotechnology); rabbit anti-ZONAB (A303-070A, Bethyl Laboratories); rabbit anti-human transferrin (A0061, Dako); rabbit anti-human Gc-globulin (also known as VDBP, A0021, Dako); sheep anti-Megalin (gift from P. Verroust and R. Kozyraki, INSERM); rabbit anti-phospho-S6 Ribosomal Protein (4858, Cell Signaling Technology); rabbit anti-S6 Ribosomal Protein (2217, Cell Signaling Technology); rabbit anti-phospho-p70 S6 kinase 1 (9234, Cell Signaling Technology); rabbit anti-p70 S6 kinase 1 (2708, Cell Signaling Technology); rabbit anti-phospho-4EBP1 (9451, Cell Signaling Technology); rabbit anti-4EBP1 (9644S, Cell Signaling Technology); rabbit anti-Raptor (2280, Cell Signaling Technology); rabbit anti-RagA (4357, Cell Signaling Technology); rabbit anti-RagC (5466, Cell Signaling Technology); rabbit anti-phospho-AKT (13038, Cell Signaling Technology); rabbit anti-mTOR (7C10, Cell Signaling Technology), WGA FITC Conjugate (L 4895, Sigma-Aldrich), Torin1 (CAS 1222998-36-8, TOCRIS Bioscience), Cysteamine (M6500-25G, Sigma-Aldrich), Rapamycin (CAS 53123-88-9, Sigma-Aldrich); L-CDME(857327-5G, Sigma-Aldrich), L-Cystine (C7602-25G),UO126 (#9903, Cell Signaling Technology). Biotinylated Lotus Tetragonolobus Lectin (LTL; B-1325 Vector Laboratories).

***Ctns* mouse model.** Experiments were conducted on age- and gender-matched *Ctns*$^{-/-}$ and *Ctns*$^{+/+}$ littermates (C57BL/6 background). Mice were maintained under temperature-and humidity-controlled conditions with 12 h light/12 h dark cycles with free access to appropriate standard diet in accordance with the institutional guidelines of National Institutes of Health Guide for the Care and Use of Laboratory Animals. Kidney tissues and/or urines were collected for analyses. The mouse study protocols (University of Zurich) were approved by the local legal authority (Veterinary Office, Canton of Zurich, Switzerland).

Generation and maintenance of *Ctns* rat model. The *Ctns*$^{-/-}$ rat model has been produced and obtained by PolyGene AG by using CRISPR/Cas9 technology. This system was used to introduce site-specific double strand breaks into the genome inducing insertions and deletions by the endogenous repair mechanism of non-homologous end joining. Two single guide RNAs (sgRNAs) targeting the same region in the exon 3 of the *Ctns* gene were selected: CRISPR1a: ACCAACGTCAGCATTACCCT(TGG),CRISPR1b:CCATTTACCAGCTTCACAGT(GGG). The sgRNAs sequences were blasted against the rat genome for off-targets. A total of 146 rat embryos was injected with the combination of CRISPRs 1a/b. From these embryos, 90 survived and could be transferred into foster rats. A total of 34 pups was born from these injections. These pups were analyzed for changes in the *Ctns* locus. PCR was used to amplify the *Ctns* region surrounding the CRISPR-target site using the following primer combination: CTNS_R:5'-ACACCCGAAGTACATGCAGA-3', CTNS_L:5'ACAGAGATGGG AAGAGCACA-3'. The resulting PCR product was digested by T7 endonuclease. Five animals show a positive signal indicating insertion or deletion in the *Ctns* locus. These changes were analyzed via PCR and sequencing. The following primer combinations were used 5’–AGGCACGATGGAGCAGTAAAG–3’ and 5’–ATGCACGAATGAGACCAGACC–3’. Here we selected and used a *Ctns* rat line harboring a deletion of 12bp and insertion of 8bp resulting in a premature stop codon in the exon 3 of *Ctns* gene. This mutation results in a nonsense-mediated decay of the mRNA. Experiments were conducted on age- and gender-matched *Ctns*$^{-/-}$ and *Ctns*$^{+/+}$ littermates (Sprague-Dawley background). Rats were maintained under temperature- and humidity-controlled conditions with 12 h light/12 h dark cycles with free access to appropriate standard diet in accordance with the institutional guidelines of National Institutes of Health Guide for the Care and Use of Laboratory Animals. Kidney tissues and/or urines were collected for analyses at the time of sacrifice. The protocols for the rat study (University of Zurich) were approved by the local legal authority (Veterinary Office, Canton of Zurich, Switzerland).

Renal function parameters. The mice were placed overnight in metabolic cages with ad libitum access to food and drinking water; urine was collected over ice. Urine from rats were collected at the moment of sacrifice. Urine and blood parameters were measured by using a UniCel DxC 800 pro Synchron (Beckman Coulter, Fullerton, CA, USA), whereas urinary Clara cell protein (CC16) concentration was measured in duplicate by enzyme-linked immunosorbent assay (ELISA; BIOMATIK EKU03200-mouse) (ABEXA; abx492145-rat).

Cystine measurement. Kidney tissues from mice or rats, or primary cultured cells were homogenized and lysed with Nethylmaleimide (NEM) solution containing 5.2 mmol l^{-1} N-ethylmaleide in 10 mmol l^{-1} potassium phosphate buffer adjusted to pH 7.4. The lysates were collected and precipitated with sulfosalicylic acid (12% w/v) and centrifuged at 10,000 r.p.m. for 10 min at 10 °C. The resulting supernatant was dissolved in citrate loading buffer (Biochrom Ltd, Cambridge, UK) and 50 µl of this solution was analyzed by Biochrom 30 Plus Amino Acid Analyzer (Biochrom Ltd). The protein pellet was dissolved in 0.1 mol l^{-1} NaOH solution and the protein concentration was determined by Biuret method. The concentration of amino acids was measured by using a lithium high performance physiological column (Biochrom) followed by postcolumn derivatization with ninhydrin. The amino acids were identified according to the retention time and the ratio of the area between the two wavelengths (570 nm and 440 nm) and quantified by using EZChrom Elite software (Agilent Technologies Inc., Pleasanton, California, USA). Cystine concentration was normalized to the protein concentration and reported in nmol per mg protein.

Kidney isolation and primary cultures of mouse PT cells. The kidneys were collected from *Ctns* mice or rats: one kidney was split transversally and one half was fixed and processed for immunostaining, whereas the other half was flash frozen, homogenized by Dounce homogenizer in 1 ml of RIPA buffer that contains protease and phosphatase inhibitors, and processed for western blot analysis. The contralateral kidney of the rat was flash frozen and used for RT-qPCR analysis. The contralateral kidney of the mice was taken to generate primary culture of proximal tubule cells (mPTCs). Freshly micro-dissected PT segments were seeded onto collagen-coated chamber slides (C7182, Sigma-Aldrich) and/or collagen-coated 6- or 24-well plates (145380 or 142475, Thermo Fisher Scientific), and cultured at 37 °C and 5% CO2 in Dulbecco’s modified Eagle’s medium/F12 (21041-025, Thermo Fisher Scientific) with 0.5% dialyzed fetal bovine serum (FBS), 15mM HEPES (H0887, Sigma-Aldrich), 0.55mM sodium pyruvate (P2256, Sigma-Aldrich), 0.1 ml l^{-1} nonessential amino acids (M7145, Sigma-Aldrich), hydrocortisone, human epidermal growth factor, epinephrine, insulin, triiodothyronine, transferrin (TF), and gentamicin/ amphotericin (Single Quots kit, CC-4127, Lonza), pH 7.40, 325 mOsm kg^{-1}. The medium was replaced every 48 h. Confluent monolayers of mPTCs were expanded from the tubular fragments after 6–7 days, characterized by a high endocytic uptake capacity. These cells were mycoplasma free. All experiments were performed on confluent monolayers grown on chamber slides or plates.

Starvation and treatments in *Ctns* mPTCs. *Ctns* mPTCs were starved by incubation in amino acid-free RPMI medium 1640 (US Biological) for 120 minutes, and stimulated with a standard amino acid mixture composed of MEM nonessential amino acid solution, MEM essential amino acid solution, and L-glutamine (Invitrogen, Thermo Fisher Scientific) for 60 minutes. At the indicated time-points, starved mPTCs were stimulated with Cystine (0.15 mM) or Cystine Dimethyl Ester (CDME, 0.15 mM). After stimulation, the final concentration of amino acids in solution was the same as in the in growth cell medium. mTOR kinase activity in *Ctns*$^{-/-}$ cells was inhibited by addition of either Rapamycin (1µM) or Torin1 (250 nM) or Cysteamine (100 µM) in starvation medium for 6h. U0126 inhibitor of MAPK /ERK pathway was used as control (50 µM 6h in starvation medium). Rescue experiments were performed by treating mPTCs with either Rapamycin (1µM) or Torin1 (250 nM) for 6h in growth cell medium.

Immunofluorescence and confocal microscopy. Fresh mouse or rat kidneys were fixed by perfusion with 50–60 ml of 4% PFA in PBS (158127, Sigma-Aldrich) before being snap-frozen in cryogenic Tissue-Tek OCT compound (Electron Microscopy Sciences, Hatfield, USA). The embedded tissues were sectioned at 5 µm and processed for immunofluorescent staining as previously described. The slides were quenched with 50mM NH4Cl, blocked with 5% BSA in PBS Ca/Mg (D1283, Sigma-Aldrich) for 30 min and stained with the primary antibodies diluted in blocking buffer overnight at 4 °C. After two washes in 0.1% Tween 20 (v/v in PBS), the slides were incubated with the corresponding fluorophore-conjugated Alexa secondary antibodies (Invitrogen) diluted in blocking buffer at room temperature for 1 h and counterstained with 1 µg LTL when appropriate and 1 µM 4’,6-diamino-2-phenylindole dihydrochloride (DAPI; D1306, Thermo Fischer Scientific). The slides were mounted in Prolong Gold Anti-fade reagent (P36930, Thermo Fisher Scientific), acquired on Leica SP8 confocal laser scanning microscope (Center for Microscopy and Image Analysis, University of Zurich) equipped with a Leica APO × 63 NA 1.4 oil-immersion objective at a definition of 1,024 × 1,024 pixels (average of 8 or 16 scans), adjusting the pinhole diameter to 1 Airy unit for each emission channel to have all of the intensity values between 1 and 254 (linear range). The micrographs were processed with Adobe Photoshop (version CS5, Adobe System, Inc., San Jose, USA) software. Quantitative image analysis was performed by selecting randomly ∼ 5 visual fields per each slide that included at least three to five PTs (LTL positive), using the same setting parameters (i.e., pinhole, laser power, and offset gain and detector amplification below pixel saturation). ImageJ software was used for the analysis.The mPTCs were fixed in 4% PFA and processed for immunofluorescent staining as previously described. Briefly, after incubation with blocking/permeabilization solution (0.1% Saponin,0.5% BSA and 50 mM NH_4Cl in PBS), mPTCs were stained overnight with the appropriate primary antibodies and 45 min with the suitable fluorophore-conjugated Alexa secondary antibodies (Invitrogen). Immunostained mPTCs were analyzed by a Leica SP5 confocal laser scanning microscope using the settings described above. The quantitative cell image analyses were performed by using the open-source cell image analysis software CellProfiler™. In particular, the specific module "Measure-Object-Intensity-Distribution" was used to score the number of LAMP1+ and BSA+ structures and the diameter of LAMP1+ vesicles. The pipeline "Cell/particle counting and scoring the percentage of stained objects" was used to score either the numbers of LAMP1+ vesicles containing mTOR or Pepstatin A. The module "MeasureObjectIntensityDistribution" was used to score the fluorescence intensity of LAMP1+ structures contained into perinuclear region (area defined by the first 10 bin) and peripheral region (area defined by the last 10 bin) of the cells. Briefly, the software generates 20 concentrically bin around the nucleus of each cell and 15 calculates the intensity distribution for each bin. The "Cytoplasm–Nucleus Translocation Assay" was used to score the numbers of Bromodeossiuridine (BrdU) - positive cells. The fluorescence intensity of cellular ROS was measured by using ImageJ.

Endocytosis assay. The endocytic uptake was monitored in mPTCs cells following incubation for 60 min at 4 °C with 50 µg ml^{-1} bovine serum albumin (BSA)–Alexa- Fluor-488 (A13100, Thermo Fisher Scientific) in complete HEPES-buffered Dulbecco's modified Eagle's medium. The cells were given an acid wash and warmed to 37 °C in growth cell medium for 15 min before being fixed and processed for immunofluorescence analyses.

Lysosomal activity. The detection of lysosomal activity was performed in live mPTCs using Bodipy-FL-PepA (P12271, Thermo Fischer Scientific) according to the manufacturer's specifications. The cells were pulsed with 1 µM Bodipy-FL-Pepstatin A in Live Cell Imaging (A14291DJ, Thermo Fischer Scientific) medium for 1 h at 37 °C followed by fixation and immunostaining with anti-LAMP1 and subsequently analyzed by confocal microscopy.

ROS detection. The cells were pulsed with 5 µM CellROX Green Reagent (C10444, Thermo Fisher Scientific) for 10 min in live-cell imaging at 37 ° C. After washing, the cells were subsequently analysed by confocal microscopy.

Proliferation assay. mPTCs were incubated with BrdU (1.5 µg ml^{-1}; Sigma-Aldrich) in accordance with the manufacturer's protocol. BrdU-labeled cells were immunostained with rat anti-BrdU antibody (Oxford Biotechnology; 1:500), followed by the specific secondary biotinylated goat anti-rat antibody (1:300; Jackson Immunoresearch), mounted with the Prolong Gold Anti-fade reagent and subsequently analyzed by confocal microscopy.

Electron microscopy. mPTCs were fixed in 2% PFA/2.5% glutaraldehyde (for zebrafish) and 4% PFA/0.1% glutaraldehyde (for cells) in 100 nM sodium cacodylate, at pH 7.43, dehydrated, and embedded in LR-White resin (LADD Research Industries). The grids were viewed on a Philips CM100 transmission electron microscope at 80 kV. Autophagic vacuoles were identified and categorized as autophagosomes or autophagolysosomes according to standard criteria. The term autophagic vacuole was used when the differentiation between autophagosome and autophagolysosomes was not possible. The number of autophagic vacuoles was determined by using i-TEM software (Olympus, Germany).

Quantitative real-time PCR. Total RNA was extracted from rat kidney tissues using Aurum Total RNA Fatty and Fibrous Tissue Kit (Bio-Rad, Hercules, CA). One microgram of RNA was used to perform the reverse transcriptase reaction with iScript cDNA Synthesis Kit (Bio-Rad). Changes in mRNA levels of the target genes were determined by relative reverse transcriptase-quantitative PCR with a CFX96 Real-Time PCR Detection System (Bio-Rad) using iQ SYBR Green Supermix (Bio-Rad). The analyses were performed in duplicate with 100 nM of both sense and anti-sense primers in a final volume of 20 µl using iQ SYBR Green Supermix (Bio-Rad). Specific primers were designed using Primer3. PCR conditions were 95 °C for 3 min followed by 40 cycles of 15 s at 95 °C, 30 s at 60 °C. The PCR products were sequenced with the BigDye terminator kit (Perkin Elmer Applied Biosystems) using ABI3100 capillary sequencer (Perkin Elmer Applied Biosystems). The efficiency of each set of primers was determined by dilution curves (Supplementary Table 1 and 2). The program geNorm version 3.4 was applied to characterize the expression stability of the candidate reference genes in kidneys and six reference genes were selected to calculate the normalization factor. The relative changes in targeted genes over Gapdh mRNAs were calculated using the $2^{-\Delta\Delta Ct}$ formula.

Western blotting. Proteins were extracted from mouse or rat kidney tissues or mPTCs, lysed using a buffer, which contains protease (1836153001, Roche) and phosphatase inhibitors (04906845001, PhosSTOP Sigma), followed by sonication and centrifugation at 14,000 g for 10 min at 4 ° C. The samples were thawed on ice, normalized for protein (20 µg per lane), dissolved in Laemmli sample buffer, and separated by SDS-PAGE under reducing conditions. After blotting onto polyvinylidene difluoride and blocking with 5% non-fat milk (1706404, Bio-Rad Laboratories) diluted in PBS, the membranes were incubated overnight at 4 °C with primary antibody, washed, incubated with peroxidase-labeled secondary antibody, and visualized with enhanced chemiluminescence (WBKLS0050, Millipore, Life technologies). For re-probing, the membranes were rinsed, incubated for 30 min at 55 °C in a stripping buffer (62.5 mmol l^{-1} Tris-HCl, 2% SDS, 100mM mercaptoethanol, adjusted to pH 7.4), before incubation with primary antibodies. Quantitative analyses were performed by scanning the blots and measuring the relative density of each band normalized to β-actin, GAPDH, or α-tubulin with ImageJ software.

Data analysis and statistics. The quantitative data were expressed as means ± standard error of the mean (s.e.m.). Differences between experimental groups were evaluated using analysis of variance followed by post hoc test, when appropriate. When only two groups were compared, unpaired or paired two tailed Student's t-tests were used as appropriate. No statistical methods were used to predetermine the sample size. The sample size (n of biological replicates derived from distinct mice) of each experimental group is described in figure legends. GraphPad Prism software was used for all statistical analyses. Statistical significance was set at a $P < 0.05$

REFERENCES

1. Devuyst, O. and Luciani, A. (2015) Chloride transporters and receptor-mediated endocytosis in the renal proximal tubule. The Journal of physiology, 593, 4151-4164.

2. Gahl, W.A., Thoene, J.G. and Schneider, J.A. (2002) Cystinosis. The New England journal of medicine, 347, 111-121.

3. Festa, B.P., Chen, Z., Berquez, M., Debaix, H., Tokonami, N., Prange, J.A., Hoek, G.V., Alessio, C., Raimondi, A., Nevo, N. et al. (2018) Impaired autophagy bridges lysosomal storage disease and epithelial dysfunction in the kidney. Nature communications, 9, 161.

4. Andrzejewska, Z., Nevo, N., Thomas, L., Chhuon, C., Bailleux, A., Chauvet, V., Courtoy, P.J., Chol, M., Guerrera, I.C. and Antignac, C. (2016) Cystinosin is a Component of the Vacuolar H+-ATPase-Ragulator-Rag Complex Controlling Mammalian Target of Rapamycin Complex 1 Signaling. Journal of the American Society of Nephrology : JASN, 27, 1678-1688.

5. Zoncu, R., Bar-Peled, L., Efeyan, A., Wang, S., Sancak, Y. and Sabatini, D.M. (2011) mTORC1 senses lysosomal amino acids through an inside-out mechanism that requires the vacuolar H(+)-ATPase. Science (New York, N.Y.), 334, 678-683.

6. Settembre, C., Fraldi, A., Medina, D.L. and Ballabio, A. (2013) Signals from the lysosome: a control centre for cellular clearance and energy metabolism. Nature reviews. Molecular cell biology, 14, 283-296.

7. Rega, L.R., Polishchuk, E., Montefusco, S., Napolitano, G., Tozzi, G., Zhang, J., Bellomo, F., Taranta, A., Pastore, A., Polishchuk, R. et al. (2016) Activation of the transcription factor EB rescues lysosomal abnormalities in cystinotic kidney cells. Kidney international, 89, 862-873.

8. Sardiello, M., Palmieri, M., di Ronza, A., Medina, D.L., Valenza, M., Gennarino, V.A., Di Malta, C., Donaudy, F., Embrione, V., Polishchuk, R.S. et al. (2009) A gene network regulating lysosomal biogenesis and function. Science (New York, N.Y.), 325, 473-477.

9. Prange, J.A., Bieri, M., Segerer, S., Burger, C., Kaech, A., Moritz, W. and Devuyst, O. (2016) Human proximal tubule cells form functional microtissues. Pflugers Archiv : European journal of physiology, 468, 739-750.

10. Yu, Y., Kudchodkar, S.B. and Alwine, J.C. (2005) Effects of simian virus 40 large and small tumor antigens on mammalian target of rapamycin signaling: small tumor antigen mediates hypophosphorylation of eIF4E-binding protein 1 late in infection. Journal of virology, 79, 6882-6889.

11. Xie, J., Wang, X. and Proud, C.G. (2016) mTOR inhibitors in cancer therapy. F1000Research, 5.

12. Puertollano, R. (2014) mTOR and lysosome regulation. F1000prime reports, 6, 52.

13. Bar-Peled, L. and Sabatini, D.M. (2014) Regulation of mTORC1 by amino acids. Trends in cell biology, 24, 400-406.

14.Wyant, G.A., Abu-Remaileh, M., Frenkel, E.M., Laqtom, N.N., Dharamdasani, V., Lewis, C.A., Chan, S.H., Heinze, I., Ori, A. and Sabatini, D.M. (2018) NUFIP1 is a ribosome receptor for starvation-induced ribophagy. Science (New York, N.Y.), 360, 751-758.

15. Kalatzis, V., Nevo, N., Cherqui, S., Gasnier, B. and Antignac, C. (2004) Molecular pathogenesis of cystinosis: effect of CTNS mutations on the transport activity and subcellular localization of cystinosin. Human molecular genetics, 13, 1361-1371.

16.Wilmer, M.J., Emma, F. and Levtchenko, E.N. (2010) The pathogenesis of cystinosis: mechanisms beyond cystine accumulation. American journal of physiology. Renal physiology, 299, F905-916.

17. Pisoni, R.L., Acker, T.L., Lisowski, K.M., Lemons, R.M. and Thoene, J.G. (1990) A cysteine-specific lysosomal transport system provides a major route for the delivery of thiol to human fibroblast lysosomes: possible role in supporting lysosomal proteolysis. The Journal of cell biology, 110, 327-335.

18. Settembre, C., Zoncu, R., Medina, D.L., Vetrini, F., Erdin, S., Erdin, S., Huynh, T., Ferron, M., Karsenty, G., Vellard, M.C. et al. (2012) A lysosome-to-nucleus signalling mechanism senses and regulates the lysosome via mTOR and TFEB. The EMBO journal, 31, 1095-1108.

19. Ivanova, E.A., van den Heuvel, L.P., Elmonem, M.A., De Smedt, H., Missiaen, L., Pastore, A., Mekahli, D., Bultynck, G. and Levtchenko, E.N. (2016) Altered mTOR signalling in nephropathic cystinosis. Journal of inherited metabolic disease, 39, 457-464.

20. Abu-Remaileh, M., Wyant, G.A., Kim, C., Laqtom, N.N., Abbasi, M., Chan, S.H., Freinkman, E. and Sabatini, D.M. (2017) Lysosomal metabolomics reveals V-ATPase- and mTOR-dependent regulation of amino acid efflux from lysosomes. Science (New York, N.Y.), 358, 807-813.

21. Rong, Y., McPhee, C.K., Deng, S., Huang, L., Chen, L., Liu, M., Tracy, K., Baehrecke, E.H., Yu, L. and Lenardo, M.J. (2011) Spinster is required for autophagic lysosome reformation and mTOR reactivation following starvation. Proceedings of the National Academy of Sciences of the United States of America, 108, 7826-7831.

22. Zheng, Y. and Jiang, Y. (2015) mTOR Inhibitors at a Glance. Molecular and cellular pharmacology, 7, 15-

23. Nei, M., Xu, P. and Glazko, G. (2001) Estimation of divergence times from multiprotein sequences for a few mammalian species and several distantly related organisms. Proceedings of the National Academy of Sciences of the United States of America, 98, 2497-2502.

Figure 1

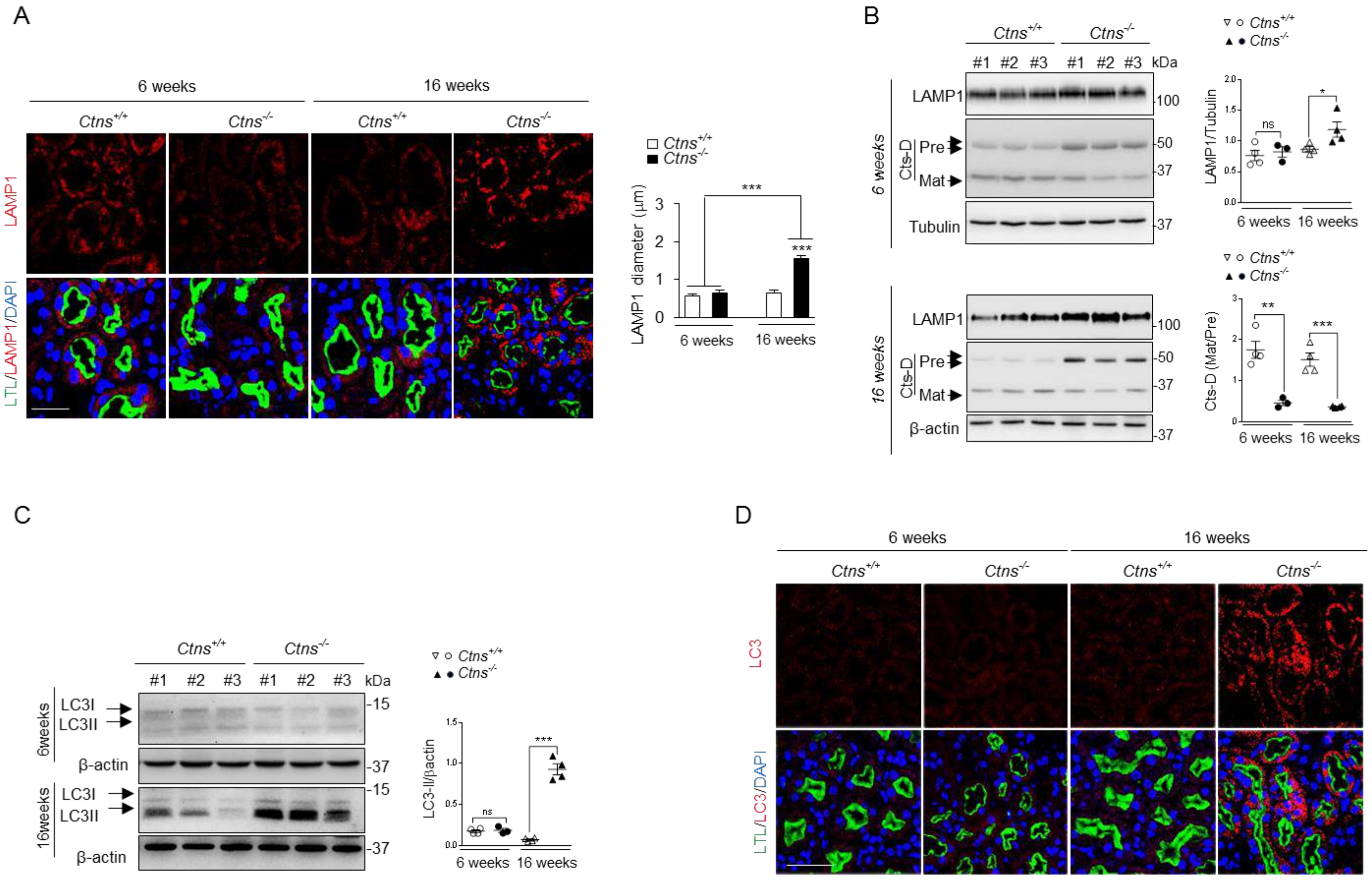

Figure 1. Abnormal lysosome dynamics and autophagy in proximal tubules of *Ctns*$^{-/-}$ mice (**A**) Representative confocal micrographs of LAMP1^{+} structures (red) and quantification of the diameter of LAMP1^{+} vesicles contained in LTL^{+} (green) proximal tubules from 6 and 16 weeks old *Ctns* mice.(two-tailed unpaired Student's t-test, ***P < 0.001 relative to 6 weeks old *Ctns*$^{+/+}$/ *Ctns*$^{-/-}$ and 16 weeks old *Ctns*$^{+/+}$ kidneys). (**B**) Western blotting and densitometry analyses of LAMP1and Cts-D protein levels in whole kidney lysates from *Ctns* mice (two-tailed unpaired Student's t-test, *P < 0.05 (LAMP1) and **P < 0.01, ***P < 0.001 (Cts-D) relative to 6 or 16 weeks old *Ctns*$^{+/+}$ kidneys, n=3-4 mice per group). α-Tubulin and β-actin were used as a loading control. (**C**) Western blotting and densitometry analyses of LC3 protein levels in whole kidney lysates from *Ctns* mice (two-tailed unpaired Student's t-test, ***P < 0.001 relative to 16 weeks old *Ctns*$^{+/+}$ kidneys, n=3-4 mice per group). β-actin was used as a loading control. (**D**) Representative confocal micrographs of LC3+ (red) structures and LTL+ (green) proximal tubule from 6 and 16 weeks old *Ctns* mice. Nuclei counterstained with DAPI (blue) in **A** and **D**. Plotted data represent mean ± SEM.

Figure 2

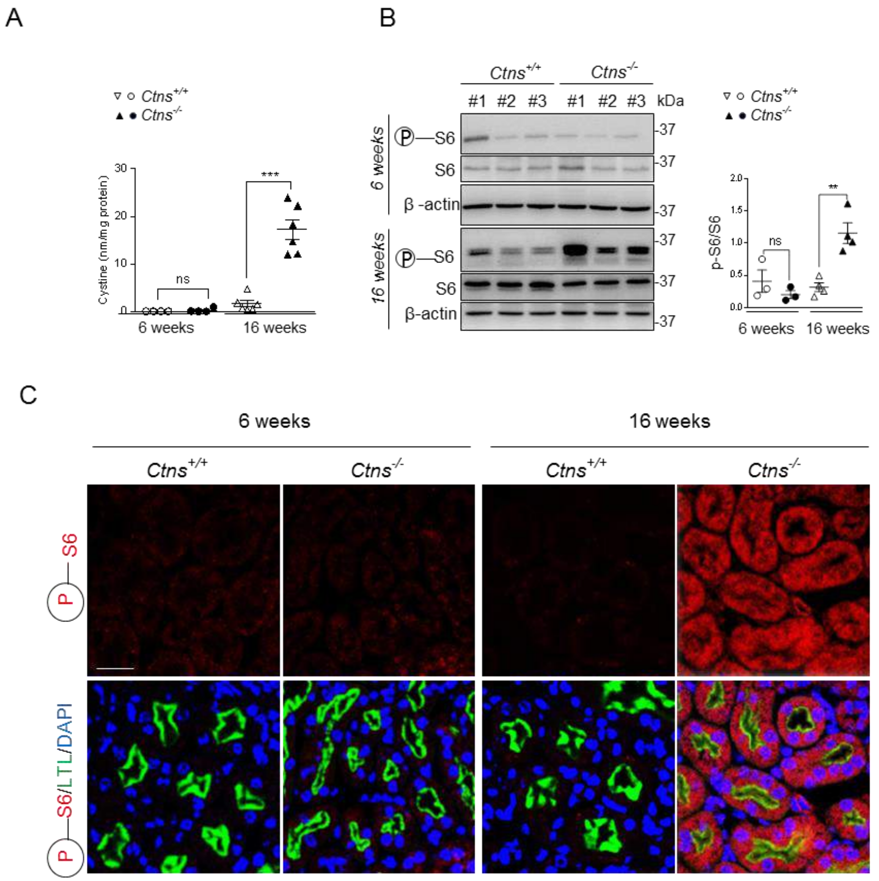

Figure 2. Cystine storage and abnormal mTORC1 signalling in *Ctns*$^{-/-}$ kidneys. (**A**) Intracellular cystine levels were measured by HPLC in kidneys derived from 6 (n=4 mice per group) and 16 weeks old (two-tailed unpaired Student's t-test, ****P*<0.001 relative to 16 weeks old *Ctns*$^{+/+}$ kidneys, n=6 mice per group) *Ctns* mice. (**B**) Western blotting and densitometry analysis of S6 and p-S6 protein levels in whole kidney lysates from 6 (n=3 mice per group) and 16 weeks old (two-tailed unpaired Student's t-test **P < 0.01 relative to 16 weeks old *Ctns*$^{+/+}$ kidneys, n=4 mice per group) *Ctns* mice. β-actin was used as a loading control. (**C**) Representative confocal micrographs of p-S6^{+} structures (red) and LTL^{+} (green) proximal tubules in kidneys derived from 6 and 16 weeks old *Ctns* mice. Nuclei counterstained with DAPI (blue).

Figure 3

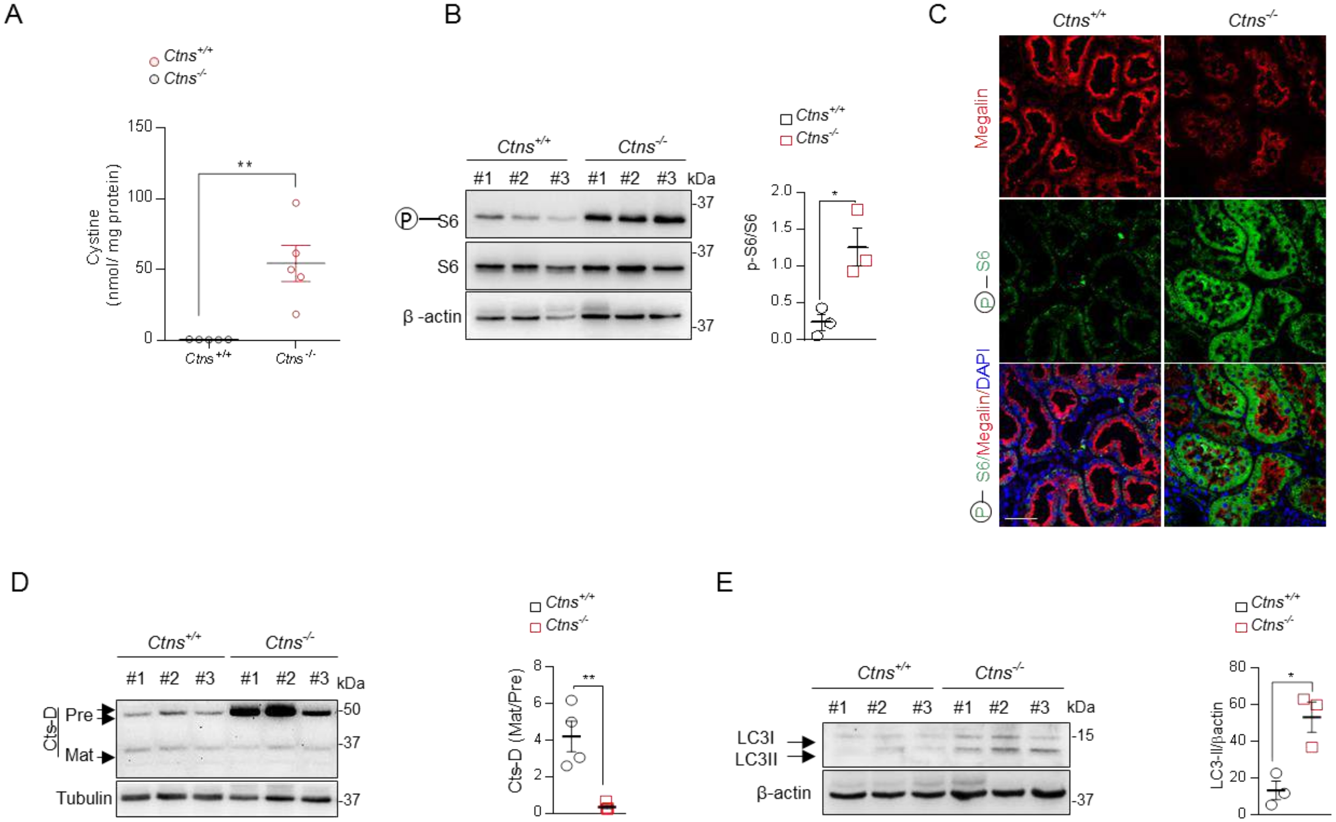

Figure 3. Cystine storage is associated with abnormal mTORC1 signaling and impaired lyso-autophagy in *Ctns*$^{-/-}$ rats. (**A**) Intracellular cystine levels were measured by HPLC in 20 weeks old *Ctns* rat kidneys. (n=5 rats per group, two-tailed unpaired Student's t-test, **P < 0.01 relative to *Ctns*$^{+/+}$ kidneys). (**B**) Western blotting and densitometry analysis of S6 and p-S6 protein levels in whole kidney lysates derived from 20 weeks old *Ctns* rat kidneys (two-tailed unpaired Student's t-test, *P < 0.05 relative to *Ctns*$^{+/+}$ kidneys; n=3 rats per group). (**C**) Representative confocal micrographs of p-S6^{+} structures (green) and Megalin^{+} (red) proximal tubules derived from *Ctns* rat kidneys. Nuclei counterstained with DAPI (blue). (**D**) Western blotting and densitometry analyses of Cts-D protein levels in whole kidney lysates from *Ctns* rats (two-tailed unpaired Student's t-test, **P < 0.01 relative to *Ctns*$^{+/+}$ kidneys, n = 3-4 rats per group). α-Tubulin was used as a loading control. (**E**) Western blotting and densitometry analyses of LC-3 protein levels in whole kidney lysates from *Ctns* rats (two-tailed unpaired Student's t-test, *P < 0.05 relative to *Ctns*$^{+/+}$ kidneys, n=3 rats per group). β-actin was used as a loading control. Scale bar 50μm

Figure 4

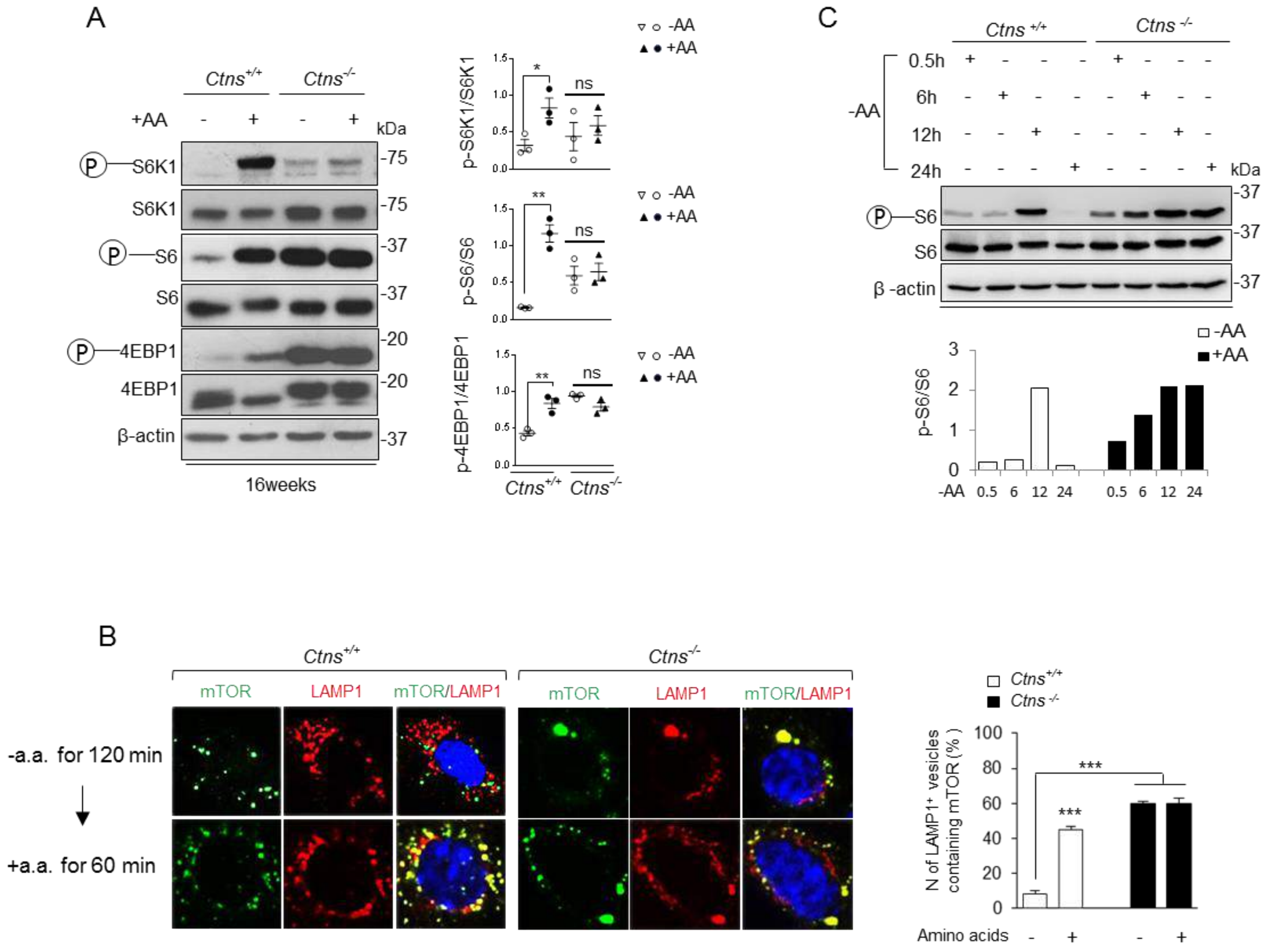

Figure 4. Altered mTORC1 sensing in mPTCs derived from *Ctns*$^{-/-}$ symptomatic mice. (**A**) Western blotting and densitometry analyses of phosphorylated and total form of S6 K1, S6 and 4EBP1 protein levels in starved (RPMI, 120 minutes) and amino acids replenished (60 minutes) 16 weeks old *Ctns* mPTCs (n=3 mice per group). β-actin was used as loading control. (**B**) 16 weeks old *Ctns* mPTCs were immune-stained with anti-mTOR (green) and anti-LAMP1 (red) antibodies. Quantification of mTOR/LAMP1^{+} vesicles (in percentage of total LAMP1; n = 5 randomly selected fields per condition, with each containing ~ 20–25 cells). Nuclei counterstained with DAPI (blue).(**C**) Western blotting and graphical representation of p-S6/S6 ratio at each time point analysed over 24 hours of starvation (RPMI) in 16 weeks old *Ctns* mPTCs. β-actin was used as loading control. Plotted data represent mean ± SEM; two tailed unpaired Student's *t* test, *P < 0.05, ***P*<0.01, ****P*<0.001 relative to starved or amino acids replenished *Ctns*$^{+/+}$or *Ctns*$^{-/-}$ mPTCs.

Figure 5

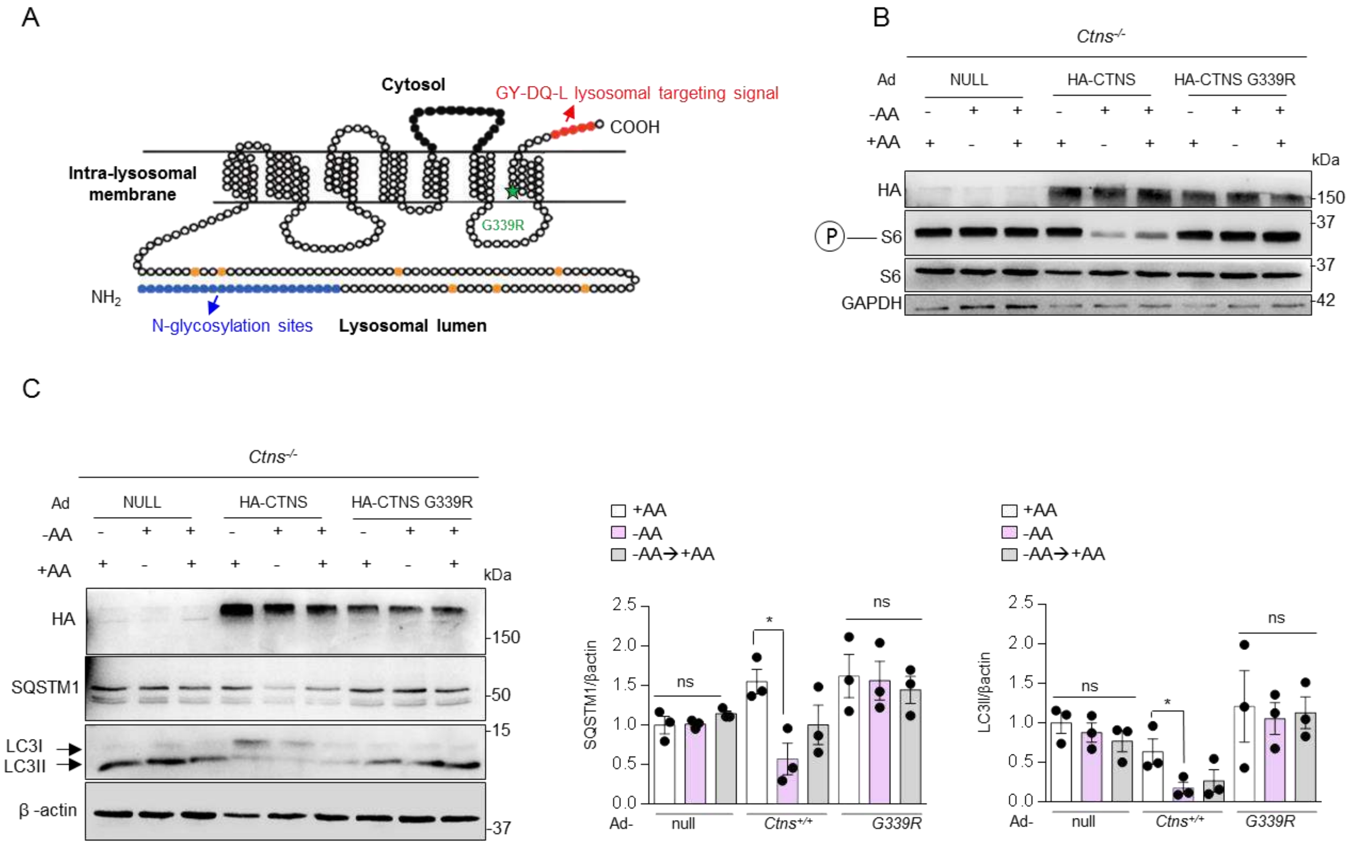

Figure 5. Cystinosin transport activity is key for maintaining mTORC1 sensing and lyso-autophagy flux. (**A**) Schematic representation of the predicted cystinosin structure. Blue indicates the N-terminal uncleavable signal peptide, orange indicates the seven potential N-glycosylation sites, black indicates the third cytoplasmic loop, and red indicates the C-terminal GY-DQ-L lysosomal targeting signal. A green star in the sixth transmembrane domain associated with cystine transport indicated the position of the G339R missense mutation. (**B-C**) *Ctns* mPTCs were transduced with either Null (Ad-NULL) or hemagglutinin-tagged CTNS (Ad- HA-CTNS) or hemagglutinin-tagged CTNS G339R (Ad-HA-CTNS G339R) bearing adenoviral particles for 2 days. (**B**) Western blotting of Hemagglutinin tag (HA) and the phosphorylated and total form of S6 protein level in *Ctns* mPTCs in basal, starved (RPMI, 120 minutes) or amino acids replenished (60 minutes) condition. GAPDH was used as loading control. (**C**) Western blotting and densitometry analyses of Hemagglutinin tag (HA), SQSTM1 and LC3 protein level in *Ctns* mPTCs in basal, starved (RPMI, 120 minutes) or amino acids (60 minutes) replenished condition (n=3 mice per group). β-actin was used as loading control. Plotted data represent mean ± SEM; two tailed unpaired Student's *t* test, $^{*}P < 0.05$, relative to starved *Ctns*$^{+/+}$or *Ctns*$^{-/-}$ mPTCs.

Figure 6

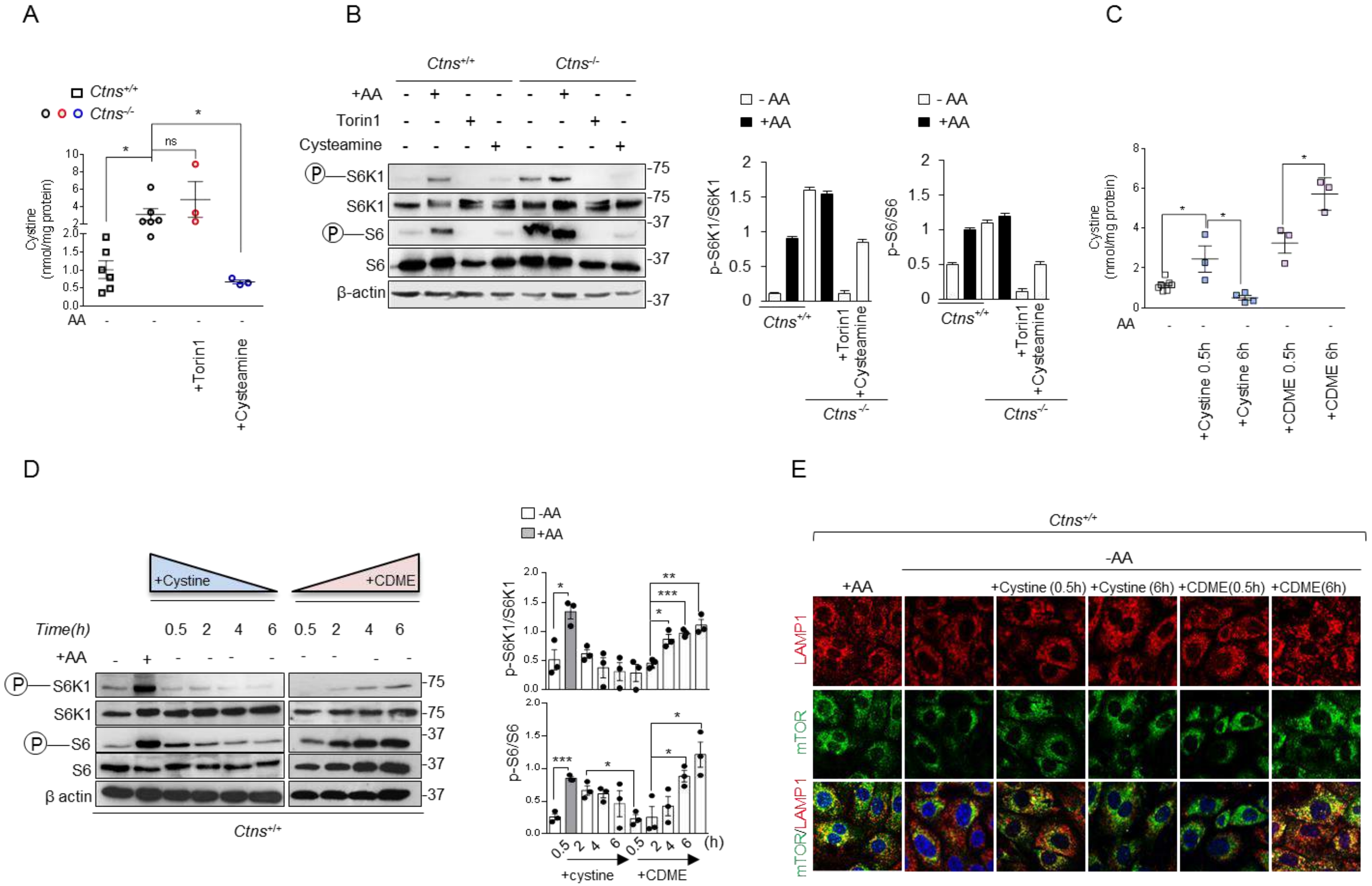

Figure 6. Cystine accumulation drives mTORC1 activation. (**A**) Cystine levels in *Ctns* mPTCs either starved (RPMI, 120 minutes) or starved and supplemented with Torin1 (250 nM) or cysteamine (100 µM) were assessed by HPLC (*Ctns*$^{+/+}$ starved n=6 ; *Ctns*$^{-/-}$ starved n=6; *Ctns*$^{-/-}$ starved +Torin1 n=3; *Ctns*$^{-/-}$ starved +Cysteamine n=3; two tailed unpaired Student's *t* test, *P < 0.05, relative to starved *Ctns*$^{-/-}$ mPTCs) (**B**) Western blotting and densitometry analyses of phosphorylated and total form of S6 K1 and S6 protein levels in starved (RPMI, 120 minutes), amino acids replenished (60 minutes) and starved *Ctns* mPTCs supplemented with either Torin1 (250 nM) or cysteamine (100 µM). β-actin was used as loading control (n=2 mice per group). (**C**) Cystine levels in *Ctns*$^{+/+}$ mPTCs either starved (RPMI, 120 minutes) or starved and supplemented with Cystine (0.15 mM) or supplemented with CDME (0.15 mM), at the indicated time points, were assessed by HPLC (starved n=7 ; +Cystine 0.5h n=3; +Cystine 6h n=4; +CDME 0.5h n=3; +CDME 6h n=3; two tailed unpaired Student's *t* test, ***P < 0.001, relative to *Ctns*$^{+/+}$ mPTCs +Cystine 0.5h or +CDME 0.5h). (**D**) Western blotting and densitometry analyses of phosphorylated and total form of S6 K1 and S6 protein levels in starved (RPMI, 120 minutes), amino acids replenished (60 minutes) and starved *Ctns*$^{+/+}$ mPTCs supplemented with either Cystine (0.15 mM) or CDME (0.15mM) at the indicated time point. β-actin was used as loading control (two tailed unpaired Student's *t* test, *P < 0.05, ***P*<0.01, ****P*<0.001 relative to starved or cystine or CDME replenished *Ctns*$^{+/+}$ mPTCs at the indicated time points; n=3 mice per group). (**E**) Starved (RPMI, 120 minutes), amino acids replenished (60 minutes) and starved *Ctns*$^{+/+}$ mPTCs supplemented with either Cystine (0.15 mM) or CDME (0.15mM) were immune-stained with anti-mTOR (green) and anti-LAMP1 (red) antibodies and analysed at the indicated time point. Plotted data represent mean ± SEM;. Nuclei counterstained with DAPI (blue).

Figure 7

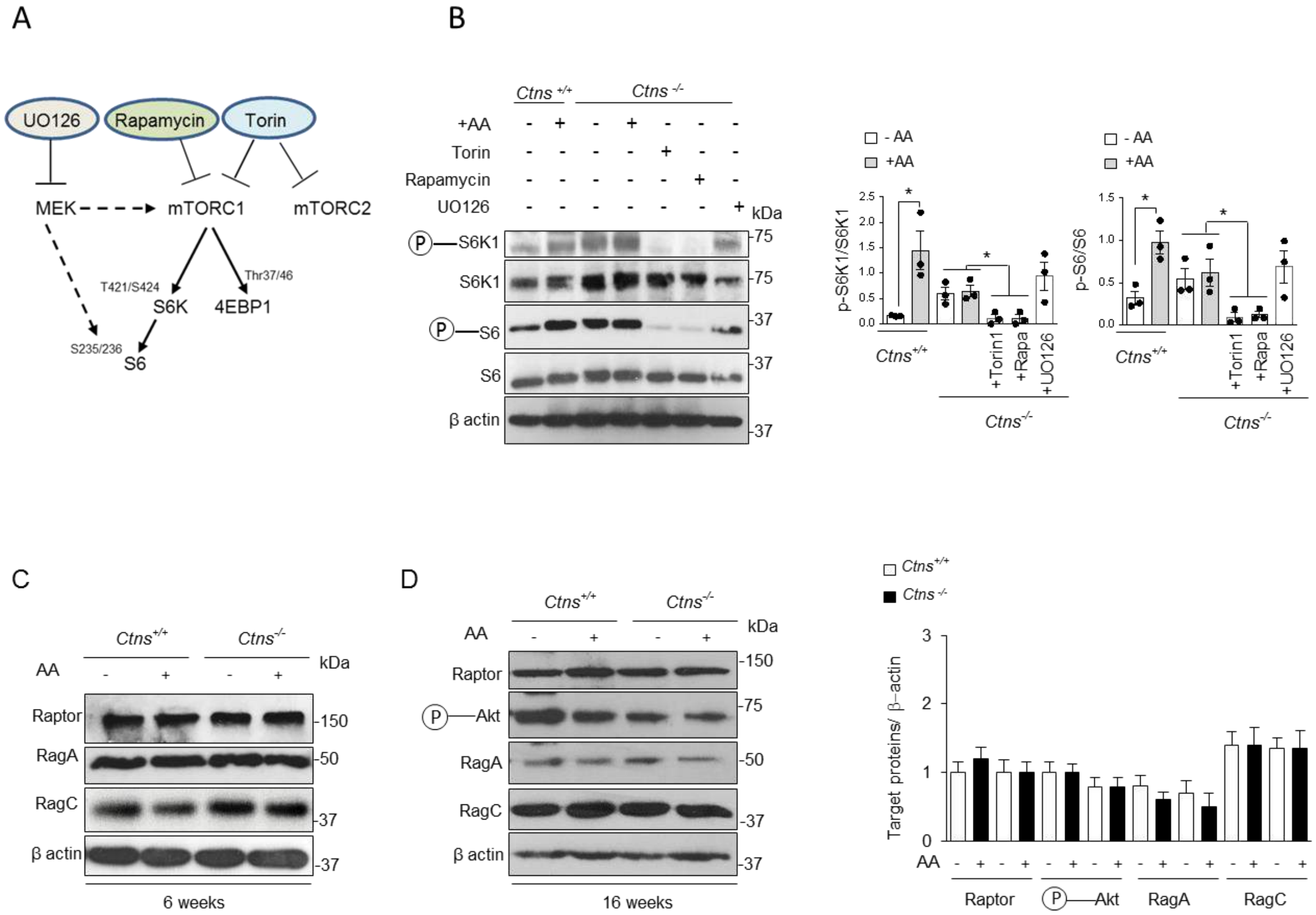

Figure 7. mTORC1 signaling is independent on MAPK/ERK pathway or homeostatic changes of its regulatory subunits in *Ctns*$^{-/-}$ mPTCs. (**A**) Graphical scheme showing the molecular pathways inhibited by UO126, Rapamycin and Torin1. (**B**) Western blotting and densitometry analyses of phosphorylated and total form of S6 K1 and S6 protein levels in starved (RPMI, 120 minutes), amino acids replenished (60 minutes) and starved mPTCs supplemented with either Torin (250 nM) or Rapamycin (1µM) or U0126 (50 µM) . β-actin was used as loading control (two tailed unpaired Student's *t* test, *P < 0.05; relative to starved or amino acids replenished *Ctns*$^{+/+}$or *Ctns*$^{-/-}$ mPTCs n=3 mice per group). (**C-D**) Western blotting and densitometry analyses of Raptor, RAG A, RAG C and p-AKT protein levels in starved (RPMI, 120 minutes) and amino acids replenished (60 minutes) mPTCs derived from 6 and 16 weeks *Ctns* mice. Plotted data represent mean ± SEM.

Figure 8

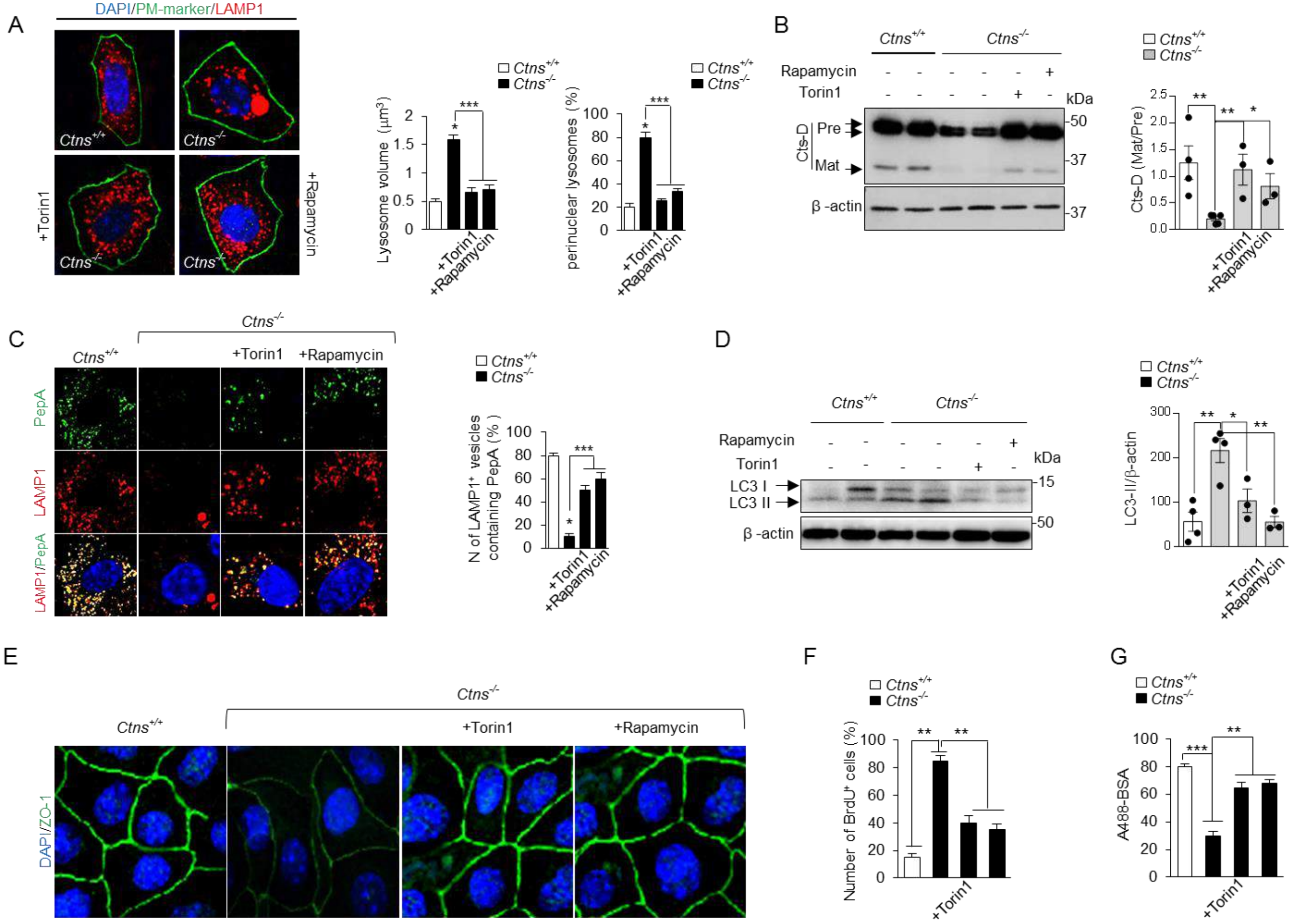

Figure 8. mTORC1 Inhibition in *Ctns*$^{-/-}$ mPTCs rescues lyso-autophagy pathway & downstream PT dysfunction. (**A-G**) *Ctns* mPTCs were analysed in either baseline or in media supplemented with Torin1 (250 nM) or Rapamycin (1µM). (**A**) *Ctns* mPTCs were immune-stained with anti-PM marker (green) and anti-LAMP1 (red) antibodies. Quantification of the size and position of LAMP1^{+} vesicles (n =5 randomly selected fields per condition, with each containing ~ 20–25 cells). (**B** and **D**) Western blotting and densitometry analysis of Cts-D and LC3 protein levels in *Ctns* mPTCs (**C**) *Ctns* mPTCs were loaded with Bodipy-FL-PepA (1 µM, for 1 h at 37 °C, green), immunostained with anti-LAMP1 antibody (red) and analysed by confocal microscopy. Quantification of numbers of PepA/LAMP1+ structures (in percentage of total lysosomes; n = 5 randomly selected fields per condition, with each containing ~ 20–25 cell). (**E**) *Ctns* mPTCs were immunostained with anti-ZO-1 (green) antibody and analysed by confocal microscopy. (**F**) *Ctns* mPTCs were loaded with bromodeoxyuridine, immunostained with anti-BrdU antibody and analysed by confocal microscopy. Quantification of numbers of BrdU+ cells (in percentage of total nuclei) obtained from five randomly selected fields per condition, with each containing ~ 20–25 cells. (**G**) *Ctns* mPTCs were loaded with Al647-BSA and imaged by confocal microscopy. Quantification of numbers of Al647-BSA+ structures (n = 49–85 cells pooled from three mouse kidneys per condition; each point representing the number of BSA+ structures in a cell). Plotted data represent mean ± SEM; two tailed unpaired Student's *t* test, *P < 0.05, ***P*<0.01, ****P*<0.001 relative to *Ctns*$^{+/+}$or *Ctns*$^{-/-}$ mPTCs in basal condition. Nuclei counterstained with DAPI (blue)

Aberrant mTORC1 Activation Underlies Proximal Tubule Dysfunction Associated with Lysosomal Storage in Cystinosis

Beatrice Paola Festa, Patrick Krohn, Marine Berquez, Alessio Cremonesi, Huguette Debaix, Alessandro Luciani and Olivier Devuyst

Supplementary Information

Suppl. Figures 1-4

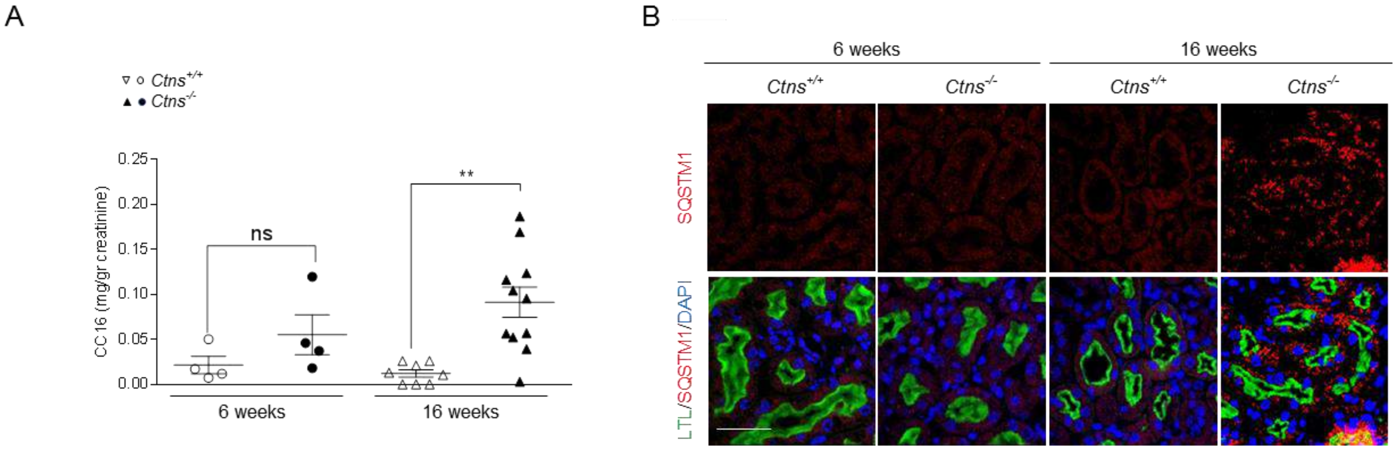

Supplementary Figure 1. Proximal tubular dysfunction and impaired autophagy in Ctns$^{-/-}$ mouse kidneys. (**A**) CC16 was measured by Elisa in urine collected from 6 (n=4 mice per group) and 16 weeks old mice (two-tailed unpaired Student's t-test, $**P<0.01$ relative to 16 weeks old *Ctns*$^{+/+}$, n=8-11 mice per group). (**B**) Representative confocal micrographs of SQSTM1 structures (red) and LTL (green) proximal tubules from 6 and 16 weeks old *Ctns* mouse kidneys. Nuclei counterstained with DAPI (blue).

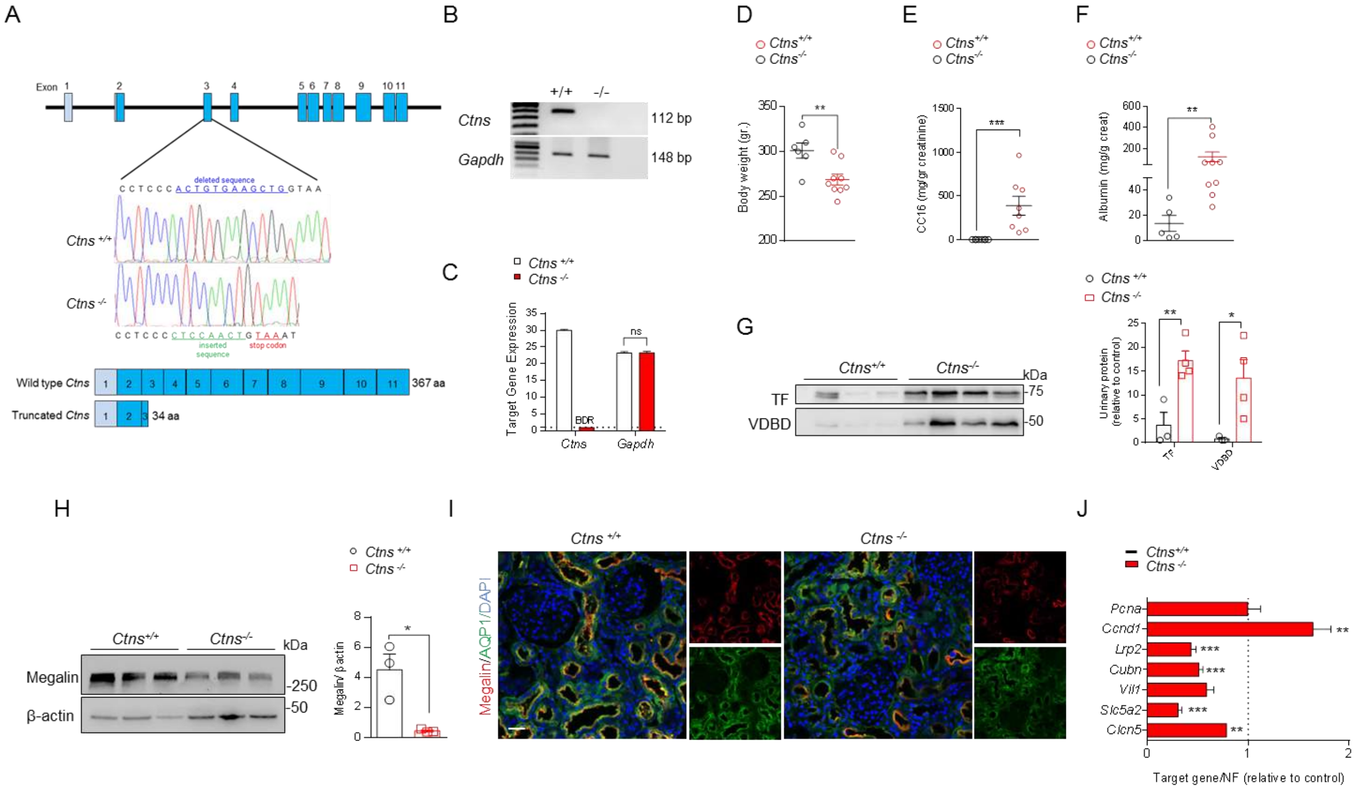

Supplementary Figure 2. Validation of the proximal tubule dysfunction in *Ctns*$^{-/-}$ rat model. (**A**) CRISPR/Cas9- induced deletion (blue)/insertion (green), generates a frame shift of the open reading frame, resulting in premature stop codon (TGA, red) in exon 3. (**B**) Genomic DNA analyses of *Ctns* and *Gapdh* by PCR and agarose gel electrophoresis isolated from kidney biopsies of *Ctns* rats. (**C**) *Ctns* and *Gapdh* expression in kidneys biopsies were analyzed by quantitative RT-PCR. (n=3 rats per group). (**D**) Dot plot representing the measurement of body weight (n= 6-9 rats per group), (**E**) urinary CC16 (n=6-8 rats per group) and (**F**) urinary albumin (n= 5-9 rats per group). (**G**) Western blotting and densitometry analyses of urinary Transferrin (TF) and Vitamin D Binding Protein (VDBP) (n= 3-4 rats per group). (**H**) Western blotting and densitometry quantification of Megalin in kidneys lysates (n= 3 rats per group). (**I**) Kidneys were immune-stained with anti- Megalin (red) antibody and stained afterwards with AQP1 (green, proximal tubule marker). Nuclei counterstained with DAPI (blue). Scale bars: 25 µm. (**J**) The mRNA kidney levels of *Pcna*, *Ccnd1*, *Lrp2*, *Cubn*, *Vil1*, *Slc5a2* and *Clcn5* were analyzed by real-time qPCR. Gene target expression normalized to NF and relative to *Ctns*$^{+/+}$ rats (n = 5 rats per group). All the urine parameters were normalized to urinary creatinine concentration. Plotted data represent mean ± SEM. Two-tailed unpaired Student's t-test, $^{*}P < 0.05$, $^{**}P<0.01$, $^{***}P<0.001$ relative *Ctns*$^{+/+}$ rats.

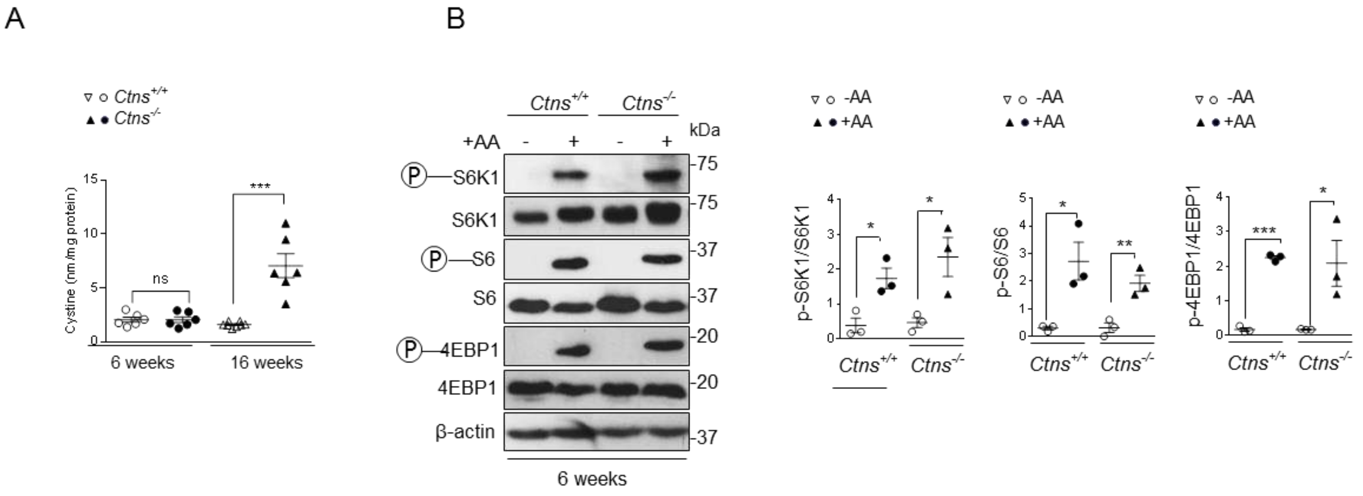

Supplementary Figure 3. mTORC1 sensing in mPTCs derived from *Ctns*$^{-/-}$asymptomatic mice. (**A**) Intracellular cystine levels were measured by HPLC in mPTCs derived from 6 (two-tailed unpaired Student's t-test, ns, not significant, n=6 mice per group) and 16 week old (two-tailed unpaired Student's t-test, ***P<0.001, n=6 mice per group) *Ctns* mice. (**B**) Western blotting and densitometry analyses of phosphorylated and total form of S6 K1, S6 and 4EBP1 protein levels in starved (RPMI, 120 minutes) and amino acids replenished (60 minutes) 6 weeks old *Ctns* mPTCs. β-actin was used as loading control (n=3 mice per group). Plotted data represent mean ± SEM; two tailed unpaired Student's *t* test, *P < 0.05, **P<0.01, ***P<0.001 relative to starved or amino acids replenished *Ctns*$^{+/+}$or *Ctns*$^{-/-}$ mPTCs.

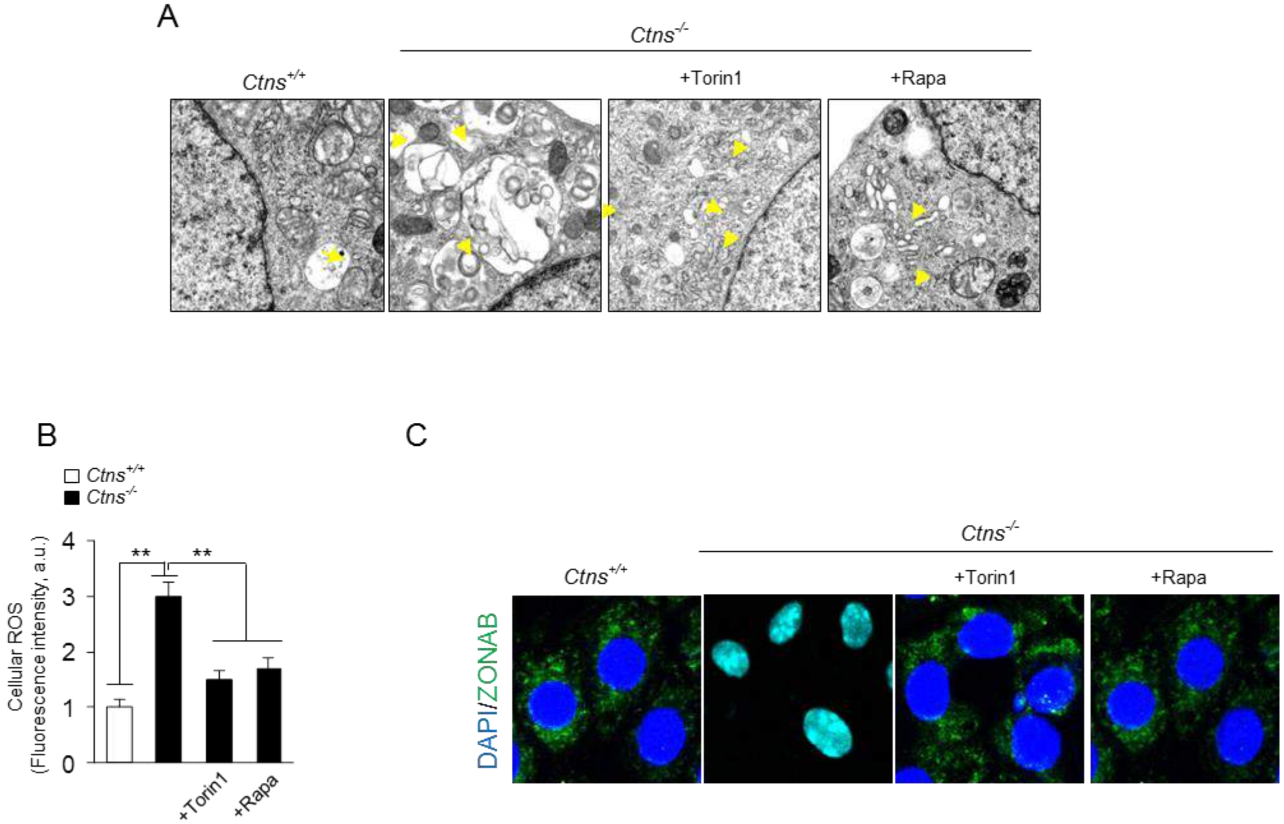

Supplementary Figure 4. mTORC1 Inhibition in $Ctns^{-/-}$ **mPTCs rescues PT dysfunction and reduces intracellular accumulation of ROS** (**A-C**) mPTCs were analysed in either baseline or in media supplemented with Torin1 (250 nM) or Rapamycin (1µM). (**A**) Representative electron micrograph of autophagic vesicles in *Ctns* mPTCs (**B**) *Ctns* mPTCs were loaded with CellROX (cellular ROS probe; 5 µM for 10 min at 37 °C) and analysed by live confocal microscopy. Quantification of CellROX fluorescence intensity was obtained from five randomly selected fields per condition, with each containing ~ 20–25 cells (**C**) mPTCs were immunostained with anti-ZONAB (green) antibody and analysed by confocal microscopy. Nuclei counterstained with DAPI (blue). Plotted data represent mean ± SEM; two tailed unpaired Student's *t* test, $^{*}P < 0.05$, $^{***}P<0.001$ relative to $Ctns^{+/+}$or $Ctns^{-/-}$ mPTCs in basal condition.

IV. DISCUSSION AND PERSPECTIVES

The epithelial cells lining the PT of the kidney carry out the reabsorption of ~80% of ions and solutes, which are daily filtered through the glomerulus and that would otherwise be lost in the urine. The expression of multi-ligand endocytic receptors megalin and cubilin and the recycling-degradative activity of the endolysosomal network sustain the terminal differentiation of the epithelial PT cells, hence their reabsorptive activity (107). Rare, congenital disorders involving the endocytic receptors (e.g. Donnai–Barrow and Imerslund-Gräsbeck syndrome) or the endolysosomal pathway (e.g. Dent disease 1 and 2, Lowe syndrome and cystinosis) cause PT dysfunctions, associated with RFS and severe metabolic complications including CKD (87). Although these disorders show marked clinical overlap, their genetic causes are heterogeneous and affect proteins with very different roles along the endolysosomal compartment. *CLCN5*, mutated in Dent disease 1, encodes an electrogenic H^+/Cl^- exchange transporter 5 (ClC-5), which contributes to the acidification of EEs (86). *OCRL*, mutated in Dent disease 2/Lowe syndrome, encodes an inositol polyphosphate 5-phosphatase OCRL acting at the clathrin-coated vesicles, EEs and lysosomes where it controls the homeostasis of $PI(4,5)P_2$ -essential modulators of membrane trafficking (34). Finally, *CTNS*, mutated in cystinosis, encodes a H^+-coupled lysosomal transporter, allowing the export of cystine from the lysosomal lumen to the cytosol (96). Although the past two decades have witnessed tremendous progresses in understanding the role of ClC-5, OCRL and CTNS in maintaining the endolysosomal trafficking, further work is needed to understand the molecular mechanisms linking loss of function of these proteins with disorders of the kidney PT. The lack of adequate cellular models phenocopying critical aspects of epithelial transport and the absence of animal models mimicking the PT diseases hinder the progression of these investigations. In this thesis, in order to elucidate how loss of function of endolysosomal genes lead to PT dysfunction, we characterized faithful disease mouse models for Dent disease, Lowe Syndrome and nephropathic cystinosis and derived well differentiated primary culture of PT cells from the kidneys of these disease-mouse models. By using cutting-edge technologies and genetic and pharmacological manipulations *in vitro* and *in vivo*, we unveiled new pathogenic cascades linking defects in endocytosis, vesicular trafficking, lysosomal function and autophagy with the loss of differentiation and function of PT cells. These studies allowed us to validate new druggable targets for endolysosomal disorders affecting the kidney PT.

In the first part of this thesis, we characterized the first OCRL-deficient mouse model mimicking renal and extra-renal manifestations encountered in patients with Dent disease 2/Lowe syndrome. Our studies show that OCRL-deficient mice exhibit locomotor defects and a global impairment of the muscular apparatus. Furthermore, the absence of OCRL drives endolysosomal defects and epithelial dysfunction in the kidney PT resulting in LMW proteinuria. In this work, we also evidenced a partial convergence of disease-mechanisms and kidney tubular dysfunction between mouse models deficient in ClC-5 (Dent disease1) and OCRL (Lowe syndrome/ Dent disease 2). Altogether, these findings provide new insights into the mechanisms of endocytosis and the pathogenesis of Dent disease/Lowe syndrome.

One of the major limitations to assess the role of OCRL in the pathogenesis of PT dysfunction is the lack of OCRL-deficient mouse models that faithfully reproduce the clinical phenotype described in patients. Indeed, *Ocrl* KO mice show no kidney, eye or brain defects. The absence of kidney phenotype in *Ocrl* KO mice is due to the compensatory role of INPP5B, the closest paralogue of OCRL in mice and humans (45% of sequence identity) (108). Indeed, the double kidney tubular deletion of OCRL and INPP5B in mice results in a remarkable PT endocytic dysfunction phenocopying the kidney defect observed in Dent disease 2/Lowe syndrome (109). Despite the clinical similarity with the human disorders, investigations of this mouse strain do not allow to discriminate the individual biological role of OCRL and INPP5B in the pathophysiology of the kidney disease. In our studies, we overcame this issue by using a mouse model where mouse *Inpp5b* was replaced by human *INPP5B* in a whole body *Ocrl*$^{Y/-}$ mouse (92). The reinsertion of the human gene did not compensate for the PT endocytic defect caused by the loss of OCRL function and provided a genetic background, which allowed the identification of cellular dysfunctions due to the single loss of OCRL activity. How INPP5B compensates the PT endocytic defects caused by the loss of OCRL function in mice but not in human remains unclear. Although these two enzymes share many common interactors and present similar intracellular localization, OCRL is involved in the process of endocytosis in PT cells but not INPP5B (34). Thus, it is unlikely that differences in the expression or splicing of INPP5B between mice and human can fully account for the compensation of the endocytic defect observed in *Ocrl* KO mice. More studies are required to understand the mechanisms underlying the murine rescue operated by *Inpp5b*.

The *Ocrl*$^{Y/-}$ mice exhibited a specific defect in clathrin-receptor mediated endocytosis (110), which was mirrored by a selective LMW proteinuria occurring early and in absence of changes in other urine metabolites or signs of renal failure. These data indicate that *Ocrl*$^{Y/-}$ transgenic mice faithfully mimics the partial Fanconi syndrome described in the majority of patients carrying mutations in *OCRL* (34), thus validate this *in vivo* system as a reliable tool for kidney therapeutic interventions. The LMW proteins are reabsorbed by megalin (LRP2) and cubilin endocytic receptors expressed at the apical membrane of PT cells (107). Our analysis revealed a remarkable decrease of megalin receptor in the kidneys of OCRL-deficient mice. These data explain the massive LMW proteinuria observed in *Ocrl*$^{Y/-}$ transgenic mice and are in line with previous results obtained from *ocrl*$^{-/-}$ zebrafish model, demonstrating the evolutionary conservation of the role of OCRL in endocytosis (111).

When we compared the renal phenotype of OCRL-deficient mice with those of ClC-5-deficient mice, we observed an overlap of many pathological features. Also *Clcn5*$^{Y/-}$ mice showed a defective megalin expression associated with an impaired RME and LMW proteinuria. However, this mouse model presented a PT dysfunction, which was more severe compared to the OCRL-deficient mice with extended defects to the fluid-phase endocytosis and a complete Fanconi syndrome characterized by glycosuria, phosphaturia and calciuria. These differences could be explained by the broader function of ClC-5 compared to OCRL during the endocytic process. Despite both proteins have been described to be involved in the modulation of actin during the maturation steps of the clathrin-mediated endocytosis, ClC-5 plays an additional role in sustaining the acidification of apical early endosomes, which is key for the global trafficking of the endosomal-recycling compartment (90, 91). Accordingly, the loss of ClC-5 function would result in a wider dysfunction of the apical apparatus of PT cells. This could explain why the transport defects observed in the ClC-5-deficient mouse model were extended also to substances, which are not reabsorbed via receptor-mediated processes. On the contrary, OCRL function is specifically involved in clathrin-mediated endocytosis, which is needed for the receptor-mediated uptake of proteins (91). This would explain the selective LMW proteinuria observed in Lowe syndrome mouse model. Further studies are needed to better understand the cross-talk between these two proteins and their biological overlapping functions.

The mechanism by which the loss of OCRL or ClC-5 might affect megalin protein levels remains to be clarified. A transcriptional effect seems unlikely, as we did not observe changes in *Lrp2* mRNA levels between control and OCRL- or ClC-5 -deficient mice. The decrease of apical megalin may reflect an increased shedding of the receptor in the urine in response to the endolysosomal engorgement observed in our disease mouse models (17). Preliminary data (not shown in this thesis) indicating a higher abundance of megalin/LRP2 fragments in *Ocrl*$^{Y/-}$ urines compared to controls, support this hypothesis. By contrast, no megalin fragments were detected in the urines of *Clcn5*$^{Y/-}$ mice, suggesting that the absence of ClC-5 does not trigger the mechanism of shedding. These differences might be related to the specific roles of OCRL or ClC-5 in the homeostasis of PT cells. For instance, the lack of OCRL severely disrupts membrane trafficking and induces the misrouting of lysosome enzymes to the plasma membrane (see below, 91). This event could result in an increased concentration of proteases at the apical surface and in the urine (112), which would facilitate the cleavage of the endocytic receptors and their release in the lumen. Although we observed a defective lysosomal function in ClC-5 deficient cells, this defect is not characterized by mis-trafficking of the lysosomal enzymes (data not shown) but rather due to defective acidification of the endolysosomal compartment (113), which impairs lysosomal proteolysis. The latter could drive an aberrant degradative response from the proteasome compartment, which in turn could increase the turnover of megalin. The rescue of megalin levels observed in ClC-5 deficient cells upon inhibition of proteasome activity supports this hypothesis (data not shown). Further studies have to address whether additional pathophysiological mechanisms contribute to the reduction of megalin in our models (eg. urinary excretion of LRP2-containing exosomes) (114). Because impaired homeostasis of megalin is a central event in the pathogenesis of Lowe syndrome and Dent disease, these insights could help to identify crucial targets for therapeutic approaches.

Despite the marked decrease of megalin, a significant pool of this receptor was still detected in *Ocrl*$^{Y/-}$ kidneys. Given the dramatic loss of LMW proteins in the urine, we reasoned that this pool was not active. To further explore the trafficking defects, which could impede the reabsorptive function of the residual megalin receptor, we investigated differentiated and polarized primary cultures of proximal tubular cell (mPTCs) derived from the kidneys of *Ocrl*$^{Y/-}$ mice (115). These cells recapitulated critical aspects of the disease *in vitro,* including the ectopic accumulation of PI(4,5)P_2 at the EEs (116, 117). The dynamic of these phosphoinositides is critical for actin assembly at the plasma membrane ruffles and early endosomes, hence, for the regulation of membrane trafficking during endocytosis (118). Accordingly, the endosomal accumulation of PI(4,5)P_2 in *Ocrl*$^{Y/-}$ mPTCs triggers an aberrant F-actin polymerization, which impairs the recycling of residual megalin, thus impeding the endocytic uptake. Further analysis evidencing an intracellular redistribution of CI-MPR and TfR (Transferrin Receptor) suggested that this actin-trapping mechanism might affect the trafficking of other receptors crossing the EEs (91). Hence, this mechanism represents an appealing druggable target for rescuing the epithelial dysfunction associated with the disease.

Previous studies have used pharmacological (Latrunculin B) approaches to sequester actin monomers or genetic approaches (silencing of N-WASP or SNX9) to inhibit the actin nucleating machinery. Both approaches led to alleviation of actin phenotypes and defective endocytic uptake in both kidney cells and fibroblasts derived from patients (91, 119). Since the actin defects depend on the aberrant accumulation of PI(4,5)$P_{2,}$ restoring the correct levels of these phosphoinositides represents an additional therapeutic strategy (91). In recent years multiple efforts have been directed in the development of drugs targeting these molecular pathways and suitable for human use. Along these lines, recent studies from *Daste et al.,* demonstrate that in addition to PI(4,5)P_2, the presence of PI(3)P is fundamental to catalyse actin assembly at the membranes of the endocytic pathway (120, 33). They demonstrated that PI(3)P is an important mediator in the actin comet phenotype in *Ocrl* knockout RPE cells using PI3-kinase inhibitors (120). The possible application of PI3-kinase inhibitors in Lowe syndrome is significant because PI 3-kinases are a major drug target in developing cancer therapeutics, and there are a range of drugs already approved and others, with isoform selectivity, in clinical trials (121). As Lowe syndrome is a rare disease, repurposing an existing therapeutic treatment is a time and cost effective option.

It has been recently shown that upon cargo arrival in the lysosomal lumen OCRL translocates on the lysosomes to degrade PI(4,5)P_2. This event is fundamental for enabling lysosomal activity under cargo overload conditions (122). Here, we demonstrated that the lack of OCRL induced an abnormal lysosome accumulation of PI(4,5)P_2 , which resulted in perturbed lysosome dynamics and proteolytic function *in vivo* and *in vitro*. The impairment of lysosomal function could be due to the mis-trafficking of the receptors regulating the transport of lysosome enzymes from the Golgi to the endosomes to the lysosomal compartment. Our data showing a peripheral mis-localization of the CI-MPR (which is a carrier of cathepsin D), along with increased levels of cathepsin D in the plasma support this hypothesis.

Defects in lysosomal proteolysis could trigger a block of the autophagy flux. Studies in human immortalized cells show that the lack of OCRL induces an accumulation of autophagosomes due to an impairment of lysosomal-autophagosomal fusion (122). On the contrary, in our preliminary data obtained from kidneys and cells from *Ocrl*$^{Y/-}$ mice (data not shown), the amount of autophagosomes was reduced rather than increased. The same decrease was observed in presence of Bafylomycin, thus excluding the possibility of an accelerated lysosomal degradation of autophagosomes. Hence, we are tempted to speculate that the decreased autophagosomal levels detected in our system could be caused by a decrease autophagosomal biogenesis. This could be a plausible hypothesis if we take in account that the endocytic pathway is fundamental for the transport of ATG (autophagy related) proteins to the platforms for autophagosomal biogenesis and OCRL-deficient mice exhibit strong endocytic defects (123). Furthers studies are needed to clarify the molecular mechanisms, which operate in different species in absence of OCRL function.

Despite the marked kidney PT dysfunction and mild muscular and locomotor defects, OCRL-deficient mice did not show any sign of neurological or behavioural abnormalities, classically associated with the human disease. This discrepancy between mice and humans could be partly explained by interspecies differences in the brain-specific expression of enzymes with similar functions or in the role of OCRL in neurons. Indeed, previous studies suggest a partial overlapping function between OCRL and the 5-phosphatase Synaptojanin 1 in the brain (124). The lack of OCRL in patient-derived cells disrupts the homeostasis of $PI(4,5)P_2$ and causes endocytic defects similar to those observed in absence of Synaptojanin 1 (125). However, while Synaptojanin 1 is the key player in clathrin-mediated endocytosis at synapses, OCRL may function at clathrin-coated pits that participate in a housekeeping form of endocytosis in neurons (119). This would explain why disruption of OCRL function leads to the cognitive deficiencies observed in Lowe syndrome patients. Based on these considerations, we could hypothesize that in the mouse brain Synaptojanin 1 could compensate for OCRL, explaining the absence of neurological symptoms in OCRL-deficient mice. Future investigations (e.g. double KO) using the mouse model that we describe in this thesis could help to substantiate these speculations.

These enzymatic compensations (INPP5B, potentially Synaptojanin 1) are relevant for the design of therapeutic interventions. The cellular aberrations observed in absence of the 5-phosphatase activity of OCRL are primarily due the disruption of $PI(4,5)P_2$ homeostasis (91), which is a direct substrate of OCRL and a key regulator of the endolysosomal trafficking. One strategy to rebalance the $PI(4,5)P_2$ pool, in the absence of OCRL, could be to harness the redundancy of the phospholipid enzymes by acting on other kinases and phosphatases involved in the metabolism of these lipids. As phosphoinositides are key for the function of many organs and their perturbation have been described in many diseases, the production of enzymatic inhibitors or activators controlling their metabolism has been a major target for the pharmaceutical companies in the last years and led to the generation of a range of drugs already approved and others in clinical trials (121). A current limitation is that the methodologies used to analyse the phosphoinositides profiles in tissue and cells rely heavily on imaging approaches, which are not rigorous enough for quantitative analyses and barely adaptable to drug-screening purposes. In recent years emerged a great interest to implement these technologies and new methods of quantifications, involving mass spectrometry, are developing (126, 127). Progresses in this direction would facilitate the investigations and validation of novel treatment in Lowe syndrome.

Collectively, these studies validate the first mouse model of Lowe syndrome and provide new insights in the role of OCRL in cellular trafficking of multiligand receptors. Partial convergence of disease-mechanisms and renal phenotype observed in *Ocrl*$^{Y/-}$ and *Clcn5*$^{Y/-}$ mice suggest shared pathological pathway in Dent disease 1 and 2. These insights open new scenario for successful therapeutic interventions in Lowe Syndrome and Dent disease.

In the second part of this thesis, we combined cutting-edge technologies *in vitro* and *in vivo* to decipher the link between lysosomal impairment and epithelial dysfunction in cystinosis. We demonstrated that lysosomal dysfunction results in defective autophagy-mediated clearance of damaged mitochondria, excessive oxidative stress, disruption of TJs integrity and activation of a signalling pathway causing epithelial cell proliferation and dedifferentiation, with loss of reabsorptive capacity of PT cells. This work uncovers the fundamental role of the lysosome-mediated autophagic clearance in safeguarding epithelial differentiation and open new therapeutic options to restore epithelial transport downstream of the primary lysosomal defect.

Since cystinosis is a typical lysosomal storage disorder, we first investigated the lysosomal phenotype of PT cells derived from *Ctns*$^{-/-}$ mice. The loss of CTNS function in PT cells induced a major alteration of the lysosomal dynamics (101, 128), which was paralleled by an increased number of autophagosomes. Similar lysosomes and autophagosomes defects were detected in the pronephric tubules of *Ctns*-deficient zebrafish demonstrating the evolutionary conservation of these disease-pathways across vertebrates. These events along with the accumulation of the autophagy receptor SQSTM1, which is normally degraded within lysosomes, suggest an impairment of the autophagy flux. Further evidences demonstrating the inability of *Ctns*$^{-/-}$ PT cells to degrade autophagy cargo include: (i) the aberrant number of autophagosomes observed under growth conditions, (ii) the failure to clear them under starvation-induced autophagy and (iii) the inability of Bafilomycin to further increase the autophagosomes level. These findings were akin to the block of the autophagy flux observed in other lysosomal storage diseases, indicating that this family of disorders could share similar pathological mechanisms (129). We exclude that these changes in autophagy were related to increased autophagosomes production or to delayed fusion between lysosomes and autophagosomes, as in cystinotic cells the upstream events regulating autophagosomes biogenesis were unaffected and LC3-marked autophagosomes were correctly delivered inside the LAMP1-marked lysosomes. In contrast with our observation, autophagy flux was found to be fully functional in fibroblasts derived from *Ctns*$^{-/-}$ mice (130). The cause for this discrepancy could be related to tissue -specific effects of cystinosin depletion and further studies are required to examine this aspect.

Because the autophagy flux relies on the degradative capacity of lysosomes (129), an impaired lysosomal function may explain the accumulation of autophagosomes in cystinotic cells. Confirming this hypothesis, our data showed that cystinosin deficiency affected lysosome function by inhibiting the processing/maturation of the cathepsins within the endolysosomal compartment. Indeed, the reinsertion of cystinosin in *Ctns*$^{-/-}$ cells resulted in restored maturation of cathepsin D and a rescued autophagy-lysosome degradative activity. Defective processing/maturation of cathepsins could be explained by alterations of the lysosomal acidification due to disrupted activity of the V-ATPase complex in absence of CTNS. This hypothesis is supported by recent studies showing that V-ATPase is part of CTNS interactome, thus the activity of these proteins could be interconnected (102). We exclude that the decreased cathepsin D activation was due to a defective delivery of the enzymes from the Golgi to the lysosomal compartment, as no changes in the trafficking of this protease were observed in cystinotic cells. Altogether these findings suggest a role of cystinosin -beyond its cystine transport activity- in maintaining the lysosomal function. Alternatively, defective lysosomal proteolysis can result from dysregulation of mTORC1-master regulator of lysosomal biogenesis and autophagy. As mTORC1 is activated by raised amino acids concentration inside lysosomes, we thought that cystine lysosomal storage might sustain mTORC1 activity and negatively regulate lysosome function by suppressing TFEB/MiTF signaling (104). This hypothesis has been explored in the third part of this thesis.

The association of impaired lysosomal dynamics and altered degradative capacity observed in cystinotic cells and mice is strikingly similar to the cellular changes caused by the endolysosomal accumulation of $PI(4,5)P_2$ detected in patients and mice with Lowe syndrome (122). These data suggest that lysosomal accumulation of cystine or $PI(4,5)P_2$ may have similar functional consequences on the epithelial phenotype, emphasizing the role of endolysosomes as crucial signaling hub to ensure cellular homeostasis.

Regardless of the mechanisms, the block of the autophagy flux detected in *Ctns*$^{-/-}$ PT cells leads to the accumulation of autophagy substrates, such as ubiquitinated proteins and dysfunctional, ROS-producing mitochondria. This is in line with previous studies reporting similar results in other lysosomal storage disorders with deficit in autophagy and substantiates the importance of autophagy as cellular quality control machinery preserving the integrity of subcellular compartments, especially mitochondria (131, 132). Similar to our findings in the cystinosis model, genetic or pharmacologic blockage of basal autophagy in PT cells resulted in disrupted mitochondria homeostasis leading to apical dedifferentiation and consequent decrease in the uptake capacity. These data highlight the importance of maintaining a healthy mitochondria pool to sustain the transport activity of PT cells.

The next step was to identify the mechanisms bridging the excessive accumulation of damaged mitochondria-producing ROS and epithelial dysfunction. Recent advances have shown the role of TJs in safeguarding epithelial cell function. In particular, the TJ protein ZO-1 represses the nuclear translocation of ZONAB, a transcriptional factor that promotes cell proliferation and inhibits PT differentiation during kidney ontogeny (83).Of note; previous studies demonstrate that

TJs integrity is very sensitive to the level of oxidative stress. Accordingly, we found that increased levels of mitochondrial ROS in *Ctns*$^{-/-}$ cells induced a Gα12-Src mediated phosphorylation of the ZO-1 and its consequent misrouting to enlarged, non-degradative endolysosomes (79, 133). In turn, the loss of TJs integrity promotes ZONAB signaling and the transcription of target genes increasing cell proliferation and decreasing cell differentiation resulting in defective endocytosis. Gain- and loss-of-function approaches targeting Gα12 or ZO-1/ZONAB axis and pharmacological interventions neutralizing oxidative stress or blocking the activation of Gα12/Src signaling (eg. Src-inhibitors) restored epithelial function in *Ctns*$^{-/-}$ PT cells, indicating the key role of these pathways in maintaining the PT transport activity. Aberrations of ZO-1-1/ZONAB axis were observed in other disorders characterized by epithelial dysfunction, such as cystic fibrosis and RFS caused by PT accumulation of κ light chains (134, 135). These findings highlight the importance of TJs as essential regulators of epithelial cell differentiation.

The identification of mitochondria oxidative stress as a central event in the pathogenesis of cystinosis allowed us to set up a mitochondrial-targeted therapeutic intervention with Mito-TEMPO anti-oxidant, which significantly rescued the integrity of TJs and the differentiation and endocytic uptake capacity of *Ctns*$^{-/-}$ PT cells. These data extend the previous findings showing that swan-neck deformities of PT segments could be delayed in *Ctns*$^{-/-}$ mice by administrating mitoquinone, an anti-oxidant compound that acts on mitochondria (136).

Altogether these studies decipher the pathogenic cascade bridging lyso-autophagy defects with impaired epithelial transport activity in cystinosis, thus offering new druggable targets for therapeutics. However, how the lack of CTNS compromises the identity of the lysosome and disrupts the autophagy pathway driving PT dysfunction remained unclear. We decided to examine this aspect in the last chapter of the thesis.

In the third part of this thesis, we demonstrate that cystine accumulation in cystinosis triggers the hyper-activation of mTORC1, which in turn, drives the progression of the lysosomal disease leading to autophagy defects and consequent PT dysfunction. Alterations of mTORC1 were detected in *Ctns*$^{-/-}$ mouse and rat models, demonstrating the evolutionary conservation of this disease-mechanism. *In vitro* treatment with specific and powerful mTORC1 inhibitors rescued the primary lysosomal defect and the downstream pathogenic cascade associated to it, thus improving the function of cystinotic PT cells. Collectively, these studies unveiled a novel link between defective mTORC1 activity, lysosome-autophagy degradation pathways and epithelial dysfunction in cystinosis, thus providing new therapeutic perspectives for this and similar lysosomal storage disorders.

By performing time-course analyses on the kidneys of *Ctns*$^{-/-}$ mice, we noticed that signs of lysosome dysfunction were already shown in presymptomatic mice in absence of alterations related to cystine homeostasis, autophagy and PT function. The lysosome dysfunction became more prominent in the symptomatic stage, where it was accompanied by the simultaneous appearance of raised level of cystine, autophagy defects and LMW proteinuria. These data are in line with previous studies investigating the time course of the pathological events characterizing the progression of the kidney disease in *Ctns*$^{-/-}$ mice. Indeed, *Chevronnay et al.* demonstrated that a mild impairment of lysosomal morphology in cystinotic mice precedes the formation of cystine crystals and appears when the PT dysfunction is barely detectable. They also showed that lysosomal disruption becomes more severe when cystine crystallizes inside the lysosomal lumen. This event was concomitant to the onset of Fanconi syndrome and PT dedifferentiation. Interestingly, the authors suggest a compensatory mechanism of lysosomal exocytosis in *Ctns*$^{-/-}$ mice, which would help the cells in clearing their storage, as observed in other LSD (137). This hypothesis was supported by the later studies of *Rega et al.* showing that cells derived from cystinotic patients exhibit an abnormal translocation of the mediator of lysosomal exocytosis TFEB (transcription factor EB) into the nucleus (104). Based on these considerations, we speculate that the absence of cystine accumulation observed here in the kidneys derived from *Ctns*$^{-/-}$ mice at early stages could be due to this excretion mechanism of lysosomes-containing cystine in the tubular lumen. This process might reach saturation over time and lead to the appearance of cystine crystals in the later stages of the disease. Further studies, including inhibition of possible compensation mechanisms, are needed to test this hypothesis.

In order to identify the molecular players driving the progression of the lysosome disease and related deleterious effects on PT function, we investigated mTORC1. This kinase was an obvious candidate because: (i) mTORC1 is a master regulator of lysosomal function and autophagy, which are both disrupted in cystinosis (138); (ii) mTORC1 activity is modulated by the fluctuation of amino acids in the lysosomal lumen and cystinosis is a disorder characterized by the lysosome storage of amino acids (70); (iii) mTORC1 complex has been previously shown to be part of the cystinosin interactome (102). Our analysis showed that mTORC1 was aberrantly activated in the kidneys of *Ctns*$^{-/-}$ mice and rats, suggesting the evolutionary conservation of this disease-phenotype. Further studies showed that mTORC1 sensing was impaired in *Ctns*$^{-/-}$ mPTCs, as proved by its persistent status of activation during starvation. These data are in line with recent studies on human CTNS-iPSC, which suggest an upregulation of gene signatures involved in the regulation of mTORC1 and its downstream targets (139). On the contrary, our data contrast with prior work on immortalized PT cells derived from CTNS-deficient mice or human patients, showing a downregulation of mTORC1 (102). The causes for these discrepancies remain unclear but may be related to metabolic differences between cell types or to the process of immortalization performed by infecting the cells with SV40 T antigen. Indeed, it has been previously shown that this virus significantly inhibits the phosphorylation of the signalling effectors directly downstream of mTORC1; therefore the use of this method is not appropriate for measuring the level of mTORC1 activation (106).

Next, we asked how the lack of CTNS might induce the aberrant activation of mTORC1. Given that in MDCK (Madin-Darby Canine Kidney cells) and 3T3 (3-day transfer, inoculum 3×10^5 cells- murine fibroblast) stably transfected with cystinosin, CTNS has been shown to interact with many regulatory subunits of mTORC1 complex (102), we could hypothesize a role of this transporter in negatively modulating mTORC1 activity by a protein-protein interaction mechanism, independent on cystine transport. In this scenario we would expect an activation of mTORC1 already in *Ctns*$^{-/-}$ mice at presymptomatic stage, in absence of increased cystine levels. Yet, our data show that mTORC1 activity was comparable to wild-type in pre-symptomatic *Ctns* $^{-/-}$ mice, suggesting that the absence of cystinosin alone is not sufficient to activate mTORC1. From these evidences we cannot exclude a role for cystinosin in regulating mTORC1 complex or vice versa, and therefore further studies are needed to clarify the biological relevance of these protein-protein interactions at the lysosomal membrane. More likely, the abnormal mTORC1 activity could be triggered by the storage of cystine characterizing cystinotic cells. Indeed, multiple studies showed a direct correlation between lysosomal amino acid concentrations and mTORC1 signaling (70). Evidences supporting the latter hypothesis are: (i) the appearance of mTORC1 activation concomitantly to the increase of cystine levels in the kidney of symptomatic *Ctns* $^{-/-}$ mice; (ii) the striking decrease of mTORC1 activation detected in *Ctns*$^{-/-}$ mPTCs upon treatment with the cystine-depleting agent cysteamine; (iii) the progressive mTORC1 activation observed upon CDME overload in wild-type PT cells. These experiments led us to conclude that cystine accumulation is a key event triggering mTORC1 dysfunction in cystinosis. However, whether the progressive lysosomal accumulation of other metabolites might contribute to mTORC1 activation remains to be clarified. Indeed, the lysosomal defects observed in *Ctns*$^{-/-}$ mice might drive a progressive accumulation of undigested autophagy substrates in the lysosomal lumen, which could concur with cystine to sustain mTORC1 signal. Analyses of the metabolomics and proteomics profile of lysosome fractions isolated from cystinotic mice at different stages would help to elucidate these issues (140).

Irrespective of the upstream mechanisms, mTORC1 hyper-activation could exert a negative feedback on the lysosomal function by limiting lysosome biogenesis through the inhibition of

MiTF/TFEB transcription factors (141). This is consistent with the decreased number of lysosomes in the cytosol of *Ctns* $^{-/-}$ mPTCs and in line with the enlarged and dysfunctional status of the remaining lysosomal pool. This hypothesis is further supported by a recent study showing that genetic and pharmacologic activation of the transcription factor TFEB rescued lysosome abnormalities in cystinotic kidney cells (104).

Supporting the central role of mTORC1 dysregulation in the pathogenesis of cystinosis, we demonstrated that *in vitro* inhibition of mTORC1 pathway by Torin1 and Rapamycin successfully restored lysosomal function, normalized the abnormal level of autophagy markers and all the cellular aberrations downstream this cascade. The mechanism of rescue resulting from Torin1 and Rapamycin treatment could be due to their action (i) on the lysosomal function, through the activation of TFEB, which might increase the number of lysosomes and lysosomal enzymes, (ii) on autophagy pathway, by boosting the degradation of damaged cellular bulk, and therefore restoring the physiologic cellular homeostasis (141). Similarly, Hollywood et al. showed that Everolimus, a derivative of Rapamycin, was also able to repair the impaired lyso-autophagy path observed in CTNS-iPSC (139). These findings are important as they open realistic therapeutic opportunities for patients with cystinosis. Since mTOR inhibitors are clinically used with reasonable safety profile, their repurposing for cystinosis would be appealing (142). Furthermore, as aberrant activation of mTORC1 has been reported in other genetic disorders associated with lysosomal storage and autophagy defects, we believe that these families of diseases could share common pathological mechanisms (143, 144).

Having demonstrated that cystine accumulation is responsible for mTORC1 dysregulation, which in turn plays a central role in driving the progression of the lyso-autophagy defect, one might ask why treatment with the cystine-depleting agent cysteamine is not effective in curing cystinosis (145). One explanation is provided by previous studies reporting that cysteamine has an inhibitory effect on the late stage of autophagy (146). Thus, it is likely that while cysteamine may restore lysosomal activity by depleting cystine and lowering mTORC1 levels, its inhibitory effect on autolysosome maturation induces a further block of the autophagy flux.

In conclusion, we identified key pathogenic mechanisms linking lysosomal storage and defective lyso-autophagy pathway in cystinosis. These findings substantiate the role of mTORC1 in preserving lysosomal activity, which is crucial for properly functioning of specialized epithelial cells. mTORC1 inhibition offers a promising therapeutic strategy for rescuing the epithelial damage observed in this and potentially other lysosomal storage disorders.

The investigations performed during this thesis contribute in understanding how perturbation of phosphatidylinositol homeostasis, lysosomal function and autophagy impact on the endocytic pathway, with ensuing defects in differentiation and transport functions in PT cells. Since our investigations address the early stages of disease, before any structural, irreversible damage of the kidney, we will be able, in the following studies, to use genetic and pharmacologic tools to target the pathways (actin dynamics, autophagy, mTORC1, oxidative stress) and verify the consequences on the phenotype. Being able to correct some of the early defects could alleviate major clinical consequences of increased urinary losses of vitamins and solutes.

More generally, these studies on the endolysosomal disorders improve our knowledge of fundamental processes (differentiation and morphogenesis, regulation of lysosomal function and autophagy) that maintain cell homeostasis and govern transport functions responsible for the handling of essential nutrients and solutes by the kidney.

REFERENCES

1. Eckardt, K.U., Coresh, J., Devuyst, O., Johnson, R.J., Kottgen, A., Levey, A.S. and Levin, A. (2013) Evolving importance of kidney disease: from subspecialty to global health burden. *Lancet (London, England)*, **382**, 158-169.

2. Brown, D., Bouley, R., Paunescu, T.G., Breton, S. and Lu, H.A. (2012) New insights into the dynamic regulation of water and acid-base balance by renal epithelial cells. *American journal of physiology. Cell physiology*, **302**, C1421-1433.

3. Zhuo, J.L. and Li, X.C. (2013) Proximal nephron. *Comprehensive Physiology*, **3**, 1079-1123.

4. Fromm, M., Piontek, J., Rosenthal, R., Gunzel, D. and Krug, S.M. (2017) Tight junctions of the proximal tubule and their channel proteins. *Pflugers Archiv : European journal of physiology*, **469**, 877-887.

5. Eshbach, M.L. and Weisz, O.A. (2017) Receptor-Mediated Endocytosis in the Proximal Tubule. *Annual review of physiology*, **79**, 425-448.

6. Nielsen, R., Christensen, E.I. and Birn, H. (2016) Megalin and cubilin in proximal tubule protein reabsorption: from experimental models to human disease. *Kidney international*, **89**, 58-67.

7. Bhargava, P. and Schnellmann, R.G. (2017) Mitochondrial energetics in the kidney. *Nature reviews. Nephrology*, **13**, 629-646.

8. Greger, R. (1996) Greger, R. and Windhorst, U. (eds.), In *Comprehensive Human Physiology: From Cellular Mechanisms to Integration*. Springer Berlin Heidelberg, Berlin, Heidelberg, in press., pp. 1517-1544.

9. Curthoys, N.P. and Moe, O.W. (2014) Proximal tubule function and response to acidosis. *Clinical journal of the American Society of Nephrology : CJASN*, **9**, 1627-1638.

10. Dusso, A.S. (2011) Kidney disease and vitamin D levels: 25-hydroxyvitamin D, 1,25-dihydroxyvitamin D, and VDR activation. *Kidney international supplements*, **1**, 136-141.

11. Christensen, E.I. and Birn, H. (2002) Megalin and cubilin: multifunctional endocytic receptors. *Nature reviews. Molecular cell biology*, **3**, 256-266.

12. McMahon, H.T. and Boucrot, E. (2011) Molecular mechanism and physiological functions of clathrin-mediated endocytosis. *Nature reviews. Molecular cell biology*, **12**, 517-533.

13. He, K., Marsland, R., III, Upadhyayula, S., Song, E., Dang, S., Capraro, B.R., Wang, W., Skillern, W., Gaudin, R., Ma, M. *et al.* (2017) Dynamics of phosphoinositide conversion in clathrin-mediated endocytic traffic. *Nature*, **552**, 410-414.

14. Welling, P.A. and Weisz, O.A. (2010) Sorting it out in endosomes: an emerging concept in renal epithelial cell transport regulation. *Physiology (Bethesda, Md.)*, **25**, 280-292.

15. Saito, A., Pietromonaco, S., Loo, A.K. and Farquhar, M.G. (1994) Complete cloning and sequencing of rat gp330/"megalin," a distinctive member of the low density lipoprotein receptor gene family. *Proceedings of the National Academy of Sciences of the United States of America*, **91**, 9725-9729.

16. Takeda, T., Yamazaki, H. and Farquhar, M.G. (2003) Identification of an apical sorting determinant in the cytoplasmic tail of megalin. *American journal of physiology. Cell physiology*, **284**, C1105-1113.

17. Biemesderfer, D. (2006) Regulated intramembrane proteolysis of megalin: linking urinary protein and gene regulation in proximal tubule? *Kidney international*, **69**, 1717-1721.

18. Willnow, T.E., Rohlmann, A., Horton, J., Otani, H., Braun, J.R., Hammer, R.E. and Herz, J. (1996) RAP, a specialized chaperone, prevents ligand-induced ER retention and degradation of LDL receptor-related endocytic receptors. *The EMBO journal*, **15**, 2632-2639.

19. Nielsen, R., Courtoy, P.J., Jacobsen, C., Dom, G., Lima, W.R., Jadot, M., Willnow, T.E., Devuyst, O. and Christensen, E.I. (2007) Endocytosis provides a major alternative pathway for lysosomal biogenesis in kidney proximal tubular cells. *Proceedings of the National Academy of Sciences of the United States of America*, **104**, 5407-5412.

20. Willnow, T.E., Nykjaer, A. and Herz, J. (1999) Lipoprotein receptors: new roles for ancient proteins. *Nature cell biology*, **1**, E157-162.

21. Leheste, J.R., Rolinski, B., Vorum, H., Hilpert, J., Nykjaer, A., Jacobsen, C., Aucouturier, P., Moskaug, J.O., Otto, A., Christensen, E.I. *et al.* (1999) Megalin knockout mice as an animal model of low molecular weight proteinuria. *The American journal of pathology*, **155**, 1361-1370.

22. Bork, P. and Beckmann, G. (1993) The CUB domain. A widespread module in developmentally regulated proteins. *Journal of molecular biology*, **231**, 539-545.

23. Kozyraki, R., Fyfe, J., Verroust, P.J., Jacobsen, C., Dautry-Varsat, A., Gburek, J., Willnow, T.E., Christensen, E.I. and Moestrup, S.K. (2001) Megalin-dependent cubilin-mediated endocytosis is a major pathway for the apical uptake of transferrin in polarized epithelia. *Proceedings of the National Academy of Sciences of the United States of America*, **98**, 12491-12496.

24. Strope, S., Rivi, R., Metzger, T., Manova, K. and Lacy, E. (2004) Mouse amnionless, which is required for primitive streak assembly, mediates cell-surface localization and endocytic function of cubilin on visceral endoderm and kidney proximal tubules. *Development (Cambridge, England)*, **131**, 4787-4795.

25. Seetharam, B., Christensen, E.I., Moestrup, S.K., Hammond, T.G. and Verroust, P.J. (1997) Identification of rat yolk sac target protein of teratogenic antibodies, gp280, as intrinsic factor-cobalamin receptor. *The Journal of clinical investigation*, **99**, 2317-2322.

26. Honing, S., Ricotta, D., Krauss, M., Spate, K., Spolaore, B., Motley, A., Robinson, M., Robinson, C., Haucke, V. and Owen, D.J. (2005) Phosphatidylinositol-(4,5)-bisphosphate regulates sorting signal recognition by the clathrin-associated adaptor complex AP2. *Molecular cell*, **18**, 519-531.

27. Oleinikov, A.V., Zhao, J. and Makker, S.P. (2000) Cytosolic adaptor protein Dab2 is an intracellular ligand of endocytic receptor gp600/megalin. *The Biochemical journal*, **347 Pt 3**, 613-621.

28. Hinshaw, J.E. and Schmid, S.L. (1995) Dynamin self-assembles into rings suggesting a mechanism for coated vesicle budding. *Nature*, **374**, 190-192.

29. Boucrot, E., Saffarian, S., Massol, R., Kirchhausen, T. and Ehrlich, M. (2006) Role of lipids and actin in the formation of clathrin-coated pits. *Experimental cell research*, **312**, 4036-4048.

30. Bocking, T., Aguet, F., Harrison, S.C. and Kirchhausen, T. (2011) Single-molecule analysis of a molecular disassemblase reveals the mechanism of Hsc70-driven clathrin uncoating. *Nature structural & molecular biology*, **18**, 295-301.

31. Rothnie, A., Clarke, A.R., Kuzmic, P., Cameron, A. and Smith, C.J. (2011) A sequential mechanism for clathrin cage disassembly by 70-kDa heat-shock cognate protein (Hsc70) and auxilin. *Proceedings of the National Academy of Sciences of the United States of America*, **108**, 6927-6932.

32. Haucke, V. (2005) Phosphoinositide regulation of clathrin-mediated endocytosis. *Biochemical Society transactions*, **33**, 1285-1289.

33. Daste, F., Walrant, A., Holst, M.R., Gadsby, J.R., Mason, J., Lee, J.E., Brook, D., Mettlen, M., Larsson, E., Lee, S.F. *et al.* (2017) Control of actin polymerization via the coincidence of phosphoinositides and high membrane curvature. *The Journal of cell biology*, **216**, 3745-3765.

34. De Matteis, M.A., Staiano, L., Emma, F. and Devuyst, O. (2017) The 5-phosphatase OCRL in Lowe syndrome and Dent disease 2. *Nature reviews. Nephrology*, **13**, 455-470.

35. Zhen, Y. and Stenmark, H. (2015) Cellular functions of Rab GTPases at a glance. *Journal of cell science*, **128**, 3171-3176.

36. van der Sluijs, P., Hull, M., Webster, P., Male, P., Goud, B. and Mellman, I. (1992) The small GTP-binding protein rab4 controls an early sorting event on the endocytic pathway. *Cell*, **70**, 729-740.

37. Perez Bay, A.E., Schreiner, R., Benedicto, I., Paz Marzolo, M., Banfelder, J., Weinstein, A.M. and Rodriguez-Boulan, E.J. (2016) The fast-recycling receptor Megalin defines the apical recycling pathway of epithelial cells. *Nature communications*, **7**, 11550.

38. Hu, Y.B., Dammer, E.B., Ren, R.J. and Wang, G. (2015) The endosomal-lysosomal system: from acidification and cargo sorting to neurodegeneration. *Translational neurodegeneration*, **4**, 18.

39. Zifarelli, G. (2015) A tale of two CLCs: biophysical insights toward understanding ClC-5 and ClC-7 function in endosomes and lysosomes. *The Journal of physiology*, **593**, 4139-4150.

40. Luzio, J.P., Parkinson, M.D., Gray, S.R. and Bright, N.A. (2009) The delivery of endocytosed cargo to lysosomes. *Biochemical Society transactions*, **37**, 1019-1021.

41. Huotari, J. and Helenius, A. (2011) Endosome maturation. *The EMBO journal*, **30**, 3481-3500.

42. Hille-Rehfeld, A. (1995) Mannose 6-phosphate receptors in sorting and transport of lysosomal enzymes. *Biochimica et biophysica acta*, **1241**, 177-194.

43. Schroder, B.A., Wrocklage, C., Hasilik, A. and Saftig, P. (2010) The proteome of lysosomes. *Proteomics*, **10**, 4053-4076.

44. Settembre, C. and Ballabio, A. (2014) Lysosomal adaptation: how the lysosome responds to external cues. *Cold Spring Harbor perspectives in biology*, **6**.

45. Chieregatti, E. and Meldolesi, J. (2005) Regulated exocytosis: new organelles for non-secretory purposes. *Nature reviews. Molecular cell biology*, **6**, 181-187.

46. Coutinho, M.F., Prata, M.J. and Alves, S. (2012) Mannose-6-phosphate pathway: a review on its role in lysosomal function and dysfunction. *Molecular genetics and metabolism*, **105**, 542-550.

47. Saftig, P. and Klumperman, J. (2009) Lysosome biogenesis and lysosomal membrane proteins: trafficking meets function. *Nature reviews. Molecular cell biology*, **10**, 623-635.

48. Yoshimori, T., Yamamoto, A., Moriyama, Y., Futai, M. and Tashiro, Y. (1991) Bafilomycin A1, a specific inhibitor of vacuolar-type H(+)-ATPase, inhibits acidification and protein degradation in lysosomes of cultured cells. *The Journal of biological chemistry*, **266**, 17707-17712.

49. Rabinowitz, J.D. and White, E. (2010) Autophagy and metabolism. *Science (New York, N.Y.)*, **330**, 1344-1348.

50. Settembre, C., Fraldi, A., Jahreiss, L., Spampanato, C., Venturi, C., Medina, D., de Pablo, R., Tacchetti, C., Rubinsztein, D.C. and Ballabio, A. (2008) A block of autophagy in lysosomal storage disorders. *Human molecular genetics*, **17**, 119-129.

51. Luzio, J.P., Pryor, P.R. and Bright, N.A. (2007) Lysosomes: fusion and function. *Nature reviews. Molecular cell biology*, **8**, 622-632.

52. Yu, L., McPhee, C.K., Zheng, L., Mardones, G.A., Rong, Y., Peng, J., Mi, N., Zhao, Y., Liu, Z., Wan, F. *et al.* (2010) Termination of autophagy and reformation of lysosomes regulated by mTOR. *Nature*, **465**, 942-946.

53. Sridhar, S., Patel, B., Aphkhazava, D., Macian, F., Santambrogio, L., Shields, D. and Cuervo, A.M. (2013) The lipid kinase PI4KIIIbeta preserves lysosomal identity. *The EMBO journal*, **32**, 324-339.

54. Ballabio, A. and Gieselmann, V. (2009) Lysosomal disorders: from storage to cellular damage. *Biochimica et biophysica acta*, **1793**, 684-696.

55. Surendran, K., Vitiello, S.P. and Pearce, D.A. (2014) Lysosome dysfunction in the pathogenesis of kidney diseases. *Pediatric nephrology (Berlin, Germany)*, **29**, 2253-2261.

56. Mizushima, N., Levine, B., Cuervo, A.M. and Klionsky, D.J. (2008) Autophagy fights disease through cellular self-digestion. *Nature*, **451**, 1069-1075.

57. Kimura, T., Takahashi, A., Takabatake, Y., Namba, T., Yamamoto, T., Kaimori, J.Y., Matsui, I., Kitamura, H., Niimura, F., Matsusaka, T. *et al.* (2013) Autophagy protects kidney proximal tubule epithelial cells from mitochondrial metabolic stress. *Autophagy*, **9**, 1876-1886.

58. Anding, A.L. and Baehrecke, E.H. (2015) Autophagy in Cell Life and Cell Death. *Current topics in developmental biology*, **114**, 67-91.

59. Hurley, J.H. and Young, L.N. (2017) Mechanisms of Autophagy Initiation. *Annual review of biochemistry*, **86**, 225-244.

60. Menzies, F.M., Fleming, A., Caricasole, A., Bento, C.F., Andrews, S.P., Ashkenazi, A., Fullgrabe, J., Jackson, A., Jimenez Sanchez, M., Karabiyik, C. *et al.* (2017) Autophagy and Neurodegeneration: Pathogenic Mechanisms and Therapeutic Opportunities. *Neuron*, **93**, 1015-1034.

61. Mizushima, N., Noda, T., Yoshimori, T., Tanaka, Y., Ishii, T., George, M.D., Klionsky, D.J., Ohsumi, M. and Ohsumi, Y. (1998) A protein conjugation system essential for autophagy. *Nature*, **395**, 395-398.

62. Noda, N.N., Kumeta, H., Nakatogawa, H., Satoo, K., Adachi, W., Ishii, J., Fujioka, Y., Ohsumi, Y. and Inagaki, F. (2008) Structural basis of target recognition by Atg8/LC3 during selective autophagy. *Genes to cells : devoted to molecular & cellular mechanisms*, **13**, 1211-1218.

63. Tanida, I., Ueno, T. and Kominami, E. (2004) LC3 conjugation system in mammalian autophagy. *The international journal of biochemistry & cell biology*, **36**, 2503-2518.

64. Rubinsztein, D.C., Marino, G. and Kroemer, G. (2011) Autophagy and aging. *Cell*, **146**, 682-695.

65. Mizushima, N. and Levine, B. (2010) Autophagy in mammalian development and differentiation. *Nature cell biology*, **12**, 823-830.

66. Laplante, M. and Sabatini, D.M. (2012) mTOR signaling in growth control and disease. *Cell*, **149**, 274-293.

67. Rubinsztein, D.C., Codogno, P. and Levine, B. (2012) Autophagy modulation as a potential therapeutic target for diverse diseases. *Nature reviews. Drug discovery*, **11**, 709-730.

68. Sancak, Y., Bar-Peled, L., Zoncu, R., Markhard, A.L., Nada, S. and Sabatini, D.M. (2010) Ragulator-Rag complex targets mTORC1 to the lysosomal surface and is necessary for its activation by amino acids. *Cell*, **141**, 290-303.

69. Sancak, Y., Peterson, T.R., Shaul, Y.D., Lindquist, R.A., Thoreen, C.C., Bar-Peled, L. and Sabatini, D.M. (2008) The Rag GTPases bind raptor and mediate amino acid signaling to mTORC1. *Science (New York, N.Y.)*, **320**, 1496-1501.

70. Bar-Peled, L. and Sabatini, D.M. (2014) Regulation of mTORC1 by amino acids. *Trends in cell biology*, **24**, 400-406.

71. Settembre, C., Zoncu, R., Medina, D.L., Vetrini, F., Erdin, S., Erdin, S., Huynh, T., Ferron, M., Karsenty, G., Vellard, M.C. *et al.* (2012) A lysosome-to-nucleus signalling mechanism senses and regulates the lysosome via mTOR and TFEB. *The EMBO journal*, **31**, 1095-1108.

72. Ma, M.K.M., Yung, S. and Chan, T.M. (2018) mTOR Inhibition and Kidney Diseases. *Transplantation*, **102**, S32-s40.

73. Fanning, A.S. and Anderson, J.M. (2009) Zonula occludens-1 and -2 are cytosolic scaffolds that regulate the assembly of cellular junctions. *Annals of the New York Academy of Sciences*, **1165**, 113-120.

74. Denker, B.M. and Sabath, E. (2011) The biology of epithelial cell tight junctions in the kidney. *Journal of the American Society of Nephrology : JASN*, **22**, 622-625.

75. Dimitratos, S.D., Woods, D.F., Stathakis, D.G. and Bryant, P.J. (1999) Signaling pathways are focused at specialized regions of the plasma membrane by scaffolding proteins of the MAGUK family. *BioEssays : news and reviews in molecular, cellular and developmental biology*, **21**, 912-921.

76. Bauer, H., Zweimueller-Mayer, J., Steinbacher, P., Lametschwandtner, A. and Bauer, H.C. (2010) The dual role of zonula occludens (ZO) proteins. *Journal of biomedicine & biotechnology*, **2010**, 402593.

77. Zihni, C., Mills, C., Matter, K. and Balda, M.S. (2016) Tight junctions: from simple barriers to multifunctional molecular gates. *Nature reviews. Molecular cell biology*, **17**, 564-580.

78. Meyer, T.N., Schwesinger, C. and Denker, B.M. (2002) Zonula occludens-1 is a scaffolding protein for signaling molecules. Galpha(12) directly binds to the Src homology 3 domain and regulates paracellular permeability in epithelial cells. *The Journal of biological chemistry*, **277**, 24855-24858.

79. Yu, W., Beaudry, S., Negoro, H., Boucher, I., Tran, M., Kong, T. and Denker, B.M. (2012) H2O2 activates G protein, alpha 12 to disrupt the junctional complex and enhance ischemia reperfusion injury. *Proceedings of the National Academy of Sciences of the United States of America*, **109**, 6680-6685.

80. Pozzi, A. and Zent, R. (2010) ZO-1 and ZONAB interact to regulate proximal tubular cell differentiation. *Journal of the American Society of Nephrology : JASN*, **21**, 388-390.

81. Balda, M.S., Garrett, M.D. and Matter, K. (2003) The ZO-1-associated Y-box factor ZONAB regulates epithelial cell proliferation and cell density. *The Journal of cell biology*, **160**, 423-432.

82. Sourisseau, T., Georgiadis, A., Tsapara, A., Ali, R.R., Pestell, R., Matter, K. and Balda, M.S. (2006) Regulation of PCNA and cyclin D1 expression and epithelial morphogenesis by the ZO-1-regulated transcription factor ZONAB/DbpA. *Molecular and cellular biology*, **26**, 2387-2398.

83. Lima, W.R., Parreira, K.S., Devuyst, O., Caplanusi, A., N'Kuli, F., Marien, B., Van Der Smissen, P., Alves, P.M., Verroust, P., Christensen, E.I. *et al.* (2010) ZONAB promotes proliferation and represses differentiation of proximal tubule epithelial cells. *Journal of the American Society of Nephrology : JASN*, **21**, 478-488.

84. van der Wijst, J., Belge, H., Bindels, R.J.M. and Devuyst, O. (2019) Learning Physiology From Inherited Kidney Disorders. *Physiological reviews*, **99**, 1575-1653.

85. Karatzas, A., Paridis, D., Kozyrakis, D., Tzortzis, V., Samarinas, M., Dailiana, Z. and Karachalios, T. (2017) Fanconi syndrome in the adulthood. The role of early diagnosis and treatment. *Journal of musculoskeletal & neuronal interactions*, **17**, 303-306.

86. Devuyst, O., Christie, P.T., Courtoy, P.J., Beauwens, R. and Thakker, R.V. (1999) Intra-renal and subcellular distribution of the human chloride channel, CLC-5, reveals a pathophysiological basis for Dent's disease. *Human molecular genetics*, **8**, 247-257.

87. Devuyst, O. and Thakker, R.V. (2010) Dent's disease. *Orphanet journal of rare diseases*, **5**, 28.

88. Christensen, E.I., Devuyst, O., Dom, G., Nielsen, R., Van der Smissen, P., Verroust, P., Leruth, M., Guggino, W.B. and Courtoy, P.J. (2003) Loss of chloride channel ClC-5 impairs endocytosis by defective trafficking of megalin and cubilin in kidney proximal tubules. *Proceedings of the National Academy of Sciences of the United States of America*, **100**, 8472-8477.

89. Novarino, G., Weinert, S., Rickheit, G. and Jentsch, T.J. (2010) Endosomal chloride-proton exchange rather than chloride conductance is crucial for renal endocytosis. *Science (New York, N.Y.)*, **328**, 1398-1401.

90. Hryciw, D.H., Wang, Y., Devuyst, O., Pollock, C.A., Poronnik, P. and Guggino, W.B. (2003) Cofilin interacts with ClC-5 and regulates albumin uptake in proximal tubule cell lines. *The Journal of biological chemistry*, **278**, 40169-40176.

91. Vicinanza, M., Di Campli, A., Polishchuk, E., Santoro, M., Di Tullio, G., Godi, A., Levtchenko, E., De Leo, M.G., Polishchuk, R., Sandoval, L. *et al.* (2011) OCRL controls trafficking through early endosomes via PtdIns4,5P(2)-dependent regulation of endosomal actin. *The EMBO journal*, **30**, 4970-4985.

92. Bothwell, S.P., Chan, E., Bernardini, I.M., Kuo, Y.M., Gahl, W.A. and Nussbaum, R.L. (2011) Mouse model for Lowe syndrome/Dent Disease 2 renal tubulopathy. *Journal of the American Society of Nephrology : JASN*, **22**, 443-448.

93. Gahl, W.A., Thoene, J.G. and Schneider, J.A. (2002) Cystinosis. *The New England journal of medicine*, **347**, 111-121.

94. Kalatzis, V., Cherqui, S., Antignac, C. and Gasnier, B. (2001) Cystinosin, the protein defective in cystinosis, is a H(+)-driven lysosomal cystine transporter. *The EMBO journal*, **20**, 5940-5949.

95. Town, M., Jean, G., Cherqui, S., Attard, M., Forestier, L., Whitmore, S.A., Callen, D.F., Gribouval, O., Broyer, M., Bates, G.P. *et al.* (1998) A novel gene encoding an integral membrane protein is mutated in nephropathic cystinosis. *Nature genetics*, **18**, 319-324.

96. Cherqui, S. and Courtoy, P.J. (2017) The renal Fanconi syndrome in cystinosis: pathogenic insights and therapeutic perspectives. *Nature reviews. Nephrology*, **13**, 115-131.

97. Schneider, J.A. (1995) Approval of cysteamine for patients with cystinosis. *Pediatric nephrology (Berlin, Germany)*, **9**, 254.

98. Nevo, N., Chol, M., Bailleux, A., Kalatzis, V., Morisset, L., Devuyst, O., Gubler, M.C. and Antignac, C. (2010) Renal phenotype of the cystinosis mouse model is dependent upon genetic background. *Nephrology, dialysis, transplantation : official publication of the European Dialysis and Transplant Association - European Renal Association*, **25**, 1059-1066.

99. Levtchenko, E., de Graaf-Hess, A., Wilmer, M., van den Heuvel, L., Monnens, L. and Blom, H. (2005) Altered status of glutathione and its metabolites in cystinotic cells. *Nephrology, dialysis, transplantation : official publication of the European Dialysis and Transplant Association - European Renal Association*, **20**, 1828-1832.

100. Levtchenko, E.N., Wilmer, M.J., Janssen, A.J., Koenderink, J.B., Visch, H.J., Willems, P.H., de Graaf-Hess, A., Blom, H.J., van den Heuvel, L.P. and Monnens, L.A. (2006) Decreased intracellular ATP content and intact mitochondrial energy generating capacity in human cystinotic fibroblasts. *Pediatric research*, **59**, 287-292.

101. Raggi, C., Luciani, A., Nevo, N., Antignac, C., Terryn, S. and Devuyst, O. (2014) Dedifferentiation and aberrations of the endolysosomal compartment characterize the early stage of nephropathic cystinosis. *Human molecular genetics*, **23**, 2266-2278.

102. Andrzejewska, Z., Nevo, N., Thomas, L., Chhuon, C., Bailleux, A., Chauvet, V., Courtoy, P.J., Chol, M., Guerrera, I.C. and Antignac, C. (2016) Cystinosin is a Component of the Vacuolar H+-ATPase-Ragulator-Rag Complex Controlling Mammalian Target of Rapamycin Complex 1 Signaling. *Journal of the American Society of Nephrology : JASN*, **27**, 1678-1688.

103. Ivanova, E.A., van den Heuvel, L.P., Elmonem, M.A., De Smedt, H., Missiaen, L., Pastore, A., Mekahli, D., Bultynck, G. and Levtchenko, E.N. (2016) Altered mTOR signalling in nephropathic cystinosis. *Journal of inherited metabolic disease*, **39**, 457-464.

104. Rega, L.R., Polishchuk, E., Montefusco, S., Napolitano, G., Tozzi, G., Zhang, J., Bellomo, F., Taranta, A., Pastore, A., Polishchuk, R. *et al.* (2016) Activation of the transcription factor EB rescues lysosomal abnormalities in cystinotic kidney cells. *Kidney international*, **89**, 862-873.

105. Kumar, S.H. and Rangarajan, A. (2009) Simian virus 40 small T antigen activates AMPK and triggers autophagy to protect cancer cells from nutrient deprivation. *Journal of virology*, **83**, 8565-8574.

106. Yu, Y., Kudchodkar, S.B. and Alwine, J.C. (2005) Effects of simian virus 40 large and small tumor antigens on mammalian target of rapamycin signaling: small tumor antigen mediates hypophosphorylation of eIF4E-binding protein 1 late in infection. *Journal of virology*, **79**, 6882-6889.

107. Devuyst, O. and Luciani, A. (2015) Chloride transporters and receptor-mediated endocytosis in the renal proximal tubule. *The Journal of physiology*, **593**, 4151-4164.

108. Janne, P.A., Suchy, S.F., Bernard, D., MacDonald, M., Crawley, J., Grinberg, A., Wynshaw-Boris, A., Westphal, H. and Nussbaum, R.L. (1998) Functional overlap between murine Inpp5b and Ocrl1 may explain why deficiency of the

murine ortholog for OCRL1 does not cause Lowe syndrome in mice. *The Journal of clinical investigation*, **101**, 2042-2053.

109. Inoue, K., Balkin, D.M., Liu, L., Nandez, R., Wu, Y., Tian, X., Wang, T., Nussbaum, R., De Camilli, P. and Ishibe, S. (2017) Kidney Tubular Ablation of Ocrl/Inpp5b Phenocopies Lowe Syndrome Tubulopathy. *Journal of the American Society of Nephrology : JASN*, **28**, 1399-1407.

110. Erdmann, K.S., Mao, Y., McCrea, H.J., Zoncu, R., Lee, S., Paradise, S., Modregger, J., Biemesderfer, D., Toomre, D. and De Camilli, P. (2007) A role of the Lowe syndrome protein OCRL in early steps of the endocytic pathway. *Developmental cell*, **13**, 377-390.

111. Oltrabella, F., Pietka, G., Ramirez, I.B., Mironov, A., Starborg, T., Drummond, I.A., Hinchliffe, K.A. and Lowe, M. (2015) The Lowe syndrome protein OCRL1 is required for endocytosis in the zebrafish pronephric tubule. *PLoS genetics*, **11**, e1005058.

112. Norden, A.G., Lapsley, M., Igarashi, T., Kelleher, C.L., Lee, P.J., Matsuyama, T., Scheinman, S.J., Shiraga, H., Sundin, D.P., Thakker, R.V. *et al.* (2002) Urinary megalin deficiency implicates abnormal tubular endocytic function in Fanconi syndrome. *Journal of the American Society of Nephrology : JASN*, **13**, 125-133.

113. Stauber, T. and Jentsch, T.J. (2013) Chloride in vesicular trafficking and function. *Annual review of physiology*, **75**, 453-477.

114. De, S., Kuwahara, S., Hosojima, M., Ishikawa, T., Kaseda, R., Sarkar, P., Yoshioka, Y., Kabasawa, H., Iida, T., Goto, S. *et al.* (2017) Exocytosis-Mediated Urinary Full-Length Megalin Excretion Is Linked With the Pathogenesis of Diabetic Nephropathy. *Diabetes*, **66**, 1391-1404.

115. Terryn, S., Jouret, F., Vandenabeele, F., Smolders, I., Moreels, M., Devuyst, O., Steels, P. and Van Kerkhove, E. (2007) A primary culture of mouse proximal tubular cells, established on collagen-coated membranes. *American journal of physiology. Renal physiology*, **293**, F476-485.

116. Zhang, X., Hartz, P.A., Philip, E., Racusen, L.C. and Majerus, P.W. (1998) Cell lines from kidney proximal tubules of a patient with Lowe syndrome lack OCRL inositol polyphosphate 5-phosphatase and accumulate phosphatidylinositol 4,5-bisphosphate. *The Journal of biological chemistry*, **273**, 1574-1582.

117. Zoncu, R., Perera, R.M., Balkin, D.M., Pirruccello, M., Toomre, D. and De Camilli, P. (2009) A phosphoinositide switch controls the maturation and signaling properties of APPL endosomes. *Cell*, **136**, 1110-1121.

118. Senju, Y., Kalimeri, M., Koskela, E.V., Somerharju, P., Zhao, H., Vattulainen, I. and Lappalainen, P. (2017) Mechanistic principles underlying regulation of the actin cytoskeleton by phosphoinositides. *Proceedings of the National Academy of Sciences of the United States of America*, **114**, E8977-e8986.

119. Nandez, R., Balkin, D.M., Messa, M., Liang, L., Paradise, S., Czapla, H., Hein, M.Y., Duncan, J.S., Mann, M. and De Camilli, P. (2014) A role of OCRL in clathrin-coated pit dynamics and uncoating revealed by studies of Lowe syndrome cells. *eLife*, **3**, e02975.

120. Gallop, J.L., Walrant, A., Cantley, L.C. and Kirschner, M.W. (2013) Phosphoinositides and membrane curvature switch the mode of actin polymerization via selective recruitment of toca-1 and Snx9. *Proceedings of the National Academy of Sciences of the United States of America*, **110**, 7193-7198.

121. Fruman, D.A., Chiu, H., Hopkins, B.D., Bagrodia, S., Cantley, L.C. and Abraham, R.T. (2017) The PI3K Pathway in Human Disease. *Cell*, **170**, 605-635.

122. De Leo, M.G., Staiano, L., Vicinanza, M., Luciani, A., Carissimo, A., Mutarelli, M., Di Campli, A., Polishchuk, E., Di Tullio, G., Morra, V. *et al.* (2016) Autophagosome-lysosome fusion triggers a lysosomal response mediated by TLR9 and controlled by OCRL. *Nature cell biology*, **18**, 839-850.

123. Puri C., Renna M., Bento C.F., Moreau K., Rubinsztein D.C., ATG16L1 meets ATG9 in recycling endosomes: additional roles for the plasma membrane and endocytosis in autophagosome biogenesis. *Autophagy*, **10**, 182-184.

124. Cremona, O., Di Paolo, G., Wenk, M.R., Luthi, A., Kim, W.T., Takei, K., Daniell, L., Nemoto, Y., Shears, S.B., Flavell, R.A. *et al.* (1999) Essential role of phosphoinositide metabolism in synaptic vesicle recycling. *Cell*, **99**, 179-188.

125. Mani, M., Lee, S.Y., Lucast, L., Cremona, O., Di Paolo, G., De Camilli, P. and Ryan, T.A. (2007) The dual phosphatase activity of synaptojanin1 is required for both efficient synaptic vesicle endocytosis and reavailability at nerve terminals. *Neuron*, **56**, 1004-1018.

126. Balla, T., Szentpetery, Z. and Kim, Y.J. (2009) Phosphoinositide signaling: new tools and insights. *Physiology (Bethesda, Md.)*, **24**, 231-244.

127. Kielkowska, A., Niewczas, I., Anderson, K.E., Durrant, T.N., Clark, J., Stephens, L.R. and Hawkins, P.T. (2014) A new approach to measuring phosphoinositides in cells by mass spectrometry. *Advances in biological regulation*, **54**, 131-141.

128. Gaide Chevronnay, H.P., Janssens, V., Van Der Smissen, P., N'Kuli, F., Nevo, N., Guiot, Y., Levtchenko, E., Marbaix, E., Pierreux, C.E., Cherqui, S. *et al.* (2014) Time course of pathogenic and adaptation mechanisms in cystinotic mouse kidneys. *Journal of the American Society of Nephrology : JASN*, **25**, 1256-1269.

129. Settembre, C., Fraldi, A., Medina, D.L. and Ballabio, A. (2013) Signals from the lysosome: a control centre for cellular clearance and energy metabolism. *Nature reviews. Molecular cell biology*, **14**, 283-296.

130. Napolitano, G., Johnson, J.L., He, J., Rocca, C.J., Monfregola, J., Pestonjamasp, K., Cherqui, S. and Catz, S.D. (2015) Impairment of chaperone-mediated autophagy leads to selective lysosomal degradation defects in the lysosomal storage disease cystinosis. *EMBO molecular medicine*, **7**, 158-174.

131. Galluzzi, L., Pietrocola, F., Bravo-San Pedro, J.M., Amaravadi, R.K., Baehrecke, E.H., Cecconi, F., Codogno, P., Debnath, J., Gewirtz, D.A., Karantza, V. *et al.* (2015) Autophagy in malignant transformation and cancer progression. *The EMBO journal*, **34**, 856-880.

132. Narendra, D., Kane, L.A., Hauser, D.N., Fearnley, I.M. and Youle, R.J. (2010) p62/SQSTM1 is required for Parkin-induced mitochondrial clustering but not mitophagy; VDAC1 is dispensable for both. *Autophagy*, **6**, 1090-1106.

133. Meyer, T.N., Hunt, J., Schwesinger, C. and Denker, B.M. (2003) Galpha12 regulates epithelial cell junctions through Src tyrosine kinases. *American journal of physiology. Cell physiology*, **285**, C1281-1293.

134. Luciani, A., Sirac, C., Terryn, S., Javaugue, V., Prange, J.A., Bender, S., Bonaud, A., Cogne, M., Aucouturier, P., Ronco, P. *et al.* (2016) Impaired Lysosomal Function Underlies Monoclonal Light Chain-Associated Renal Fanconi Syndrome. *Journal of the American Society of Nephrology : JASN*, **27**, 2049-2061.

135. Ruan, Y.C., Wang, Y., Da Silva, N., Kim, B., Diao, R.Y., Hill, E., Brown, D., Chan, H.C. and Breton, S. (2014) CFTR interacts with ZO-1 to regulate tight junction assembly and epithelial differentiation through the ZONAB pathway. *Journal of cell science*, **127**, 4396-4408.

136. Galarreta, C.I., Forbes, M.S., Thornhill, B.A., Antignac, C., Gubler, M.C., Nevo, N., Murphy, M.P. and Chevalier, R.L. (2015) The swan-neck lesion: proximal tubular adaptation to oxidative stress in nephropathic cystinosis. *American journal of physiology. Renal physiology*, **308**, F1155-1166.

137. Gaide Chevronnay, H.P., Janssens, V., Van Der Smissen, P., N'Kuli, F., Nevo, N., Guiot, Y., Levtchenko, E., Marbaix, E., Pierreux, C.E., Cherqui, S. *et al.* (2014) Time course of pathogenic and adaptation mechanisms in cystinotic mouse kidneys. *Journal of the American Society of Nephrology : JASN*, **25**, 1256-1269.

138. Puertollano, R. (2014) mTOR and lysosome regulation. *F1000prime reports*, **6**, 52.

139. Hollywood, J.A., Przepiorski, A., Harrison, P.T., Wolvetang, E.J., Davidson, A.J. and Holm, T.M. (2019) Use of human iPSCs and kidney organoids to develop a cysteamine/mTOR inhibition combination therapy to treat cystinosis. *bioRxiv*, in press., 595264.

140. Abu-Remaileh, M., Wyant, G.A., Kim, C., Laqtom, N.N., Abbasi, M., Chan, S.H., Freinkman, E. and Sabatini, D.M. (2017) Lysosomal metabolomics reveals V-ATPase- and mTOR-dependent regulation of amino acid efflux from lysosomes. *Science (New York, N.Y.)*, **358**, 807-813.

141. Napolitano, G. and Ballabio, A. (2016) TFEB at a glance. *Journal of cell science*, **129**, 2475-2481.

142. Thomson, A.W., Turnquist, H.R. and Raimondi, G. (2009) Immunoregulatory functions of mTOR inhibition. *Nature reviews. Immunology*, **9**, 324-337.

143. Castellano, B.M., Thelen, A.M., Moldavski, O., Feltes, M., van der Welle, R.E., Mydock-McGrane, L., Jiang, X., van Eijkeren, R.J., Davis, O.B., Louie, S.M. *et al.* (2017) Lysosomal cholesterol activates mTORC1 via an SLC38A9-Niemann-Pick C1 signaling complex. *Science (New York, N.Y.)*, **355**, 1306-1311.

144. Bartolomeo, R., Cinque, L., De Leonibus, C., Forrester, A., Salzano, A.C., Monfregola, J., De Gennaro, E., Nusco, E., Azario, I., Lanzara, C. *et al.* (2017) mTORC1 hyperactivation arrests bone growth in lysosomal storage disorders by suppressing autophagy. *The Journal of clinical investigation*, **127**, 3717-3729.

145. Brodin-Sartorius, A., Tete, M.J., Niaudet, P., Antignac, C., Guest, G., Ottolenghi, C., Charbit, M., Moyse, D., Legendre, C., Lesavre, P. *et al.* (2012) Cysteamine therapy delays the progression of nephropathic cystinosis in late adolescents and adults. *Kidney international*, **81**, 179-189.

146. Wan, X.M., Zheng, F., Zhang, L., Miao, Y.Y., Man, N. and Wen, L.P. (2011) Autophagy-mediated chemosensitization by cysteamine in cancer cells. *International journal of cancer*, **129**, 1087-1095.

CURRICULUM VITAE

Date of birth: 25 June, 1987, Avellino, Italy
Current position PhD student at the University of Zurich
Work address: Institute of Physiology, University of Zurich,
Winterthurerstrasse 190,
CH-8057, Zurich, Switzerland
Phone: + 41 (0)76 3229210
Email: beatrice.paola.festa@gmail.com

Education and Research Experience:

2014- Present	PhD student in Integrative Molecular Medicine. Faculty of Science, University of Zurich, Zurich, Switzerland. Supervisor: Prof. Dr. med. Olivier Devuyst. Project title: New Insights and Therapeutic Approaches in Endolysosomal Disorders Affecting the Kidney Proximal Tubule.
2014	M.Sc. in Medical Biotechnology. Grade obtained 110/110. Faculty of Biotechnology, University of Naples Federico II, Naples, Italy. Supervisors: Prof. Stefano Bonatti and Dr. Roman Polishchuk. Project title: Evaluating the Impact of JNK and p38 Inhibitors on Wilson Disease-Relevant Mutants.
2012- 2014	Master internship. Laboratory of Dr. Roman Polishchuk. Telethon Institute of Genetics and Medicine (TIGEM), Naples, Italy.

Teaching & Courses:

2017	Rare Disease Initiative Zurich (RADIZ) summer school, Tagungszentrum Schloss Au, Wädenswil, Zurich, Switzerland.
2015- 2016	Teaching assistant in physiology practical laboratory, Faculty of Medicine, University of Zurich, Zurich, Switzerland.
2014	Course in laboratory animal science (mice/rats). FELASA Category B.

Research Interests:

Understanding of the basic mechanisms and cellular signaling governing autophagy in order to (i) decipher the role of this pathway in the pathogenesis of human diseases and (ii) developing evidenced-based therapeutic strategies.

Oral, Poster Presentations & Awards:

- Swiss National Centre of Competence in Research (NCCR) kidney retreat, Murten, Switzerland. February, 2019
- EMBO workshop "Lysosomes and Metabolism", Naples, Italy. May, 2018
- Life Science Switzerland (LS2) Annual Meeting "Metabolism & Signaling in the Life Sciences", Lausanne, Switzerland. February, 2018
- Swiss National Centre of Competence in Research (NCCR) kidney retreat, Murten, Switzerland. February, 2018 *Awarded*
- Fall semester award for outstanding academic work, Faculty of Science, University of Zurich, Zurich, Switzerland. 2018
- Drug Discovery Network Zurich (DDNZ) Symposium, ETH, Zurich, Switzerland. February, 2017
- Gordon Research Conference (GRC) on Lysosomal Disease, Lucca, Italy. March, 2017.
- Rare Disease Initiative Zurich (RADIZ) summer school, Tagungszentrum Schloss Au, Wädenswil, Zurich, Switzerland. June, 2017
- Biennial congress of the Italian Association of Cell Biology and Differentiation (ABCD), Bologna, Italy. September, 2017. *Awarded*
- Rare Disease Initiative Zurich (RADIZ) Symposium, Zurich, Switzerland. November, 2017
- 11th retreat of the PhD program in Integrative Molecular Medicine (imMed), Magglingen, Bern, Switzerland. June, 2016. *Awarded*

Publications:

1. Festa BP, Berquez M, Gassama A, Amrein I, Ismail HM, Samardzija M, Staiano L, Luciani A, Grimm C, Nussbaum RL, De Matteis MA, Dorchies OM, Scapozza L, Wolfer DP, Devuyst O. OCRL deficiency impairs endolysosomal function in a humanized mouse model for Lowe syndrome and Dent disease. ***Human Molecular Genetics.*** **2018** Dec 26; DOI: 10.1093/hmg/ddy449

2. Luciani A, Festa BP, Chen Z and Devuyst O. Defective autophagy degradation and abnormal tight junction-associated signaling drive epithelial dysfunction in cystinosis. ***Autophagy.*** **2018** May 28;14(7):1157-1159.

3. Festa BP, Chen Z, Berquez M, Debaix H, Tokonami N, Prange JA, Hoek GV, Alessio C, Raimondi A, Nevo N, Giles RH, Devuyst O, Luciani A. Impaired autophagy bridges lysosome storage disease and epithelial dysfunction in the kidney. ***Nature Communications.*** **2018** Jan 11; 9(161).

4. Chesi G, Hegde RN, Iacobacci S, Concilli M, Parashuraman S, Festa BP, Polishchuk EV, Di Tullio G, Carissimo A, Montefusco S, Canetti D, Monti M, Amoresano A, Pucci P, van de Sluis B, Lutsenko S, Luini A, Polishchuk RS. Identification of p38 MAPK and JNK as new targets for correction of Wilson disease-causing ATP7B mutants. ***Hepatology.*** **2016** Jun: 63(6):1842-59.

5. Fieten H, Gill Y, Martin AJ, Concilli M, Dirksen K, van Steenbeek FG, Spee B, van den Ingh TS, Martens EC, Festa P, Chesi G, van de Sluis B, Houwen RH, Watson AL, Aulchenko YS, Hodgkinson VL, Zhu S, Petris MJ, Polishchuk RS, Leegwater PA, Rothuizen J. The Menkes and Wilson disease genes counteract in copper toxicosis in Labrador retrievers: a new canine model for copper-metabolism disorders. ***Disease Models & Mechanisms***. **2016** Jan; 9(1):25-38.

Referees:

Prof. Dr. med. Olivier Devuyst
Institute of physiology, University of Zurich, Zurich, Switzerland
Tel +41 (0) 44 635 50 82
Email: olivier.devuyst@uzh.ch

Dr. Roman Polishchuk
Telethon Institute of Genetics and Medicine (TIGEM), Naples, Italy
Tel +39 081 19230636
Email: polishchuk@tigem.it

ACKNOWLEDGEMENTS

I would like to begin by acknowledging my mentor, Prof. Olivier Devuyst, for the continuous support of my Ph.D. study and related research, for his patience, motivation, and immense knowledge. His guidance helped me in all the time of research and writing of this thesis.

Every result described in this thesis was accomplished with the help and support of the fellow lab mates. In particular, I thank Alessandro Luciani for his advices and knowledge and many insightful discussions and suggestions. I thank Huguette Debaix and Nadine Nägele for their technical guidance during my PhD. I would like to express my gratitude to my dear friend Marine Berquez, who has been present during all my period spent in the laboratory. Her continuous support (moral and practical) and positivity has been a precious treasure for me. I will never forget all our adventures. I will look back at the time I spent with her as a wonderful enjoyable time of my life and I will miss her a lot. I am thankful to Alkaly Gassama, for his constructive criticism and friendly advice. I am also sincerely grateful to Alkaly to have been an honest and wise friend…someone you can always count on.

I would like to thank the members of my thesis committee: Prof. Andrew Hall, Prof. Prisca Liberali, Prof. Francesco Emma and Prof. Carmine Settembre, for their insightful comments and encouragement, but also for the hard questions which incented me to widen my research from various perspectives

Finally I would like to thank Eric Olinger. He has provided me with endless support, understanding and love throughout my PhD period. Without his sense of humor and optimisms, I would have never made it. I would like to thank Eric to get the best out of me with patience, day by day. A very special thanks goes to my brother Mariano and his wife Chiara. Without their love, encouragement and unconditional support, I would not have finished this thesis. Lastly, I dedicate this thesis to my loving parents, Anna and Antonio. I am very grateful for the emotional and intellectual support they have given me throughout my life. They have provided me with endless opportunities and instilled the idea that nothing is impossible with hard work and dedication. I will always thank them for teaching me this notion and I will never give up on my objectives.